

Dissertation zur Erlangung des Doktorgrades
der Fakultät für Chemie und Pharmazie
der Ludwig-Maximilians-Universität München

Synthesis and Functionalization of
Multifunctional Large-Pore Mesoporous Silica
Nanoparticles for Intracellular Protein
Delivery

Hsin-Yi Chiu

aus

Taoyuan, Taiwan

2017

Erklärung

Diese Dissertation wurde im Sinne von § 7 der Promotionsordnung vom 28. November 2011 von Herrn Prof. Dr. Thomas Bein betreut.

Eidesstattliche Versicherung

Diese Dissertation wurde eigenständig und ohne unerlaubte Hilfe bearbeitet.

München, 08.08.2017

Hsin-Yi Chiu

Dissertation eingereicht am 13.06.2017

1. Gutachter: Prof. Dr. Thomas Bein
2. Gutachter: Prof. Dr. Heinrich Leonhardt

Mündliche Prüfung am 25.07.2017

To my family

Acknowledgement

I would like to express my gratitude to those people who are important to me and accompanied me during my PhD time. Without your help and support, this doctoral dissertation could not be achieved.

My deepest gratitude goes first to my doktorvater, Prof. Thomas Bein, for his constant support and enlightening guidance throughout my PhD odyssey. Thank you for sharing me with your profound knowledge, invaluable ideas and suggestions in science which makes all the challenging projects possible and accomplished. Your kindness, patience and generous support in every stage of my PhD life are greatly appreciated.

I also want to express my deepest thankful to my co-supervisor, Prof. Heinrich Leonhardt, for his constant inspiration and encouragement during my PhD study. I enjoyed the time discussing science with you, and your clever and humorous way of talking. Thank you for sharing me not only science knowledge but also life experience which encourages me to be a good scientist.

I want to thank Dr. Hanna Engelke, my important scientific mentor, for her great help and support behind me. Thank you for advising me every time when I struggled in the science or life.

I want to thank Dr. Karin Möller, who is not only a nice colleague but also like a mother to me. I enjoyed the time working with you and talking to you in the lab not only about science but also everything. I am also appreciated that you take care of me so much and share life experience with me, making me feel like home in Germany.

I want to express many thanks to Regina Huber, the strongest support for me in AK Bein, for her great assistance in all the administrative matters. My life in LMU and in Germany became much easier with all your help.

I want to thank the members of mesobio group: Christian Argyo, Alexandra Schmidt, Stefan Niedermayer, Bastian Rühle, Stefan Datz, Noggi (Constantin von Schirnding), and Dorothee Gößl for their help and inspiring discussion in the lab. I really enjoyed working with you in the interesting drug delivery research topic.

I shall express my thanks to Dr. Weihua Qing, Dr. Wen Deng and Dr. Yan Li for their guidance in the lab and life in Germany in my first year of PhD, making me involved in the new environment quickly.

Many thanks to my collaboration partners: Jack Bates, Dr. Jonas Helma and James Frank, for their contributions in these projects. Thanks to Dr. Steffen Schmidt, Dr. Markus Döblinger, Dr. Hartmann Harz and Andreas Maiser for helping me in microscopy measurement. Also thanks to Tina Reuther for her great support in the lab.

I'm also grateful to my officemates: Maria Lohse, Erika Virmani, Alexander Hufnagel that we shared such a nice working atmosphere during my writing time and encouraged each from time to time.

I want to thank the whole members in AK Bein and AG Leonhardt with all the help and nice working atmosphere.

I want to thank the CeNS office, Marilena and Susanne Hennig, who provides all the help in bureaucratic administration tasks. And thanks to IDK and SFB1032 for funding me during the years working in Germany.

Last but not least, I deeply thank my beloved family who gave me the greatest support all the time. Without all your support and encouragement, everything is not possible for me to be here.

Abstract

Mesoporous silica nanoparticles (MSNs) feature several advantageous properties that render them promising nanoagents for applications in nanomedicine. Specifically, MSNs contain high surface area and large pore volume for high drug loading capacity, tunable pore size and internal surface chemistry for accommodation of a variety of guest molecules, stable frameworks for the protection of cargos from premature degradation, and versatile functionalization on the external surface for a broad spectrum of applications (e.g., controlled release or targeted delivery). Although the debut of MSNs in intracellular drug delivery was later than for the other advanced nanocarriers, such as liposomes and polyplexes, the significant recent progress of MSNs in biomedical research makes them one of the major family of nanomaterials for drug delivery systems. Moreover, since the recent development of siRNA and protein therapies have progressed rapidly, the synthesis of large-pore MSNs for encapsulating such sizable biomolecules becomes highly desirable.

The present work focuses on synthesizing and tailoring the surface properties of large-pore MSNs to create robust and multifunctional nanovehicles for protein delivery. Two types of large-pore MSNs with distinct mesostructures were synthesized: the SBA-15 MSNs and the stellate MSNs. The SBA-15 MSNs feature ordered hexagonal mesostructure with narrow pore size distribution of 7 nm. The synthesis was achieved by employing dual surfactants, FC-4 and Pluornic P123, in mildly acidic conditions for silica condensation followed by a hydrothermal treatment for ordered mesostructure formation. However, the as-synthesized silica particles exhibit a broad size distribution. After size separation by filtration, the resulting particles in suspension are in the size range of 100 – 200 nm. On the contrary, the stellate MSNs display homogeneous particle morphology and narrow particle size distribution (around 100 nm) upon completion of the silica condensation. The particles contain ultra-large pores (10 – 30 nm) with a conical shape that allows for efficient diffusion and accommodation of macromolecules. The synthesis of stellate MSNs was conducted *via* a facile route where tetraethoxysilane (TEOS, silica precursor) condenses around surfactant micelles formed by cetyltrimethylammonium p-toluene sulfonate (CTATos) in a near neutral precursor solution. This synthesis method appears to be amenable for upscaling. A delayed co-condensation approach was applied for both the synthesis of SBA-15 MSNs and stellate MSNs, yielding core-shell bifunctionalized SBA-15 MSNs and stellate MSNs, respectively. Cellular studies demonstrated good cellular uptake efficiencies and good biocompatibilities

for both the SBA-15 MSNs and stellate MSNs, respectively. Due to the favorable particle morphology and the facile synthesis approach, stellate MSNs were used in the following applications.

Core-shell stellate MSNs were modified with a aza-dibenzocyclooctyne (DBCO)-derivative on their inner surface to enable copper-free click chemistry reactions for immobilization of azide-terminated cargos. For example, 5-carboxytetramethylrhodamine azide (5-TAMRA Azide) dye was used as model cargo for *in vitro* cargo release tracking. In combination with stimuli-responsive linkers, such as redox-sensitive disulfide bridged or pH-sensitive acetal linkers between DBCO moieties and the surface of MSNs, we were able to control the cargo uptake and trigger the cargo release in buffers under specific conditions (e.g., buffers containing reducing agent glutathione or low pH).

To construct a generalized nanocarrier for protein delivery, nitrilotriacetic acid-metal ion (NTA-M²⁺) complexes were employed as anchors on the internal surface of stellate MSNs for pH-responsive controlled His-tagged protein immobilization and release. In a joint project with Prof. Leonhardt (LMU), we intended to directly transport chromobodies (fluorescently labeled single domain antibody fragments) intracellularly *via* our large-pore MSNs for antigen targeting and visualization in living cells. The NTA-Ca-modified MSNs demonstrated a high chromobody loading capacity (70 µg/mg MSN) and the successful transport of chromobodies into living cells. Several strategies were applied in order to resolve the endosomal entrapment of the internalized MSN-Cbs (chromobody-loaded MSNs). Among these strategies, the endosomolytic agent chloroquine enabled the most significant enhancement of chromobody release in the cytosol.

To systematically study the protein delivery efficiency of the NTA-M²⁺-complex-modified MSNs, a cell sensor based on a chemically inducible two-component fluorescent system was established for tracking the MSN-mediated protein delivery process. The cell sensor is background-free and molecularly ratiometric, which exclusively detects delivered protein that is both functionally viable and bioavailable. We applied this sensor in parallel with the MTT assay to maximize the protein delivery efficiency as well as the biocompatibility of our NTA-Ni-modified stellate MSNs. The *in vitro* protein transfection efficiency reaches up to 80% after optimizing the MSN incubation concentration to 100 µg/ml. Furthermore, in this study we demonstrated a novel protein delivery tracking approach in live cell imaging with good

temporal resolution, and disentangled the timing of protein uptake from that of sensor dynamics through the use of built-in chemically inducible components.

Finally, in a collaborative project with Prof. Trauner (LMU), two types of photoswitchable supported lipid bilayers (SLBs) based on two different photo-sensitive lipids, AzoPC (azobenzene-containing phospholipid) and DC_{8,9}PC (1,2-bis(10,12-tricosadiynoyl)-sn-glycero-3-phosphocholine), were created on the surface of stellate MSNs. AzoPC and DC_{8,9}PC exhibit distinct photochemical responses (photoisomerization for AzoPC and photopolymerization for DC_{8,9}PC) and are sensitive to different wavelength ranges (320 – 350 nm for AzoPC, 254 nm for DC_{8,9}PC). Upon irradiation with the appropriate wavelengths, both AzoPC-SLB and DC_{8,9}PC-SLB capped MSNs demonstrated photo-induced cargo release abilities.

To summarize, we have established versatile large-pore multifunctional MSNs and demonstrated their stimuli-responsive controlled release abilities for several possible applications. Successful intracellular protein delivery using our large-pore multifunctional MSNs was also performed. We envision these large-pore multifunctional MSNs to provide a new platform for the facile delivery of biomacromolecules in future applications of nanomedicine.

Table of contents

1	Introduction.....	1
1.1	Mesoporous Silica Materials	1
1.1.1	Ordered Porous Materials	1
1.1.2	The Development of Mesoporous Silica Materials	1
1.1.3	Large-Pore Mesoporous Silica Nanoparticles	4
1.1.4	Multifunctional Mesoporous Silica Nanoparticles for Drug Delivery	8
1.2	Intracellular Protein Delivery	12
1.2.1	Protein Therapy.....	12
1.2.2	Intracellular Protein Delivery Strategies.....	14
1.2.3	Endosomal Escape	18
1.3	References	24
2	Characterization Techniques.....	33
2.1	Nitrogen Physisorption.....	33
2.2	Dynamic Light Scattering (DLS)	38
2.3	Zeta Potential Measurement.....	39
2.4	Infrared (IR) and Raman Spectroscopy.....	41
2.5	UV-Vis Spectroscopy.....	43
2.6	Thermogravimetric Analysis (TGA).....	43
2.7	X-ray Diffraction (XRD).....	44

2.8	Fluorescence Spectroscopy	46
2.9	Electron Microscopy	47
2.9.1	Transmission Electron Microscopy (TEM)	48
2.9.2	Scanning Electron Microscopy (SEM)	50
2.9.3	Scanning Transmission Electron Microscopy (STEM)	51
2.10	Confocal Microscopy	52
2.11	References	55
3	Synthesis and Functionalization of Ordered Large-Pore Mesoporous Silica Nanoparticles for Biomedical Applications	57
3.1	Introduction	57
3.2	Results and Discussion.....	60
3.3	Conclusion.....	69
3.4	Experimental	69
3.5	Appendix	77
3.6	References	79
4	Clickable Multifunctional Large-Pore Mesoporous Silica Nanoparticles as Nanocarriers	83
4.1	Introduction	84
4.2	Results and Discussion.....	86
4.3	Conclusion.....	96
4.4	Experimental	97
4.5	Appendix	103

4.6	References	107
5	Intracellular Chromobody Delivery by Mesoporous Silica Nanoparticles for Antigen Targeting and Visualization in Real Time	111
5.1	Introduction	112
5.2	Results	114
5.3	Discussion	127
5.4	Experimental	128
5.5	Appendix	136
5.6	References	142
6	Optimisation and Live Cell Tracking of Nanoparticle Mediated Protein Delivery Through an Inducible Split Venus Based System.....	145
6.1	Introduction	146
6.2	Results and Discussion.....	149
6.3	Conclusion.....	157
6.4	Experimental	158
6.5	Appendix	165
6.6	References	167
7	Photoswitchable Supported Lipid Bilayers on Large-Pore Mesoporous Silica Nanoparticles For Controlled Release Applications.....	171
7.1	Introduction	171
7.2	Results and Discussion.....	175
7.3	Conclusions and Outlook	181

7.4	Experimental	182
7.5	Appendix	186
7.6	References	187
8	Conclusions and Outlook	189
9	Curriculum Vitae.....	193

1 Introduction

1.1 Mesoporous Silica Materials

1.1.1 Ordered Porous Materials

Porous materials are of interest in scientific research because they contain unique surface and structural properties which can interact with atoms, ions and molecules.¹ Before the early 1990s, crystalline microporous zeolites (mainly composed of aluminosilicates) were regarded as the prototype of ordered porous materials. For decades, zeolites had shown great success in industrial applications such as catalysis, separation and ion exchange.^{2,3} Despite of these successes, the micropores of zeolites ranging from about 0.3 – 1.4 nm still restrict their uses to the adsorption and diffusion of small molecules. Offering to overcome the mass transfer bottleneck for large molecules as well as to broaden the application range of porous materials beyond the traditional uses as catalysts and adsorbents, a new type of silica-based molecular sieves containing ordered pore size larger than 2 nm has emerged in the 1990s.⁴⁻⁶ Motivated by these pioneering studies, the synthesis of mesoporous silica materials with different porous structures and dimensions has developed rapidly and has opened up a new perspective for the applications of porous materials.

1.1.2 The Development of Mesoporous Silica Materials

In the early 1990s, ordered mesoporous silica materials have been synthesized independently in the group of Kato in Japan⁴ and at the Mobil Research and Development Corporation.^{5,7} Beck and co-workers at Mobil first proposed the “template” concept in the synthesis approach, using quaternary ammonium salts such as cetyltrimethylammonium bromide (CTAB) or cetyltrimethylammonium chloride (CTAC) as structure-directing agents to form liquid crystalline micelles in solution. Upon addition of silicate gels (dissolved in basic solution) to the surfactant solution, the mixture was reacted at elevated temperature (about 100 – 150 °C) in order to attain ordered mesostructures. After template removal by calcination, the resulting materials featured long-range ordered mesopores surrounded by amorphous silica walls, high surface areas of about 1000 cm²/g, and narrow pore size distributions in the range of 3 – 5 nm. When incorporating auxiliary agents into the liquid crystalline micelles, the pore size could be expanded to 10 nm. This new type of mesoporous silica molecular sieves was named the M41S family.^{5,7} Representatives of the M41S

materials are hexagonal-pore-structured MCM-41 (MCM implies Mobil Composition of Matter), cubic-pore-structured MCM-48 and lamellar-structured MCM-50 (Figure 1.1). The alteration of porous structures can be achieved by adjusting the molar composition of the reaction solution.⁸

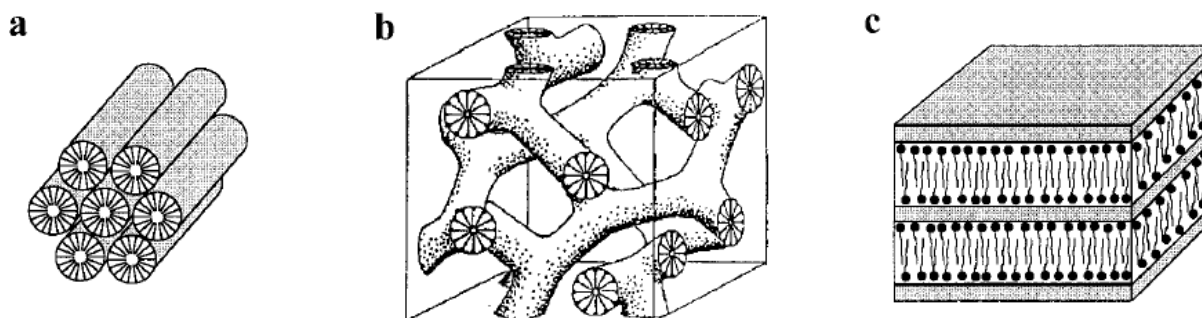


Figure 1.1 Three mesoporous silica representatives in the M41S family.⁸ (a) MCM-41 (2D hexagonal pore structure). (b) MCM-48 (3D cubic pore structure). (c) MCM-50 (1D lamellar structure).

A few years later, another prominent type of mesoporous silica materials, designated as SBA (Santa Barbara Amorphous) materials, has been synthesized at the University of California, Santa Barbara.^{6,9} Stucky *et al.* employed non-ionic triblock-copolymers as structure-directing agents in an acidic synthesis condition, in which they obtained mesoporous silicas with large pores of 5 – 30 nm. The structure directing triblock-copolymers are composed of poly(ethylene oxide)_x-poly(propylene oxide)_y-poly(ethylene oxide)_x (PEO_x-PPO_y-PEO_x) units with variable x and y chain lengths. During the synthesis, the copolymers formed micellar aggregates where the hydrophobic PPO units aggregate into cores and the hydrophilic PEO units extend into water and associate with a silicate corona.^{10,11} The micelles then pack into large cylindrical domains followed by silica condensation around the micellar domains. Hydrothermal treatment at 100 °C is subsequently performed to gain an ordered porous structure. By applying different triblock copolymers that contain variable x and y compositions, distinct mesostructures can be obtained. The most well-known SBA-type materials are SBA-15 and SBA-16, the former is templated by Pluronic P123 and exhibits 2D hexagonal mesopores while the latter is templated by Pluronic F127 and contains a 3D cubic mesostructure (Figure 1.2).

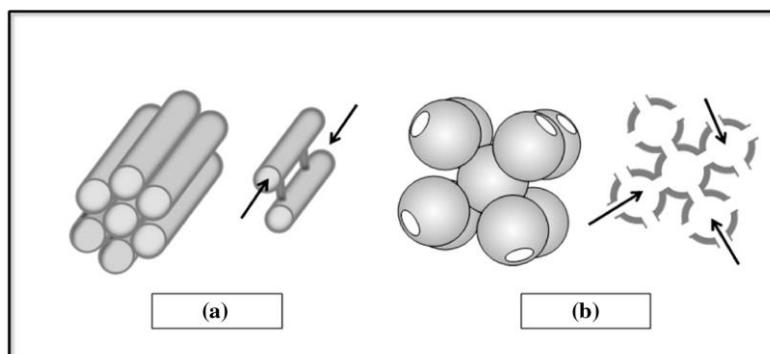


Figure 1.2 Schematic illustration of the porous structures of (a) SBA-15 (channel-like) and (b) SBA-16 (nanocage-like).¹²

Following the achievements of MCM-type and SBA-type mesoporous silica synthesis, the soft-templating technique has been widely expanded in the following years for the synthesis of diverse mesostructured silica materials. Several extended applications for mesoporous silica materials were subsequently accomplished, for example, high performance liquid chromatography for biomolecule separation,¹³ low dielectric constant films in microelectronic devices,^{14,15} and controlled release of drug molecules.¹⁶ Among the variety of applications, controlled release of drugs is of particular interest owing to the unique structural properties of mesoporous silica materials, including high surface area and large pore volume that enable a high level of guest molecule immobilization.

Over the years, scientists spent great efforts on controlling the particle size and morphology of mesoporous silica materials to make them suitable for biomedical applications. It has been suggested to confine the particle size to smaller than 200 nm in order to achieve better cellular uptake efficiency.¹⁷ Therefore, the synthesis of nanosized mesoporous silicas with colloidal stability became prevalent in the last years of the 20th century. Around 2003, Lin and his co-workers presented MCM-41-type mesoporous silica nanoparticles (MSNs) capped with chemically removable CdS nanoparticles for controlled drug release and applied the system in living cells.¹⁸ This research has prompted the rapid development of nanomedicine applications of MSNs. Since then, a large number of studies regarding MSNs for the delivery of a variety of therapeutics have been published.¹⁹⁻²¹ However, most of the drug delivery tasks have been achieved using small-pore (≤ 4 nm) MSNs. For sizable biomolecules such as siRNA, proteins and plasmid DNA, large-pore MSNs are required to achieve high loading and to encapsulate the cargos inside the mesopores for better protection from degradation in physiological environments.

1.1.3 Large-Pore Mesoporous Silica Nanoparticles

In general, there are two major strategies to synthesize large-pore (> 5 nm) mesoporous silica materials: (i) using amphiphilic copolymers as structure-directing templates and (ii) incorporating organic pore-swelling agents into the surfactant micelles to increase the size of templates and thus the pores.²² In 2004, Ying *et al.* introduced a cationic fluorocarbon surfactant FC-4 ($\text{C}_3\text{F}_7\text{O}(\text{CFCF}_3\text{CF}_2\text{O})_2\text{CFCF}_3\text{CONH}(\text{CH}_2)_3\text{N}^+(\text{C}_2\text{H}_5)_2\text{CH}_3\text{I}$) into the synthesis of mesoporous silica materials templated by nonionic triblock copolymers.²³ In this study, FC-4 was used as co-surfactant in combination with different triblock copolymers including Pluronic F127, P123, P65 and F108, respectively. After a slow silica condensation process in mildly acidic solutions (pH 1.6-1.8) at a moderate temperature (35 °C), the nanosized (50 – 300 nm) silica particles featuring different mesostructures and pore sizes (5 – 30 nm) were obtained (Figure 1.3 and Table 1.1). The authors proposed that the FC-4 surfactant served as a particle growth inhibitor to confine the particle sizes in the synthesis process whereas the copolymers acted as structure-directing agents to enable ordered mesostructure formation. The resulting large-pore MSNs containing ordered mesopores and well-defined particle sizes were regarded as promising nanocarriers for encapsulation and delivery of sizable biomolecules. Thereafter, several research groups have adopted this synthetic strategy and applied the synthesized large-pore MSNs for different applications²⁴⁻²⁷ (for a detailed review, please see Chapter 3).

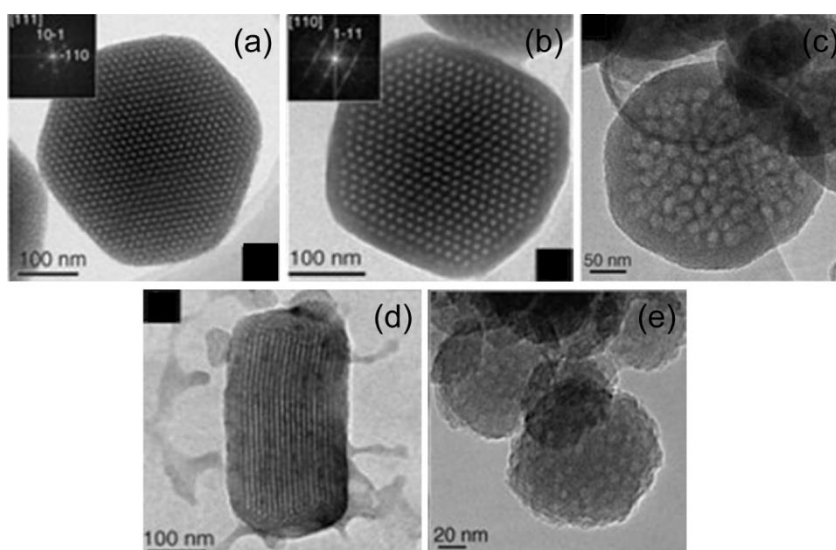


Figure 1.3 Mesoporous silica nanoparticles obtained in the fluorocarbon-surfactant-mediated synthesis.²³ (a) IBN-1, (b) IBN-2, (c) IBN-3, (d) IBN-4 and (e) IBN-5.

Table 1.1 Characteristics of mesoporous silica nanoparticles obtained in the fluorocarbon-surfactant-mediated synthesis.²³

Sample	Mesostructure	Template	BET surface area (m ² /g)	Pore volume (cm ³ /g)	Pore size (nm)
IBN-1	3D cubic (<i>Im3m</i>)	F127	779	0.73	5.8
IBN-2	3D cubic (<i>Im3m</i>)	F127+TMB	804	0.65	9.5
IBN-3	Mesocellular foam	P65+TMB	821	0.72	19.5
IBN-4	2D hexagonal (<i>p6m</i>)	P123	709	0.88	6.4
IBN-5	Disordered	F108	575	0.54	5.2

Although the fluorocarbon-mediated synthesis strategy yields large-pore MSNs with highly ordered mesostructures, the as-synthesized materials often contain significant amounts of bulk silica showing some particle agglomeration, resulting in broad particle size distributions of the samples.²⁸ The long synthesis process including 24 h of silica condensation and at least another 24 h for hydrothermal treatment also makes this approach somewhat less attractive.

On the contrary, using cetyltrimethylammonium (CTA⁺) salts (e.g., CTAC or CTAB) for MSN synthesis under base-catalyzed conditions is more facile and produces more homogeneous particle sizes. By inclusion of organic auxiliary agents in the surfactant solutions, it is possible to enlarge the pore size of MSNs. Several organic molecules such as 1,3,5-trimethylbenzene (TMB),²⁹ decane,³⁰ N,N-dimethylhexadecylamine (DMHA)²⁸ and 1,3,5-triisopropylbenzene (TiPB)^{31,32} were employed in the CTAC or CTAB templated MSN synthesis for pore size expansion. However, the pore expansion effect is limited in that the resulting pore sizes are only in the range of 5 – 6 nm. Nevertheless, our colleagues in the group have reported that these medium-pore MSNs are already sufficient for encapsulation of siRNA. The controlled loading and release of siRNA with these medium-pore MSNs are better than with the large-pore MSNs synthesized in the FC-4-mediated approach.³²

Inspired by the aforementioned cetyltrimethylammonium templating MSN synthesis approach, Zhang and coworkers established a facile route to synthesize monodispersed stellate MSNs (Figure 1.4) having ultra-large pores in the range of 10 – 20 nm and particle

size of about 100 nm.³³ Impressively, they are able to produce MSNs at a kilogram scale. They used cetyltrimethylammonium tosylate (CTATos) as templating surfactant and triggered silicate condensation at near neutral conditions where the tosylate (Tos⁻) counterions compete with negative silicates in the surfactant-silicate self-assembly process, yielding more agglomeration of micelles and thus modifying the silica framework to create a stellate shape (Figure 1.5). The conical pore shape with large pore mouth is accessible for the mass transfer and the adsorption of large cargos. In this thesis, we also adopted this synthesis strategy in addition to surface functionalization to construct multifunctional large-pore MSNs for intracellular protein delivery (see Chapter 5 and Chapter 6).³⁴

Other significant synthesis methods for different types of large-pore MSN synthesis are also worth noting: (i) the amphiphilic block copolymer (polystyrene-*b*-poly (acrylic acid), PS-*b*-PAA) and CTAB co-templated large-pore MSNs;^{35,36} (ii) modified swelling agent pore-expansion synthesis strategy (using TMB and ethanol for pore etching at high temperature);³⁷ (iii) hollow silica nanospheres synthesized using a water-in-oil microemulsion as template,³⁸ etc. (Figure 1.6).

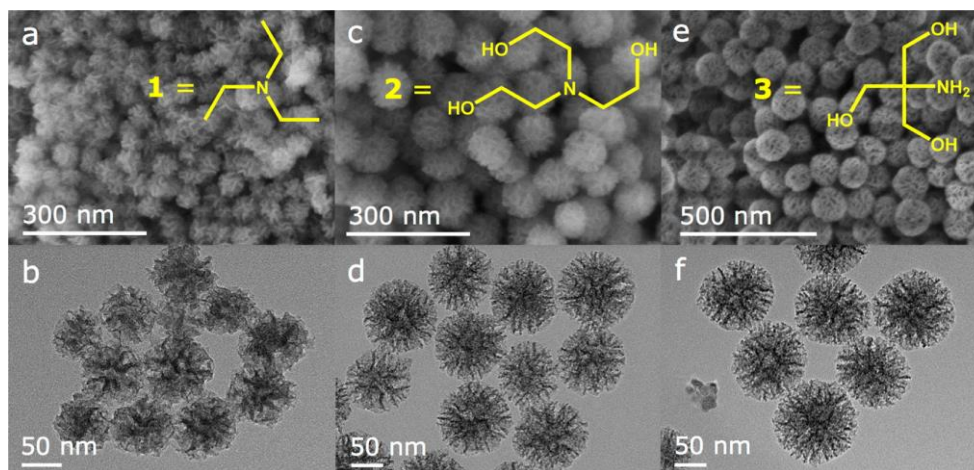


Figure 1.4 SEM (top) and TEM (bottom) images of stellate MSNs synthesized using CTATos as templating surfactant.³³ MSNs synthesized using triethylamine (a, b) or triethanolamine (c, d) or 2-amino-2-(hydroxymethyl)propane-1,3-diol (e, f) as catalytic small organic amines (SOAs) for silica condensation.

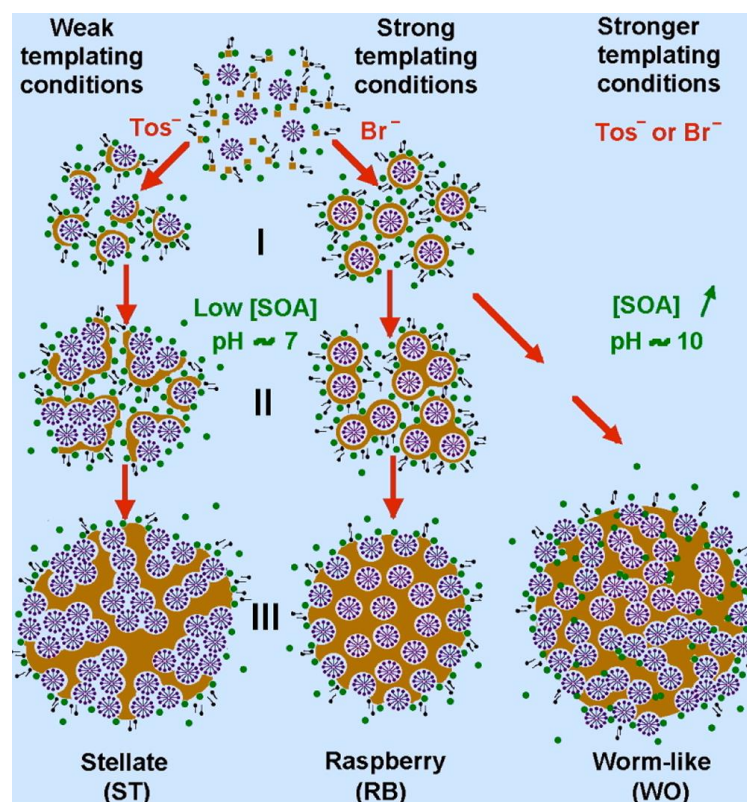


Figure 1.5 Proposed MSN synthesis mechanisms at low or high pH in solutions using CTATos or CTAB as templating surfactants.³³

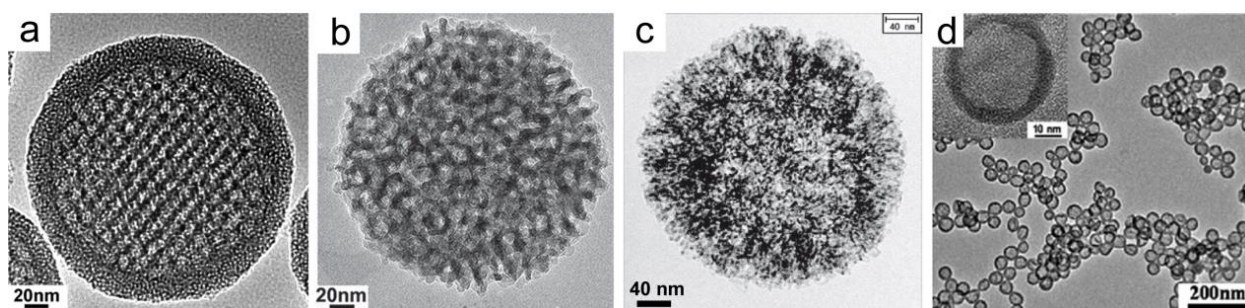


Figure 1.6 Large-pore MSNs synthesized by different methods. (a) Core-shell structured dual-mesoporous silica nanosphere synthesized via PS-*b*-PAA and CTAB co-templated approach.³⁵ (b) Large-pore silica nanosphere synthesized via PS-*b*-PAA and CTAB co-templated approach with high ethanol content.³⁶ (c) Irregular large-pore MSNs obtained from a modified swelling agent pore-expansion strategy.³⁹ (d) Hollow silica nanospheres synthesized using a water-in-oil microemulsion as template.³⁸

1.1.4 Multifunctional Mesoporous Silica Nanoparticles for Drug Delivery

MSNs feature several advantageous properties including high surface area, large pore volume, tunable pore size, stable frameworks, ease of surface modification and good biocompatibility that renders them suitable for drug delivery applications. Specifically, the high surface area and large pore volume enables encapsulation of decent amounts of therapeutics; tunable pore size allows for immobilization of cargos in various sizes; the stable silica framework can protect cargos from enzymatic or chemical degradation; ease of surface modification enables the attachment of functional assemblies, e.g., targeting ligands and stimuli-responsive gatekeepers, etc.. MSNs have shown great success in the delivery of a variety of therapeutics including anti-cancer drugs,⁴⁰⁻⁴⁴ oligonucleotides^{25,32,39,44,45} and proteins⁴⁶⁻⁴⁸ either *in vitro* or *in vivo* for disease treatment or for biological research. In addition to drug delivery, MSNs can also be used for imaging purposes⁴⁹ either at the cellular level for cell biology³⁴ studies or for disease diagnosis such as magnetic resonance imaging (MRI)⁵⁰⁻⁵² and positron emission tomography (PET).⁵³ Figure 1.7 demonstrates a multifunctional MSN model as an autonomous nanoagent for different biomedical applications. The integrated functions ideally include a porous framework for cargo loading, a gate keeper system for controlled cargo release, tracking markers for particle tracing, spacer molecules (e.g., polyethylene glycol, PEG) to enhance the solubility and biocompatibility, targeting ligands to enable a specific targeting delivery, and endosomal escape agents to trigger cargo release from trapped endosomes.

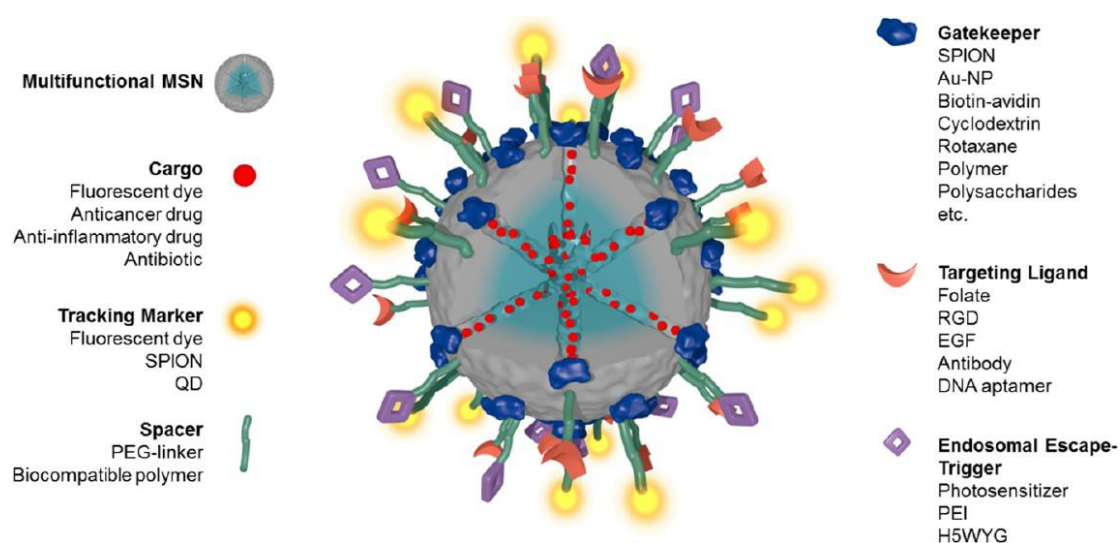


Figure 1.7 Schematic representation of a multifunctional mesoporous silica nanoparticle serving as an autonomous nanoagent in biomedical applications.¹⁹

In order to attach these functional features on the surface of the MSNs, incorporation of organic functional groups, e.g., amino groups, thiol groups, carboxylic groups, etc., into the silica framework to enable a subsequent chemical cross-linking process is required. The incorporation of functional groups can be achieved by either post-synthetic grafting or co-condensation methods. In the post-synthetic grafting approach, functional silanes attach to the surface of MSNs after the particle structure is formed. This can be performed before or after surfactant extraction, hence resulting in only outer shell or entire surface functionalization. In the co-condensation synthesis process, organosilanes and tetraethoxysilane (TEOS) undergo hydrolysis and condensation simultaneously in solution, leading to the incorporation of functional groups in the silica framework during particle formation. By employing a delayed co-condensation strategy, site-selective core-shell bifunctional MSNs can be obtained.⁵⁴ Apart from the intention of performing cross-linking chemistry to attach functional ligands, surface functionalization also allows for the alteration of hydrophobic/hydrophilic properties of the MSNs that can strongly affect their cargo immobilization behavior. For example, several studies have shown that functionalization with positively charged moieties (e.g., amino groups or positively charged polymer) is required to enhance the loading/adsorbing efficiency for negatively charged siRNA or DNA.^{24,25,32,55}

When Lin and co-workers first initiated the idea of engineering MSNs as drug delivery systems in 2003, they also presented the concept of introducing stimuli-responsive gatekeepers in MSN systems for controlled cargo release.¹⁸ The original proposal of stimuli-responsive drug delivery can be dated to the late 1970s with the use of thermosensitive liposomes for the local release of drugs through hyperthermia.⁵⁶ Thanks to the development of materials chemistry and nanomedicine, the inclusion of stimuli-responsive moieties in the drug delivery system enables the delivery of payload in spatio-, temporal- and dosage-controlled manners. For the MSN-based drug delivery system, capping the pores to prevent premature leakage of cargos and triggering the release at the targeted destination have also been suggested. Various stimuli-responsive gating systems have been successfully applied to MSNs for controlled cargo release.^{19,57} The response triggers of these strategies can be classified based on (i) exogenous stimuli: variations in temperature,⁵⁸ light,^{31,59} magnetic field,⁶⁰ ultrasound intensity⁶¹ and electric potential⁶² or (ii) endogenous stimuli: changes in pH,^{34,41,63} enzyme concentration^{40,64,65} and redox gradients^{18,66} (Figure 1.8).

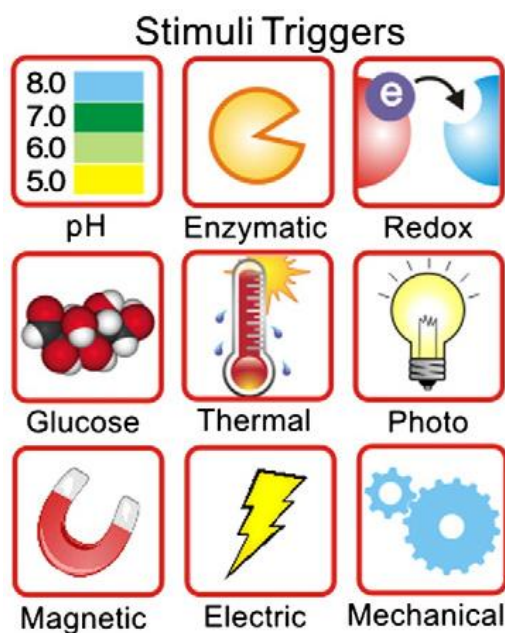


Figure 1.8 Schematic representation of different stimuli triggers for drug controlled release.⁶⁷

Other surface coatings including PEG chains and supported lipid bilayers (SLBs) have been reported to enhance the dispersity, biocompatibility and *in vivo* circulation half-life of the MSNs.^{19,68-70} Different types of endosomal escape agents, for example, fusogenic peptides,⁷¹ high buffering capacity dendrimers⁷² and cationic polymers³² have been incorporated into MSNs and demonstrated the endosomal destabilization ability in triggering cargo release.

Although targeting-ligand-attached MSNs showed significant efficiency for cellular targeting *in vitro*,^{31,71,73} the *in vivo* targeting efficacy needs to be further investigated. For cancer targeting therapy, there are several *in vivo* barriers which can hinder the site-specific accumulation of nanocarriers.^{68,74,75} For instance, nanoparticles can be taken up by the liver, spleen or the macrophage system in the body depending on the sizes and surface characteristics of the nanocarriers. Choi *et al.* used quantum dots as model system to study the biodistribution of different sizes and surface charges of nanoparticles in rodents upon intravenous administration.⁷⁶ The results indicated that particles with diameters < 5.5 nm rapidly undergo renal clearance. On the other hand, zwitterionic or neutral organic-coated particles with a hydrodynamic diameter expanded to > 15 nm can prevent the renal excretion as well as the adsorption of serum proteins. It has also been reported that particles with more hydrophobic surfaces tend to be captured by the liver, followed by spleen and lungs.⁷⁷ Moreover, in the blood stream nanoparticles are likely to be coated with some opsonin

proteins (e.g., fibronectin, thrombospondin, laminin, etc.). The adsorbed proteins can interact with specific plasma membrane receptors on phagocytic cells, leading to the internalization and clearance of the protein-nanoparticle complexes. The phagocytic clearance is the main clearance pathway for nanoparticles to be removed from the blood circulation.⁶⁸ Therefore attachment of a hydrophilic PEG shell, “don’t eat-me” marker CD47, “self” peptides to create stealth nanoparticles, or coating particles with supported-lipid bilayers are beneficial strategies to enhance the circulation half-lives of nanocarriers.⁷⁵

1.2 Intracellular Protein Delivery

1.2.1 Protein Therapy

Proteins perform the most dynamic and diverse functions of any large biomolecules within organisms, including catalyzing biochemical reactions, DNA replication, responding to stimuli, and transporting objects from one location to the other.⁷⁸ This vast array of biological activities can also make proteins potent therapeutics. Protein therapy can have several advantages over treatments performed with small-molecule drugs,⁷⁸ for example: (i) proteins exhibit a highly specific and complex set of functions that cannot be imitated by simple organic compounds; (ii) the highly specific action of proteins implies fewer interferences with other non-related biological processes, causing less adverse effects on normal cell behavior; (iii) proteins are naturally existent in the body, thus therapeutic proteins derived from natural proteins may be less likely to elicit immune responses. Furthermore, protein therapy is considered to be safer for the treatment of genetic disorders than gene therapy which has the potential risk of insertional mutagenesis.

Thanks to the invention of recombinant DNA technology, protein production has become more facile and cost-effective, which has aided in the development of the modern biopharmaceutical industry. Recombinant technology for protein therapeutics manufacture allows for large-scale production, precise transcription and translation of human genes, which decreases the chances of immunological rejection, modification of proteins or selection of particular gene variants to improve protein function and specificity, and reduction of exposure to animal or human diseases during production.⁷⁸ In 1982, the recombinant human insulin (Humulin[®]) developed by Genentech⁷⁹ was approved by the US Food and Drug Administration (FDA) and became the first commercial protein therapeutic. Up to 2013, about 91 recombinant-protein-based new molecular entities in total have been approved by the FDA as therapeutics.⁸⁰ Protein therapeutics can be classified into four major groups based on their pharmacological activities,⁷⁸ the details are listed in Table 1.2.

Table 1.2 Functional classification of protein therapeutics.⁷⁸

Group I: Enzymes and regulatory proteins	
<i>Pharmacological activities</i>	Ia. Replacing a protein that is deficient or abnormal Ib. Augmenting an existing pathway Ic. Providing a novel function or activity
<i>Examples of therapeutic application</i>	Ia. Insulin for diabetes treatment; pooled immunoglobulins for primary immunodeficiencies treatment Ib. Erythropoietin for haematopoietic defect treatment Ic. Collagenase for the digestion of collagen in the necrotic base of wounds
Group II: Targeted proteins	
<i>Pharmacological activities</i>	IIa. Interfering with a molecule or organism IIb. Delivering other compounds or proteins
<i>Examples of therapeutic application</i>	IIa. Cetuximab, a monoclonal antibody that binds epidermal growth factor receptor (EGFR) and impairs cancer cell growth and proliferation, for colorectal cancer and head and neck cancer treatment. IIb. Gemtuzumab ozogamicin, a monoclonal antibody (against CD33)-calicheamicin (a chemotherapeutic agent) complex, for CD33-positive acute myeloid leukaemia treatment.
Group III: Protein vaccines	
<i>Pharmacological activities</i>	IIIa. Protecting against a deleterious foreign agent IIIb. Treating an autoimmune disease IIIc. Treating cancer
<i>Examples of therapeutic application</i>	IIIa. Hepatitis B vaccine composed of recombinant hepatitis B surface antigen (HBsAg) proteins IIIb. Anti-Rhesus (Rh) immunoglobulin G for the protection of an Rh-negative mother at the time of delivery of an Rh-positive neonate IIIc. Sipuleucel-T (trade name: Provenge [®]) for prostate cancer treatment
Group IV: Protein diagnostics	
<i>Pharmacological activities</i>	<i>In vitro</i> or <i>in vivo</i> medical diagnostics
<i>Examples of therapeutic application</i>	Natural and recombinant HIV antigens for HIV infection detection (by means of ELISA or western blot)

1.2.2 Intracellular Protein Delivery Strategies

Intracellular delivery of therapeutic proteins is of great importance for the treatment of protein deficient/malfunction diseases as well as cancer. Besides the clinical applications, intracellular protein delivery is likewise of significance in scientific research for the investigation and manipulation of cellular processes. However, many constraints including instability and low cell-membrane permeability of proteins usually result in poor intracellular delivery efficiency.⁸¹⁻⁸³ In order to overcome these challenges, substantial effort has been devoted to develop better techniques capable of packing proteins in a proper formulation, thus transporting proteins to cytosolic compartments in a more efficient manner.

Cell-penetrating peptides (CPPs) are short peptides of less than 30 amino acids that feature the ability of penetrating through the cell membrane and translocating different cargos into cells. CPPs were the first tools used in protein transduction⁸⁴ and to date are the best evaluated and widely used tools for intracellular macromolecule delivery.⁸⁵ The well-known cell-penetrating peptides include the trans-activating transcriptional activator (TAT) peptide from HIV-1, penetratin peptide from *Drosophila* antennapedia homeoprotein, VP22 peptide from the herpes simplex virus VP22 protein and the synthetic polyarginine peptides, etc.. There are two major pathways for CPP-mediated cargo delivery: (i) direct translocation across cell membranes through an energy-independent mechanism and (ii) endocytosis.⁸⁶ The uptake mechanism is highly dependent on the conjugated cargo. It was reported that certain CPPs can directly translocate across the plasma membrane when the attached cargos are small in size.⁸⁷ However, when conjugated to macromolecules or when used at low concentrations, CPP-cargo complexes would be taken up by cells *via* an endocytic pathway.⁸⁸ In this case, most of the cargo would be trapped in endosomes. Many reports have indicated that the CPPs can subsequently induce an endosomal escape pathway and further promote the cargo release.⁸⁷ Nevertheless, the endosomolytic activity of CPPs is still very poor comparing to the efficiency of internalization by cells. The CPP-mediated cellular delivery often requires covalent conjugation of CPPs with proteins *via* genetic encoding, which makes this approach difficult to be generalized, and sometimes the conjugation might alter the properties and functions of proteins. Recently Erazo-Oliveras *et al.* reported a highly efficient CPP-mediated protein delivery approach by simple co-incubation of dimeric fluorescent dye-labelled TAT (dfTAT) and targeted proteins in cell culture medium. They achieved cytosolic delivery in several cell lines and demonstrated simultaneous delivery of multiple molecules.⁸⁹ Although

the CPP-based protein delivery strategy exhibits high efficiency *in vitro*, the toxicity and immunogenicity of CPPs are still concerns when exploited *in vivo*.⁸⁶

Alternatively, nanocarriers can be good candidates for transporting exogenous proteins intracellularly. Nanocarrier-based delivery systems offer the ability to tailor their physical and chemical properties through controlled synthesis for cargo accommodation, and can be modified with multiple functionalities for tuning the delivery processes. The potential benefits of employing nanocarriers in intracellular delivery include high molecular loading, packaging the cargos and protecting them from degradation, increasing the possibility of reaching the intended intracellular compartments, and controlling the cargo release with appropriate spatiotemporal dynamics.⁹⁰ When applied *in vivo*, nanocarriers are capable of shielding proteins from eliciting immune responses of the body, and in addition, the bigger size of the packed nanocarrier-protein complexes can make it easier to escape rapid renal filtration.^{91,92} A variety of nanocarriers have been developed for drug delivery, including lipid-based nanocarriers, polymeric nanocarriers, inorganic nanocarriers and protein-mediated nanocarriers (Figure 1.9(a)). The cargo loading can be achieved by facile routes such as direct conjugation *via* chemical crosslinking, physical adsorption on the external/internal surface or encapsulation in the framework of nanocarriers (Figure 1.9(b)).⁹²

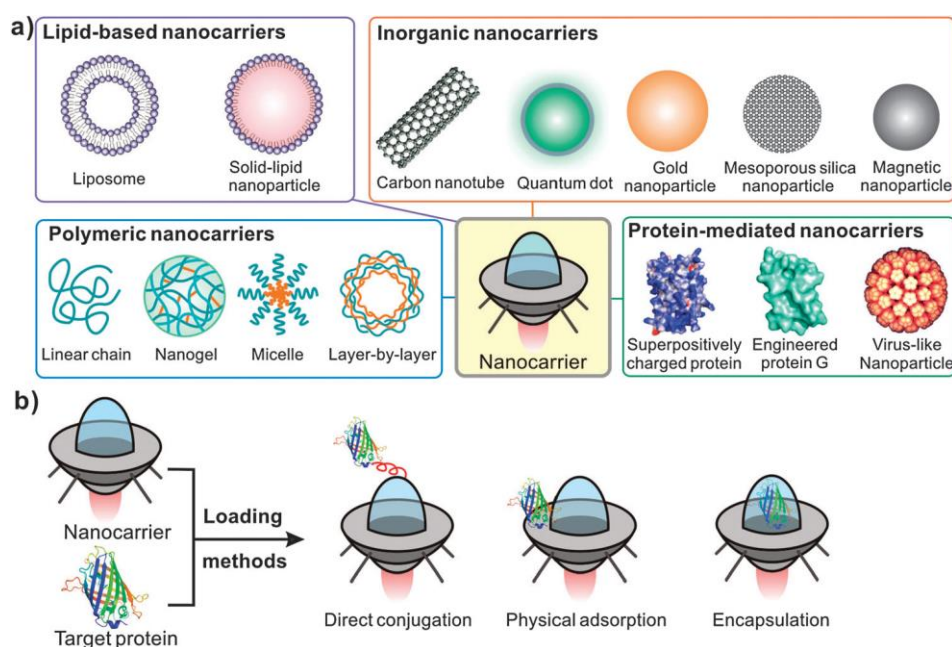


Figure 1.9 Different types of nanocarriers (a) and cargo loading methods (b).⁹²

In the following sections we will review some commonly used nanocarriers for applications in drug delivery.

Liposomes: liposomes are a class of lipid-based vesicles capable of adhering to plasma membranes followed by entering cells through endocytosis or liposome-cell fusion.⁹³ Liposomes feature versatility in compositions and functions, and have shown great abilities in the delivery of various cargos like small molecules, siRNA, DNA and proteins.⁹³⁻⁹⁵ The advantages of using liposomes as drug delivery vehicles are their high loading capacity (strongly depending on cargo), the capability of delivering hydrophilic and hydrophobic drugs simultaneously, good biocompatibility and biodegradability, and high cellular uptake efficiency.⁹³ There are various types of liposomes that can be classified either by their compositional character or the stimuli-responses, for example, conventional (neutral) liposomes, cationic liposomes, pH-sensitive liposomes, thermo-sensitive liposomes and long-circulating liposomes.⁹³ Among these types, pH-sensitive and cationic liposomes are the mostly used carriers for cellular delivery due to their ability of promoting endosomal release of the cargos (for details, see “Endosomal Escape” chapter).^{91,96} However, the stability is a major consideration of liposomes either for storage or during the delivery process.⁹³ For instance, the fusion and breakage of liposomes may lead to drug leakage.

Polymeric nanocarriers: polymers can be synthesized with defined composition and modified with various functionalities (e.g., conjugation with targeting ligand) that render them attractive vectors for protein delivery. The most famed and commonly used polymeric nanocarriers are polymeric micelles, which are normally comprised of amphiphilic block copolymers. The amphiphilic block copolymers form micelles (5 – 100 nm) in solution when the concentration of the polymer is above a critical micelle concentration (CMC),⁹⁷ where the hydrophobic blocks of the polymer aggregate into a micellar core while the hydrophilic blocks associate with the surrounding water through hydrogen bonding thus forming a hydrophilic outer shell. The mostly used block copolymers usually contain PEG chains as the hydrophilic blocks and poly(propylene oxide)s, poly(L-amino acid)s or poly(ester)s as hydrophobic blocks.⁹⁸ With the polymeric micelles, drugs or biologically active substances can be encapsulated in the hydrophobic core. For protein encapsulation, the hydrophobic core is made by complexing a section of polymer chain with protein molecules *via* electrostatic interactions, hydrophobic interactions, or other noncovalent interactions. However, the stability of the micellar complexes and the potential protein denaturation during

complexation are still problematic.⁹¹ The complexes may dissociate rapidly upon dilution or through the competitive binding of serum with polymers *in vivo*.⁹¹ To resolve this problem, introducing an additional cross linkage, for example, disulfide bridge, during micellar assembly may enhance the stability of the complexes. Inspired by this concept, Yan *et al.* developed an *in-situ* polymerization method to cross link neutral/positively charged monomers using non-degradable and degradable crosslinkers around the protein to form single protein nanocapsules for cellular delivery.⁹⁹ Various stimuli-responsive polymers (also called smart polymers) are applicable for building up the polymeric drug delivery platform in a stimuli-responsive manner for controlled drug release.¹⁰⁰ These include temperature-sensitive polymers (e.g., poly(N-isopropylacrylamide)), pH-sensitive polymers (e.g., poly(vinylpyridine)), light-sensitive polymers (e.g., modified poly(acrylamide)), electric field-responsive polymers (e.g., poly(ethyloxazoline)) and ultrasound-responsive polymers (e.g., ethylenevinylacetate).¹⁰⁰

Although liposomes and polymeric nanocarriers feature several attractive advantages, their properties are highly dependent on the specific formulation. For example, changing one property like loading efficiency affects numerous other properties such as size, charge and stability.⁶⁹ Therefore it is difficult to design a universal nanocarrier platform for different cargos based on one type of lipid or polymer component.

Inorganic nanocarriers: inorganic nanocarriers such as gold nanoparticles, carbon nanotubes and mesoporous silica nanoparticles (MSNs) all have been reported to show successful intracellular protein delivery.⁹¹ Gold nanoparticles can be easily synthesized and functionalized, and feature low cytotoxicity, bioinertness and cellular imaging ability.¹⁰¹ Proteins can assemble with gold nanoparticles into complexes and can be released from the complexes by the trigger of glutathione (GSH).¹⁰² Carbon nanotubes (CNTs) have attracted numerous biological studies recently due to their water-soluble and biocompatible nature. It has been revealed that single walled carbon nanotubes (SWNTs) possess the ability to shuttle various molecular cargos including proteins and nucleic acids into living cells.⁹¹ Pantarotto *et al.* reported that SWNTs were able to insert and diffuse through cell membranes *via* the energy-independent non-endocytic mechanism.¹⁰³ Others have demonstrated that proteins (e.g. streptavidin, BSA, cytochrome c, etc.) were able to bind to the nanotube sidewalls through noncovalent and nonspecific adsorption, then the CNT-protein complexes were internalized by cells *via* energy-dependent endocytosis.⁹¹ Among the inorganic materials,

MSNs exhibit superior multiple functionalities (see Chapter 1.1.3) and have been used to deliver a variety of proteins for disease treatment, cellular function modification or bio-imaging. The examples include human proteasome delivery to delay tau aggregation that leads to Alzheimer disease,⁴⁷ superoxide dismutase delivery against external oxidative stress that leads to apoptosis,⁴⁶ Cre protein delivery for gene editing,⁴⁸ and chromobody delivery for cellular antigen visualization and targeting.³⁴

Other strategies like induced transduction by osmocytosis and propanebetaine (iTOP method)¹⁰⁴ and commercially available cationic lipid mediated delivery of negatively supercharged GFP-fused proteins¹⁰⁵ also showed high protein transduction efficiency *in vitro* and *in vivo* (only the latter).

Despite the promising development of all kinds of delivery strategies that are capable of transporting protein into cells, efficient escape from endosomal entrapment of those internalized carrier-cargo complexes is still a great challenge.

1.2.3 Endosomal Escape

Cargos or nanocarriers internalized by cells *via* the endocytosis pathway are often trapped in the cytosolic vesicles where their ultimate fate will be to be degraded in acidic lysosomes or transported back to the cell surface by recycling endosomes (Figure 1.10),^{92,96,106,107} instead of reaching the cytosol where they can perform their intended action. Hence, addressing endosomal escape is a significant step to achieve an appropriate therapeutic effect intracellularly.

Understanding the endosomal escape mechanisms is important for constructing a cellular delivery system. Scientists have learned from viruses and bacteria on how to evade the entrapment of cellular vesicles during their infectious process in the host cells. These natural mechanisms are highly efficient and the best models to imitate when conducting cellular delivery by non-viral vectors. Based on the extensive studies performed during the past decades, several endosomal escape mechanisms have been proposed.^{96,106,107}

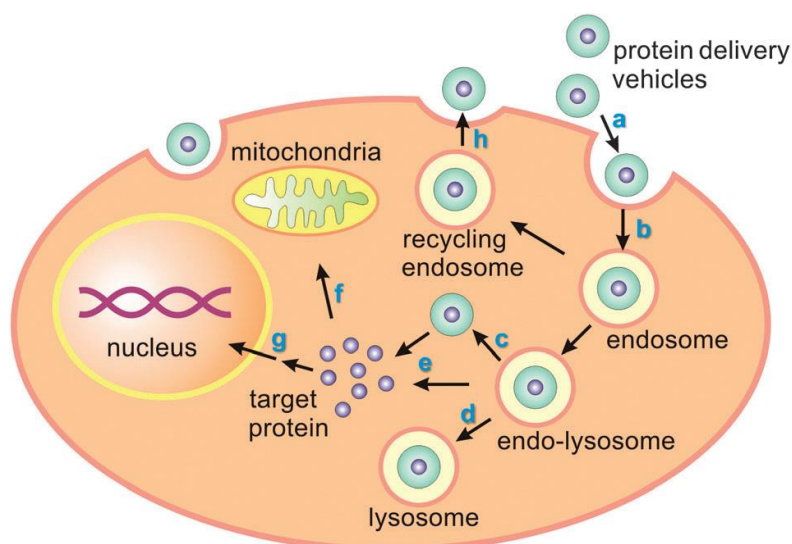


Figure 1.10 Schematic representation of endocytic process for protein delivery vehicles.⁹² (a) Protein shuttled vehicles attach on cell membrane and enter the cell *via* endocytosis; (b) the internalized vehicles are trapped in endosomes; (c) the shuttled vehicle undergoes endosomal escape; (d) non-escaped vehicle and its payload are sorted to lysosome and degraded in the acidic milieu; (e) proteins are released from endosomes and diffuse through cytosol; (f) targeting proteins are transported to specific organelle; (g) cargos diffuse into nucleus and participate in cellular functions; (h) exocytosis of the shuttled vehicle by the recycling endosome.

Membrane fusion:

In nature, enveloped viruses can trigger endosomal escape by fusion of their viral envelope with the endosomal membrane in order to release the viral contents to the cytoplasm of the infected cells.¹⁰⁸ Inspired by the natural pathway, scientists have identified some viral entry peptides, studied their membrane destabilization mechanisms and even modified their sequence to improve the endosomal escape efficiency as well as their biocompatibility. The viral entry peptides can be classified into three different categories based on their amino acid residues and the slightly different mechanism of action in endosomes.⁹⁶ The first type is anionic amphiphilic peptides containing glutamate residues and hydrophobic segments. These peptides are capable of undergoing conformational changes from a random coil to an α -helix under acidic conditions (pH 5 – 5.5). These α -helical domains allow the envelope-bound peptides to induce membrane fusion with the endosomes, therefore these types of peptides are

also called fusogenic peptides. The haemagglutinin subunit HA2 of influenza virus and its derivatives INF7 and E5WYG are representatives of fusogenic peptides.

The second type of viral entry peptides contains abundant histidine residues capable of being protonated in mildly acidic environments and destabilizing the endosomal membrane *via* cationic interactions and an osmotic buffering effect (see the section on “proton sponge effect”). H5WYG is a typical example of this type of peptides and has shown efficient transfection efficiency for nucleic acids and high endosomal escape efficiency when incorporated into supported lipid bilayer-coated mesoporous silica nanoparticles.^{71,109} Some peptides like GALA,¹¹⁰ consisting of both glutamate residues for pH-dependent conformational change and histidines for protonation buffering, are able to trigger different membrane destabilization mechanisms, consequently attaining high transfection efficiency. The third type is cationic amphiphilic peptides with copious lysine residues such as K5 and KALA. This type of peptides can induce pH-dependent membrane destabilization by cationic interactions (explained below) with the endosomal membrane.

It was proposed that some lipid-based nanocarriers also possess the membrane fusion ability to release their payload to the cytoplasm. Cationic lipids such as 1,2-dioleoyl-3-trimethylammonium-propane (DOTAP) and 1,2-di-O-octadecenyl-3-trimethylammonium propane (DOTMA) are able to induce a “flip-flop” mechanism, inverting the negatively charged endosomal membrane (mainly the cytoplasm-facing leaflet) to attach on their positively charged phospholipids, thus creating a connection between the lipid enveloped milieu and the cytoplasm^{96,106} (Figure 1.11). The fusogenic lipid 1,2-dioleoyl-sn-glycero-3-phosphoethanolamine (DOPE) is often incorporated into cationic lipoplexes as endosomolytic helper lipid to enhance the endosomolytic ability. DOPE is pH sensitive and will undergo a conformational transition from a lamellar structure to an inverted hexagonal liquid crystalline phase upon acidification. This conformational change allows for the destabilization of the endosomal membrane.⁹⁶

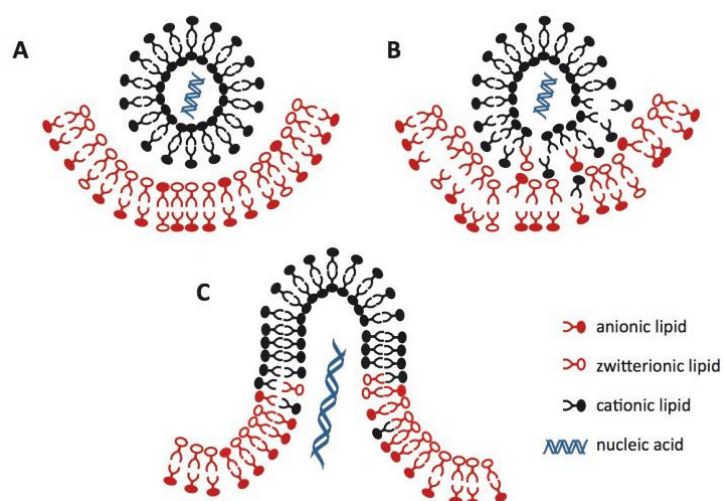


Figure 1.11 Flip-flop mechanism induced by cationic lipid for endosomal membrane fusion.⁹⁶ (a) A lipid-based nanocarrier was internalized by cell and trapped in the endosome. (b) The electrostatic attraction between cationic lipids on nanocarrier and anionic lipids presenting in the cytoplasmic-facing side of endosomal membrane facilitates the diffusion of endosomal lipids into cationic lipid compartment, forming charge-neutralized ion pairs. (c) The displacement of the endosomal lipid results in the flip-flop membrane fusion and therefore enables the release of the payload into the cytoplasm.

Pore formation:

Persistent membrane destabilization or insertion of peptides/pore forming proteins across the membrane can cause pore formation on the endosomal membrane, resulting in leakage of contents from the endosome to the cytoplasm. A well-known pore forming peptide is melittin, a major component of bee venom, which is characterized with the pore formation ability for membrane disruption and high cytotoxic activity.¹⁰⁷ It is reported that¹¹¹ the cationic melittin can form α -helical structure in aqueous solution. The α -helical structure in combination with the cationic character enables melittin to insert into lipid bilayers, subsequently leading to the membrane destabilization.

Proton sponge effect (pH-buffering effect): the proton sponge effect^{96,106,107,112} is mediated by agents with high buffering capacity that can buffer endosomal acidification by adsorbing protons and eventually cause osmotic swelling and membrane rupture of endosomes. Molecules having protonable residues, such as secondary and tertiary amine groups with pK_a close to endosomal/lysosomal pH, adsorb protons when exposed to the mildly acidic (\sim pH 6) endosomal compartment, consequently resisting a further acidification of the endosomes.

Subsequently, more protons will be continuously pumped into endosomes with the attempt to acidify the compartment. The accumulation of positive charges inside endosomes induces a passive influx of chloride anions through ion channels to balance the transmembrane voltage differences. The increased ion concentration then causes an extensive inflow of water, leading to osmotic swelling and rupture of the endosomes (Figure 1.12). Various substances including cationic polymers (e.g., polyethylenimine, PEI), polyamidoamine (PAMAM) dendrimers, chloroquine and histidine-rich molecules feature the buffering ability.¹⁰⁶ Chloroquine, a lysosomotropic agent, is used in this study for endosomal destabilization. Chloroquine is able to diffuse through the cell membrane and will be accumulated in endosomes/lysosomes after being protonated. The effects of chloroquine on endosomal compartments are dosage-dependent. At low concentrations ($< 100 \mu\text{M}$), chloroquine serves as an inhibitor for endosomal acidification and maturation. At high concentrations ($> 100 \mu\text{M}$), chloroquine is able to destabilize the endosomes and subsequently trigger cytosolic cargo release.¹¹² In our study, chloroquine was used in high concentration ($500 \mu\text{M}$) as a “shock” in the culture medium for cell incubation (at room temperature for 5 – 10 min), which induces an efficient endosomal release of proteins delivered by MSNs.

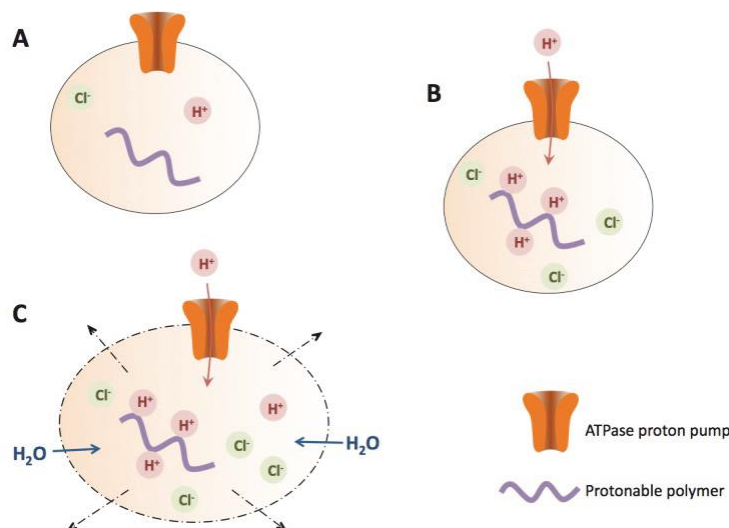


Figure 1.12 Schematic representation of the proton sponge effect hypothesis.⁹⁶ (a) The buffering agent (e.g., protonable polymer) is accumulated in the endosome. (b) The membrane-bound proton pump actively transports protons into endosome. The buffering agent is protonated and therefore resists the acidification of the endosome. (c) Continuous proton pumping leads to the influx of chloride anions and water, eventually causing osmotic swelling and rupture of the endosomal membrane.

Photochemically-induced membrane disruption: the technique based on photochemical-induced membrane disruption for endosomal escape of trapping contents is designated as photochemical internalization (PCI).^{96,107} The PCI technique is mediated by photosensitizers that can be activated and generate singlet oxygen upon illumination with light. This singlet oxygen is highly reactive and is capable of destabilizing or destroying the endosomal/lysosomal membrane. Since the generated singlet oxygen has a short lifetime, the toxicity to the other organelles in the cell is limited while the impact on endosomal membrane rupture is sufficient for cargo release.¹⁰⁷ A number of photosensitizers have been applied to trigger endosomal release of internalized contents, including meso-tetra-(para-sulfo phenyl) porphyrin (TPPS₄), meso-tetraphenyl porphyrin disulphonate (TPPS_{2a}), protoporphyrin-IX (PpIX), aluminum phthalocyaninedisulfonate (AIPcS_{2a}) and dendrimer phthalocyanine (DPc).^{31,41,59,107} Among these substances, the red light photosensitizer AIPcS_{2a} exhibits superior biocompatibility to the other photosensitizers owing to the lower phototoxicity and deeper tissue penetration when applying red light in the experiment.³¹

1.3 References

- 1 Davis, M. E. Ordered porous materials for emerging applications. *Nature* **417**, 813-821 (2002).
- 2 Davis, M. E. & Lobo, R. F. Zeolite and molecular sieve synthesis. *Chem. Mater.* **4**, 756-768 (1992).
- 3 Corma, A. From Microporous to Mesoporous Molecular Sieve Materials and Their Use in Catalysis. *Chem. Rev.* **97**, 2373-2420 (1997).
- 4 Yanagisawa, T., Shimizu, T., Kuroda, K. & Kato, C. The Preparation of Alkyltriethylnoninium–Kaneinite Complexes and Their Conversion to Microporous Materials. *Bull. Chem. Soc. Jpn.* **63**, 988-992 (1990).
- 5 Beck, J. S. *et al.* A new family of mesoporous molecular sieves prepared with liquid crystal templates. *J. Am. Chem. Soc.* **114**, 10834-10843 (1992).
- 6 Zhao, D., Huo, Q., Feng, J., Chmelka, B. F. & Stucky, G. D. Nonionic Triblock and Star Diblock Copolymer and Oligomeric Surfactant Syntheses of Highly Ordered, Hydrothermally Stable, Mesoporous Silica Structures. *J. Am. Chem. Soc.* **120**, 6024-6036 (1998).
- 7 Kresge, C. T., Leonowicz, M. E., Roth, W. J., Vartuli, J. C. & Beck, J. S. Ordered mesoporous molecular sieves synthesized by a liquid-crystal template mechanism. *Nature* **359**, 710-712 (1992).
- 8 Raman, N. K., Anderson, M. T. & Brinker, C. J. Template-based approaches to the preparation of amorphous, nanoporous silicas. *Chem. Mater.* **8**, 1682-1701 (1996).
- 9 Zhao, D. *et al.* Triblock Copolymer Syntheses of Mesoporous Silica with Periodic 50 to 300 Å Pores. *Science* **279**, 548-552 (1998).
- 10 Flodström, K., Wennerström, H. & Alfredsson, V. Mechanism of Mesoporous Silica Formation. A Time-Resolved NMR and TEM Study of Silica–Block Copolymer Aggregation. *Langmuir* **20**, 680-688 (2004).
- 11 Khodakov, A. Y., Zholobenko, V. L., Imperor-Clerc, M. & Durand, D. Characterization of the initial stages of SBA-15 synthesis by in situ time-resolved small-angle X-ray scattering. *J. Phys. Chem. B* **109**, 22780-22790 (2005).
- 12 dos Santos, S. M. L. *et al.* Synthesis and characterization of ordered mesoporous silica (SBA-15 and SBA-16) for adsorption of biomolecules. *Microporous Mesoporous Mater.* **180**, 284-292 (2013).
- 13 Zhao, J. *et al.* Biomolecule separation using large pore mesoporous SBA-15 as a substrate in high performance liquid chromatography. *Chem. Commun.*, 752-753 (2002).
- 14 Baskaran, S. *et al.* Low Dielectric Constant Mesoporous Silica Films Through Molecularly Templated Synthesis. *Adv. Mater.* **12**, 291-294 (2000).

- 15 Yang, C. M., Cho, A. T., Pan, F. M., Tsai, T. G. & Chao, K. J. Spin-on Mesoporous Silica Films with Ultralow Dielectric Constants, Ordered Pore Structures, and Hydrophobic Surfaces. *Adv. Mater.* **13**, 1099-1102 (2001).
- 16 Vallet-Regi, M., Rámila, A., del Real, R. P. & Pérez-Pariente, J. A New Property of MCM-41: Drug Delivery System. *Chem. Mater.* **13**, 308-311 (2001).
- 17 Rejman, J., Oberle, V., Zuhorn, I. S. & Hoekstra, D. Size-dependent internalization of particles via the pathways of clathrin- and caveolae-mediated endocytosis. *Biochem. J.* **377**, 159-169 (2004).
- 18 Lai, C. Y. *et al.* A mesoporous silica nanosphere-based carrier system with chemically removable CdS nanoparticle caps for stimuli-responsive controlled release of neurotransmitters and drug molecules. *J. Am. Chem. Soc.* **125**, 4451-4459 (2003).
- 19 Argyo, C., Weiss, V., Bräuchle, C. & Bein, T. Multifunctional Mesoporous Silica Nanoparticles as a Universal Platform for Drug Delivery. *Chem. Mater.* **26**, 435-451 (2014).
- 20 Slowing, II, Vivero-Escoto, J. L., Wu, C. W. & Lin, V. S. Mesoporous silica nanoparticles as controlled release drug delivery and gene transfection carriers. *Adv. Drug Del. Rev.* **60**, 1278-1288 (2008).
- 21 Mamaeva, V., Sahlgren, C. & Linden, M. Mesoporous silica nanoparticles in medicine--recent advances. *Adv Drug Deliv Rev* **65**, 689-702 (2013).
- 22 Jana, S. K., Nishida, R., Shindo, K., Kugita, T. & Namba, S. Pore size control of mesoporous molecular sieves using different organic auxiliary chemicals. *Microporous Mesoporous Mater.* **68**, 133-142 (2004).
- 23 Han, Y. & Ying, J. Y. Generalized fluorocarbon-surfactant-mediated synthesis of nanoparticles with various mesoporous structures. *Angew. Chem. Int. Ed. Engl.* **44**, 288-292 (2004).
- 24 Gao, F., Botella, P., Corma, A., Blesa, J. & Dong, L. Monodispersed mesoporous silica nanoparticles with very large pores for enhanced adsorption and release of DNA. *J. Phys. Chem. B* **113**, 1796-1804 (2009).
- 25 Hartono, S. B. *et al.* Poly-L-lysine functionalized large pore cubic mesostructured silica nanoparticles as biocompatible carriers for gene delivery. *ACS Nano* **6**, 2104-2117 (2012).
- 26 Meka, A. K. *et al.* Facile Synthesis of Large-Pore Bicontinuous Cubic Mesoporous Silica Nanoparticles for Intracellular Gene Delivery. *ChemNanoMat* **2**, 220-225 (2016).
- 27 Tu, J. *et al.* Mesoporous Silica Nanoparticles with Large Pores for the Encapsulation and Release of Proteins. *ACS applied materials & interfaces* **8**, 32211-32219 (2016).
- 28 Möller, K. & Bein, T. Talented Mesoporous Silica Nanoparticles. *Chem. Mater.* (2016).

- 29 Slowing, H., Trewyn, B. G. & Lin, V. S. Mesoporous silica nanoparticles for intracellular delivery of membrane-impermeable proteins. *J. Am. Chem. Soc.* **129**, 8845-8849 (2007).
- 30 Kao, K.-C., Lin, T.-S. & Mou, C.-Y. Enhanced Activity and Stability of Lysozyme by Immobilization in the Matching Nanochannels of Mesoporous Silica Nanoparticles. *The Journal of Physical Chemistry C* **118**, 6734-6743 (2014).
- 31 Mackowiak, S. A. *et al.* Targeted drug delivery in cancer cells with red-light photoactivated mesoporous silica nanoparticles. *Nano Lett.* **13**, 2576-2583 (2013).
- 32 Möller, K. *et al.* Highly efficient siRNA delivery from core-shell mesoporous silica nanoparticles with multifunctional polymer caps. *Nanoscale* **8**, 4007-4019 (2016).
- 33 Zhang, K. *et al.* Facile large-scale synthesis of monodisperse mesoporous silica nanospheres with tunable pore structure. *J. Am. Chem. Soc.* **135**, 2427-2430 (2013).
- 34 Chiu, H. Y. *et al.* Intracellular chromobody delivery by mesoporous silica nanoparticles for antigen targeting and visualization in real time. *Sci Rep* **6**, 25019 (2016).
- 35 Niu, D., Ma, Z., Li, Y. & Shi, J. Synthesis of core-shell structured dual-mesoporous silica spheres with tunable pore size and controllable shell thickness. *J. Am. Chem. Soc.* **132**, 15144-15147 (2010).
- 36 Niu, D. *et al.* Monodispersed and ordered large-pore mesoporous silica nanospheres with tunable pore structure for magnetic functionalization and gene delivery. *Adv. Mater.* **26**, 4947-4953 (2014).
- 37 Kim, M. H. *et al.* Facile synthesis of monodispersed mesoporous silica nanoparticles with ultralarge pores and their application in gene delivery. *ACS Nano* **5**, 3568-3576 (2011).
- 38 Lin, Y. S. *et al.* Synthesis of hollow silica nanospheres with a microemulsion as the template. *Chem Commun (Camb)*, 3542-3544 (2009).
- 39 Na, H. K. *et al.* Efficient functional delivery of siRNA using mesoporous silica nanoparticles with ultralarge pores. *Small* **8**, 1752-1761 (2012).
- 40 van Rijt, S. H. *et al.* Protease-mediated release of chemotherapeutics from mesoporous silica nanoparticles to ex vivo human and mouse lung tumors. *ACS Nano* **9**, 2377-2389 (2015).
- 41 Niedermayer, S. *et al.* Multifunctional polymer-capped mesoporous silica nanoparticles for pH-responsive targeted drug delivery. *Nanoscale* **7**, 7953-7964 (2015).
- 42 Lu, J., Li, Z., Zink, J. I. & Tamanoi, F. In vivo tumor suppression efficacy of mesoporous silica nanoparticles-based drug-delivery system: enhanced efficacy by folate modification. *Nanomedicine* **8**, 212-220 (2012).

- 43 Hwang, A. A., Lu, J., Tamanoi, F. & Zink, J. I. Functional nanovalves on protein-coated nanoparticles for in vitro and in vivo controlled drug delivery. *Small* **11**, 319-328 (2015).
- 44 Meng, H. *et al.* Codelivery of an optimal drug/siRNA combination using mesoporous silica nanoparticles to overcome drug resistance in breast cancer in vitro and in vivo. *ACS Nano* **7**, 994-1005 (2013).
- 45 Dengler, E. C. *et al.* Mesoporous silica-supported lipid bilayers (protocells) for DNA cargo delivery to the spinal cord. *J Control Release* **168**, 209-224 (2013).
- 46 Chen, Y. P. *et al.* A new strategy for intracellular delivery of enzyme using mesoporous silica nanoparticles: superoxide dismutase. *J. Am. Chem. Soc.* **135**, 1516-1523 (2013).
- 47 Han, D. H. *et al.* Direct cellular delivery of human proteasomes to delay tau aggregation. *Nat. Commun.* **5**, 5633 (2014).
- 48 Martin-Ortigosa, S. *et al.* Mesoporous silica nanoparticle-mediated intracellular cre protein delivery for maize genome editing via loxP site excision. *Plant Physiol.* **164**, 537-547 (2014).
- 49 Feng, Y. *et al.* The application of mesoporous silica nanoparticle family in cancer theranostics. *Coord. Chem. Rev.* **319**, 86-109 (2016).
- 50 Matsushita, H. *et al.* Multifunctional core-shell silica nanoparticles for highly sensitive (19)F magnetic resonance imaging. *Angew. Chem. Int. Ed. Engl.* **53**, 1008-1011 (2014).
- 51 Taylor, K. M. *et al.* Mesoporous silica nanospheres as highly efficient MRI contrast agents. *J. Am. Chem. Soc.* **130**, 2154-2155 (2008).
- 52 Kempen, P. J. *et al.* Theranostic mesoporous silica nanoparticles biodegrade after pro-survival drug delivery and ultrasound/magnetic resonance imaging of stem cells. *Theranostics* **5**, 631-642 (2015).
- 53 Lee, S. B. *et al.* Mesoporous silica nanoparticle pretargeting for PET imaging based on a rapid bioorthogonal reaction in a living body. *Angew. Chem. Int. Ed. Engl.* **52**, 10549-10552 (2013).
- 54 Cauda, V., Schlossbauer, A., Kecht, J., Zurner, A. & Bein, T. Multiple core-shell functionalized colloidal mesoporous silica nanoparticles. *J. Am. Chem. Soc.* **131**, 11361-11370 (2009).
- 55 Li, Y., Hei, M., Xu, Y., Qian, X. & Zhu, W. Ammonium salt modified mesoporous silica nanoparticles for dual intracellular-responsive gene delivery. *Int. J. Pharm.* **511**, 689-702 (2016).
- 56 Yatvin, M., Weinstein, J., Dennis, W. & Blumenthal, R. Design of liposomes for enhanced local release of drugs by hyperthermia. *Science* **202**, 1290-1293 (1978).

- 57 Sun, R., Wang, W., Wen, Y. & Zhang, X. Recent Advance on Mesoporous Silica Nanoparticles-Based Controlled Release System: Intelligent Switches Open up New Horizon. *Nanomaterials* **5**, 2019-2053 (2015).
- 58 Schlossbauer, A. *et al.* A programmable DNA-based molecular valve for colloidal mesoporous silica. *Angew. Chem. Int. Ed. Engl.* **49**, 4734-4737 (2010).
- 59 Schlossbauer, A. *et al.* Cascaded photoinduced drug delivery to cells from multifunctional core-shell mesoporous silica. *Adv Healthc Mater* **1**, 316-320 (2012).
- 60 Ruhle, B., Datz, S., Argyo, C., Bein, T. & Zink, J. I. A molecular nanocap activated by superparamagnetic heating for externally stimulated cargo release. *Chem Commun (Camb)* **52**, 1843-1846 (2016).
- 61 Paris, J. L., Cabanas, M. V., Manzano, M. & Vallet-Regi, M. Polymer-Grafted Mesoporous Silica Nanoparticles as Ultrasound-Responsive Drug Carriers. *ACS Nano* **9**, 11023-11033 (2015).
- 62 Zhao, P. *et al.* A study of chitosan hydrogel with embedded mesoporous silica nanoparticles loaded by ibuprofen as a dual stimuli-responsive drug release system for surface coating of titanium implants. *Colloids Surf. B. Biointerfaces* **123**, 657-663 (2014).
- 63 Liu, R. *et al.* pH-responsive nanogated ensemble based on gold-capped mesoporous silica through an acid-labile acetal linker. *J. Am. Chem. Soc.* **132**, 1500-1501 (2010).
- 64 Liu, J. *et al.* Enzyme responsive mesoporous silica nanoparticles for targeted tumor therapy in vitro and in vivo. *Nanoscale* **7**, 3614-3626 (2015).
- 65 Bernardos, A. *et al.* Enzyme-responsive intracellular controlled release using nanometric silica mesoporous supports capped with "saccharides". *ACS Nano* **4**, 6353-6368 (2010).
- 66 Zhang, Q. *et al.* Multifunctional Mesoporous Silica Nanoparticles for Cancer-Targeted and Controlled Drug Delivery. *Adv. Funct. Mater.* **22**, 5144-5156 (2012).
- 67 Lu, Y., Sun, W. & Gu, Z. Stimuli-responsive nanomaterials for therapeutic protein delivery. *J Control Release* **194**, 1-19 (2014).
- 68 Tang, F., Li, L. & Chen, D. Mesoporous silica nanoparticles: synthesis, biocompatibility and drug delivery. *Adv. Mater.* **24**, 1504-1534 (2012).
- 69 Butler, K. S. *et al.* Protocells: Modular Mesoporous Silica Nanoparticle-Supported Lipid Bilayers for Drug Delivery. *Small* (2016).
- 70 Lu, J., Liong, M., Li, Z., Zink, J. I. & Tamanoi, F. Biocompatibility, biodistribution, and drug-delivery efficiency of mesoporous silica nanoparticles for cancer therapy in animals. *Small* **6**, 1794-1805 (2010).
- 71 Ashley, C. E. *et al.* The targeted delivery of multicomponent cargos to cancer cells by nanoporous particle-supported lipid bilayers. *Nat Mater* **10**, 389-397 (2011).

- 72 Weiss, V. *et al.* Dendronized mesoporous silica nanoparticles provide an internal endosomal escape mechanism for successful cytosolic drug release. *Microporous Mesoporous Mater.* **227**, 242-251 (2016).
- 73 Zhang, J. *et al.* Multifunctional envelope-type mesoporous silica nanoparticles for tumor-triggered targeting drug delivery. *J. Am. Chem. Soc.* **135**, 5068-5073 (2013).
- 74 Brannon-Peppas, L. & Blanchette, J. O. Nanoparticle and targeted systems for cancer therapy. *Adv. Drug Del. Rev.* **64**, 206-212 (2012).
- 75 Blanco, E., Shen, H. & Ferrari, M. Principles of nanoparticle design for overcoming biological barriers to drug delivery. *Nat. Biotechnol.* **33**, 941-951 (2015).
- 76 Choi, H. S. *et al.* Renal clearance of quantum dots. *Nat. Biotechnol.* **25**, 1165-1170 (2007).
- 77 Brigger, I., Dubernet, C. & Couvreur, P. Nanoparticles in cancer therapy and diagnosis. *Adv. Drug Del. Rev.* **54**, 631-651 (2002).
- 78 Leader, B., Baca, Q. J. & Golan, D. E. Protein therapeutics: a summary and pharmacological classification. *Nat. Rev. Drug Discov.* **7**, 21-39 (2008).
- 79 Goeddel, D. V. *et al.* Expression in Escherichia coli of chemically synthesized genes for human insulin. *Proceedings of the National Academy of Sciences* **76**, 106-110 (1979).
- 80 Kinch, M. S. An overview of FDA-approved biologics medicines. *Drug Discov. Today* **20**, 393-398 (2015).
- 81 Mitragotri, S., Burke, P. A. & Langer, R. Overcoming the challenges in administering biopharmaceuticals: formulation and delivery strategies. *Nat. Rev. Drug Discov.* **13**, 655-672 (2014).
- 82 Torchilin, V. Intracellular delivery of protein and peptide therapeutics. *Drug Discov Today Technol* **5**, e95-e103 (2008).
- 83 Pisal, D. S., Kosloski, M. P. & Balu-Iyer, S. V. Delivery of therapeutic proteins. *J. Pharm. Sci.* **99**, 2557-2575 (2010).
- 84 Derossi, D., Joliot, A. H., Chassaing, G. & Prochiantz, A. The third helix of the Antennapedia homeodomain translocates through biological membranes. *J. Biol. Chem.* **269**, 10444-10450 (1994).
- 85 Wang, F. *et al.* Recent progress of cell-penetrating peptides as new carriers for intracellular cargo delivery. *J Control Release* **174**, 126-136 (2014).
- 86 Dinca, A., Chien, W. M. & Chin, M. T. Intracellular Delivery of Proteins with Cell-Penetrating Peptides for Therapeutic Uses in Human Disease. *Int J Mol Sci* **17**, 263 (2016).

- 87 Erazo-Oliveras, A., Muthukrishnan, N., Baker, R., Wang, T. Y. & Pellois, J. P. Improving the endosomal escape of cell-penetrating peptides and their cargos: strategies and challenges. *Pharmaceuticals (Basel)* **5**, 1177-1209 (2012).
- 88 Madani, F., Lindberg, S., Langel, U., Futaki, S. & Graslund, A. Mechanisms of cellular uptake of cell-penetrating peptides. *J Biophys* **2011**, 414729 (2011).
- 89 Erazo-Oliveras, A. *et al.* Protein delivery into live cells by incubation with an endosomolytic agent. *Nat. Methods* **11**, 861-867 (2014).
- 90 Stewart, M. P. *et al.* In vitro and ex vivo strategies for intracellular delivery. *Nature* **538**, 183-192 (2016).
- 91 Du, J., Jin, J., Yan, M. & Lu, Y. Synthetic Nanocarriers for Intracellular Protein Delivery. *Curr. Drug Metab.* **13**, 82-92 (2012).
- 92 Gu, Z., Biswas, A., Zhao, M. & Tang, Y. Tailoring nanocarriers for intracellular protein delivery. *Chem. Soc. Rev.* **40**, 3638-3655 (2011).
- 93 Laouini, A. *et al.* Preparation, Characterization and Applications of Liposomes: State of the Art. *Journal of Colloid Science and Biotechnology* **1**, 147-168 (2012).
- 94 Perche, F. & Torchilin, V. P. Recent trends in multifunctional liposomal nanocarriers for enhanced tumor targeting. *J Drug Deliv* **2013**, 705265 (2013).
- 95 Pattni, B. S., Chupin, V. V. & Torchilin, V. P. New Developments in Liposomal Drug Delivery. *Chem. Rev.* **115**, 10938-10966 (2015).
- 96 Liang, W. & W. Lam, J. K. Endosomal Escape Pathways for Non-Viral Nucleic Acid Delivery Systems. (2012).
- 97 Oerlemans, C. *et al.* Polymeric micelles in anticancer therapy: targeting, imaging and triggered release. *Pharm. Res.* **27**, 2569-2589 (2010).
- 98 Kedar, U., Phutane, P., Shidhaye, S. & Kadam, V. Advances in polymeric micelles for drug delivery and tumor targeting. *Nanomedicine* **6**, 714-729 (2010).
- 99 Yan, M. *et al.* A novel intracellular protein delivery platform based on single-protein nanocapsules. *Nat Nanotechnol* **5**, 48-53 (2010).
- 100 Priya James, H., John, R., Alex, A. & Anoop, K. R. Smart polymers for the controlled delivery of drugs - a concise overview. *Acta Pharm Sin B* **4**, 120-127 (2014).
- 101 Ghosh, P., Han, G., De, M., Kim, C. K. & Rotello, V. M. Gold nanoparticles in delivery applications. *Adv Drug Deliv Rev* **60**, 1307-1315 (2008).
- 102 Verma, A., Simard, J. M., Worrall, J. W. & Rotello, V. M. Tunable reactivation of nanoparticle-inhibited beta-galactosidase by glutathione at intracellular concentrations. *J. Am. Chem. Soc.* **126**, 13987-13991 (2004).

- 103 Pantarotto, D., Briand, J. P., Prato, M. & Bianco, A. Translocation of bioactive peptides across cell membranes by carbon nanotubes. *Chem Commun (Camb)*, 16-17 (2004).
- 104 D'Astolfo, D. S. *et al.* Efficient intracellular delivery of native proteins. *Cell* **161**, 674-690 (2015).
- 105 Zuris, J. A. *et al.* Cationic lipid-mediated delivery of proteins enables efficient protein-based genome editing in vitro and in vivo. *Nat. Biotechnol.* **33**, 73-80 (2015).
- 106 Martens, T. F., Remaut, K., Demeester, J., De Smedt, S. C. & Braeckmans, K. Intracellular delivery of nanomaterials: How to catch endosomal escape in the act. *Nano Today* **9**, 344-364 (2014).
- 107 Varkouhi, A. K., Scholte, M., Storm, G. & Haisma, H. J. Endosomal escape pathways for delivery of biologicals. *J Control Release* **151**, 220-228 (2011).
- 108 Harrison, S. C. Viral membrane fusion. *Nat. Struct. Mol. Biol.* **15**, 690-698 (2008).
- 109 Midoux, P., Kichler, A., Boutin, V., Maurizot, J. C. & Monsigny, M. Membrane permeabilization and efficient gene transfer by a peptide containing several histidines. *Bioconjug Chem* **9**, 260-267 (1998).
- 110 Li, W., Nicol, F. & Szoka, F. C., Jr. GALA: a designed synthetic pH-responsive amphipathic peptide with applications in drug and gene delivery. *Adv Drug Deliv Rev* **56**, 967-985 (2004).
- 111 Kokot, G., Mally, M. & Svetina, S. The dynamics of melittin-induced membrane permeability. *Eur. Biophys. J.* **41**, 461-474 (2012).
- 112 El-Sayed, A., Futaki, S. & Harashima, H. Delivery of macromolecules using arginine-rich cell-penetrating peptides: ways to overcome endosomal entrapment. *AAPS J* **11**, 13-22 (2009).

2 Characterization Techniques

2.1 Nitrogen Physisorption

Gas sorption measurement is an essential technique for the determination of the surface areas, pore size distributions and pore volumes of porous materials. The use of nitrogen in sorption analysis for pore size evaluation originates from the late 1940s. To date, nitrogen is still one of the most commonly used gaseous adsorptives in the sorption measurement.¹ During the nitrogen sorption process, the gas adsorbs on the surface of a solid substrate (adsorbent) mainly *via* weak van-der-Waals forces where no chemical bond formation is involved. Therefore nitrogen sorption is classified as physisorption. The measurement is typically performed at a constant temperature at 77 K (the boiling point of nitrogen at 1 atm) where nitrogen is stepwise injected to the system. The equilibrium pressure at each nitrogen injection point is recorded. Thus, the amount of adsorbed nitrogen can be calculated. By plotting the adsorbed nitrogen volume against the equilibrium relative pressure p/p_0 (p_0 refers to the saturation pressure of the adsorptive), the isotherm is obtained. The isotherm curves are used to indicate the porous features of the adsorbents and their patterns were originally classified into six types according to IUPAC in 1985.² In 2015, scientists refined the original IUPAC isotherms³ and the updated classification figures are shown in Figure 2.1. The material characteristics corresponding to different isotherm types are listed in Table 2.1.

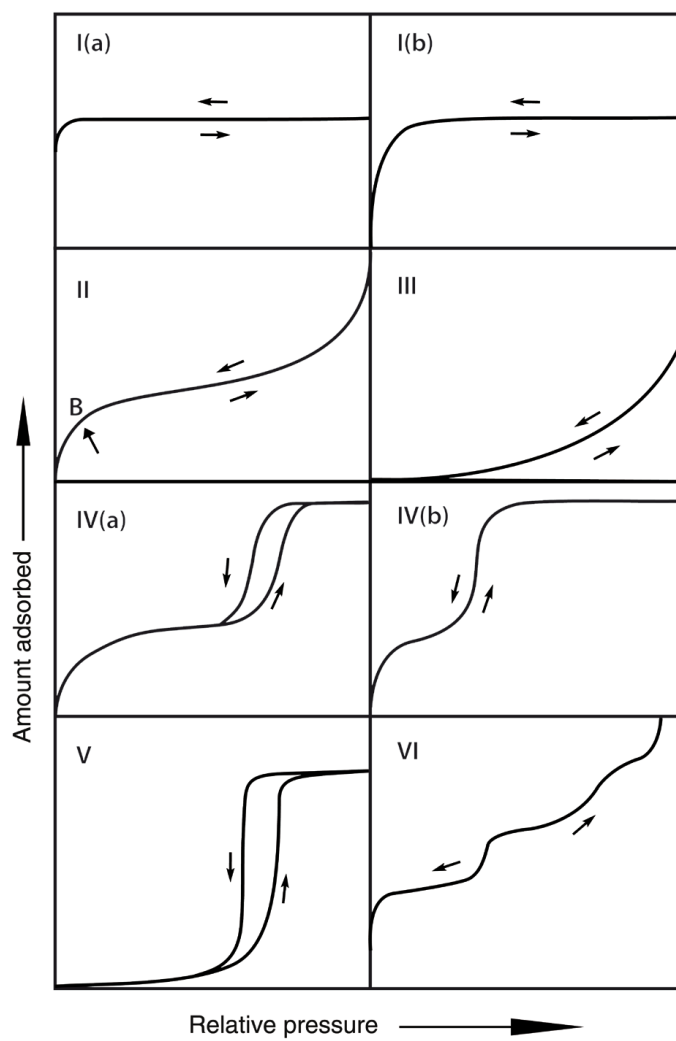


Figure 2.1 Classification of isotherms defined in the new IUPAC physisorption report.³

Table 2.1 Types of isotherms classified by IUPAC and their corresponding materials.³

Isotherm types	Corresponding material characters
I	<p>Microporous (pore size < 2 nm) materials having relatively small external surfaces. The limiting gas uptake is determined by the accessible micropore volume.</p> <p>Type I(a): materials containing mainly narrow micropores (< ~ 1 nm).</p> <p>Type I(b): materials having broad pore size distributions including wider micropores and possibly narrow mesopores (~ 2.5 nm).</p>
II	<p>Nonporous or macroporous (pore size > 50 nm) materials. Gas adsorbed on the surfaces of the adsorbent from monolayer adsorption followed by unrestricted multilayer adsorption.</p>
III	<p>Nonporous or macroporous materials having weak interaction with the adsorbate, therefore the monolayer-multilayer adsorption transition point B is absent.</p>
IV	<p>Mesoporous (pore size between 2 nm and 50 nm) materials. The monolayer-multilayer adsorption followed by a capillary condensation in the mesopores. Adsorption reaches a final saturation plateau after capillary condensation.</p> <p>Type IV(a): Materials containing pore width wider than 4 nm where the capillary condensation is accompanied by a hysteresis.</p> <p>Type IV(b): Materials having mesopores of smaller width (< 4 nm) thereby the isotherms are completely reversible. Conical and cylindrical mesopores that are closed at the tapered end can also result in the reversible type IV(b) isotherm.</p>
V	<p>Materials exhibit weak interactions with adsorbate in the low p/p_0 range but undergo capillary condensation at higher p/p_0. For example, using water for the sorption measurement on hydrophobic microporous and mesoporous adsorbents.</p>
VI	<p>Nonporous materials with highly uniform surfaces inducing layer-by-layer adsorption.</p>

Mesoporous silica materials typically show Type IV(a) isotherms in the nitrogen sorption analysis. During the adsorption measurement, capillary condensation, meaning the gas condenses to a liquid-like phase and fills out the pores completely, is observed.⁴⁻⁶ When desorption is performed, more energy (external pressure reduced) is needed to overcome the reversible liquid-vapor transition. Therefore the adsorption branch and desorption branch do not coincide and yield a hysteresis loop in the sorption isotherm. The hysteresis loops can be classified into several types (Figure 2.2) depending on the pore structures of the adsorbents.

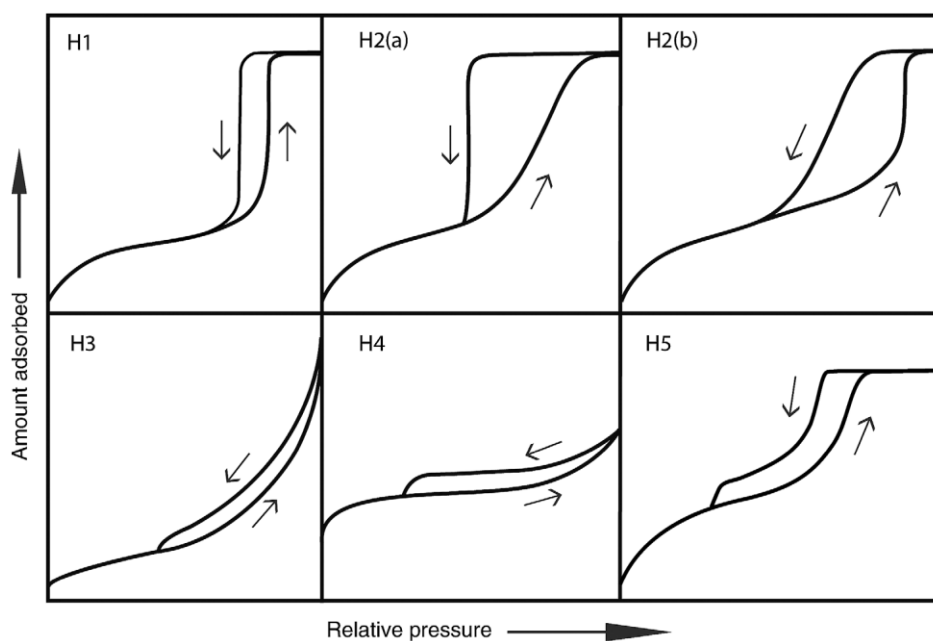


Figure 2.2 Hysteresis loops classified in the new IUPAC physisorption report.³

There are several models that can be used to interpret isotherm curves such as Langmuir⁷ and Brunauer-Emmett-Teller (BET).⁸ The Langmuir model describes the adsorption process based on some simplified assumptions, for example, (i) the adsorption only occurs in a monolayer, (ii) the adsorbate behaves as ideal gas without interactions between adsorbed molecules and (iii) the adsorbent has an ideal solid surface where all the binding sites are equal. Brunauer, Emmett and Teller later extended the Langmuir theory to multilayer adsorption, in which they hypothesized (i) that the gas adsorbs on the adsorbent in unlimited layers, (ii) the interactions among the adsorbates are neglected and (iii) the Langmuir theory can be applied to each adsorption layer. The BET equation can be expressed as follow (Eq. 2.1).

$$\frac{n}{n_m} = \frac{c \cdot \frac{p}{p_0}}{\left(1 - \frac{p}{p_0}\right) \left(1 + c - \frac{p}{p_0}\right)} \quad (\text{Eq. 2.1})$$

Equation 2.1 BET equation. n : the amount of the adsorbate at equilibrium pressure p , n_m : monolayer capacity, C : BET constant, p : equilibrium pressure, p_0 : saturation vapor pressure of the adsorbate.

By transforming the physisorption isotherm into a linear BET plot, the BET monolayer capacity n_m can be evaluated, thereafter the BET surface area can be calculated (Eq. 2.2).

$$a_s(\text{BET}) = n_m \cdot L \cdot \sigma_m / m \quad (\text{Eq. 2.2})$$

Equation 2.2 Formula for BET surface area calculation. $a_s(\text{BET})$: BET specific surface area of the adsorbent (of mass m), L : Avogadro constant, σ_m : molecular cross-sectional area (0.162 nm² for N₂).

For mesoporous materials containing no macropores, the pores are filled with the condensed adsorbate in the normal liquid state after capillary condensation. The total pore volume, V_p , is then derived from the amount of adsorbed gas at a relative pressure close to unity (e.g., $p/p_0 = 0.95$).² The pore size distribution of the investigated sample is one of the most important pieces of information that we want to obtain from the sorption analysis. In early times, the pore size analysis of mesoporous materials was mostly based on the Kelvin equation. This model assumes that the pore width is related to the radius of the meniscus formed by condensed adsorbate. However, this model ignores the thickness of the adsorbate layers formed on the porous surface prior to condensation⁹. Also, this assumption is only applicable in cylindrical pores and in parallel-sided slits.¹⁰ Barrett, Joyner and Halenda (BJH) modified the Kelvin equation by combining a standard isotherm (the t-curve) to account for the pre-adsorbed multilayer film.¹¹ However, the standard t-curve is not properly accounting for the enhanced surface forces in narrow mesopores, therefore the BJH method (as well as the Kelvin equation) underestimates the pore size for narrow mesopores (for pore diameters $< \sim 10$ nm, the pore size will be underestimated by $\sim 20 - 30\%$).³ To overcome the limitations of the Kelvin equation, several microscopic models including molecular simulation (Monte Carlo simulation) and density functional theory (DFT) can be applied for the proper calculation of the size of micropores and small mesopores. The DFT model takes

into consideration the interaction potentials for the fluid-adsorbent and fluid-fluid interactions and provides various methods for different pore structures which lead to a pore size distribution estimation that is more realistic and versatile compared to the Kelvin equation.⁵ The DFT method can be sub-categorized into local density functional theory (LDFT) and non-local density functional theory (NLDF) based on their predictions regarding the adsorbed fluid density profiles on the adsorbent.⁹ The NLDF approach is suitable for estimating the strongly interacting boundaries found for MSNs, therefore we applied this approach for the pore size distribution calculation of the mesoporous silica nanoparticles in this work.

2.2 Dynamic Light Scattering (DLS)

Dynamic light scattering (DLS) is a convenient and useful technique to determine the size distribution and colloidal stability of particles and polymers in suspensions.¹² This technique is typically valuable for analyzing particles having sizes in the sub-micron range. DLS is also referred to as photon correlation spectroscopy, as the measurement applies the photon auto-correlation function to analyze the intensity fluctuations of the scattered laser light from the particles in suspension. Upon illumination of the particles, the Brownian motion of the particles in solution leads to intensity fluctuations (resulting from the constructive and destructive interferences) of the scattered light which is then detected by the DLS instrument. Particle size is correlated to the speed of Brownian motion: the smaller the particle, the faster the Brownian motion is. Hence, the small particles cause the intensity to fluctuate more rapidly than the large ones. DLS measures the hydrodynamic particle size according to the translational diffusion coefficient D derived from the Stokes-Einstein equation (Eq. 2.3). The translational diffusion coefficient D depends on several factors, such as ionic strength in the solution, texture of particle surface and shape of particle. The hydrodynamic particle size was then obtained from a correlation function using various algorithms.

$$d(H) = \frac{kT}{3\pi\eta D} \quad (\text{Eq. 2.3})$$

Equation 2.3 Stokes-Einstein equation. $d(H)$: hydrodynamic diameter, D : translational diffusion coefficient, k : Boltzmann's constant, T : absolute temperature, η : viscosity.

The size distribution obtained from the correlation function is based on scattering intensity. For small (particle size $< 1/10$ wavelength of the illuminating light) and monodispersed particles, the intensity-derived particle size distribution matches well with the real situation. The relation between particle size and the scattering intensity can be described by Rayleigh scattering (Eq. 2.4).

$$I = I_0 \frac{1 + \cos^2 \theta}{2R^2} \left(\frac{2\pi}{\lambda} \right)^4 \left(\frac{n^2 - 1}{n^2 + 2} \right)^2 \left(\frac{d}{2} \right)^6 \quad (\text{Eq. 2.4})$$

Equation 2.4 Rayleigh scattering. I : intensity of the scattered light, I_0 : intensity of the incoming light, θ : scattering angle, R : distance to the particle, λ : wavelength of the incoming light, n : refractive index of the particle, d : particle diameter.

Since the scattering intensity is proportional to d^6 , a small portion of large particles or agglomerates in the solution would dominate the intensity-derived particle size distribution and thus compromise the result. Therefore, for large particles or samples containing broad particle size distributions, Mie theory has to be applied. Alternatively, a conversion to volume-weighted (proportional to d^3) or number-weighted (proportional to d) size distribution is accessible to gain more accurate information.

2.3 Zeta Potential Measurement

Zeta potential, also known as electrokinetic potential, is the electric potential difference between the bulk fluid and the stationary layer of fluid adhered to the dispersed particle.¹³ Zeta potential is positive if the potential increases from the bulk liquid phase towards the surface of the particle.¹³ This potential difference is also responsible for the electrokinetic phenomena of the particles.¹⁴ Particles in aqueous suspension often carry surface charges owing to the ionization of their surface groups, differential loss of ions from the particles, or adsorption of charged substances. The strength of the surface charge affects the distribution of ions in the surrounding solution, generating a counter ion double layer around the surface of the particle (Figure 2.3).¹⁵ The electric double layer consists of a dense inner layer (Stern layer) of bound ions and a slipping outer layer where the ions are more diffusive. While the surface-charged particle is undergoing a Brownian motion in the dispersing medium, the adhered electrical double layer moves accordingly. The potential at the interface between the drifting electrical double layer and the bulk medium is referred to as zeta potential.

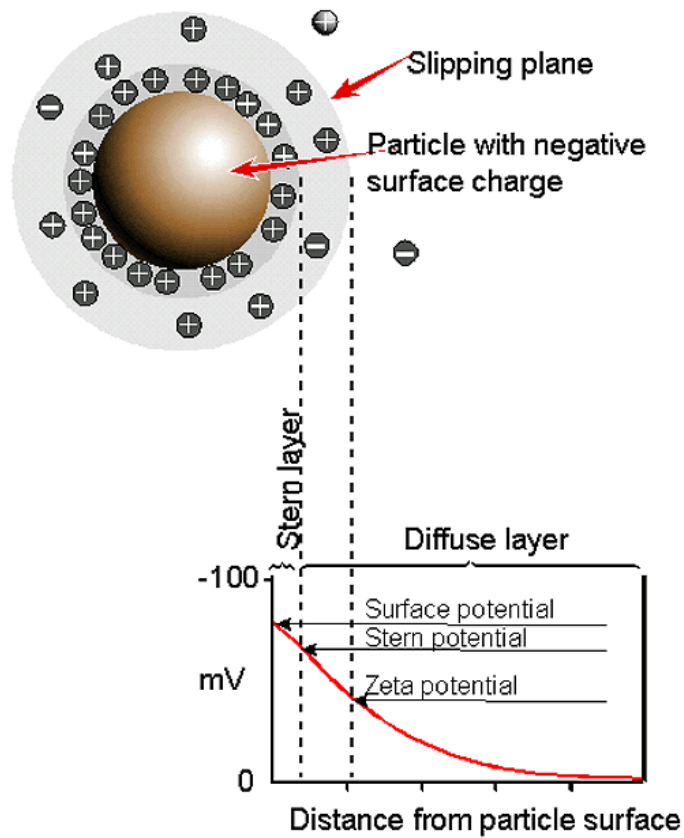


Figure 2.3 Scheme of the electric double layer surrounding a dispersed particle carrying negative surface charge and the corresponding potentials on the boundaries of different layers.¹⁵

The zeta potential of particles is often highly dependent on the pH value of the dispersing solution that causes the protonation or deprotonation of the surface groups of the particles. Zeta potential is determined by measuring the electrophoretic mobility of particles in solution under an applied external electric field. By applying the Henry equation (Eq. 2.5), zeta potential can be calculated. As can be seen from the equation, the electrophoretic mobility of the particles not only depends on the zeta potential of the particles but also depends on the strength of the external electric field, the dielectric constant and the viscosity of the solution.

$$U_E = \frac{2\varepsilon\zeta f(\kappa a)}{3\eta} \quad (\text{Eq. 2.5})$$

Equation 2.5 Henry equation. U_E : electrophoretic mobility, ε : dielectric constant of the sample, ζ : zeta potential, $f(\kappa a)$: Henry function, η : viscosity of the solution.

For a zeta potential measurement, an electric field with known strength is applied to a capillary cell containing the particle suspension. The electrophoretic mobility of dispersed particles is obtained by measuring the particles' velocity with Laser Doppler Velocimetry (LDV).¹⁶ When a laser beam strikes the sample, the scattering light from the moving particles interferes with a reference beam thereby causing a fluctuating signal due to the Doppler shift. The frequency shift of the fluctuating signal is used to determine the velocity of the drifting particles. The Henry function $f(ka)$ measures the ratio of the particle radius to the electrical double layer thickness. For particles larger than 200 nm, a Smoluchowski approximation ($f(ka) = 1.5$) is applied. In this case, an aqueous solution with moderate electrolyte concentration is suitable for the measurement. For particles smaller than 200 nm, a Huckel approximation ($f(ka) = 1.0$) is fitting well. In this case, using a low dielectric constant solvent (e.g., non-aqueous medium) is suggested for the measurement.

2.4 Infrared (IR) and Raman Spectroscopy

Infrared (IR) and Raman spectroscopy are two common methods that can be used to identify the chemical bonding of molecules in a compound. The chemical bonding information of the functional groups is obtained by characterizing the vibrational modes in the system. For IR spectroscopy, the radiation in the mid-infrared ($200 - 4000 \text{ cm}^{-1}$) is mostly used to induce a vibrational excitation of the covalently bonded molecules and the intensity of the transmitted or scattered light from the samples are collected.¹⁷ Molecules undergo various vibrational motions such as stretching, bending, twisting, etc. when provided with energy. When the energy of the incident radiation matches energy differences of the vibrational states of the molecule, an absorption spectrum can be observed. An interferometer is used for the IR spectroscopy measurement and the resulting Fourier transformed frequency-dependent spectrum provides a fingerprint map which is used to identify the vibrational bands of specific functional groups.¹⁸

For Raman spectroscopy, monochromatic light (usually generated from a laser in the visible, near infrared or near ultraviolet range) is applied for the measurement. The introduced electromagnetic radiation interacts with the electron clouds around chemical bonds and the resulting inelastic scattering is collected. Typically, when a sample is illuminated by electromagnetic radiation, most of the incident light is scattered and released without changing frequency, i.e. Rayleigh scattering (Figure 2.4). In Raman spectroscopy

measurements, the elastic Rayleigh scattering is filtered out and the inelastic scattering is detected. The inelastically scattered photon will either shift to a lower frequency (Stokes shift) or towards higher frequency (anti-Stokes shift) depending on the vibrational state of the excited molecules (Figure 2.4). The photon energy shifting indicates the vibrational modes of the chemical bonds in the system. Therefore the characteristics of the functional groups are obtained.

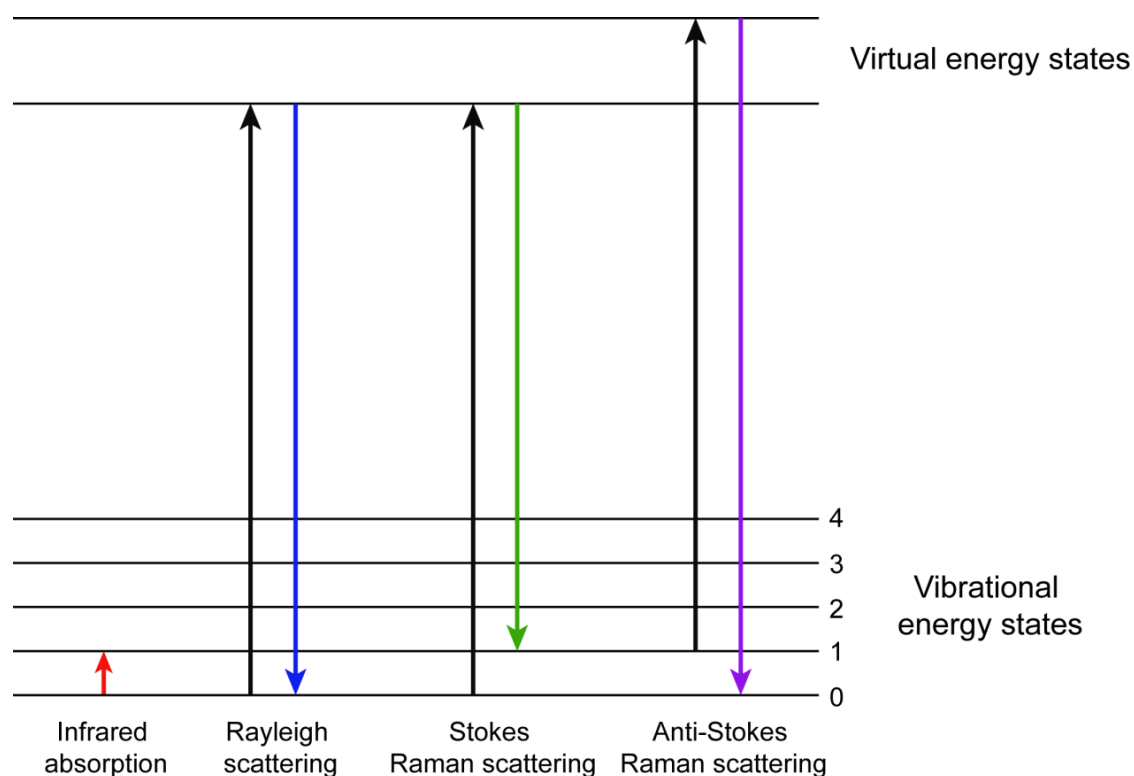


Figure 2.4 Energy level diagram showing the scattering processes involved in Raman spectroscopy.

Since IR and Raman spectroscopy rely on different physical processes, the general selection rules for observable vibrational states are different, but complementary. For IR-active samples, the dipole moment of the molecules has to change during the vibration. For Raman-active samples, the polarizability of the chemical bonds in the sample has to change during vibration.

2.5 UV-Vis Spectroscopy

Ultraviolet and visible (UV-Vis) absorption spectroscopy is widely used in analytical chemistry for quantitative (e.g., determination of protein concentration) or qualitative (e.g., detection of functional groups) analysis of samples.^{17,18} The analyte is irradiated by electromagnetic waves in the ultraviolet and visible range, and the attenuation of the incident light caused by absorption is measured. Photon energy in the UV-Vis range is able to excite the valence electrons from the ground state to an excited electronic state. When the photon energy of the incident light corresponds to the electronic transition energy, light absorption occurs at this specific wavelength. When the investigated substance is dispersed in solution, the concentration of the investigated substance (light absorbing species) can be quantified *via* the Beer-Lambert Law (Eq. 2.6) when measuring the sample in a fixed path length cell.

$$A = \log \frac{I_0}{I} = \varepsilon \cdot c \cdot l \quad (\text{Eq. 2.6})$$

Equation 2.6 Beer-Lambert Law. A : absorbance, I_0 : intensity of incident light, I : intensity of transmitted light, ε : molar extinction coefficient of the analyte, l : path length.

2.6 Thermogravimetric Analysis (TGA)

Thermogravimetric analysis (TGA) measures the mass loss of a material with respect to increasing temperature.^{19,20} In this study, TGA is used to determine the content of organic functional groups in the mesoporous silica framework. The sample is heated up to 900 °C with a constant heating rate in a furnace, and a constant gas flow consisting of inert gas or synthetic air is applied to remove the combusted or desorbed components from the sample. The mass loss of the sample is measured by a sensitive thermobalance during the heating process. The resulting decomposition pattern (mass loss as a function of temperature) provides information on the amount of the organic functional groups as well as the temperature stability of the investigated sample.

2.7 X-ray Diffraction (XRD)

X-rays are a form of electromagnetic radiation that has a wavelength in the range of 0.01 to 10 nm. X-rays carry high photon energy (100 eV to 100 keV) and are capable of ionizing atoms, disrupting molecular bonds and passing through many materials without being much absorbed or scattered. X-rays are generated whenever highly energetic charged particles (electrons or ions) strike matter. In X-ray crystallography, usually a metal like copper or tungsten is used as the target to generate X-rays.^{18,21,22} An electron beam is produced by heating a metal filament (the cathode) while applying a high voltage in the vacuum tube to accelerate the electrons towards the metal target. During the collision, some electrons approach the nucleus of the metal atom due to the attraction between positive protons and negative electrons and then the electrons are deflected by the strong electric field near the nucleus. The deflection causes energy loss of the electrons where a small portion of the lost energy is emitted as X-rays in a continuous spectrum (Bremsstrahlung). On the other hand, some electrons with high energy can knock out an orbital electron from the inner electron shell of the metal atom resulting in an electron vacancy. Electrons from higher energy levels then drop to the vacancy thereafter producing a series of discrete X-rays. The discrete X-ray spectrum is corresponding to the electronic transition energies of the targeted metal (the anode) and thus called characteristic radiation. Copper is one of the most common materials used as an anode because it gives a wavelength suitable for many diffraction experiments. When using copper as an anode, the characteristic wavelength (Cu-K_α) is 1.54182 Å. Typically, monochromatic X-rays are used in an X-ray diffraction measurement. This can be achieved by introducing monochromators or blocking filters.¹⁸

The monochromatic X-ray from the characteristic radiation has a wavelength in the Ångström range, which is at the same order of magnitude as the distance of atoms in a solid material. When a solid sample is irradiated with X-rays, the radiation is scattered by the atoms of the investigated sample. If the sample contains regular structures, the scattered X-ray will experience constructive and destructive interference. This process is called diffraction (Figure 2.5).

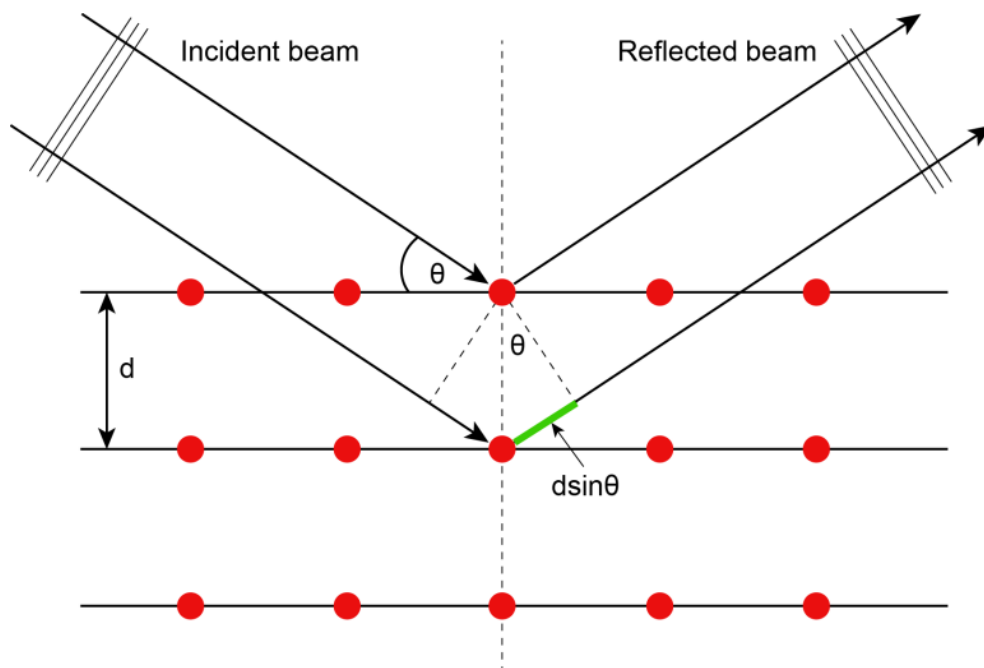


Figure 2.5 Illustration of the X-ray diffraction in a crystalline material.

The diffraction pattern can be used to identify and characterize the crystalline structure of a material while the lattice distance of the material can be calculated using Bragg's law (Eq. 2.7).

$$n\lambda = 2d \sin \theta \quad (\text{Eq. 2.7})$$

Equation 2.7 Bragg's law. n : order of interference, λ : wavelength of incident X-rays, d : lattice spacing, θ : angle of incidence.

In this study, X-ray diffraction was applied to characterize the ordered mesostructure of the MSNs where the ordered mesopores define the lattice planes of the sample. The X-ray scattering was performed in small angles ($2\theta = 0.1 - 10^\circ$).

2.8 Fluorescence Spectroscopy

Fluorescence spectroscopy is a type of electromagnetic spectroscopy used to measure the fluorescence of a sample. Some molecules, usually containing several combined aromatic groups or heterocycles with several π bonds, are able to absorb light energy of a specific wavelength in the UV or visible spectrum and re-emit light at a longer wavelength.^{23,24} This process is referred to as fluorescence, which is also a form of photoluminescence. The mechanism of fluorescence can be clarified in a Jablonski diagram (Figure 2.6).

Generally, fluorescence undergoes three main processes: excitation, non-radiative relaxation and fluorescence emission. An incident light (generated by an incandescent lamp or a laser source) carrying photon energy $h\nu_{\text{ex}}$ firstly hits the fluorescent material, and triggers an excitation of electrons from the ground state (S_0) to an excited state (S_1 : the first, S_2 : the second excited singlet energy states). The excited molecules subsequently undergo vibrational relaxation upon collision with their environment and typically drop to the vibrational ground state of the electronic excited state. Ultimately, the electrons fall back to the ground state (S_0), meanwhile releasing photon energy $h\nu_{\text{em}}$ that yields fluorescence emission. The released photon has a lower energy than the absorbed photon due to the vibrational relaxation of the electrons in the excited state. Therefore the fluorescence emission features a red-shift compared to the incident light.

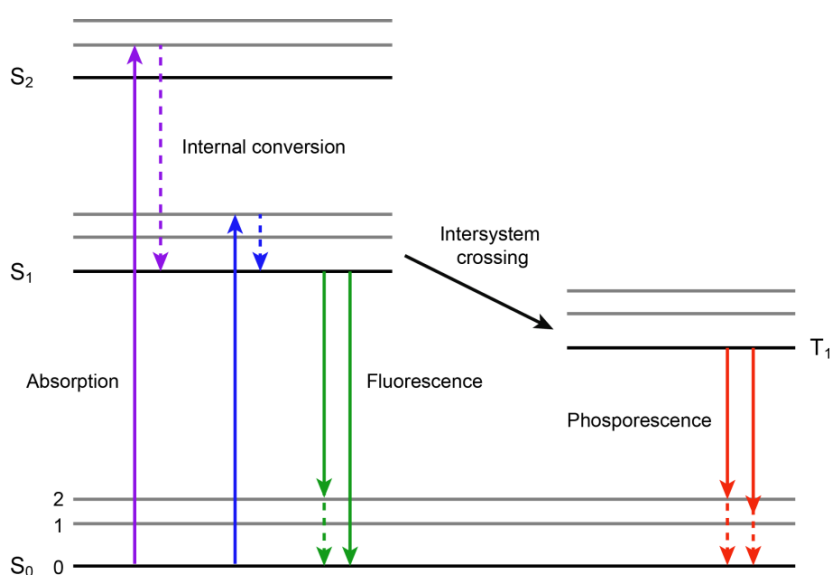


Figure 2.6 Jablonski diagram for the interpretation of fluorescence process.

Besides fluorescence emission, other electronic relaxation pathways such as quenching, fluorescence energy transfer, intersystem crossing (resulting in phosphorescence or delayed fluorescence) and non-radiative relaxation (energy dissipates in the form of heat) may also occur.

2.9 Electron Microscopy

Microscopes are instruments used to observe small objects or the microscopic structure of a material. The technique of using such an instrument to investigate a sample is called microscopy. Conventional optical microscopes using visible light (wavelength: 400 – 800 nm) for specimen illumination have a resolution limit in the range of 200 nm. Electron microscopes using a beam of highly accelerated electrons as illumination source are able to achieve high resolution images down to 0.05 – 0.1 nm, due to the shorter wavelength of the electron beam.¹⁴ This powerful technique can be used to characterize the structure of a material down to an atomic level, and is important for studies in nanotechnology. In a typical electron microscope the electrons are generated by a tungsten filament or a field emission gun and the emitted electrons are accelerated by a potential difference. Electrostatic and/or electromagnetic lenses are used to focus either the emitted electron beam on the investigated specimen or the transmitted electrons to form a magnified image. When the highly accelerated electrons hit matter, the electrons follow different pathways or undergo different conversions²⁵ (Figure 2.7), for example, they transmit through the matter or they are scattered followed by energy loss. These various types of signals can be collected. The electron micrographs are then produced using a specialized digital camera and a frame grabber to capture the image. In order to reach high-resolution images, electron microscopes generally work under high vacuum conditions to avoid beam attenuation caused by electron collision with gas molecules. In general, electron microscopes can be classified into two major types: transmission electron microscopes and scanning electron microscopes, depending on the electron beam probing approach and the signal types being collected.

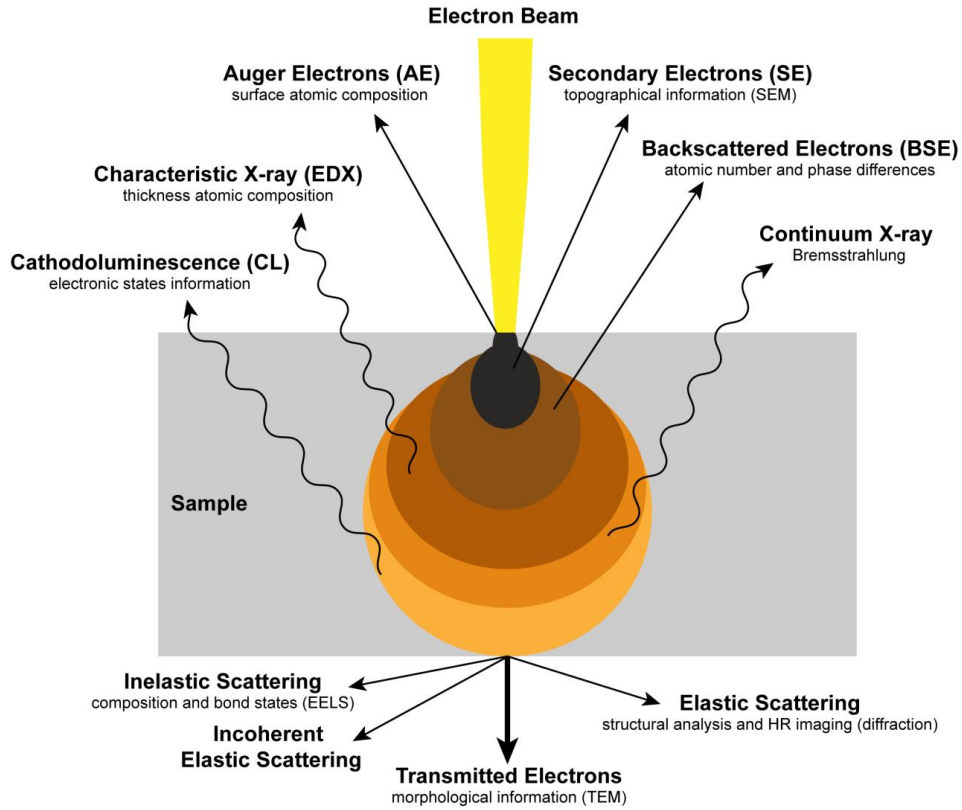


Figure 2.7 Schematic representation of electron beam interactions with matter and the corresponding scattering pathways.

2.9.1 Transmission Electron Microscopy (TEM)

The transmission electron microscope (Figure 2.8) is the original form of an electron microscope. The highly accelerated electron beam (40 to 400 keV) serving as an illumination source enables the imaging in high resolution down to an atomic level, where the wavelength of the electron beam is related to the accelerating voltage U (Eq. 2.8).²⁵ Typically, the accelerating voltages between 80 kV and 200 kV are used in TEM where the wavelength produced under this voltage corresponds to 0.15 Å and 0.0251 Å, respectively.

$$\lambda = \frac{hc}{\sqrt{2m_0E \left(1 + \frac{E}{2m_0c^2}\right)}} \quad (\text{Eq. 2.8})$$

Equation 2.8 The relation between the wavelength of an electron beam with its accelerating voltage.²⁶ λ : wavelength of electrons, h : Planck constant, c : speed of light, m_0 : mass of electron, e : elementary charge of an electron, U : accelerating voltage.

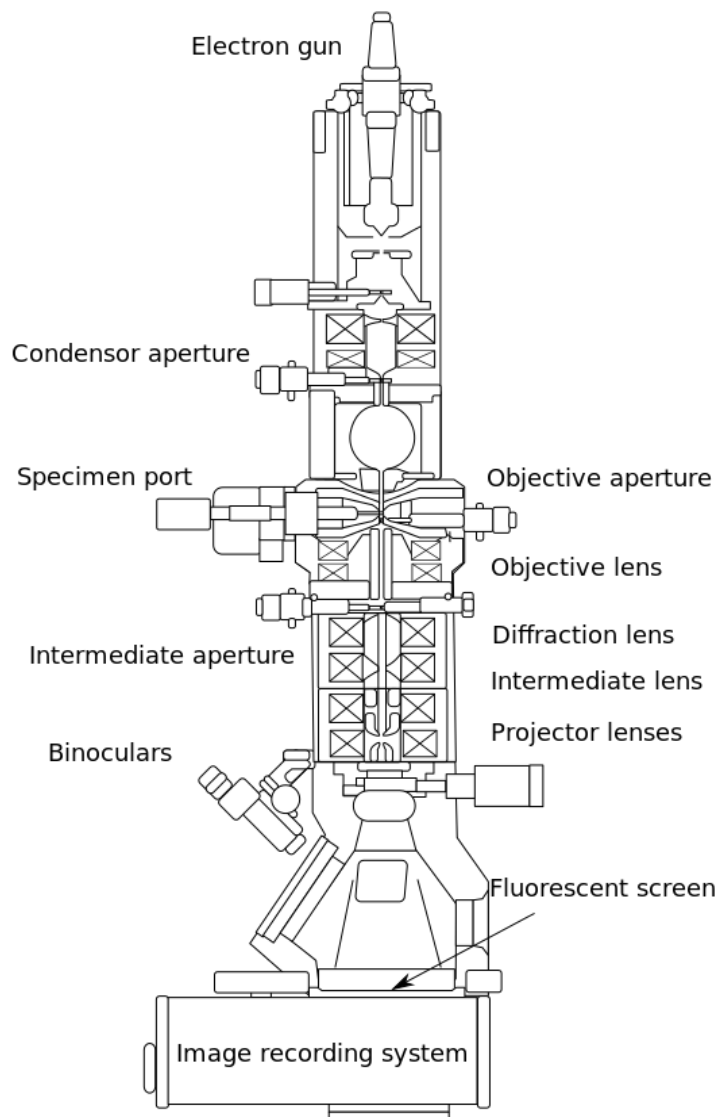


Figure 2.8 Scheme of a transmission electron microscope.²⁷

When the accelerated electron beam hits the specimen, a fraction of the electrons is transmitted through the specimen. The transmitted electrons are further focused by the electromagnetic lenses and the magnified electron image of the sample is then projected onto a phosphor-coated fluorescent viewing screen or a CCD (charge-coupled device) camera. The transmitted electrons carry the structure information such as crystallography, defects, spatial variation and composition of the investigated sample. In order to allow the electrons to pass through, the specimens for TEM analysis should be very thin (typically < 100 nm).

2.9.2 Scanning Electron Microscopy (SEM)

In scanning electron microscopy (SEM), the specimen is probed by a focused electron beam scanning across a certain area (raster scanning) on the surface of the specimen.²⁸ When the highly energetic electrons impinge the probing material, a portion of electrons transmits through the material while the other portions are scattered, accompanied by some energy loss. The energy loss of the electrons is converted into various forms such as heat, backscattered electrons, secondary electrons, and X-rays, all of which provide signals that carry the surface topography and composition information about the investigated material. In most of the SEMs, the secondary electrons emitted by the electron beam-excited atoms are collected and used to construct the final image. A schematic representation of a SEM setup is shown in Figure 2.9.

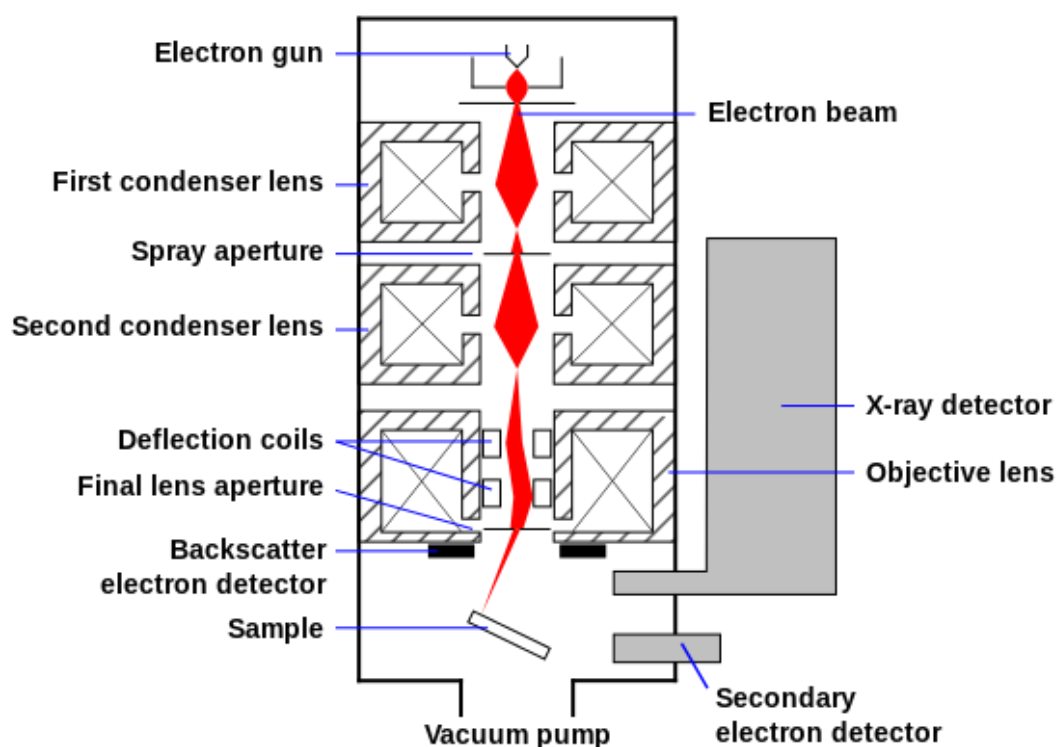


Figure 2.9 Scheme of a scanning electron microscope setup.²⁹

The accelerating voltage in SEMs is about 0.2 – 40 kV, which is lower than the accelerating voltage in TEM, hence the magnification of SEM is generally lower than that of TEMs. Nevertheless, owing to the surface probing mechanism, SEM is able to image bulk samples up to the size of many centimeters and create a great depth of field that results in a three-dimensional image of the sample. SEM offers great good flexibility in the operating

conditions: the specimen can be investigated in high or low vacuum, in wet condition (environmental SEM), and at cryogenic or elevated temperatures. The specimen for SEM imaging should be somewhat electrically conductive on the surface to avoid the accumulation of electrostatic charge that causes scanning faults or image artifacts when using secondary electron detection mode. Non-conductive materials are usually surface-coated with an ultrathin electrically conducting film, for example Au or C, before performing SEM. Alternatively, non-conductive specimens without surface coating can be imaged using environmental SEM or a low-voltage mode of operation.

2.9.3 Scanning Transmission Electron Microscopy (STEM)

Scanning transmission electron microscopy (STEM) combines the working principles of SEM and TEM, and can be performed on either type of the above-mentioned instruments.³⁰ In STEM, the electron beam is highly focused into a small area and is scanned over the specimen, resembling the SEM operation. After probing the sample, the transmitted electrons are collected to produce a variety of transmission images such as brightfield images. Due to the interactions of the sample with the highly focused electron beam, some of the transmitted electrons are inelastically scattered. In classical STEM, few electrons emerging from the sample are being collected, resulting in low signal collection efficiency. Alternatively, using high angle annular dark field (HAADF) detectors to collect the transmitted beam electrons that are elastically scattered through a higher angle provide much better image contrast and higher resolution. Since the detected signal consists of the transmitted electrons, the specimen for STEM observation must be thin but can be thicker than the sample for TEM observation. STEM can also be carried out by adding transmission detectors to a scanning electron microscope. However, this approach limits the accelerating voltage of the electron beam to around 30 keV. Another option to carry out STEM is adding scanning coils to a transmission electron microscope. In addition to avoiding some of the imaging artefacts associated with TEM, the STEM mode also allows for spectroscopic analysis of samples at the nanoscale.

2.10 Confocal Microscopy

Confocal microscopy is an optical imaging technique that is widely used in life sciences for subcellular structure visualization as well as in materials science for surface analysis.³¹ Confocal microscopy features better optical resolution and contrast than the conventional widefield optical microscopy and is able to collect serial optical sections from thick specimens to reconstruct a three-dimensional image. In conventional widefield optical microscopy, the light stream used to excite fluorophores illuminates a large area of the investigated sample (Figure 2.10(a)). The fluorescence generated by the sample from the out-of-focus region often interferes with the resolution of in-focus features. As the thickness of the specimen increases, the interference becomes more intense, therefore the resolution becomes worse. Confocal microscopy addresses the problem of the emission interference by adding a set of pinholes on the confocal plane of the lens to eliminate the out-of-focus light and thus improve the imaging resolution and contrast. The principal of light pathways in confocal microscopy is illustrated in Figure 2.11.

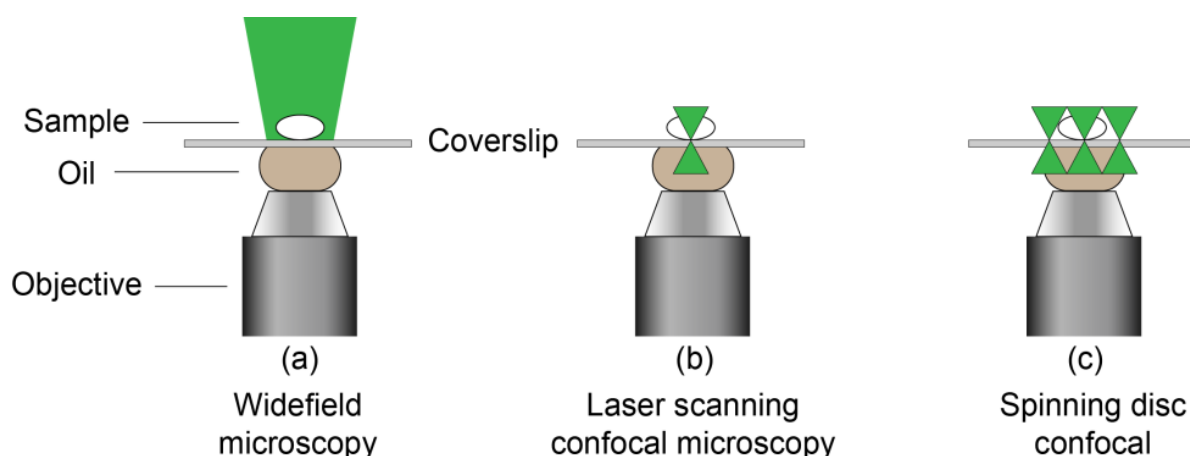


Figure 2.10 Scheme of the illumination pattern of (a) conventional widefield microscopy, (b) laser scanning confocal microscopy and (c) spinning disc confocal microscopy.³²

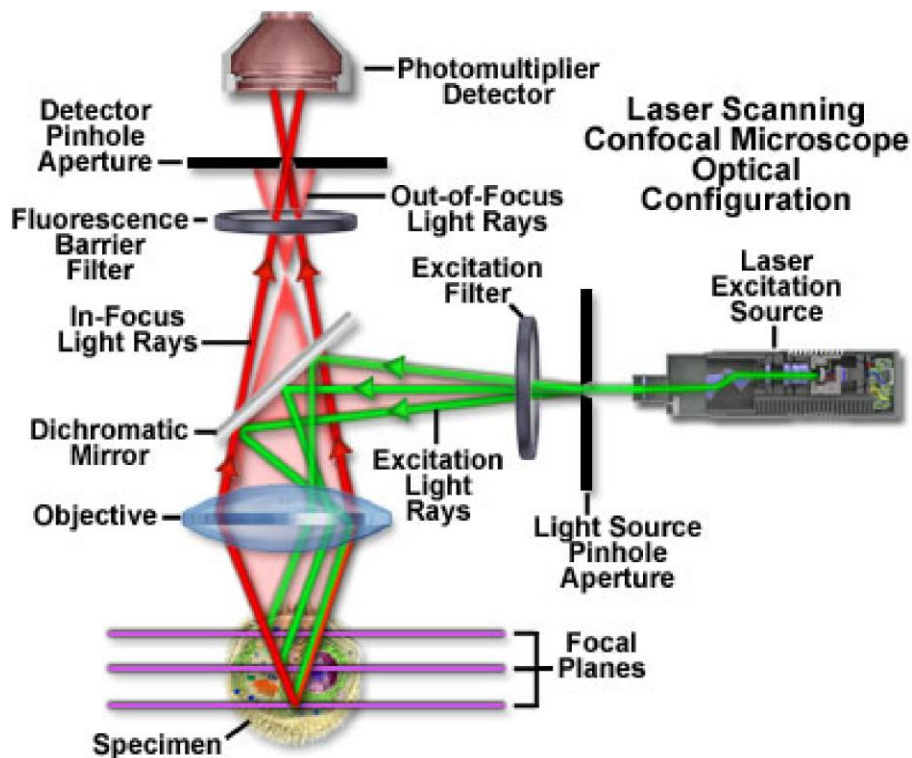


Figure 2.11 The principle of confocal microscopy.³³

A typical confocal microscope contains a set of light sources, a dichroic mirror, filters, objective lenses, a set of pinholes, a specimen stage and a photomultiplier detector. A light beam generated from the light source first passes through a pinhole aperture followed by a filter which selects the wavelength used to excite the fluorophores in the specimen. The light is subsequently reflected by a dichroic mirror and focused on a specimen through an objective lens. The excited fluorophores in the specimen then emit fluorescence that is collected by the objective, filtered by a dichroic mirror and filter, and then passes through another pinhole aperture before reaching the detector. The second pinhole placed on the focal plane selects only the fluorescence emitted from the focus point. The surface of the sample is scanned by either moving the specimen stage or the light beam. By imaging serial sections from different heights, a three-dimensional reconstitutive image can be obtained.

The most common types of confocal microscopes are laser scanning confocal microscope and spinning disc confocal microscope. As illustrated in Figure 2.10(b), the laser beam in laser scanning confocal microscopy is focused on the sample in a single point and scans the sample point by point in a raster pattern. The signal is detected sequentially from each scanning point by a photomultiplier detector until the entire image is assembled. To reach a high-resolution image, many scanning points are required, thus a longer time is needed for creating an image

as compared to widefield microscopy. This leads to a time error in observing dynamic samples. Spinning disc confocal microscopy overcomes this problem by utilizing multiple pinholes or slits to project a series of parallel excitation light beams on the specimen in multiple points simultaneously (Figure 2.10(c)). The fluorescence emitted from the specimen passes through the same pinholes or slits, and the signal is subsequently collected. Spinning disc confocal microscopy generates a parallel area-array image, such that the specimen can be adequately illuminated with lower excitation intensity, and therefore the photobleaching and phototoxicity are reduced accordingly. This technique is highly suitable for live cell imaging. In this study, all the live cell images were recorded *via* spinning disc confocal microscopy. Figure 2.12 shows a schematic representation of the spinning disc confocal microscope configuration.

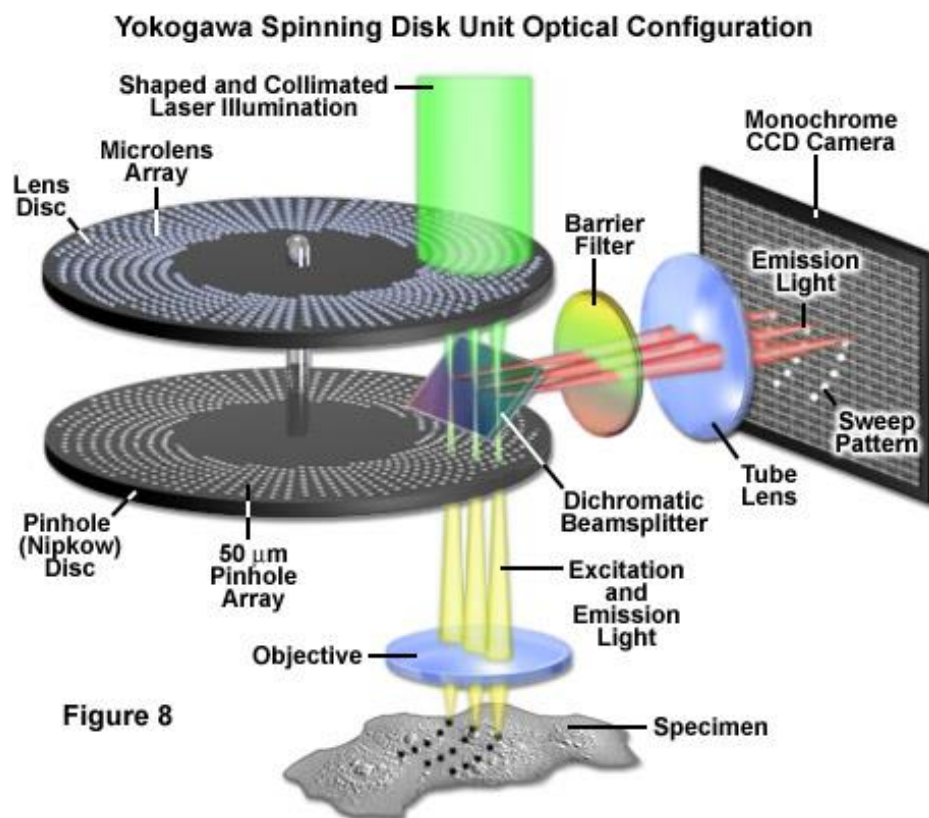


Figure 2.12 Spinning disc confocal microscope configuration.³⁴

2.11 References

- 1 Sing, K. The use of nitrogen adsorption for the characterisation of porous materials. *Colloids Surf. Physicochem. Eng. Aspects* **187-188**, 3-9 (2001).
- 2 Sing, K. S. W. *et al.* Reporting physisorption data for gas/solid systems with special reference to the determination of surface area and porosity (Recommendations 1984). *Pure Appl. Chem.* **57** (1985).
- 3 Thommes, M. *et al.* Physisorption of gases, with special reference to the evaluation of surface area and pore size distribution (IUPAC Technical Report). *Pure Appl. Chem.* **87** (2015).
- 4 Monson, P. A. Understanding adsorption/desorption hysteresis for fluids in mesoporous materials using simple molecular models and classical density functional theory. *Microporous Mesoporous Mater.* **160**, 47-66 (2012).
- 5 Landers, J., Gor, G. Y. & Neimark, A. V. Density functional theory methods for characterization of porous materials. *Colloids Surf. Physicochem. Eng. Aspects* **437**, 3-32 (2013).
- 6 Thommes, M. & Cychosz, K. A. Physical adsorption characterization of nanoporous materials: progress and challenges. *Adsorption* **20**, 233-250 (2014).
- 7 Langmuir, I. The Constitution and Fundamental Properties of Solids and Liquids. Part I. Solids. *J. Am. Chem. Soc.* **38**, 2221-2295 (1916).
- 8 Brunauer, S., Emmett, P. H. & Teller, E. Adsorption of Gases in Multimolecular Layers. *J. Am. Chem. Soc.* **60**, 309-319 (1938).
- 9 Lastoskie, C., Gubbins, K. E. & Quirke, N. Pore size distribution analysis of microporous carbons: a density functional theory approach. *The Journal of Physical Chemistry* **97**, 4786-4796 (1993).
- 10 Rouquerol, J. *et al.* Recommendations for the characterization of porous solids (Technical Report). *Pure Appl. Chem.* **66** (1994).
- 11 Barrett, E. P., Joyner, L. G. & Halenda, P. P. The Determination of Pore Volume and Area Distributions in Porous Substances. I. Computations from Nitrogen Isotherms. *J. Am. Chem. Soc.* **73**, 373-380 (1951).
- 12 Berne, B. J. & Pecora, R. *Dynamic Light Scattering: With Applications to Chemistry, Biology, and Physics*. Wiley VCH (1976).
- 13 McNaught, A. D. & Wilkinson, A. *IUPAC. Compendium of Chemical Terminology*. 2nd edn, Blackwell Scientific Publications (1997).
- 14 Hans-Jürgen Butt, Karlheinz Graf & Kappl, M. *Physics and chemistry of interface*. Wiley VCH (2003).
- 15 Zeta potential. Malvern Instruments (2016).

- 16 Zetasizer Nano User Manual. Malvern Instruments (2013).
- 17 Hesse, M., Meier, H. & Zeeh, B. *Spectroscopic Methods in Organic Chemistry*. Thieme (2008).
- 18 Mermet, J., Otto, M., Kellner, R. & Cases, M. *Analytical Chemistry: A Modern Approach to Analytical Science*. Wiley VCH (2004).
- 19 Sepe, M. P. *Thermal Analysis of Polymers*. Rapra Technology Limited (1997).
- 20 Pang, L. S. K., Saxby, J. D. & Chatfield, S. P. Thermogravimetric analysis of carbon nanotubes and nanoparticles. *The Journal of Physical Chemistry* **97**, 6941-6942 (1993).
- 21 Fratzl, P. Small-angle scattering in materials science - a short review of applications in alloys, ceramics and composite materials. *J. Appl. Crystallogr.* **36**, 397-404 (2003).
- 22 Cullity, B. D. & Stock, S. R. *Elements of X-Ray Diffraction*. Prentice Hall (2001).
- 23 Lakowicz, J. R. *Principles of Fluorescence Spectroscopy*. Plenum Press (1983).
- 24 Sauer, M., Hofkens, J. & Enderlein, J. *Handbook of Fluorescence Spectroscopy and Imaging*. Wiley VCH (2011).
- 25 Fultz, B. & Howe, J. *Transmission Electron Microscopy and Diffractometry of Materials*. Springer (2008).
- 26 Champness, P. E. *Electron Diffraction in the Transmission Electron Microscope*. Garland Science (2001).
- 27 https://commons.wikimedia.org/wiki/File:Scheme_TEM_en.png, 12.04.2017.
- 28 Reimer, L. *Scanning electron microscopy*. Springer (1998).
- 29 [https://commons.wikimedia.org/wiki/File:Schema_MEB_\(it\).svg](https://commons.wikimedia.org/wiki/File:Schema_MEB_(it).svg), 12.07.2017.
- 30 Pennycook, S. J. & Nellist, P. D. *Scanning Transmission Electron Microscopy*. Springer (2011).
- 31 Pawley, J. B. *Handbook of biological confocal microscopy*. Springer (2006).
- 32 <http://www.andor.com/learning-academy/spinning-disk-confocal-a-technical-overview>, 12.06.2017.
- 33 <http://www.olympusmicro.com/primer/techniques/confocal/confocalintro.html>, 12.04.2017. Olympus Microscopy Resource Center.
- 34 <http://zeiss-campus.magnet.fsu.edu/articles/spinningdisk/introduction.html>, 12.04.2017. ZEISS.

3 Synthesis and Functionalization of Ordered Large-Pore Mesoporous Silica Nanoparticles for Biomedical Applications

This chapter is based on the following publication:

Hsin-Yi Chiu, Heinrich Leonhardt and Thomas Bein, *Chemie Ingenieur Technik* 2017, 89, 876-886.

Dedicated to Prof. Dr. Wilhelm Schwieger on the occasion of his 65th birthday

Abstract

A dual surfactant synthetic approach was employed for the synthesis of large-pore mesoporous silica nanoparticles (MSNs). The as-synthesized mesoporous silica exhibited not only 2D hexagonal mesostructure with an average pore size of about 7 nm but also a spherical nanoparticulate morphology. A delayed co-condensation synthesis method was further employed to create site-specific core-shell bifunctional MSNs. These core-shell large-pore MSNs are biocompatible and can be efficiently taken up by cells. They are therefore promising nanocarriers for cellular delivery purposes.

3.1 Introduction

Periodically ordered mesoporous silicas containing high surface area, large pore volume, and stable silica frameworks offer a good platform for adsorbing or hosting guest molecules and therefore are widely used in separation, catalysis, and sensing.¹⁻⁴ MCM-41 (Mobile Composition of Matter No. 41) discovered by Kresge *et. al.*⁵ and SBA-15 (Santa Barbara Amorphous No. 15) discovered by Stucky *et. al.*⁶ are two leading mesoporous silica materials used in the above-mentioned research fields. They both feature highly ordered 2D hexagonal mesostructures as well as narrow pore size distributions that are accessible for mass transfer of guest molecules and evaluation of cargo uptake and release kinetics.⁷⁻⁹ In 2003 a pioneering study described the synthesis of MCM-41-type mesoporous silica nanoparticles (MSNs) as a nanocarrier system.¹⁰ In this study, Lin and co-workers also addressed the possibility of functionalizing the 200-nm sized mesoporous silica particles with a stimuli-responsive gatekeeper for the controlled release of drug molecules and neurotransmitters in

cells. Since then, the study of MSNs in biomedical applications has seen enormous growth. Apart from small drug molecules, a variety of biomolecules ranging from small-sized amino acids¹¹ to massive proteins,^{12,13} oligonucleotides¹⁴ and plasmid DNAs¹⁵ were loaded into the pores or adsorbed on the external surfaces of MCM-41-type MSNs for drug and gene delivery purposes. However, these MCM-41-type MSNs containing an organized pore structure exhibit pore size limitations up to 6 nm.¹⁶

In contrast, SBA-15-type mesoporous silica materials templated by the non-ionic triblock copolymer P123 or related copolymers exhibit large pore dimensions (ranging from 5 – 30 nm), thick walls (about 3 – 5 nm)¹⁷ and thermally stable frameworks that make them suitable for the encapsulation of biomolecules larger than 6 nm. Their rigid and stable silica frameworks provide better protection of cargos from denaturation in critical environments than MCM-41-type silica materials.¹⁸ However, a major limitation of these SBA-15-type materials resides in their bulky particle sizes, which can restrict their use in intracellular delivery.

In 2004 Ying *et. al.*¹⁹ introduced the cationic fluorinated surfactant FC-4 to the nonionic triblock copolymer-templated mesoporous silica synthesis processes, where they obtained nanosized (50 – 300 nm) particles exhibiting various mesostructures including 3D cubic, 2D hexagonal, foamlike and disordered pores depending on the type of triblock copolymer used, and tunable pore sizes in the range of 5 – 30 nm. They proposed that the fluorocarbon surfactant acted as particle growth limiting agent to confine the particle sizes, whereas the triblock copolymers served as structure-directing templates to enable ordered mesostructure formation. For the first time, this work demonstrated the preparation of large, ordered mesostructured SBA-15-type silica particles with well-defined particle sizes (< 300 nm) suitable for drug delivery applications. Following up on this work, several research groups have adopted this fluorocarbon-mediated synthetic strategy to generate large-pore mesoporous silica nanoparticles containing ordered mesopores, and further functionalized their surfaces for encapsulation or delivery of large biomolecules.²⁰⁻²³ For example, Gao *et. al.*²⁰ synthesized large, cubic mesostructured MSNs (with pore size around 17 nm and particle size in the range of 70 – 300 nm) templated by Pluronic F127 at low temperature (10 °C) and further post-synthetically grafted amino groups on the surface of the MSNs for plasmid DNA packaging. They demonstrated the large-pore MSNs to be capable of protecting DNA from degradation in the presence of enzymes in buffer. Qiao and coworkers grafted poly-L-lysine on the surface of similar MSNs (particle size about 100 – 200 nm)

containing a large pore (20 nm), cubic mesostructure for siRNA delivery in osteosarcoma cancer cells.²¹ Yu *et al.*²² introduced ethanol and KCl into a synthesis templated by Pluronic P123 and obtained highly ordered, bicontinuous cubic mesostructured large pore MSNs. After surface modification with octadecyl groups, they showed successful siRNA delivery into human colon cancer cells (HCT-116) with significant cell proliferation suppression. Kros and co-workers²³ incorporated trimethylbenzene (TMB) into a Pluronic P123 templated silica synthesis which resulted in 10 nm-wide mesochannels in cuboidal-like nanoparticles 90 ± 20 nm in length and 43 ± 7 nm in width. They modified the surfaces of these nanoparticles with amino groups and demonstrated that they enable the rapid encapsulation and release of several model proteins. All these studies indicate that using FC-4 in the triblock copolymer templated synthesis under mild acidic condition resulted in nanosized large-pore mesoporous silica particles. Furthermore, they also revealed that molecular surface modification of the MSNs can be an important factor for accommodating certain biomolecules in the mesopores.

In this study, the fluorocarbon surfactant-mediated synthesis approach for the preparation of ordered, large-pore mesoporous silica particles with nanoparticulate morphology having a particle size about 100 – 200 nm was used. The as-synthesized mesoporous silica nanoparticles templated by Pluronic P123 exhibit 2D hexagonal mesopores with an average pore size of 7 nm and a wall thickness of about 3 nm, which resembles the mesostructure of SBA-15-type materials. Various contents of thiol groups were incorporated into the silica framework *via* a co-condensation synthesis procedure. The impact of thiol content in the silica co-condensation process on the final mesostructure morphology was also studied. Further, core-shell bifunctional SBA-15-like MSNs were synthesized using a delayed co-condensation method. By applying two hydrothermal treatment steps, these core-shell MSNs retained ordered mesopores (2D hexagonal) and large pore size (8 nm).

To evaluate the potential uses of these SBA-15-like MSNs in cellular delivery, polyethylene glycol (PEG) was attached to their external surface to enhance their colloidal stability and fluorescence dyes were grafted on the internal surface for microscopic tracking. The interaction of the multifunctional SBA-15-like MSNs with cells was also examined. The results indicate that the PEGylated SBA-15-like MSNs were efficiently taken up by HeLa cells and that they showed good biocompatibility up to the concentration of 200 $\mu\text{g/ml}$. Using high-content optical microscopy, it was possible to quantify the cellular uptake efficiency of

the MSNs, being up to 98% after incubating HeLa cells with the MSNs for 24 h. Furthermore, the endosomal-binding protein RhoB (Ras homolog family member B^{24,25}) was genetically encoded and conjugating with the fluorescent protein mCherry to HeLa cells for late endosome visualization. Using confocal microscopy, the co-localization of multifunctional MSNs and RhoB-labeled late endosomes could be tracked. Interestingly, it was found that most of the SBA-15-like MSNs were not co-localized with the RhoB-labeled late endosomes.

3.2 Results and Discussion

Synthesis of un-functionalized SBA-15 MSNs

The MSNs we synthesized here exhibit features (mesostructured, pore size and wall thickness) similar to the typical SBA-15 materials; accordingly, these MSNs were named SBA-15 MSNs. The SBA-15 MSNs were synthesized using 0.25 g of P123, 0.35 g of FC-4 and 1 g of TEOS in 40 ml of 0.02 M HCl at room temperature for 24 h, followed by a hydrothermal treatment at 140 °C for further 24 h. The as-synthesized powder was then template extracted, washed with ethanol and water, and re-dispersed in ethanol. After filtering out bulk precipitates, spherical particles with a size of about 100 nm remaining in the suspension can be observed in transmission and scanning electron microscopy (Figure 3-1a - b). Dynamic light scattering (DLS) (Figure 3-1c) indicated the hydrodynamic diameter of the particles in ethanol suspension to be around 150 nm. The X-ray diffraction data of the sample powder (Figure 3-1d) show three reflections indexed as (100), (110) and (200), which is associated with a 2D hexagonal mesostructure where the spacing between each pore center a_0 (calculated from the $d_{(100)}$ spacing, Table 3-1) is about 11 nm. This well-ordered pore structure can be further confirmed by the TEM image in Figure 1a. Nitrogen sorption analysis of the sample powder showed a type IV isotherm (Figure 3-1e) and a BET specific surface area of 185 m²/g. The pore size distribution calculated *via* a NLDFT equilibrium model resulted in an average pore size of 7 nm (Figure 3-1f).

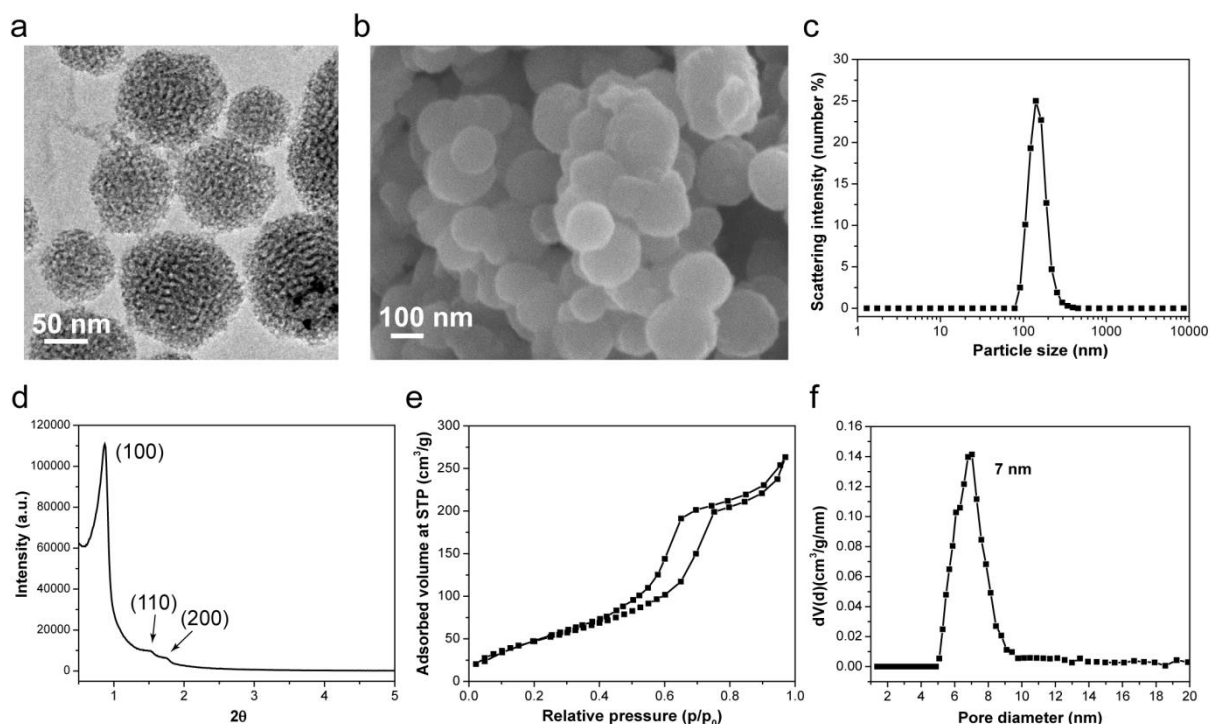


Figure 3-1. Characterization of the un-functionalized SBA-15 MSNs. (a) TEM. (b) SEM, and (c) hydrodynamic particle size measured by DLS. Filtrated particles were measured in ethanol suspension. (d) XRD pattern. The reflections are attributed to the hexagonal pore structure of the SBA-15 MSNs. (e) N₂ sorption isotherm. (f) N₂ sorption pore size distribution calculated according to the NLDFT equilibrium model.

According to the pore spacing a_0 and the average pore size measured by N₂ sorption, we estimate the wall thickness of the MSNs to be about 4 nm. The pore dimension (7 nm) of the as-synthesized SBA-15 MSNs is sufficient for adsorbing a large variety of important biomolecules.^{1,2} The narrow pore size distribution of the nanoparticles can also be favorable for adsorbing enzymes possessing a comparable size, as there appears to be evidence indicating that mesopores matching the size of encapsulated enzymes can enhance enzyme activity compared to hosts with pore sizes larger than the enzyme.²⁶⁻²⁹ In addition, 2D hexagonal pore systems confined in small particles result in short channel lengths, thus facilitating mass transfer in the mesostructure that can be favorable for immobilizing and releasing proteins.^{23,30}

Table 3-1 Detailed characterization information of the SBA-15 MSNs.

SH content in MSNs (mol %)	Particle size ^a (nm)	XRD 2 θ ^b (°)	a_0 ^c (nm)	Pore size (nm)	BET Surface area (m ² /g)	Pore volume ^d (cm ³ /g)
0 (pure silica)	138	0.91	11.2	7	185	0.38
2	195	0.95	10.7	6.6	297	0.42
5	253	0.98	10.4	6	249	0.31
7	276	1	10.2	6	421	0.57
10	293	0.98	10.4	5.4	453	0.53

^a Filtrated samples were measured by DLS in ethanol suspension.

^b Referring to (1 0 0) reflection.

^c a_0 : spacing between each pore center, calculated based on the formula: $a_0 = d_{100} \times \frac{2}{\sqrt{3}}$

^d Calculated from $p/p_0 = 0.99$.

Synthesis of thiol-functionalized SBA-15 MSNs

Thiol groups are widely used in cross-linking chemistry and can be easily applied for surface modifications. Hence, integrating thiol groups into the silica framework can enable further surface modifications of the MSNs. Here thiol-functionalized SBA-15 MSNs were synthesized *via* a co-condensation method. Various thiol contents were incorporated into the silica framework, and the as-synthesized thiol-functionalized SBA-15 MSNs were subsequently characterized (Table 3-1). According to the corresponding TEM micrographs (Figure 3-2a), all the thiol-functionalized SBA-15 MSNs exhibit spherical shapes and regular pore structures. However, as the thiol content increases, the 2D hexagonal porous structure becomes more irregular, which is also illustrated in the X-ray diffraction data (appendix Figure 3-6).

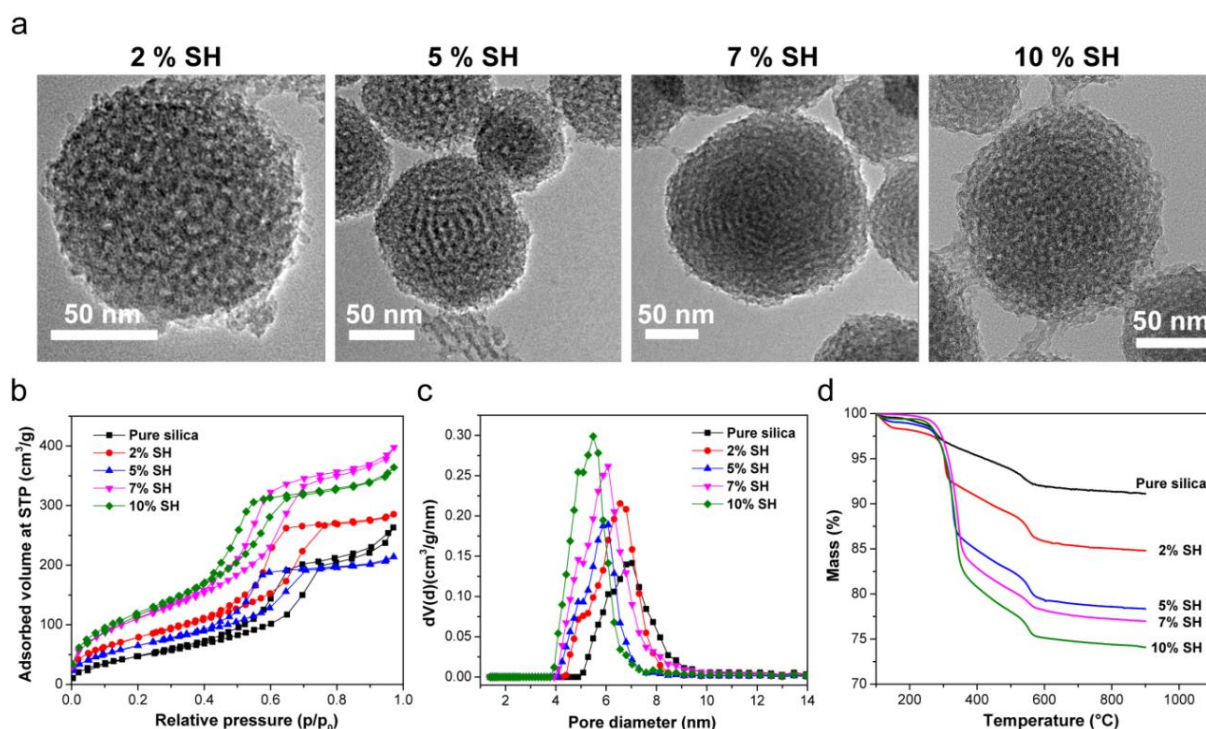


Figure 3-2. Characterization of the thiol-functionalized SBA-15 MSNs. (a) TEM images, (b) N₂ sorption isotherms, and (c) NLDFT pore size distributions. (d) Thermogravimetric analysis.

All the thiol-functionalized SBA-15 MSNs present type IV nitrogen sorption isotherms (Figure 3-2b) and have BET specific surface areas in the range of 200 – 500 m²/g (Table 3-1). Confirming the pore structure changes observed in the TEM images and the XRD data, the average pore size decreased from 7 nm to 5 nm when the thiol content in the MSNs increased from 0 mol% to 10 mol% (Figure 3-2c). The successful co-condensation of thiol groups into the silica framework can be observed with Raman spectroscopy, with an S-H vibration occurring at 2585 cm⁻¹ (appendix Figure 3-7). The thermogravimetric analysis (TGA) of the mass loss of each sample correlates with the increasing thiol content in the silica framework (Figure 3-2d). Notably, the filtrated thiol-functionalized SBA-15 MSNs are smaller than 300 nm (Table 3-1), which suggests applications in drug delivery.

Synthesis of core-shell bifunctional SBA-15 MSNs

Following the successful co-condensation synthesis of thiol-functionalized SBA-15 MSNs, a delayed co-condensation synthesis method was employed to create site-specific core-shell bifunctional SBA-15 MSNs containing 5 mol% of SH groups in the core and 1 mol% of NH₂ groups on the external shell. To preserve the small particle size, we increased the amount of the particle growth inhibitor FC-4 from 0.35 g (for un-functionalized SBA-15 MSN synthesis) to 0.5 g for the synthesis of core-shell bifunctional SBA-15 MSNs. A second hydrothermal treatment in a 2 M HCl solution was employed in the synthesis process for pore expansion in order to balance the pore shrinking from the organosilane co-condensation. As illustrated in the TEM images (Figure 3-3a), the core_{SH}-shell_{NH₂} SBA-15 MSNs present a well-defined close to spherical shape with a particle size of around 100 – 200 nm, as well as a highly ordered mesostructure. The average hydrodynamic particle size of the filtrated sample measured by DLS was about 150 nm (appendix Figure 3-8, Table 3-2). The presence of ordered mesopores in the core_{SH}-shell_{NH₂} SBA-15 MSNs was substantiated by X-ray diffraction (Figure 3-3b), where the reflections could be indexed as (100), (110) and (200), referring to a 2D hexagonal mesostructure. Nitrogen sorption revealed a type IV isotherm (Figure 3-3c) and a BET surface area of 367 m²/g (Table 3-2). The pore size distribution obtained from the NLDFT equilibrium model showed an average pore size of 7.5 nm (Figure 3-3d), where the pore expansion effect (compared to the 5 mol% thiol-functionalized particles) might be caused by the second hydrothermal treatment in an acidic environment. If the average pore size is subtracted from the a_0 (spacing between each pore center, calculated from the XRD $d_{(100)}$ spacing, see Table 2), the wall thickness of the core_{SH}-shell_{NH₂} SBA-15 MSNs is estimated to be 3 nm. The thinner wall thickness of the core_{SH}-shell_{NH₂} SBA-15 MSNs compared to the un-functionalized and thiol-functionalized samples suggests that the second hydrothermal treatment leads to a more condensed silica framework.

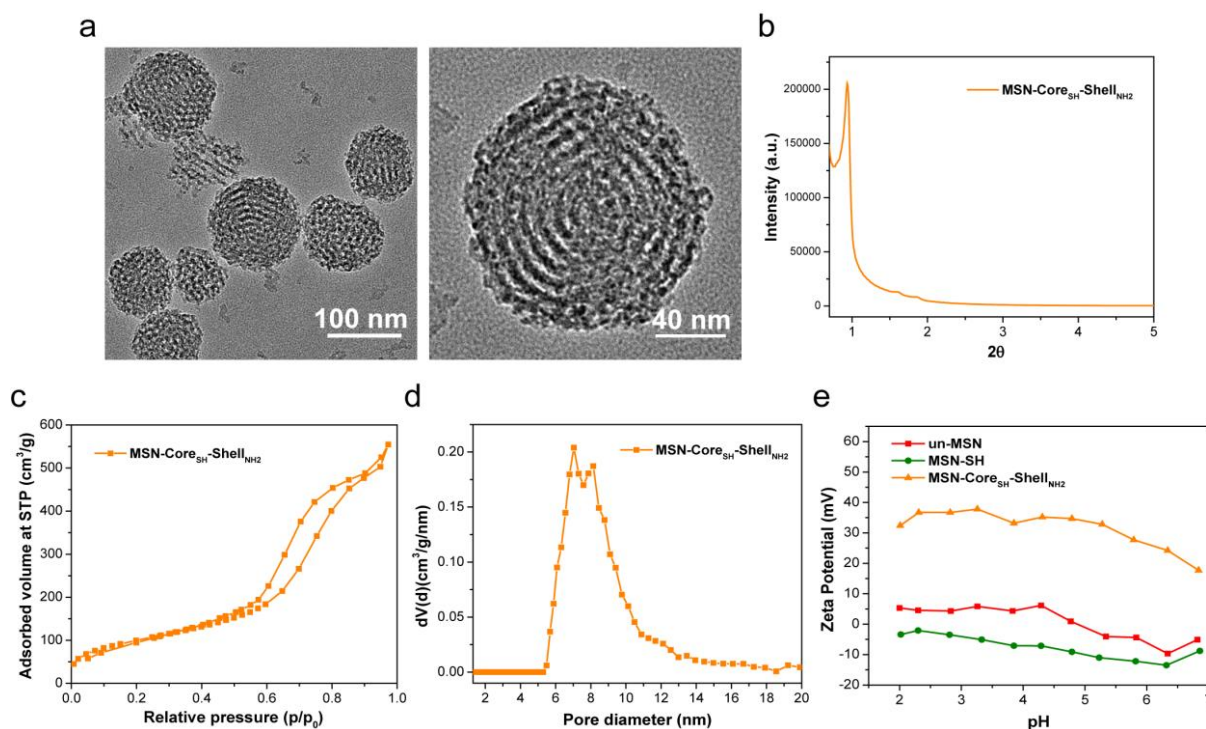


Figure 3-3. Characterization of the core_{SH}-shell_{NH₂} bifunctional SBA-15 MSNs. (a) TEM images. (b) X-ray diffraction. (c) N₂ sorption isotherm. (d) N₂ sorption NLDFT pore size distribution. (e) Zeta Potential of the un-functionalized, thiol-functionalized, and core_{SH}-shell_{NH₂} bifunctional SBA-15 MSNs, respectively.

The amino-functionalized external surface of the core_{SH}-shell_{NH₂} SBA-15 MSNs displays a significantly higher zeta potential than the un-functionalized and thiol-functionalized SBA-15 MSNs (Figure 3-3e). Summing up, here the successful synthesis of bifunctional core-shell SBA-15 MSNs was demonstrated by applying a delayed co-condensation strategy. These core_{SH}-shell_{NH₂} SBA-15 MSNs offer the possibility to integrate several spatially defined molecular surface modifications, which renders them promising multifunctional nanocarriers.

Table 3-2. Detailed characterization information of the core_{SH}-shell_{NH₂} SBA-15 MSNs

Content of functional groups in core-shell MSNs	Particle size ^a (nm)	XRD 2θ ^b (degree)	a ₀ ^c (nm)	Pore size (nm)	Surface area (m ² /g)	Pore volume ^d (cm ³ /g)
Core: 5 mol% SH	175	0.96	10.6	7.5	367	0.86
Shell: 1 mol% NH ₂						

^a Filtrated samples were measured by DLS in ethanol suspension.

^b Referring to (1 0 0) reflection.

^c a₀: spacing between each pore center, calculated based on the formula: $a_0 = d_{100} \times \frac{2}{\sqrt{3}}$

^d Calculated from p/p₀ = 0.99.

The interaction of the core-shell SBA-15 MSNs with cells

To investigate the interactions of the core-shell SBA-15 MSNs with cells, hydrophilic polyethylene glycol (PEG) was attached on the external surface of the MSNs to enhance their colloidal dispersibility, while fluorescence dyes (ATTO 488) were grafted to the core of the particles to enable tracking of the particles in confocal microscopy. The core_{ATTO488}-shell_{PEG} SBA-15 MSNs were incubated with HeLa-k cells in a culture medium (25 μg MSNs in 1 ml of cell culture medium) and the endocytosis of the MSNs was tracked by live cell confocal microscopy. It was observed that 4 h post particle incubation, the tracked particles were internalized by the cells and located near the nucleus in the cytoplasm (Figure 3-4a). In order to quantify the cellular uptake efficiency of the MSNs in a large cellular population (up to 10³ cells per investigation), a high content imaging system (Operetta[®], PerkinElmer) was used for the analysis. The MSN-treated (24 h) HeLa-k cells were fixed, DAPI and propidium iodide stained, and imaged by means of the high-content microscopy. After image segmentation through different fluorescence channels (DAPI for nuclei segmentation, propidium iodide for cytoplasm segmentation and ATTO 488 for MSN segmentation), the populations of the cells and the MSN-internalizing cells were evaluated (appendix Figure 3-9). The “cell” population implies the region containing nucleus and cytoplasm, while each cell that internalized more than two particles is referred to as “MSN-internalizing cell” (particles that locate in the cell areas were considered as being internalized by the cell). The cellular uptake efficiency was evaluated with the equation: 100% × number of the MSN-internalizing cells/number of the cells. Based on the evaluation of more than two thousands cells, the quantified cellular uptake

efficiency is 98%. This very high cellular uptake efficiency of the SBA-15 MSNs indicates their potential for carrying cargo across the cell membrane. Additionally, both the native core-shell MSNs and the PEGylated core-shell MSNs show good biocompatibility up to a concentration of 200 $\mu\text{g/ml}$ (the value of IC_{50}) in the MTT assay (Figure 3-4b).

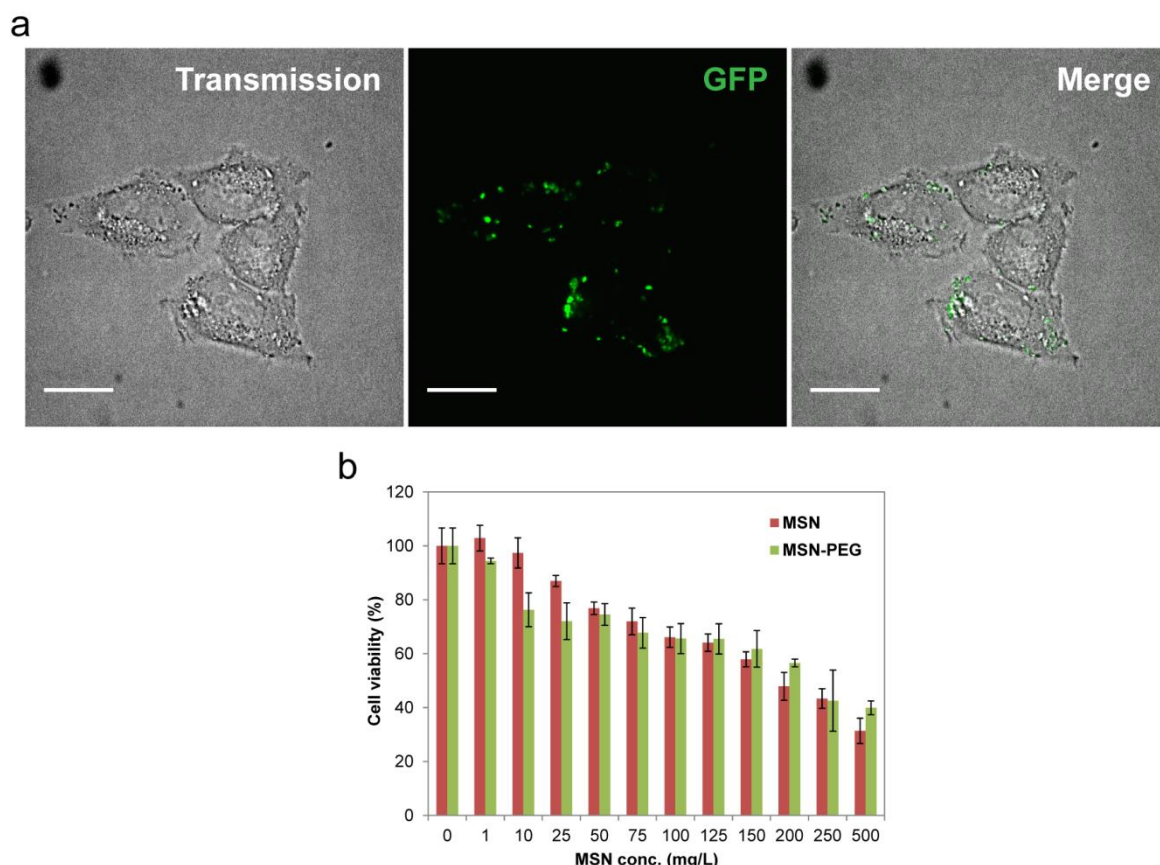


Figure 3-4. Live cell imaging for cellular uptake tracking and cytotoxicity analysis of HeLa cells with respect to the core-shell SBA-15 MSNs. (a) The $\text{core}_{\text{ATTO488}}\text{-shell}_{\text{PEG}}$ SBA-15 MSNs (green dots) were internalized by HeLa cells after 4 h incubation. (b) MTT assay for cytotoxicity analysis after 24 h incubation of MSNs with HeLa cells. MSN: $\text{core}_{\text{SH}}\text{-shell}_{\text{NH}_2}$ SBA-15 MSNs, MSN-PEG: $\text{core}_{\text{SH}}\text{-shell}_{\text{PEG}}$ SBA-15 MSNs.

Endosomal trapping of internalized nanoparticles is a major barrier for cellular delivery of membrane impermeable cargos. To investigate whether the internalized SBA-15 MSNs are trapped in endosomes or not, a plasmid was constructed that expresses an endosomal-localization protein – RhoB fused with red fluorescence protein mCherry – to genetically label the endosomes in HeLa-k cells and thereby being able to track the endosome locations in the cytoplasm. RhoB is a member of the GTPase family that was found to localize on the membrane of late endosomes, controlling cytokine trafficking and cell survival

regulation.^{24,25} 24 h after transfection with plasmid pCAG-mCherry-hRhoB-IB, the core_{ATTO488}-shell_{PEG} SBA-15 MSNs were incubated with the endosome-labeled HeLa-k cells in the culture medium. After 24 h, the cells were washed, fixed, membrane-permeabilized, stained with DAPI and subsequently imaged by confocal microscopy.

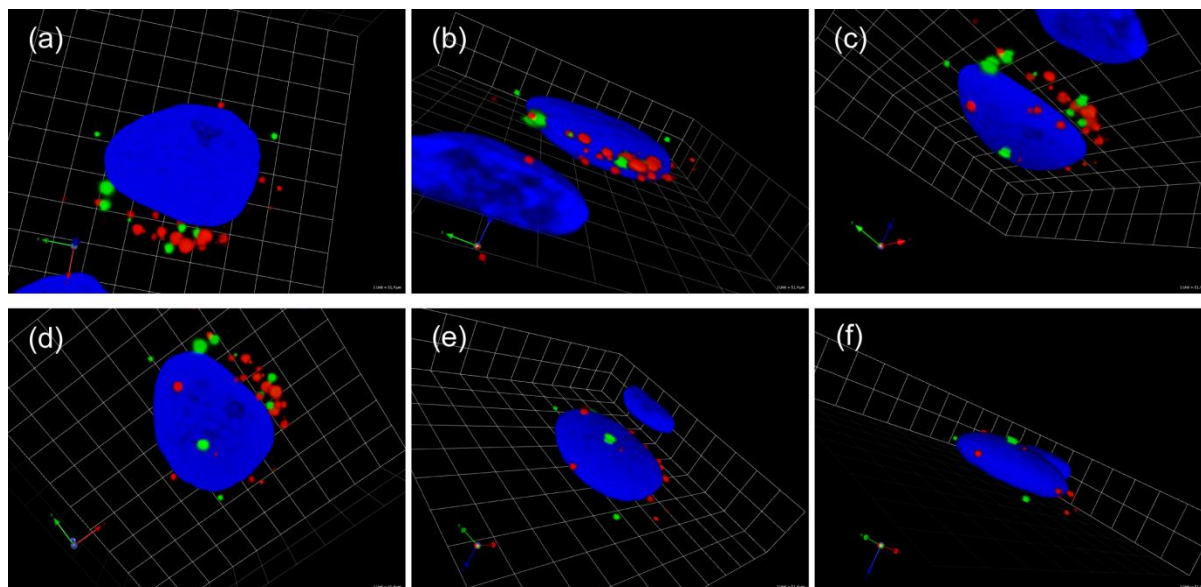


Figure 3-5. A 3D stacking confocal image of the MSN-internalized HeLa cells. (a) Top-view of the image. (b)-(f) Different view angles of the image in (a) in the sequence of z direction (blue arrow in the images) rotation. White grid in the background: 1 unit = 51.4 μm . Blue: DAPI stained nuclei, red: RhoB-mCherry-labeled late endosomes, green: core_{ATTO488}-shell_{PEG} SBA-15 MSNs.

Figure 3-5 illustrates a sequence of 3D stacking images (rotating along the z-axis) of the cells that have internalized SBA-15 MSNs. The images show that the SBA-15 MSNs (green) are located around the nucleus but that they are not co-localized with the RhoB-mCherry labeled late endosomes (red). In early studies of the endosomal escape of nanoparticles, researchers concluded that non-co-localization of particles and endosomes can serve as an indication for the endosomal escape of the particles.^{13,31-33} However, in the present study no endosomal escape agents were incorporated in the functional SBA-15 MSNs. Also, the RhoB-containing endosomes do not represent all vesicles in the cells. These findings warrant further studies into the endosomal escape mechanisms operating with our core-shell mesoporous silica nanoparticles.

3.3 Conclusion

In this study, SBA-15-like mesoporous silica nanoparticles containing well-ordered 2D hexagonal mesopores and a small particle size around 100 – 200 nm were successfully synthesized by adopting the FC-4 and P123 co-surfactant synthesis strategy. An efficient co-condensation synthesis was established to functionalize the nanoparticles with organic groups, and the method was further developed towards to a delayed co-condensation synthesis yielding spatially defined, core-shell bifunctional SBA-15 MSNs. The as-synthesized MSNs feature pore dimensions (around 7 nm) that are sufficient for the encapsulation of various biomolecules, and they could be decorated with multiple surface functionalizations. Their interactions with HeLa cells indicated that they are non-cytotoxic up to a concentration of 200 µg/ml, and that they can be efficiently taken up by the cells (cellular uptake efficiency is 98% after 24 h of particle incubation). Concluding, we view these multifunctional SBA-15 MSNs to be promising candidates for drug delivery vehicles and as nanocarriers for research on cellular delivery.

3.4 Experimental

Materials

Pluronic P123 (P123, BASF), fluorocarbon surfactant FC-4 (FC-4, Yick-Vic Chemicals), tetraethyl orthosilicate (TEOS, Aldrich, $\geq 99\%$), 3-mercaptopropyl triethoxysilane (MPTES, ABCR, $\geq 92\%$), 3-aminopropyl triethoxysilane (APTES, Aldrich, $\geq 98\%$), oxalic acid dihydrate (Sigma), poly(ethylene glycol) bis(amine) (PEG-diamine, Aldrich, $M_n = 2000$), N-(3-dimethylaminopropyl)-N-ethylcarbodiimide (EDC, Alfa-Aesar, 98 %), N-hydroxysulfosuccinimide sodium salt (sulfo-NHS, Aldrich), absolute ethanol (EtOH, Aldrich, $\geq 99.5\%$), conc. hydrochloric acid (HCl, Aldrich, 37 wt%), thiazolyl blue tetrazolium bromide (MTT, $\geq 97.5\%$, Sigma), dimethyl sulfoxide (DMSO, Applichem, molecular biology grade), Dulbecco's Modified Eagle's Medium (DMEM, Sigma), Dulbecco's Modified Eagle's Medium – phenol red free (Sigma), Dulbecco's Phosphate Buffered Saline (PBS, Sigma), Fetal Bovine Serum (FBS) Superior (Biochrom), gentamycin solution (50 mg/ml, SERVA), L-glutamine solution (200 mM, Sigma), HEPES solution (1 M, Sigma).

All reagents were used without further purification. Bi-distilled water obtained from a Millipore system (Milli-Q Academic A10) was used for all synthesis and washing steps. 2 M HCl and 0.02 M HCl were prepared using bi-distilled water and conc. hydrochloric acid.

Methods

Synthesis of un-functionalized and thiol-functionalized SBA-15 MSNs

This synthesis procedure was adapted from a fluorocarbon-surfactant-mediated MSN synthesis method previously reported by Ying *et al.*¹⁹ In a typical un-functionalized SBA-15 MSNs synthesis, 0.25 g of P123 and 0.35 g of FC-4 were dissolved in 40 ml of 0.02 M HCl at RT followed by the addition of TEOS (1 g, 4.8 mmol). For the co-condensation synthesis of thiol-functionalized SBA-15 MSNs, a portion of TEOS was replaced by MPTES (the detailed contents are listed in Table 3-3), and the mixture of TEOS and MPTES was added to the surfactant solution. The reaction solution was stirred (500 rpm) at RT for 20 h and then was transferred to a Parr autoclave for hydrothermal treatment at 140 °C for 24 h under static conditions. After cooling down the autoclave in an ambient environment, the resulting white precipitate was collected by centrifugation (19000 rpm, 43146 rcf, 20 min), re-suspended in ethanol (~ 50 ml), and subsequently template-extracted, respectively.

Table 3-3 Content of the silane precursors for the SBA-15 MSNs synthesis

SH content in MSNs	TEOS		MPTES	
(mol %)	(g)	(mmol)	(g)	(mmol)
0 (pure silica)	1 g	4.8	–	–
2	0.98 g	4.704	0.023 g	0.096
5	0.95 g	4.56	0.057 g	0.24
7	0.93 g	4.464	0.080 g	0.336
10	0.9 g	4.32	0.114 g	0.48

Synthesis of core_{SH}-shell_{NH₂} bifunctional SBA-15 MSNs

The core-shell bifunctional SBA-15 MSNs were synthesized through a delayed co-condensation method where we included 5 mol% of MPTES in the core co-condensation and 1 mol% of APTES in the shell co-condensation reactions, respectively. Briefly, 0.25 g of P123 and 0.5 g of FC-4 were dissolved in 40 ml of 0.02 M HCl at RT followed by the addition of silane precursors containing TEOS (0.85 g, 4.08 mmol) and MPTES (57.2 mg, 0.24 mmol, 5 mol% of total silane content). The mixture was stirred (500 rpm) at RT for 2 h. 0.1 g of TEOS (0.48 mmol) divided into 4 equal aliquots was added to the solution every 3 min and the mixture was continuously stirred at RT for 2 h. Afterwards, a mixture of TEOS (10 mg, 0.048 mmol) and APTES (10.6 mg, 0.048 mmol, 1 mol% of total silane content) was added. The reaction solution was stirred at RT for 20 h and was then transferred to a Parr autoclave that was heated to 140 °C for 24 h. The resulting white power was collected by centrifugation (19000 rpm, 43.146 rcf, 20 min), washed with EtOH and then H₂O, and re-suspended in 40 ml of 2 M HCl solution to perform a second hydrothermal treatment at 140 °C for 24 h. The solution was cooled down in ambient temperature. The resulting precipitates were collected by centrifugation (19000 rpm, 43.146 rcf, 20 min), re-suspended in ethanol (~50 ml) and were subsequently template-extracted.

Template extraction and particle size separation

To remove the organic surfactants from the mesopores, the as-synthesized particles were dispersed in an ethanolic solution containing 72 ml of ethanol and 8 ml of conc. HCl (37 wt%) and were subsequently heated to reflux for 1 h. Afterwards, the sample was collected by centrifugation (19000 rpm, 43.146 rcf, 20 min) and washed with EtOH and H₂O. The template extraction step was performed twice. The template-free sample was then dispersed in EtOH. Centrifugation (19000 rpm, 43.146 rcf, 20 min) was applied after each reflux and washing step to collect the particles. The subsequent particle size separation was performed by two filtration steps using filter papers (Sartorius, Grade 393 and Grade 392) for different particle size cut-off. The resulting nanosized SBA-15 particles were preserved in EtOH for further characterization, modification and applications.

PEGylation of the core_{SH}-shell_{NH₂} SBA-15 MSNs

Before PEGylation, the amino groups on the external surface of the particles were converted to carboxylic groups in order to covalently attach the PEG-diamine. 100 mg of the core_{SH}-

shell_{NH₂} SBA-15 MSNs (containing 4.8 μmol of -NH₂ groups) was mixed with an excess amount of oxalic acid (5 mg, 55 μmol) and EDC (5 μL , 28 μmol) in 10 mL of EtOH and reacted overnight. The sample was collected by centrifugation (19000 rpm, 43146 rcf, 20 min) and washed with EtOH and H₂O to remove the residual chemicals. The resulting core_{SH}-shell_{COOH} particles were dispersed in 5 mL H₂O for PEGylation. 1 mg (5 μmol) of PEG-diamine was dissolved in 5 mL H₂O, and mixed with a 5 mL aqueous solution containing EDC (3 μL , 16.8 μmol), sulfo-NHS (1.95 mg, 9 μmol) and 100 mg of the core_{SH}-shell_{COOH} particles. The mixture was stirred at RT for 2 h. The PEGylated particles were then collected and washed three times using H₂O. Centrifugation (19000 rpm, 43146 rcf, 20 min) was applied after each reaction and washing step to collect the sample. The core_{SH}-shell_{PEG} SBA-15 MSNs were stored in sterilized H₂O at a concentration of 10 mg/mL.

Fluorescent dye labeling of the core_{SH}-shell_{PEG} SBA-15 MSNs

10 mg of core_{SH}-shell_{PEG} SBA-15 MSNs was mixed with 5 μg of maleimide-terminated ATTO 488 fluorescent dye in 1 mL H₂O. The mixture was stirred at RT for 4 h followed by three washing steps with H₂O to remove residual fluorescent dye. The obtained core_{ATTO488}-shell_{PEG} particles were preserved in sterilized H₂O at a concentration of 5 mg/mL. Centrifugation (14000 rpm, 16873 rcf, 5 min) was applied after each reaction and washing step to collect the sample.

Characterization

The samples for transmission electron microscopy (TEM) were prepared by drying diluted MSN suspensions (in ethanol) on a carbon-coated copper grid at room temperature several hours before imaging. The measurement was performed at 200 kV on a Jeol JEM-2010 instrument with a CCD detection system. For scanning electron microscopy (SEM), a JEOL-6500F scanning electron microscope equipped with a field-emission gun was used. Dried sample powder was prepared on a carbon paste for measurement. The SEM was operated at an acceleration voltage of 4 kV and a working distance of 6 mm. Nitrogen sorption analysis was performed on a Quantachrome Instrument NOVA 4000e at 77 K. The samples were degassed at 120 °C under vacuum (10 mTorr) 16h before the measurement. The BET model was applied in the range of 0.05 – 0.2 relative pressure (p/p_0) to evaluate the specific surface area of the samples. Pore size distribution curves were calculated using a non-local density functional theory (NLDFT) analysis software provided by Quantachrome, using the

cylindrical pore equilibrium mode. X-ray diffraction (XRD) patterns were collected on solid samples at small angles on a Bruker D8 Discover with Ni-filtered Cu-K α radiation ($\lambda = 1.5406 \text{ \AA}$). Raman spectroscopy was performed on a LabRAM HR UV/VIS (HORIBA Jobin Yvon) Raman microscope (Olympus BX 41) equipped with a SYMPHONY CCD detection system. Dried sample powder was directly measured on a coverslip using a laser power of 10 mW at a wavelength of 633 nm (HeNe laser). Dynamic light scattering (DLS) and zeta potential measurements were performed with a Malvern Zetasizer-Nano instrument equipped with a 4 mW He-Ne laser (633 nm) and an avalanche photodiode. For DLS measurements, the samples were diluted in ethanol to a concentration of 1 mg/ml and their hydrodynamic diameters were directly recorded by the instrument. For zeta potential measurements, 1 mg of the sample was prepared in 10 mL of bi-distilled water and the solution was titrated by an add-on Zetasizer titration system (MPT-2) with diluted NaOH (0.1 M and 0.01 M) and HCl (0.1 M) as titrants. Thermogravimetric analyses (TGA) of the bulk samples were recorded on a Netzsch STA 440 C TG/DSC from room temperature to 900 °C with a heating rate of 10 °C/min in a stream of synthetic air of about 25 mL/min.

Plasmid construction (pCAG-mCherry-hRhoB-IB)

Human RhoB gene was amplified from HeLa cDNA with the forward primer RhoBfor (TAGCGATCGCATGGCGGCCATCCGC) containing an AsisI restriction site and reverse primer RhoBrev (GGGACTAGTGGCCCTCATAGCACCTTGC) containing a SpeI restriction site. The PCR products were digested with AsisI and SpeI restriction enzymes and cloned into the backbone plasmid pCAG-mCherry-IB digested with the same restriction enzymes. For the detailed plasmid map, please see appendix Figure 3-10.

Cell culture

HeLa Kyoto cells³⁴ (HeLa-k, a genetically modified HeLa cell line characterized by little cell motility) were cultured in DMEM medium supplemented with 10% FBS and 50 $\mu\text{g/ml}$ gentamycin under 5% CO₂ at 37 °C.

Live cell confocal microscopy

For real time tracking of MSN cellular uptake, live cell imaging medium containing DMEM – phenol red free (Sigma), FBS (10 %), L-glutamine (200 μM), HEPES (20 mM) and gentamycin (50 $\mu\text{g/ml}$) was used for cell incubation. HeLa-k cells were plated on a 2-well μ -

slide (ibidi, Germany) in 50% confluence for overnight incubation. The core_{ATTO488}-shell_{PEG} SBA-15 MSNs were dispersed in 1.5 mL of live cell imaging medium at a concentration of 25 µg/ml. The culture medium from the 2-well slide was replaced by the MSN-containing medium and the sample was incubated at 37°C for 4 h. Subsequently, the sample was placed in a closed live cell microscopy chamber (ACU control, Olympus, Japan) heated to 37 °C with 5 % CO₂ and 60 % humidified atmosphere, mounted on a Nikon Ti microscope (Nikon, Japan) and the live cell imaging data were acquired with an UltraVIEW Vox spinning disc confocal system (PerkinElmer, UK). Image acquisition was performed using a 63x/1.4 NA Plan-Apochromat oil immersion objective lens and the images were obtained with a cooled 14-bit EMCCD camera (C9100-50, CamLink) with a frame size of 1024 x 1024 pixels. The fluorophores on the MSNs were excited with 488 nm (10% laser output power) solid-state diode laser lines.

High-content microscopy and image analysis

HeLa-k cells (10⁶ cells) were seeded on an 18 × 18 mm coverslip in a 6-well plate containing 2 mL of DMEM for overnight incubation. The cell culture medium was then replaced by the MSN-containing cell culture medium with the particle (core_{ATTO488}-shell_{PEG} SBA-15 MSN) concentration of 25 µg/mL. After incubation (37 °C) for 24 h, the cells were washed with PBS (three times, 3 mL per wash), fixed with 3.7% of formaldehyde (in PBS, 1 mL), membrane-permeabilized with 0.5% Triton-X (in PBS, 3 mL) and DAPI (1 mL, 250 ng mL⁻¹ in PBS, Invitrogen, USA) stained followed by propidium iodide (1 mL, 10 · g mL⁻¹, Invitrogen, USA) staining. The coverslip was mounted in Vectashield anti-fading reagent (Vector Laboratories, USA) on an object slide. High-throughput images were acquired automatically with an Operetta[®] High Content Imaging System (PerkinElmer, UK) using a 40× air objective lens. DAPI, ATTO 488 and propidium iodide were excited and the emissions were recorded using standard filter sets. The exposure time was set at 400 ms, and 35 different fields (approximately 2200 cells) were imaged. The images were then analyzed with the Harmony[®] analysis software (PerkinElmer). Briefly, nuclei, cytoplasm and ATTO 488-labeled MSNs were segmented from background based on DAPI, propidium iodide and ATTO 488 fluorescence and individually identified by setting area- and intensity-based thresholds, respectively. The internalized ATTO 488-labeled MSNs were visualized as spots within the cytoplasm area. The segmented results (nuclei, cytoplasm and MSN spots) were used to define populations. Population 1: cells = DAPI-stained nucleus plus its surrounding

cytoplasm region. Population 2: cells with internalized MSNs = cells that internalize more than two MSN spots in their cytoplasm region. The evaluation of cellular uptake efficiency of HeLa-k cells with respect to MSNs was based on the calculation: population 2/population 1 \times 100%.

Laser scanning confocal microscopy

HeLa-k cells (10^6 cells) were plated on an 18×18 mm coverslip in a 6-well plate containing 2 mL of DMEM for overnight incubation. The plasmid pCAG-mCherry-hRhoB-IB was transfected into the cells with Lipofectamine 2000 reagent (Invitrogen) according to a standard protocol provided by Invitrogen. 20 h post transfection, the MSN particles (core_{ATTO488}-shell_{PEG} SBA-15 MSNs) were added to the culture medium at a concentration of 25 $\mu\text{g/mL}$ and incubated with the cells for 24 h. Subsequently, the cells were washed with PBS (three times, 3 mL per wash), fixed with 3.7% of formaldehyde (in PBS, 1 mL), membrane-permeabilized with 0.5% Triton-X (in PBS, 3 mL), and DAPI (1 mL, 250 ng mL^{-1} in PBS, Invitrogen, USA) stained. The coverslip was mounted in Vectashield anti-fading reagent (Vector Laboratories, USA) on an object slide. The co-localization of core_{ATTO488}-shell_{PEG} SBA-15 MSNs and RhoB-mCherry-labeled endosomes was analyzed using a Leica TCS SP5/AOBS confocal laser scanning microscope equipped with a UV-transmitting HCX PL 63 \times /1.4 oil objective lens. Fluorophores were excited with a 405 nm diode laser (DAPI, 10% output laser power), a 488 nm Ar laser line (ATTO 488, 10% output laser power) and a 561 nm diode-pumped solid-state (DPSS, 20% output laser power) laser line (mCherry). Images were recorded with a frame size of 512×512 pixels, a pixel size of 50 nm, a z-step size of 250 nm and a pinhole opening of 1 Airy unit. A maximum intensity projection of several confocal z-sections was then performed using Fiji ImageJ.

Cytotoxicity test

The MTT assay was applied to evaluate the cytotoxicity of MSNs. HeLa-k cells were seeded on a 96-well microplate (5×10^3 cells per well) in cell culture medium (100 μL /well) and incubated at 37 °C one day before the MTT test. 1 mg of MSNs was dispersed in 1 mL of DMEM (serum free) and the MSN-DMEM solution was subsequently diluted to different particle concentrations. The culture medium was removed from the cells followed by adding 100 μL of MSN-DMEM solutions (with various particle concentrations) to each well. The control group was incubated with 100 μL of serum-free DMEM. The cells were incubated

with MSN-DMEM solutions for 24 h, the residual particles were removed and the cells were washed with PBS three times. MTT solution (0.5 mg/ml in DMEM) was freshly prepared and added to the cells (100 μ l/well). After 4 h incubation (at 37 °C), the purple crystals metabolized from healthy cells can be observed. The MTT solution was removed and the purple crystals were dissolved in 200 μ l of DMSO. The resulting solutions were incubated at 37 °C for 1 h and the absorbance was measured at 570 nm, together with the reference absorbance at 655 nm using a Microplate reader (Infinite® M1000 PRO, TECAN). Experiments were triplicated. Error bars represent the standard deviations.

3.5 Appendix

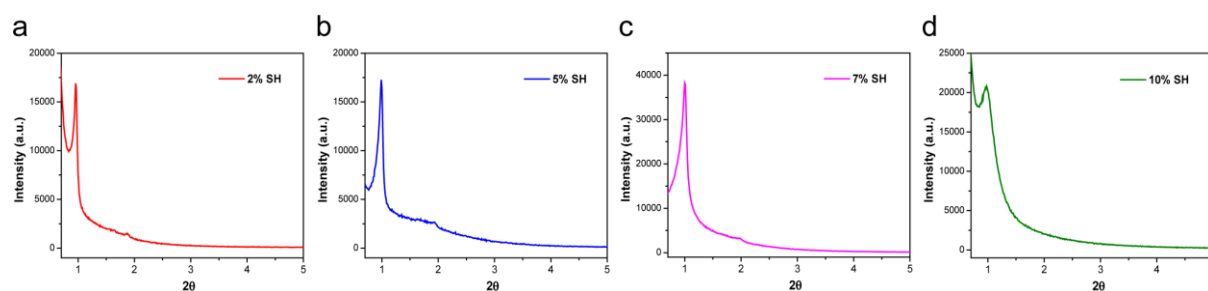


Figure 3-6. XRD of the thiol-functionalized SBA-15 MSNs. Samples with (a) 2 mol%, (b) 5 mol%, (c) 7 mol% and (d) 10 mol% of SH content in the SBA-15 MSNs.

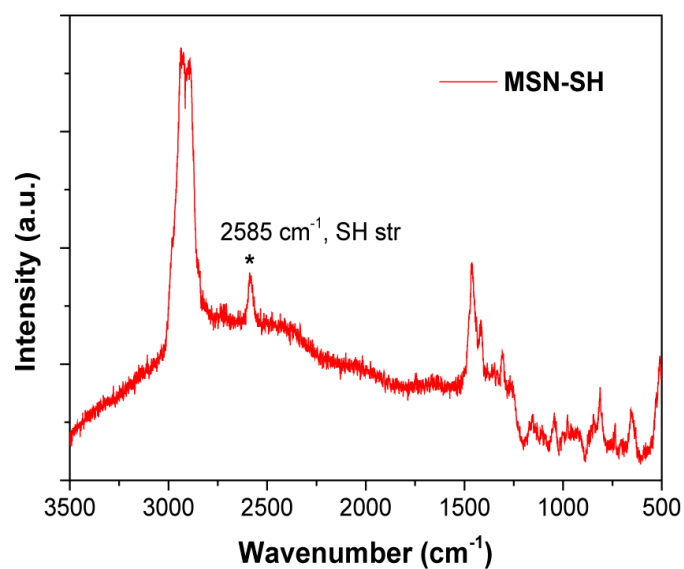


Figure 3-7. Raman spectroscopy of the thiol-functionalized (10 mol%) SBA-15 MSNs. The peak at 2585 cm^{-1} indicates the S-H stretching vibration.

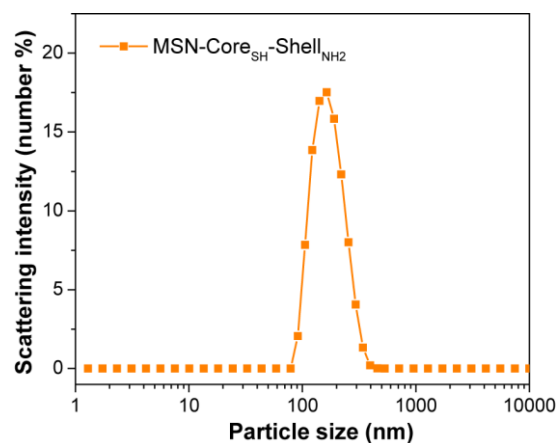


Figure 3-8. DLS measurement of the core_{SH}-shell_{NH₂} SBA-15 MSNs. The sample was measured in ethanolic suspension.

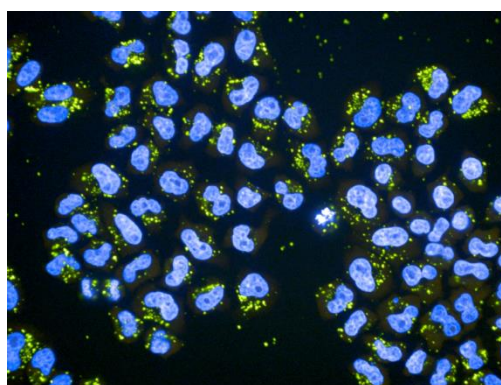


Figure 3-9. High content imaging for cellular uptake analysis. A selected image from the imaging fields is presented. The core_{ATTO488}-shell_{PEG} SBA-15 MSNs (green) were incubated with HeLa cells (25 µg MSNs/mL) for 24 h and the particles were washed away. The cells were fixed, membrane-permeabilized, and stained with DAPI (blue) and propidium iodide (red).

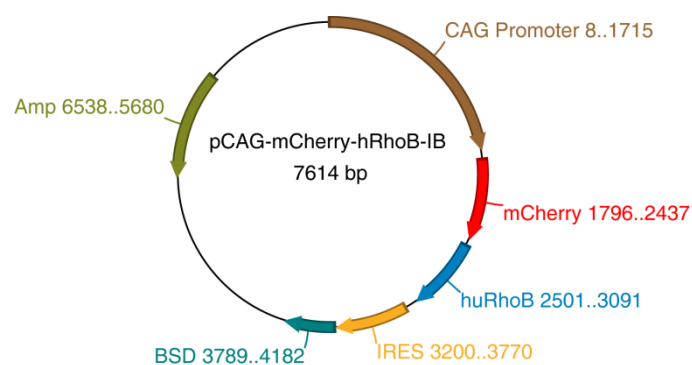


Figure 3-10. Plasmid map of the pCAG-mCherry-hRhoB-IB.

3.6 References

- 1 Hartmann, M. Ordered Mesoporous Materials for Bioadsorption and Biocatalysis. *Chem. Mater.* **17**, 4577-4593 (2005).
- 2 Hudson, S., Cooney, J. & Magner, E. Proteins in mesoporous silicates. *Angew. Chem. Int. Ed. Engl.* **47**, 8582-8594 (2008).
- 3 Popat, A. *et al.* Mesoporous silica nanoparticles for bioadsorption, enzyme immobilisation, and delivery carriers. *Nanoscale* **3**, 2801 (2011).
- 4 Knezevic, N. Z. & Durand, J. O. Large pore mesoporous silica nanomaterials for application in delivery of biomolecules. *Nanoscale* **7**, 2199-2209 (2015).
- 5 Kresge, C. T., Leonowicz, M. E., Roth, W. J., Vartuli, J. C. & Beck, J. S. Ordered mesoporous molecular sieves synthesized by a liquid-crystal template mechanism. *Nature* **359**, 710-712 (1992).
- 6 Zhao, D., Huo, Q., Feng, J., Chmelka, B. F. & Stucky, G. D. Nonionic Triblock and Star Diblock Copolymer and Oligomeric Surfactant Syntheses of Highly Ordered, Hydrothermally Stable, Mesoporous Silica Structures. *J. Am. Chem. Soc.* **120**, 6024-6036 (1998).
- 7 Andersson, J., Rosenholm, J., Areva, S. & Lindén, M. Influences of Material Characteristics on Ibuprofen Drug Loading and Release Profiles from Ordered Micro- and Mesoporous Silica Matrices. *Chem. Mater.* **16**, 4160-4167 (2004).
- 8 Cauda, V., Onida, B., Platschek, B., Mühlstein, L. & Bein, T. Large antibiotic molecule diffusion in confined mesoporous silica with controlled morphology. *J. Mater. Chem.* **18**, 5888 (2008).
- 9 dos Santos, S. M. L. *et al.* Synthesis and characterization of ordered mesoporous silica (SBA-15 and SBA-16) for adsorption of biomolecules. *Microporous Mesoporous Mater.* **180**, 284-292 (2013).
- 10 Lai, C. Y. *et al.* A mesoporous silica nanosphere-based carrier system with chemically removable CdS nanoparticle caps for stimuli-responsive controlled release of neurotransmitters and drug molecules. *J. Am. Chem. Soc.* **125**, 4451-4459 (2003).
- 11 Mortera, R. *et al.* Cell-induced intracellular controlled release of membrane impermeable cysteine from a mesoporous silica nanoparticle-based drug delivery system. *Chem Commun (Camb)*, 3219-3221 (2009).
- 12 Slowing, II, Trewyn, B. G. & Lin, V. S. Mesoporous silica nanoparticles for intracellular delivery of membrane-impermeable proteins. *J. Am. Chem. Soc.* **129**, 8845-8849 (2007).
- 13 Chen, Y. P. *et al.* A new strategy for intracellular delivery of enzyme using mesoporous silica nanoparticles: superoxide dismutase. *J. Am. Chem. Soc.* **135**, 1516-1523 (2013).

- 14 Xia, T. *et al.* Polyethyleneimine coating enhances the cellular uptake of mesoporous silica nanoparticles and allows safe delivery of siRNA and DNA constructs. *ACS Nano* **3**, 3273-3286 (2009).
- 15 Radu, D. R. *et al.* A polyamidoamine dendrimer-capped mesoporous silica nanosphere-based gene transfection reagent. *J. Am. Chem. Soc.* **126**, 13216-13217 (2004).
- 16 Slowing, II, Vivero-Escoto, J. L., Wu, C. W. & Lin, V. S. Mesoporous silica nanoparticles as controlled release drug delivery and gene transfection carriers. *Adv. Drug Del. Rev.* **60**, 1278-1288 (2008).
- 17 Wan, Y. & Zhao, D. On the controllable soft-templating approach to mesoporous silicates. *Chem. Rev.* **107**, 2821-2860 (2007).
- 18 Vinu, A., Murugesan, V. & Hartmann, M. Adsorption of Lysozyme over Mesoporous Molecular Sieves MCM-41 and SBA-15: Influence of pH and Aluminum Incorporation. *The Journal of Physical Chemistry B* **108**, 7323-7330 (2004).
- 19 Han, Y. & Ying, J. Y. Generalized fluorocarbon-surfactant-mediated synthesis of nanoparticles with various mesoporous structures. *Angew. Chem. Int. Ed. Engl.* **44**, 288-292 (2004).
- 20 Gao, F., Botella, P., Corma, A., Blesa, J. & Dong, L. Monodispersed mesoporous silica nanoparticles with very large pores for enhanced adsorption and release of DNA. *J. Phys. Chem. B* **113**, 1796-1804 (2009).
- 21 Hartono, S. B. *et al.* Poly-L-lysine functionalized large pore cubic mesostructured silica nanoparticles as biocompatible carriers for gene delivery. *ACS Nano* **6**, 2104-2117 (2012).
- 22 Meka, A. K. *et al.* Facile Synthesis of Large-Pore Bicontinuous Cubic Mesoporous Silica Nanoparticles for Intracellular Gene Delivery. *ChemNanoMat* **2**, 220-225 (2016).
- 23 Tu, J. *et al.* Mesoporous Silica Nanoparticles with Large Pores for the Encapsulation and Release of Proteins. *ACS applied materials & interfaces* **8**, 32211-32219 (2016).
- 24 Mellor, H. PRK1 Is Targeted to Endosomes by the Small GTPase, RhoB. *J. Biol. Chem.* **273**, 4811-4814 (1998).
- 25 Fernandez-Borja, M., Janssen, L., Verwoerd, D., Hordijk, P. & Neefjes, J. RhoB regulates endosome transport by promoting actin assembly on endosomal membranes through Dia1. *J. Cell Sci.* **118**, 2661-2670 (2005).
- 26 Takahashi, H. *et al.* Catalytic Activity in Organic Solvents and Stability of Immobilized Enzymes Depend on the Pore Size and Surface Characteristics of Mesoporous Silica. *Chem. Mater.* **12**, 3301-3305 (2000).
- 27 Fadnavis, N. W., Bhaskar, V., Kantam, M. L. & Choudary, B. M. Highly efficient "tight fit" immobilization of alpha-chymotrypsin in mesoporous MCM-41: a novel

- approach using precursor immobilization and activation. *Biotechnol. Prog.* **19**, 346-351 (2003).
- 28 Aburto, J. *et al.* Stability and catalytic properties of chloroperoxidase immobilized on SBA-16 mesoporous materials. *Microporous Mesoporous Mater.* **83**, 193-200 (2005).
 - 29 Lee, C. H. *et al.* Enhancing stability and oxidation activity of cytochrome C by immobilization in the nanochannels of mesoporous aluminosilicates. *J. Phys. Chem. B* **109**, 12277-12286 (2005).
 - 30 Fan, J. *et al.* Rapid and high-capacity immobilization of enzymes based on mesoporous silicas with controlled morphologies. *Chem. Commun.*, 2140 (2003).
 - 31 Huang, D. M. *et al.* Highly efficient cellular labeling of mesoporous nanoparticles in human mesenchymal stem cells: implication for stem cell tracking. *FASEB J.* **19**, 2014-2016 (2005).
 - 32 Fang, I. J., Slowing, II, Wu, K. C., Lin, V. S. & Trewyn, B. G. Ligand conformation dictates membrane and endosomal trafficking of arginine-glycine-aspartate (RGD)-functionalized mesoporous silica nanoparticles. *Chemistry* **18**, 7787-7792 (2012).
 - 33 Clemens, D. L. *et al.* Targeted intracellular delivery of antituberculosis drugs to Mycobacterium tuberculosis-infected macrophages via functionalized mesoporous silica nanoparticles. *Antimicrob. Agents Chemother.* **56**, 2535-2545 (2012).
 - 34 Landry, J. J. *et al.* The genomic and transcriptomic landscape of a HeLa cell line. *G3 (Bethesda)* **3**, 1213-1224 (2013).

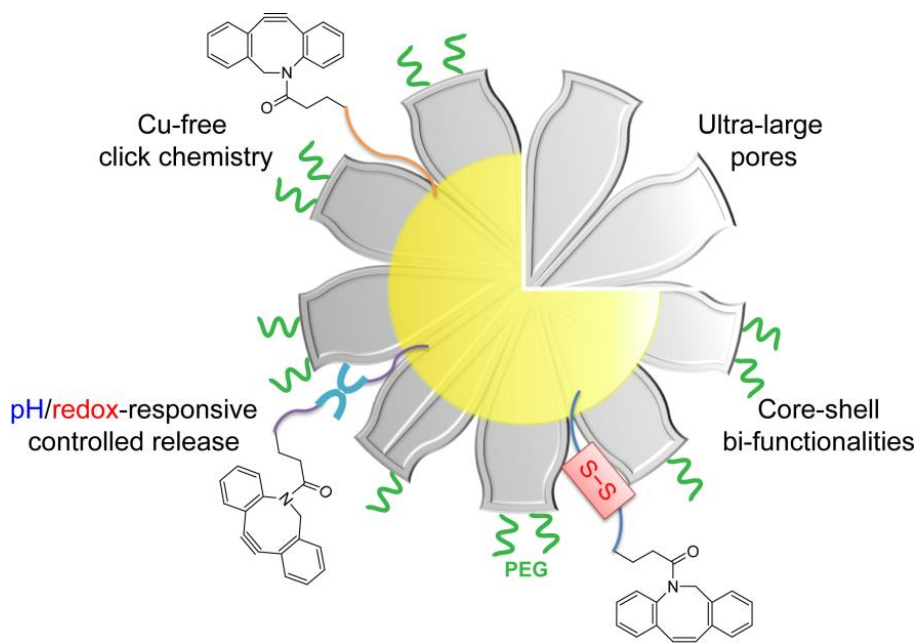
4 Clickable Multifunctional Large-Pore Mesoporous Silica Nanoparticles as Nanocarriers

This chapter is based on the following manuscript:

Hsin-Yi Chiu and Thomas Bein, *to be submitted*.

Abstract

Large-pore mesoporous silica nanoparticles (LP-MSNs) with defined particle size (< 200 nm) are promising carrier systems for the cellular delivery of macromolecules. Ideal nanocarriers should be adaptable in their surface properties to optimize host-guest interactions, thus surface functionalization of the nano-vehicles is highly desirable. In this study, we synthesized various mono-functional LP-MSNs by incorporating different organic groups into the silica framework *via* a co-condensation approach. Further, we applied a delayed co-condensation strategy to create spatially segregated core-shell bi-functional LP-MSNs. Diverse particle morphologies were obtained by adding different organosilanes to the silica precursor solution. The effect of organosilanes in the co-condensation process on particle size and pore structure formation is also discussed. Surface functional groups were then used for binding stimuli-responsive linkers. These were finally exploited for copper-free click chemistry for cargo conjugation to create a delivery system with controlled cargo release. Model cargo release experiments in buffers using these new multifunctional LP-MSNs demonstrate their ability in controlled cargo uptake and release and their potential for biomolecule delivery.



Scheme 4-1 Schematic illustration of the multifunctional large-pore MSNs established in this study for different applications.

4.1 Introduction

Since the discovery of periodically ordered mesoporous silica MCM-41 in 1992,^{1,2} scientists have spent great efforts on tailoring physical and chemical properties (i.e. particle size and morphology, pore size and structure, surface functionalities, etc.) of mesoporous silica materials and have accommodated a variety of cargos in the mesopores for the study of guest-host interactions.³⁻⁵ Nanosized mesoporous silica materials (mesoporous silica nanoparticles, MSNs) feature several favorable properties, for example, high surface area and pore volume, ease of surface functionalization and biocompatibility, which make them suitable nanocarriers for biomedical applications.^{6,7} In the past decade, multifunctional MSNs have been developed for controlled release as well as targeted delivery of various therapeutics such as anti-cancer drugs, antibiotics, etc. either *in vitro* or *in vivo*.^{6,8} However, most of the drug delivery tasks have been achieved using small-pore (≤ 4 nm) MSNs. As the development of siRNA and protein therapies has dramatically advanced in recent years,⁹⁻¹¹ the interest in developing MSNs for drug delivery purposes has turned towards synthesizing large pores for accommodating sizable biomolecules, while simultaneously retaining particle sizes smaller than 200 nm for better cellular uptake or an increased EPR (enhanced permeability and retention) effect.¹² Numerous research articles regarding the synthesis of large-pore MSNs

with suitable particle sizes have been published in the past years. Recently, Zhang *et al.* reported a synthesis using cetyltrimethylammonium p-toluenesulfonate (CTATos) as surfactant in near-neutral precursor solutions resulting in wide-pore stellate MSNs.¹³ The pore size distribution of these stellate MSNs ranging from 10 – 20 nm and their defined particle size of around 100 nm present an ideal platform for the cellular delivery of large-sized bio-macromolecules. One significant achievement of this synthesis method is that it can be used for large-scale production. Up to now, most of the reports regarding the synthesis of stellate MSNs have focused on the discussion of the pore-forming mechanism and particle size control. Only few studies have addressed the functionalization of these stellate MSNs (either by post-synthetic grafting or only shell functionalization) for optimized biomedical applications,^{14,15} while none of them has discussed the impact of different organosilanes in the precursor solution on particle morphology when undergoing silica co-condensation.

To engineer MSNs suitable for nanomedicine, molecular surface modification offers several advantages: hydrophobicity or hydrophilicity as well as the surface charge can be adjusted towards the respective guest molecules thus ensuring optimal uptake and release properties. Furthermore, a site-specific surface decoration with functional groups allows for the independent attachment of diverse linker or targeting molecules, thus creating multifunctional delivery agents. Post-synthetic grafting and co-condensation are two common methods to implant functional groups into the framework of MSNs. Post-synthetic grafting is more commonly used for functionalizing large-pore stellate MSNs since grafting does not or only negligibly impair the particle morphology or pore structure. However, challenges of post-synthetic grafting include (i) achieving site-specific localization of two or more different functional groups on the MSN surface and (ii) controlling the degree of functional groups incorporated into the silica framework. On the other hand, a co-condensation approach provides a facile route to attain a controlled degree and spatially selective functionalization in the MSN particles. In addition, the functional groups are more homogeneously distributed throughout the pore structure when performing a co-condensation synthesis. However, for this approach to result in well-defined MSNs, high concentrations and/or highly charged organosilanes are typically avoided with this approach.

In this study, we first synthesized various mono-functionalized MSNs *via* the co-condensation approach. We will discuss the prominent impact of 3-aminopropyl triethoxysilane (APTES) (when used together with tetraethyl orthosilicate (TEOS) as silica

precursors) on the final pore structure and the particle size of MSNs. We further employed our delayed co-condensation strategy^{16,17} to synthesize site-specific (spatially selective) core-shell bi-functional LP-MSNs. Aza-dibenzocyclooctyne (DBCO)-derivatives were attached to the inner surface of MSNs to enable copper-free click chemistry reactions for the conjugation of azide-terminated cargos. In combination with different stimuli-responsive linkers (e.g., redox-sensitive disulfide bridged and pH-sensitive acetal linkers) between DBCO moieties and the MSN surface, we were able to control the cargo uptake and trigger the release in specific buffer solutions. We envision these multifunctional LP-MSNs (Scheme 4-1) to be promising nanocarriers for encapsulation and controlled release of various therapeutics in a spatiotemporal manner.

4.2 Results and Discussion

Synthesis of mono-functional MSNs *via* a co-condensation method

We first chose three commonly used organosilanes carrying thiol, phenyl or amino groups for the functionalization of MSNs. Thiol and amino groups are frequently used in secondary cross-linking reactions while phenyl groups are capable of increasing the hydrophobicity of the silica surface. The three different organosilanes 3-mercaptopropyl triethoxysilane (MPTES), 3-aminopropyl triethoxysilane (APTES) and phenyltriethoxysilane (PTES) were mixed with tetraethyl orthosilicate (TEOS), respectively, and introduced as silica precursors in the co-condensation procedure. A fraction between 5% and 10% of the total amount of silica was substituted by the respective organosilane (see Table 4-2). Un-functionalized MSNs (pure silica, un-MSN) were also synthesized as control group (experimental details are described in the experimental section).

According to the TEM micrographs (Figure 4-1a-c), the resulting samples un-MSN, thiol-functionalized MSNs (MSN-SH) and phenyl-functionalized MSNs (MSN-Ph) all show a stellate silica framework with conical pore structure, with MSN-SH and MSN-Ph exhibiting a less dense central backbone and a smaller particle size than un-MSN. The SEM images (Figure 4-1e-g) further illustrate the flower-shaped morphologies of these stellate MSNs containing irregular pores. In contrast, amino-functionalized MSNs (MSN-NH₂) present a very different particle morphology (Figure 4-1d, 4-1h), i.e. a denser silica structure with small pores and a large particle size of around 200 nm.

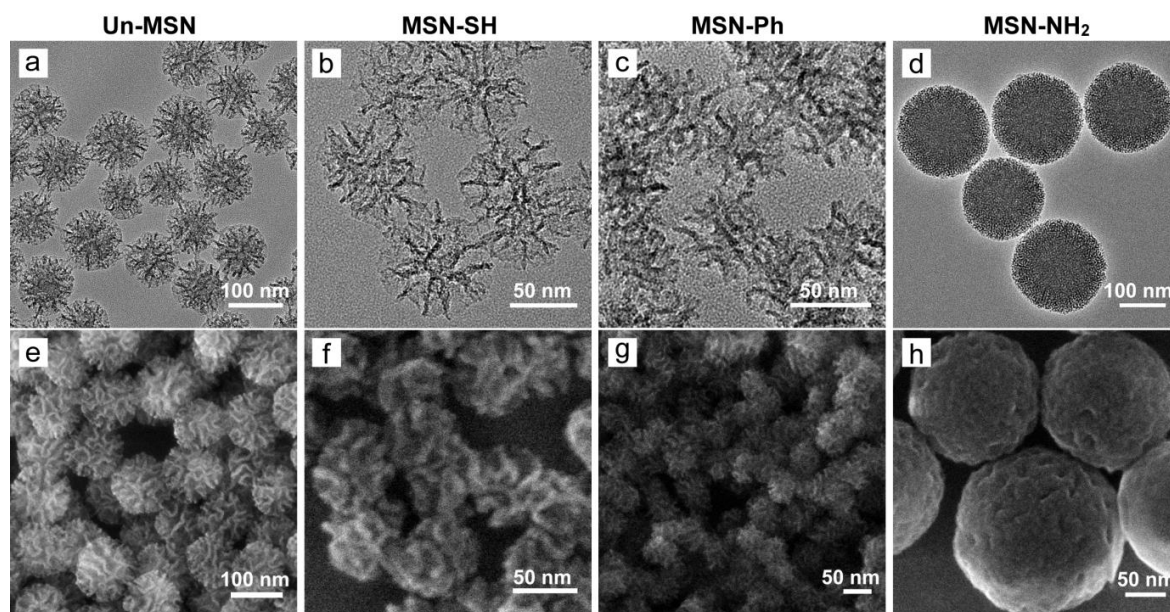


Figure 4-1 TEM and SEM micrographs of MSNs functionalized with different organic groups. (a), (e) Un-functionalized MSNs. (b), (f) Thiol-functionalized MSNs. (c), (g) Phenyl-functionalized MSNs. (d), (h) Amino-functionalized MSNs.

N₂ sorption (Figure 4-2a, 4-2b) analysis indicates high surface areas (around 520 – 890 m²/g) and wide pore size distributions (3 – 30 nm) in samples un-MSN, MSN-SH and MSN-Ph (for detailed information, please see Table 4-1). In accordance with TEM images, N₂ sorption analysis shows that both MSN-SH and MSN-Ph have wider pore size distributions and larger pore volumes than un-MSN. We note that the pore volume was evaluated at a relative pressure of $p/p_0 = 0.99$ and includes a small contribution of textural porosity (inter-particle volume) due to the small particle size. The results of the N₂ sorption also reveal that the MSN-NH₂ sample has a low surface area of only 285 m²/g, a low pore volume and a narrow pore size distribution (3 – 4 nm), correlating with the TEM picture. IR spectroscopy shows the typical Si-O-Si asymmetric stretching vibration at 1240 – 1050 cm⁻¹ (full range spectra in appendix Figure 4-6a). Additionally, an absorption band at 1629 cm⁻¹ of the bending mode of water adsorbed on the surface of MSNs clearly appears in un-MSN, MSN-SH and MSN-NH₂ indicating that these MSNs are hydrophilic. The signals of the ring C=C stretching mode at 1431 cm⁻¹ and two aromatic ring C-H stretching modes at 3059 cm⁻¹ and 3079 cm⁻¹ (indicated by *) can be observed in the MSN-Ph spectrum (Figure 4-2c, blue line). Sample MSN-NH₂ (Figure 4-2c, green line) shows the absorbance of the symmetric NH₃⁺ vibration at 1532 cm⁻¹ and of saturated primary amines at 1627 cm⁻¹ (indicated by *, this band overlaps with the physisorbed water in MSNs).

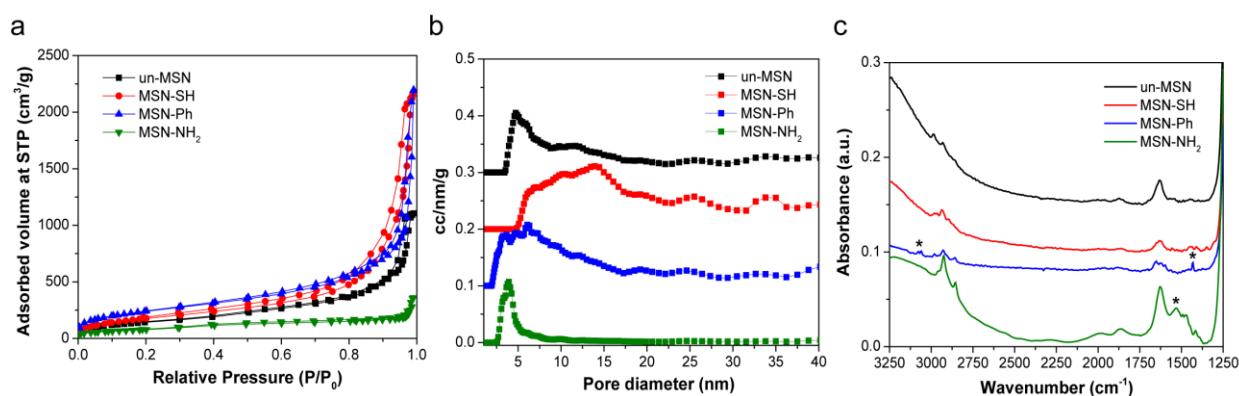


Figure 4-2 N₂ sorption (a) isotherms, (b) pore size distributions and (c) IR spectra of MSNs. The signals of the ring C=C stretching mode at 1431 cm⁻¹ and two aromatic ring C-H stretching modes at 3059 cm⁻¹ and 3079 cm⁻¹ (indicated by *) can be observed in the MSN-Ph spectrum (blue trace). The signal at 1627 cm⁻¹ (indicated by *) in the MSN-NH₂ spectrum (green trace) indicates the presence of saturated primary amines. For clarity, the pore size distribution curves in (b) are shifted along the y-axis by a value of 0.1 and the IR spectra in (c) are shifted along the y-axis by 0.05.

Table 4-1 Characterization of MSN samples

Sample	DFT ¹ Pore size distribution (nm)	Pore volume ² (cm ³ /g)	BET surface area (m ² /g)	Particle size ³ (nm)	IEP (pH)	Zeta Potential at pH 7 (mV)
Un-MSN	4.5 - 22	1.6	521	135 ± 53	3.6	-35
MSN-SH	6.0 - 30	3.2	671	117 ± 52	2.3	-30
MSN-Ph	3.5 - 22	2.4	885	50 ± 10	3.3	-28
MSN-NH₂	3.0 - 4.5	0.3	285	216 ± 56	5.6	-31

¹ Data were acquired from the adsorption branch of the isotherms.

² The total pore volume was determined at $p/p_0 = 0.99$.

³ Un-MSN, MSN-SH and MSN-NH₂ were measured by DLS, MSN-Ph was analyzed by TEM.

The amino groups in this sample also increased the isoelectric point (IEP) of the particles (IEP = pH 3.6 for un-MSN; IEP = pH 5.6 for MSN-NH₂). Thiol groups of sample MSN-SH can be detected by Raman spectroscopy (appendix Figure 4-6) showing the S-H stretching mode at 2581 cm⁻¹. Thermogravimetric analysis (TGA, appendix Figure 4-7) also demonstrates the inclusion and the different stability of the functional groups. The

decomposition of SH, Ph and NH₂ groups can be observed in a dominant weight change at 341 °C, 631 °C and 302 °C in the samples MSN-SH, MSN-Ph and MSN-NH₂, respectively. The TGA mass losses and estimated degree of organic functionalizations of the samples are listed in appendix Table 4-3.

These results show that organosilanes can be successfully introduced into the silica framework of large-pore stellate MSNs *via* a co-condensation synthesis. MPTES and PTES had only a moderate influence on the stellate formation while APTES strongly modified the co-condensation process resulting in a highly divergent silica structure. Factors that affect particle morphology and pore structure such as surfactants, catalyst agents, ratio between reactants, temperature, reaction time, stirring rate, etc. are well studied in the literature. In contrast, only few papers have discussed the influence of organosilanes on the MSN morphology.^{18,19}

The influence of organosilanes on pore structure formation

To investigate the influence of organosilanes on the pore structure formation during co-condensation, we measured the pH values (at room temperature) of the precursor solutions of all samples (Table 4-2).

The surfactant solution containing CTATos, triethanolamine and water has a pH value of about 9.7. Upon addition of TEOS, the pH value dropped to 9.3. After stirring the reaction solution for 30 minutes, part of the silicon alkoxides are hydrolyzed and condensed, and the pH value dropped further down to 9.0. When 10 mol% of TEOS was replaced by MPTES or PTES, these pH values remained nearly unchanged. However, the addition of APTES led to a higher pH value (pH 10.06) in the reaction mixture due to the basic property of the amino groups. Zhang *et al.* proposed a mechanism for the large-pore stellate MSN synthesis: they propose that at near neutral conditions the counterions Tos⁻ (X⁻) compete with the negatively charged silicates (I⁻) for the positively charged surfactant micelles (S⁺). Consequently, more Tos⁻ ions are included in the silica structure resulting in less dense silica particles and larger pores.¹³ Following this argument we propose that the increasing pH caused by the addition of APTES enhances the affinity between negatively charged silicates (I⁻) and positively charged surfactant micelles (S⁺) and thus results in expelling the counterion Tos⁻ (X⁻). Accordingly, a denser particle structure with smaller pores results. Similar observations were reported in a recently published paper from our group showing that CTATos does not influence the pore

radius in comparison to the commonly used CTAC template when the synthesis was performed at the high pH of about 12.¹⁷

Table 4-2 pH values of synthetic precursor mixtures

Sample	Silica precursors ¹ (mol%)	pH value of surfactant solution ²	pH value ³ after silane addition	pH value ⁴ after 30 min of silane addition
Un-MSN	100% TEOS	9.68	9.30	9.0
MSN-SH	90% TEOS + 10% MPTES	9.70	9.28	9.01
MSN-Ph	90% TEOS + 10% PhTES	9.65	9.31	9.03
MSN-NH₂	95% TEOS + 5% APTES	9.70	10.06	9.43

¹ 100 mol% = 9.6 mmol.

² Surfactant solution: 13.7 g of H₂O + 0.263 g of CTATos + 0.047 g of TEA.

³ All pH values were measured after 2 min of silane addition at room temperature.

⁴ All pH values were measured at room temperature.

In a previous publication,²⁰ we demonstrated the possibility to create multiply functionalized or even core-shell MSN particles, the latter by performing a time-delayed co-condensation with more than one organosilane (e.g., APTES + PTES) at high pH. Here, we applied a similar strategy for incorporating either PTES and APTES or PTES and MPTES simultaneously in the co-condensation processes to establish dual-functionalized stellate particles. According to appendix Figure 4-8, multiply functionalized MSNs were successfully synthesized. The aminogroup-containing dual functionalized MSN-Ph/NH₂ particles resemble the mono-functionalized MSN-NH₂ particles in that both of them consist of a comparably dense silica framework with a narrow pore size distribution. The reaction solution of the MSN-Ph/NH₂ particles still has a high pH value of about 9.92 compared to 10.06 in the mono-functionalized MSN-NH₂ solution, containing only half of the amino concentration, likely causing again the dense silica structure. However, the smaller APTES concentration now results in almost twice the surface area of MSN-NH₂. On the other hand, the mixed MSN-Ph/SO₃H particles resemble their mono-functionalized parent samples MSN-Ph and MSN-SH, with pore size, pore volume and particle size of MSN-Ph/SO₃H falling between those of MSN-Ph and MSN-SH.

Synthesis of core-shell bi-functional stellate MSNs using the delayed co-condensation approach

To synthesize core-shell MSNs having two functional groups precisely localized at either the internal or the external surfaces, we applied the delayed co-condensation procedure. 3-cyanopropyltriethoxysilane (CPTES, 5 mol% of total silane content) was used for co-condensation with TEOS to generate a nitrile-containing particle core while MPTES (1 mol% of total silane content) and TEOS were used to generate thiol groups on the outer surface. A shell of pure TEOS was condensed in-between to create an interlayer between the cyano- and mercapto-regions. TEM and SEM micrographs (Figure 4-3a, 4-3b) of the resulting core_{CN}-shell_{SH} particles (MSN-CN_{in}-SH_{out}) show a similar stellate morphology, particle size and pore structure as the un-MSNs particles.

According to N₂ sorption analysis, MSN-CN_{in}-SH_{out} particles possess a high surface area of 573 m²/g and a wide pore size distribution of about 2.5 – 12 nm (Figure 4-3c). The incorporated nitrile groups can be seen in the IR spectrum (Figure 4-3d, blue trace) at 2256 cm⁻¹ representing the stretching vibration of aliphatic nitriles. The nitrile groups in MSN-CN_{in}-SH_{out} could be converted into carboxylic groups by heating the sample in a hydrochloric acid solution (appendix Figure 4-9a). The obtained MSN-COOH_{in}-SH_{out} sample shows strong COO⁻ asymmetric stretching vibrations at 1556 cm⁻¹ in the IR spectrum (Figure 4-3d, magenta). To verify the presence of thiol groups on the outer surface, we applied a thiol-disulfide exchange reaction. Incubating MSN-CN_{in}-SH_{out} particles with cystamine in carbonate-bicarbonate buffer resulted in amino groups being anchored on the outer surface of the MSNs. This exchange reaction is evidenced by a dramatic increase in the zeta potential of the particles (Figure 4-3e). External mercapto-groups can be exploited for ligand attachment, e.g., PEGylation of the particles. PEG anchored to the external surface of MSNs has been reported to enhance the particle circulation time in the blood stream as well as to prevent particle degradation.^{21,22} To assemble the potential nanocarriers MSN-COOH_{in}-PEG_{out} for biomedical application, we attached PEG polymers to the outer surface of the MSN-COOH_{in}-SH_{out} particles *via* a mercapto-reactive maleimide-PEG linker (appendix Figure 4-9b). The corresponding weight increase of the PEGylation can be seen in TGA measurements (Figure 4-3f).

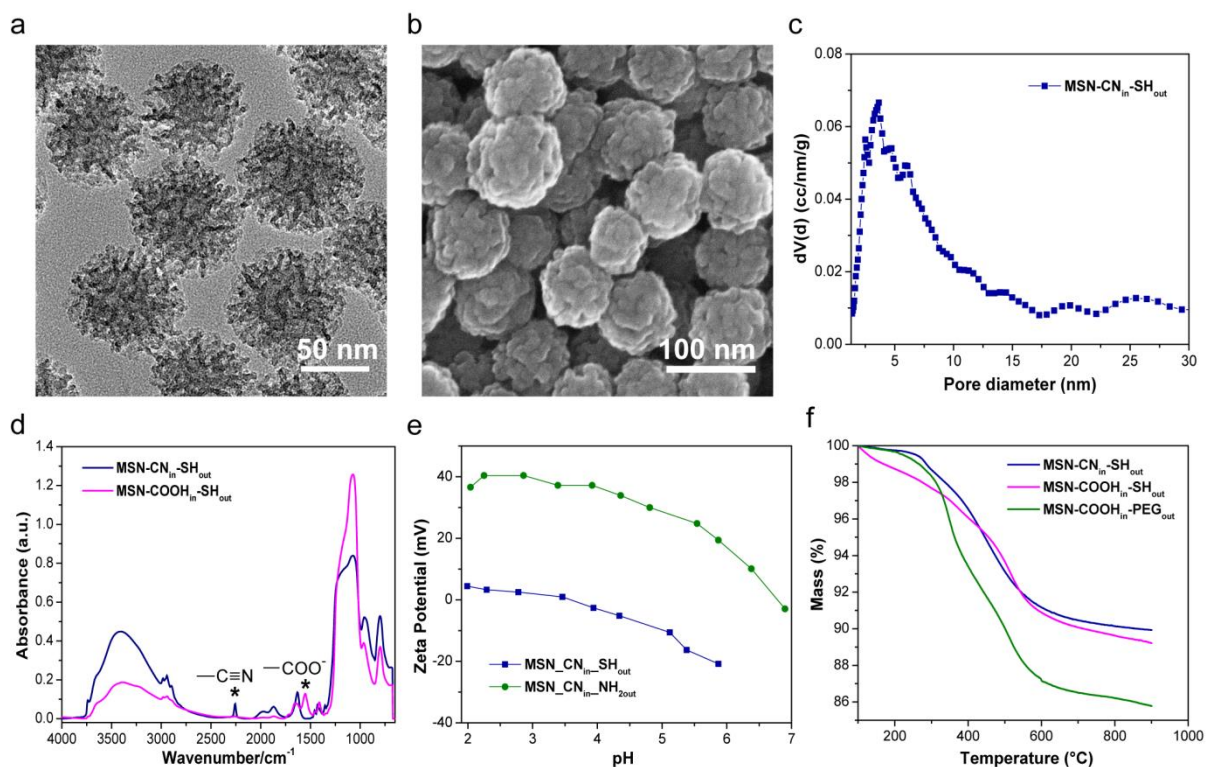


Figure 4-3 Characterization of core-shell MSNs. (a) TEM and (b) SEM images of MSN-CN_{in}-SH_{out} particles. (c) N₂ sorption-based pore size distribution obtained from the adsorption branch and calculated using NLDFT mode. (d) IR spectra. Blue: MSN-CN_{in}-SH_{out}, magenta: MSN-COOH_{in}-SH_{out}. (e) Zeta potential of MSN-CN_{in}-SH_{out} (blue) and MSN-CN_{in}-NH₂_{out} (green). (f) Thermogravimetric analysis of MSN-CN_{in}-SH_{out} (blue), MSN-COOH_{in}-SH_{out} (magenta) and MSN-COOH_{in}-PEG_{out} (green).

Copper-free click chemistry for cargo immobilization using stimuli-responsive linkers for controlled release

Several strategies have been described to modify functional groups in MSNs for cargo immobilization and controlled release. Recently, we have reported on NTA (nitrilotriacetic acid)-modified MSNs chelating metal ions (Ni²⁺, Zn²⁺ and Ca²⁺) capable of a controlled binding and pH dependent release of His-tagged fluorescence nanobodies (chromobodies). These constructs enabled the direct transport of nanobodies into living cells for antigen-visualization in real time.²³ The MSNs used in the above study were similar to the multifunctional large-pore stellate MSNs discussed in this report. Here, we present an alternative strategy for ligand coupling with the functional groups in these particles. We couple aza-dibenzocyclooctynes (DBCO) to the interior surface of the MSNs to enable a

copper-free click chemistry for guest molecule conjugations. DBCO was developed independently by the van Delft group in 2009 and the Popik group in 2010 to enhance the reaction kinetics of strain-promoted azide-alkyne cycloaddition (also referred to as copper-free click chemistry).^{24,25} Copper-free click chemistry mediated by DBCO derivatives became popular recently in bio-orthogonal conjugation applications for their high selectivity and reactivity toward azide-functionalized molecules under physiological conditions.²⁶⁻²⁹ The absence of metal catalysts in the reaction solutions also renders this type of click chemistry strategy more favorable for biological applications.

In our study, two different DBCO derivatives (DBCO-NHS ester and DBCO-S-S-NHS ester) were used to functionalize the internal surface of MSN-COOH_{in}-PEG_{out}. After a series of surface modifications (Figure 4-4a), we fabricated two types of DBCO-modified MSNs in which MSN-(S-S-DBCO)_{in}-PEG_{out} contains redox-sensitive disulfide bridges between the mesopore surface and DBCO groups while MSN-DBCO_{in}-PEG_{out} contains no stimuli-responsive linkers. Azide-terminated TAMRA dye was chosen as model cargo to carry out the copper-free click reaction with MSN-(S-S-DBCO)_{in}-PEG_{out} and MSN-DBCO_{in}-PEG_{out}. To evaluate the cargo immobilization efficacy of the DBCO-modified MSNs, time-based release experiments of the fluorescent TAMRA dye were performed in PBS at 37 °C. In brief, 0.5 mg of TAMRA dye-coupled MSNs in 200 µl PBS was loaded into a custom made Teflon cap fitting on a fluorescence cuvette. The cap was sealed with a dialysis membrane (MWCO 14,000 g/mol) which was permeable for small dye molecules but not for MSNs. The released dye in the fluorescence cuvette (filled with 3 mL PBS) was recorded by a spectrofluorometer with $\lambda_{\text{ex}} = 545 \text{ nm}$ and $\lambda_{\text{em}} = 565 \text{ nm}$. According to Figure 4-4b, the two MSN samples showed no spontaneous release and thus an efficient coupling of the TAMRA dye to the MSN host during the first 5 hours. Upon adding the reducing agent glutathione at this point (GSH, 10 mM in the final solutions) to the particle solutions and incubating the samples at 37 °C shortly for 5 min, the TAMRA dye was quickly released from the MSN-(S-S-DBCO)_{in}-PEG_{out} sample, whereas no release was observed from the MSN-DBCO_{in}-PEG_{out} sample. This result demonstrates that DBCO-modified MSNs are capable of conjugating azide-terminated molecules and are able to immobilize them stably within the particle interior. By introducing a stimuli-responsive linker between the silica surface and the cargo conjugating moiety, a controlled release of the cargo from MSNs can be achieved.

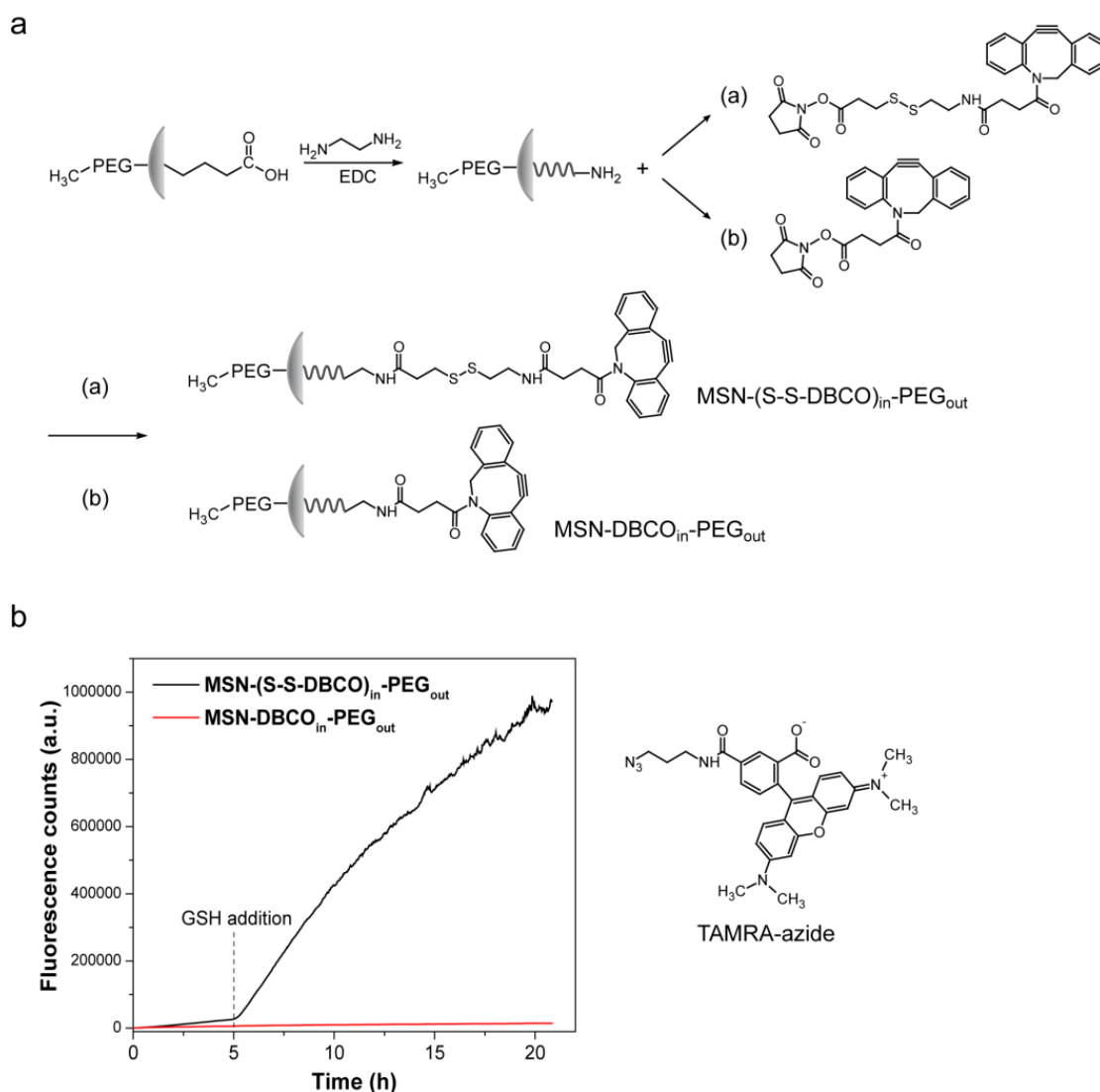


Figure 4-4 (a) Preparation of DBCO-modified MSNs. (b) Time-based release of TAMRA dyes from DBCO-modified MSNs. Azide-terminated TAMRA dye served as model cargo to be immobilized into DBCO-modified MSNs *via* copper-free click chemistry. After 5 h of release experiment initiation, glutathione (10 mM in the final concentration) was introduced to the two samples, respectively. The glutathione-added samples were incubated at 37 °C under shaking (500 rpm) for 5 min before the continuous release experiment.

As an alternative to the redox-sensitive disulfide bridge, we employed a pH-responsive linker between the MSN surface and the dye cargo to allow a stimuli-responsive cargo release. The pH-sensitive hydrolysis of the acetal linker 3,9-bis(3-aminopropyl)-2,4,8,10-tetraoxaspiro[5.5]undecane (called AK linker) was previously reported in the literature.^{30,31} We modified the MSN-COOH_{in}-PEG_{out} particles by attaching the amino terminus of the AK linker to the carboxy groups in the inner particle surface and then conjugated an amino-

reactive NHS-DBCO moiety to the residual amino group of the AK-linker (Figure 4-5a). TAMRA dyes were then again coupled to these MSN-(AKL-DBCO)_{in}-PEG_{out} samples *via* copper-free click chemistry. The dye attachment and pH-sensitive release was studied with fluorescence spectroscopy as described above.

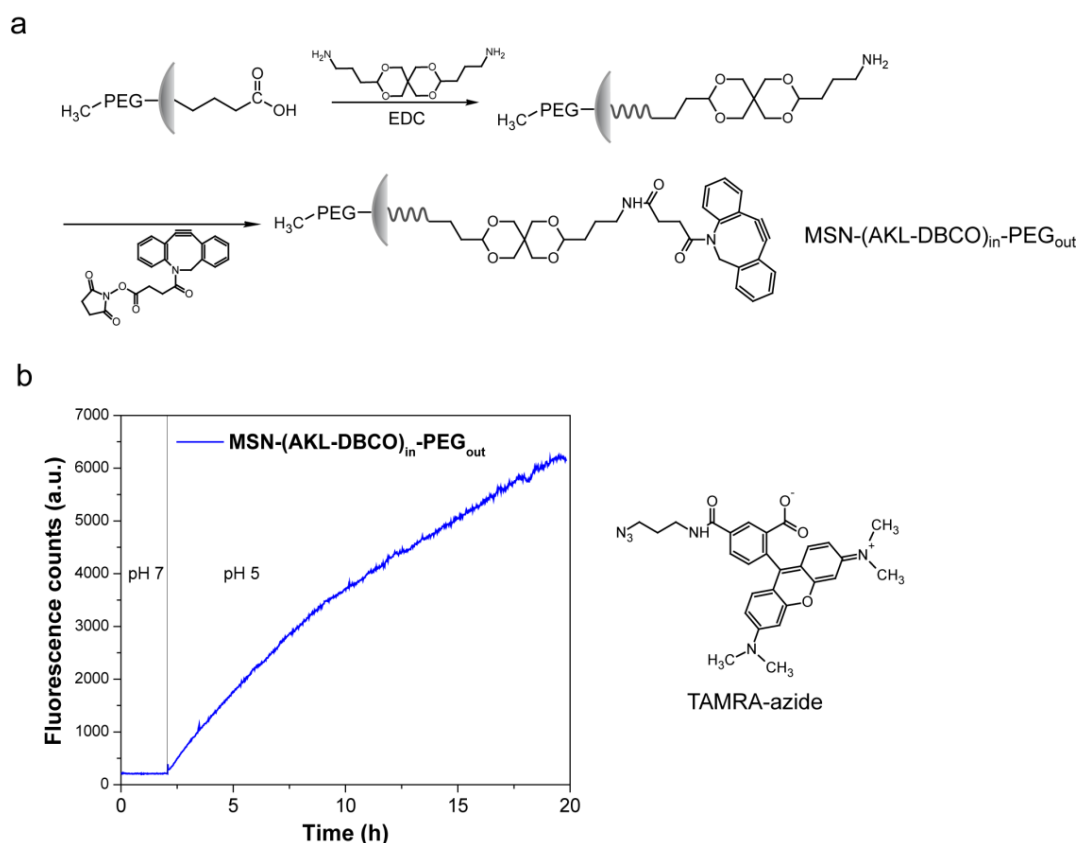


Figure 4-5 (a) Preparation of DBCO-modified MSNs with pH-responsive acetal linker (AKL). (b) Time-based release of TAMRA dyes from AKL-DBCO-modified MSNs. 2 h after release of TAMRA dyes in a pH 7 buffer, the sample was collected by centrifugation and re-dispersed in a pH 5 buffer for the following release experiment.

As illustrated in Figure 4-5b, TAMRA dyes were stably attached in the mesopores of MSN-(AKL-DBCO)_{in}-PEG_{out} without premature leakage when kept in a buffer solution at pH 7. However, the subsequent exchange of the medium with a pH 5 buffer triggered the TAMRA dye release due to the AK linker hydrolysis.

These release experiments demonstrate that DBCO derivatives are efficient elements for cargo conjugation on functionalized MSNs. Moreover, the sequential MSN modification with DBCO and stimuli-responsive linkers has no significant influence on the pore size

distribution of our large-pore nanoparticles (appendix Figure 4-10a). The successful modification with DBCO and the stimuli-responsive linker is seen in TGA results, which show an increasing mass loss after each reaction step (appendix Figure 4-10b). Detailed information about DBCO-modified MSNs is listed in appendix Figure 4-10c.

4.3 Conclusion

In summary, we were able to tailor the surface properties of large-pore stellate MSNs *via* co-condensation and post-synthetic modification into multifunctional MSNs that render promising nanocarriers for potential biomolecule delivery. Various organic functional groups could be incorporated into the silica framework by co-condensing organosilanes with TEOS. We note that the acidity or basicity of an organosilane which might alter the pH value of reaction solution (e.g., ATPES) should be used with care since they can modify the large-pore stellate particle morphology formation and result in different silica structures. A delayed co-condensation approach was used to spatially control the localization of functional groups in the mesoporous nanoparticle, hence creating a core-shell bi-functional stellate MSN structure. In addition, we demonstrated the feasibility of both external and internal MSN surface modification. DBCO derivatives were employed for copper-free click chemistry in combination with redox-sensitive disulfide bridged or pH-sensitive acetal linkers in our multifunctional MSN system to result in controlled cargo release. The synergy of surface adaptability and large pore radius in these stellate silica nanoparticles provides a promising outlook for applications in biomolecule delivery. This prospect was also demonstrated in our recent paper where similar large-pore stellate MSNs were used for the intracellular delivery of chromobodies.²³

4.4 Experimental

Materials

Tetraethyl orthosilicate (TEOS, Aldrich, $\geq 99\%$), phenyltriethoxysilane (PTES, Aldrich, $> 98\%$), (3-mercaptopropyl)triethoxysilane (MPTES, Aldrich, $\geq 80\%$), 3-aminopropyltriethoxysilane (APTES, Aldrich, 99%), 3-cyanopropyltriethoxysilane (CPTES, ABCR, 97%), cetyltrimethylammonium p-toluenesulfonate (CTATos, Sigma), triethanolamine (TEA, Aldrich, 98%), cystamine dihydrochloride (Aldrich), ethanol (EtOH, Aldrich, absolute), hydrochloric acid (HCl, Aldrich, 37%), methoxypolyethylene glycol maleimide (PEG, MW 5000, Sigma), ethylenediamine dihydrochloride (Aldrich), dibenzocyclooctyne-S-S-N-hydroxysuccinimidylester (DBCO-S-S-NHS ester, Aldrich), dibenzocyclooctyne-N-hydroxysuccinimidyl ester (DBCO-NHS ester, Aldrich), 3,9-bis(3-aminopropyl)-2,4,8,10-tetraoxaspiro[5.5]undecane (AK linker, TCI), 5-carboxytetramethylrhodamine azide (5-TAMRA Azide, Baseclick), L-glutathione reduced (GSH, Sigma), N-(3-dimethylaminopropyl)-N-ethylcarbodiimide (EDC, Alfa Aesar, 98%), saline-sodium citrate buffer (SSC buffer, Sigma), sodium carbonate (Sigma), sodium bicarbonate (Sigma), Dulbecco's phosphate-buffered saline (PBS, Gibco). Bi-distilled water was obtained from a Millipore system (Milli-Q Academic A10).

MSN synthesis

Un-functionalized MSNs (un-MSN) were synthesized based on an adapted recipe reported in the literature.¹³ In brief, TEA (0.047 g, 0.32 mmol), CTATos (0.263 g, 0.58 mmol) and H₂O (13.7 g, 0.77 mmol) were mixed in a 100 mL round bottom and stirred vigorously (1250 rpm) at 80 °C until the surfactant solution became homogeneous. TEOS (2.013 g, 9.6 mmol) was then added to the surfactant solution, and the mixture was continuously stirred at 80 °C for 2 h. The molar ratio of the above-mentioned mixture is TEOS : CTATos : TEA : H₂O = 1 : 0.06 : 0.033 : 80. The as-synthesized particles were collected by centrifugation (7197 g, 20 min) and were immediately template extracted (see below).

For functionalized MSNs (MSN-R), TEOS and organosilanes (RTES) were mixed in molar ratios as described in Table 4-2 (the total silane content remained at 9.6 mmol) for silica co-condensation. All other procedures were the same as in the un-MSN synthesis.

Core-shell bi-functional (MSN-CN_{in}-SH_{out}) MSNs were synthesized through a delayed co-condensation approach. TEOS (1.71 g, 8.2 mmol) and CPTES (116 mg, 0.48 mmol; 5 mol%) were mixed and added to the surfactant solution (as described in the previous section), and the mixture was stirred (1250 rpm) at 80 °C for 1 h. Afterwards, 201 mg of TEOS (0.96 mmol) was separated into 4 aliquots and added to the mixture every 3 minutes. The solution was further stirred for 1 h at 80 °C. A mixture of TEOS (20.1 mg, 0.096 mmol) and MPTES (28.6 mg, 0.096 mmol, 1 mol%) was then added to the solution to generate the outer shell of MSNs. The resulting solution was continuously stirred at 80 °C for 1 h. The as-synthesized particles were collected by centrifugation (7197 g, 20 min) and were subsequently template extracted.

Template extraction

To remove the organic surfactant from MSNs, 1 g of the as-synthesized particles were heated in an ethanolic solution (150 mL) containing 3 g of ammonium nitrate at 90 °C under reflux for 1 h, cooled and collected by centrifugation (7197 g, 20 min) and extracted by a second reflux at 90 °C using a 2 M HCl/ethanolic solution (150 mL) for 1 h. Afterwards, samples were washed in the sequence of EtOH, H₂O, EtOH (100 mL per wash) and were finally kept in 20 mL of EtOH. Particles were collected by centrifugation (7197 g, 20 min) after each template extraction and washing step.

Buffer preparation

a. Carbonate-bicarbonate buffer, pH 9

2 mL of 200 mM of sodium carbonate (2.2 g of sodium carbonate was dissolved in 100 mL H₂O) was slowly added to 23 mL of 200 mM of sodium bicarbonate (1.68 g of sodium bicarbonate was dissolved in 100 mL H₂O) to adjust the pH value to 9.0. By filling the buffer volume to 50 mL with H₂O the final carbonate-bicarbonate concentration of 100 mM was obtained.

b. 0.1 M MES buffer, pH 4.7

4-Morpholineethanesulfonic acid (1.95 g, 10 mmol) was dissolved in 100 mL of H₂O. 2 M NaOH was added dropwise to adjust the pH value to 4.7.

Modification of core-shell bi-functional MSNs

a. Hydrolysis of MSN-CN_{in}-SH_{out}

200 mg of MSN-CN_{in}-SH_{out} was dispersed in 20 mL of H₂O, and 60 mL of HCl (37 %) was added carefully. The sample was heated to reflux (90 °C) for 3 h and then cooled down in ambient environment. Afterwards 40 mL H₂O was added and the solution was stirred at RT overnight. 100 mL of H₂O was added to further dilute the solution before centrifugation (7197 g, 20 min) for particle collection. The resulting MSN-COOH_{in}-SH_{out} particles were washed with SSC buffer (pH 7), H₂O and EtOH (50 mL per wash), and were kept in EtOH (10 mL). Centrifugation (7197 g, 20 min) was applied after each washing step for particle collection.

b. Modification of MSN-CN_{in}-SH_{out} with cystamine

The thiol groups on the outer shell of MSN-CN_{in}-SH_{out} could be converted to amino groups by disulfide exchange of MSN-CN_{in}-SH_{out} with cystamine. In brief, cystamine dihydrochloride (22.5 mg, 0.1 mmol) was dissolved in 1 mL of H₂O as cystamine coupling solution. 10 mg of MSN-CN_{in}-SH_{out} was dispersed in 900 µL of H₂O and then mixed with 100 µL of 100 mM carbonate-bicarbonate buffer and 1 mL of cystamine coupling solution. The mixture was stirred at RT for 2 h followed by washing steps (twice with H₂O and twice with EtOH (5 mL per wash), followed by centrifugation (16873 g, 5 min) to remove excess of cystamine and the side product 2-mercaptoethylamine. The resulting MSN-CN_{in}-NH_{2out} particles were suspended in 5 mL EtOH. During the modification processes, particles were collected by centrifugation (16873 g, 5 min) in 1.5 mL Eppendorf tubes after reaction and each washing step.

c. PEGylation of MSN-COOH_{in}-SH_{out}

10 mg of MSN-COOH_{in}-SH_{out} and 10 mg of maleimide-terminated PEG were mixed in 6 mL of SSC buffer in a 10 mL-glass bottle. The mixture was stirred at RT overnight. The resulting MSN-COOH_{in}-PEG_{out} particles were washed with 10 mL of H₂O three times to remove excess free PEG molecules and were kept in 10 mL of H₂O. Centrifugation (16873 g, 5 min) was used to collect the particles after reaction and after each washing step.

d. Modification of MSN-COOH_{in}-PEG_{out} to MSN-DBCO_{in}-PEG_{out}/MSN-(S-S-DBCO)_{in}-PEG_{out}

To modify MSN-COOH_{in}-PEG_{out} with DBCO-S-S-NHS ester or DBCO-NHS ester, conversion of MSN-COOH_{in}-PEG_{out} to MSN-NH_{2in}-PEG_{out} was required. Ethylenediamine was used to convert COOH groups to NH₂ groups, the procedure was following the protocol described in the literature.³² Briefly, ethylenediamine dihydrochloride (1.33 g, 10 mmol) was dissolved in 10 mL of 0.1 M MES buffer (pH 4.7) to generate 1 M ethylenediamine coupling buffer in a 30 mL-glass bottle. The amount of 4 mg of MSN-COOH_{in}-PEG_{out} was dispersed in the ethylenediamine coupling buffer (10 mL) followed by addition of EDC (20 mg, 128.8 μmol, 2 mg/ml in the reaction solution) and the mixture was stirred at RT overnight. The resulting MSN-NH_{2in}-PEG_{out} particles were collected by centrifugation (16873 g, 5 min) and were washed with 4 mL H₂O three times to remove residual chemicals.

DBCO-S-S-NHS ester and DBCO-NHS ester were dissolved in DMSO in the concentration of 10 mM to serve as stock solutions, respectively. 2 mg of MSN-NH_{2in}-PEG_{out} particles were mixed with 1 mg of DBCO-S-S-NHS ester (170 μl from stock solution) or 1 mg of DBCO-NHS ester (240 μl from stock solution) in 1 mL PBS. The mixtures were shaken at RT for 3 h followed by washing steps (washed with 2 mL H₂O, 2 mL EtOH and 2 mL DMSO). Centrifugation (16873 g, 5 min) was performed for particle collection after each washing step. The resulting MSN-DBCO_{in}-PEG_{out} and MSN-(S-S-DBCO)_{in}-PEG_{out} particles were stored in DMSO at the concentration of 1 mg/ml.

e. Conversion of MSN-COOH_{in}-PEG_{out} to MSN-(AKL-DBCO)_{in}-PEG_{out}

A mixture of 4 mg of MSN-COOH_{in}-PEG_{out}, 5 mg of AK linker (18 μmol) and 5 μl of EDC (4.3 mg, 28 μmol) were dispersed in 1 mL SSC buffer in a 10 mL-glass bottle and were stirred at room temperature overnight. The resulting MSN-AKL_{in}-PEG_{out} particles were collected by centrifugation (16873 g, 5 min), washed with 10 mL SSC buffer and dispersed in 4 mL EtOH. 2 mg of MSN-AKL_{in}-PEG_{out} particles in 1 mL EtOH were mixed with 1 mg of DBCO-NHS ester (240 μl from stock solution) in a 1.5 mL- Eppendorf tube and the sample was shaken at RT for 2 h. The resulting MSN-(AKL-DBCO)_{in}-PEG_{out} particles were washed with 2 mL EtOH three times and stored in DMSO in the concentration of 1 mg/ml.

MSN Characterization

For transmission electron microscopy (TEM), samples were prepared by drying a diluted MSN suspension (in ethanol) on a carbon-coated copper grid at room temperature for several hours. The measurement was performed at 200 kV on a Jeol JEM-2010 instrument with a CCD detection system. Scanning electron microscopy (SEM) was performed at 30 kV on a Helios NanoLab G3 UC instrument (FEI, USA) equipped with a TLD detector. Diluted MSN suspensions (in ethanol) were dried on a carbon-coated copper grid at room temperature for several hours. Nitrogen sorption analyses were performed on a Quantachrome Instrument NOVA 4000e at 77 K. Sample outgassing was performed at 120 °C under vacuum (10 mTorr) 16 h before measurement. Pore size distribution curves were calculated by non-local density functional theory (NLDFT) procedures provided by Quantachrome based on the adsorption branch of N₂ on silica. A Thermo Scientific Nicolet iN10 IR-microscope was used to record infrared spectra of dried sample powders in reflection-absorption mode with a liquid-N₂ cooled MCT-A detector. Raman spectroscopy was performed on a Bruker Equinox 55 with a Nd:YAG laser having a wavelength of 1064 nm at a laser power of 100 mW and 3000 scans. Dynamic light scattering (DLS) and zeta potential measurements were performed on a Malvern Zetasizer-Nano instrument equipped with a 4 mW He-Ne laser (633 nm) and an avalanche photodiode. DLS measurements were directly recorded in diluted suspensions of the particles at a concentration of 1 mg/ml in ethanol. Zeta potential measurements were performed with an add-on Zetasizer titration system (MPT-2) based on diluted NaOH and HCl as titrants, and the samples were prepared by adding 1 mg of the particles to 10 mL bi-distilled water. Thermogravimetric analyses (TGA) of the powder samples (20 mg) were recorded on a Netzsch STA 440 C TG/DSC with a heating rate of 10 °C/min up to 900 °C in a stream of synthetic air of about 25 mL/min.

Release experiments

MSNs modified with DBCO-functional groups in the inner surface (MSN-DBCO_{in}-PEG_{out} / MSN-(S-S-DBCO)_{in}-PEG_{out} / MSN-(AKL-DBCO)_{in}-PEG_{out}) were used in the release experiments. 5-TAMRA azide was used as model cargo to carry out the copper-free click chemistry conjugation with DBCO modified MSNs. For dye loading, 0.5 mg of MSNs and 200 µg of 5-TAMRA azide (5 mg/ml in DMSO) were mixed in 1 mL PBS in an 1.5 mL-Eppendorf tube. The samples were incubated at 37 °C under shaking. After 2 h, TAMRA dye conjugated MSN samples were washed with 1 mL PBS three times to remove free dyes in the

solution. Centrifugation (16873 g, 5 min) was applied after each washing step for particle collection. MSN-TAMRA particles were re-dispersed in 200 μ l PBS and were transferred to a custom made Teflon cap fitting on a fluorescence cuvette. The cap was sealed with a dialysis membrane (ROTH Visking type 8/32, MWCO 14,000 g/mol) and placed on the top of a fluorescence cuvette filled with 3 mL PBS. Time-based fluorescence release experiments were performed at 37 °C on a PTI spectrofluorometer equipped with a xenon short arc lamp (UXL-75XE USHIO) and a photomultiplier detection system (Model 810/814). The excitation wavelength was set to $\lambda = 545$ nm and the emission fluorescence intensity was recorded at $\lambda = 565$ nm. All slits were adjusted to 2.0 mm. To trigger the stimuli-responsive dye release, 22 μ l of 100 mM GSH in PBS was added to MSN-DBCO-TAMRA and MSN-S-S-DBCO-TAMRA samples (each sample contains 200 μ l volume), respectively to achieve a final GSH concentration of 10 mM. The samples were incubated at 37 °C under shaking (500 rpm) for 5 min. The MSN-AKL-DBCO-TAMRA sample was transferred to an Eppendorf tube and the particles were collected by centrifugation (16873 g, 5 min). Afterwards, the sample was re-dispersed in 200 μ l of acetate buffer (pH 5) and was transferred back to the Teflon cap for the release experiment. All samples were sealed with the dialysis membranes and the release setups were reassembled. The fluorescence cuvettes for MSN-DBCO-TAMRA and MSN-S-S-DBCO-TAMRA samples were filled up with PBS containing 10 mM of GSH, while the fluorescence cuvette for MSN-AKL-DBCO-TAMRA sample was filled with acetate buffer (pH 5). Fluorescence spectra ($\lambda_{\text{ex}} = 545$ nm, $\lambda_{\text{em}} = 565$ nm) were recorded continuously overnight.

4.5 Appendix

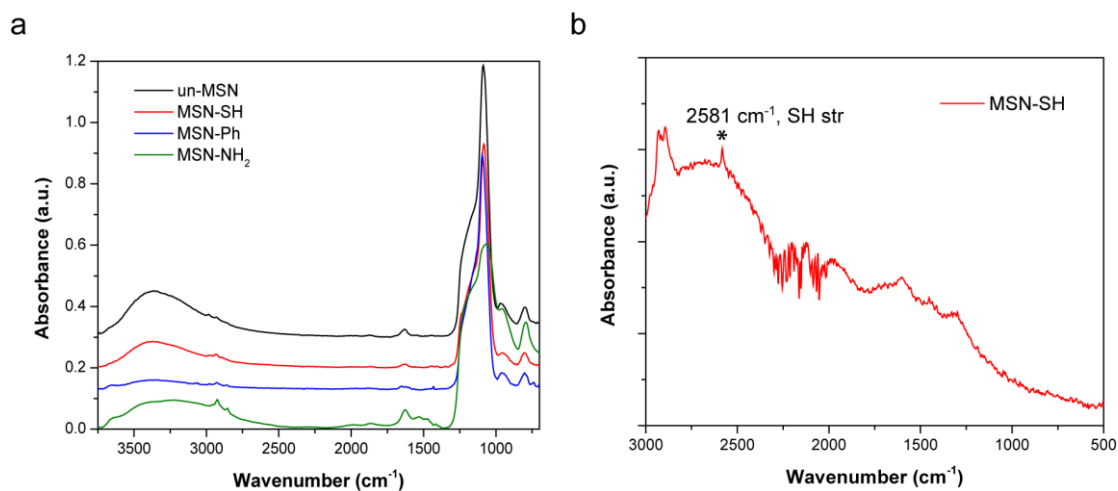


Figure 4-6 (a) Full range infrared spectra of MSNs. All curves are shifted along the y-axis by 0.1 units for clarity. (b) Raman spectrum of MSN-SH. The spectrum was obtained with a Nd:YAG laser ($\lambda = 1064$ nm) at a laser power of 100 mW and 3000 scans.

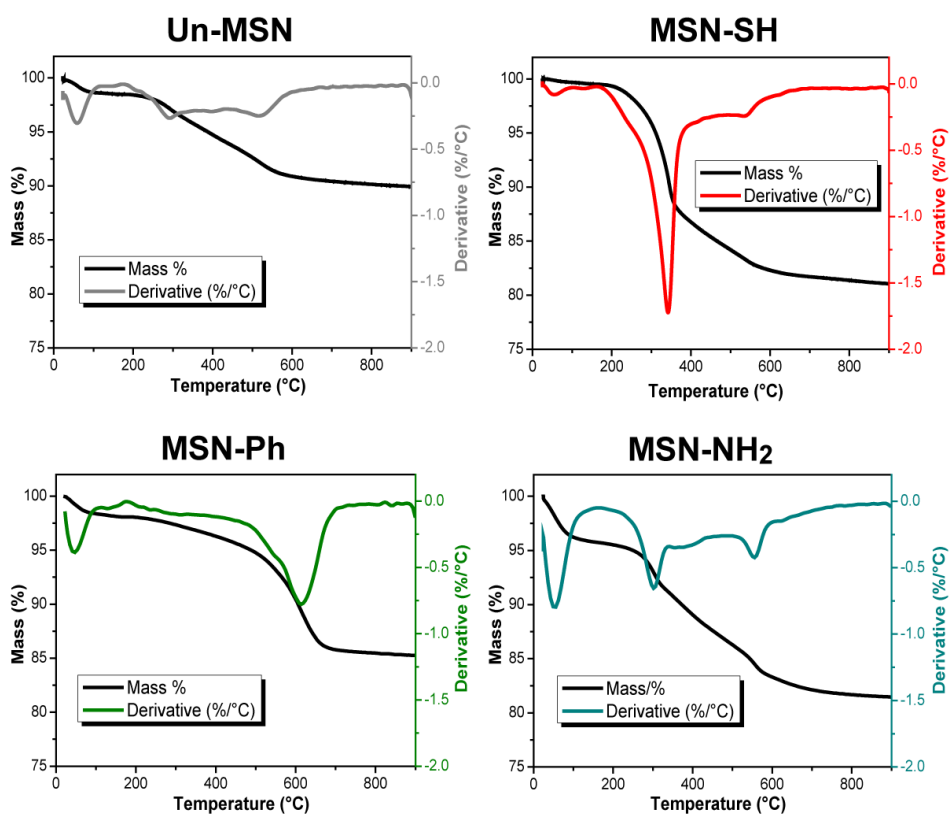


Figure 4-7 Thermogravimetric analysis of MSNs functionalized with different organic groups.

Table 4-3 TGA mass losses and estimated degree of organic functionalizations of the functionalized MSNs.

Sample	Formulation of functional group (R)	Molecular weight of functional group (MW_R)	TGA mass loss ^a (%)	Estimated degree of organic functionalization ^b (%)
MSN-SH	C_3H_6SH	75.2	18.6	15.4
MSN-Ph	C_6H_5	77.1	13.1	10.5
MSN-NH ₂	$C_3H_6NH_2$	58.1	15.0	15.4

^a Calculated based on the mass differences between 150 °C and 900 °C.

$$Mass\ loss\ (\%) = \frac{x \times MW_R}{x \times MW_R + (100 - x)MW_{SiO_2}}$$

^b Calculated based on the formulation:

,x (%) = degree of organic functional groups.

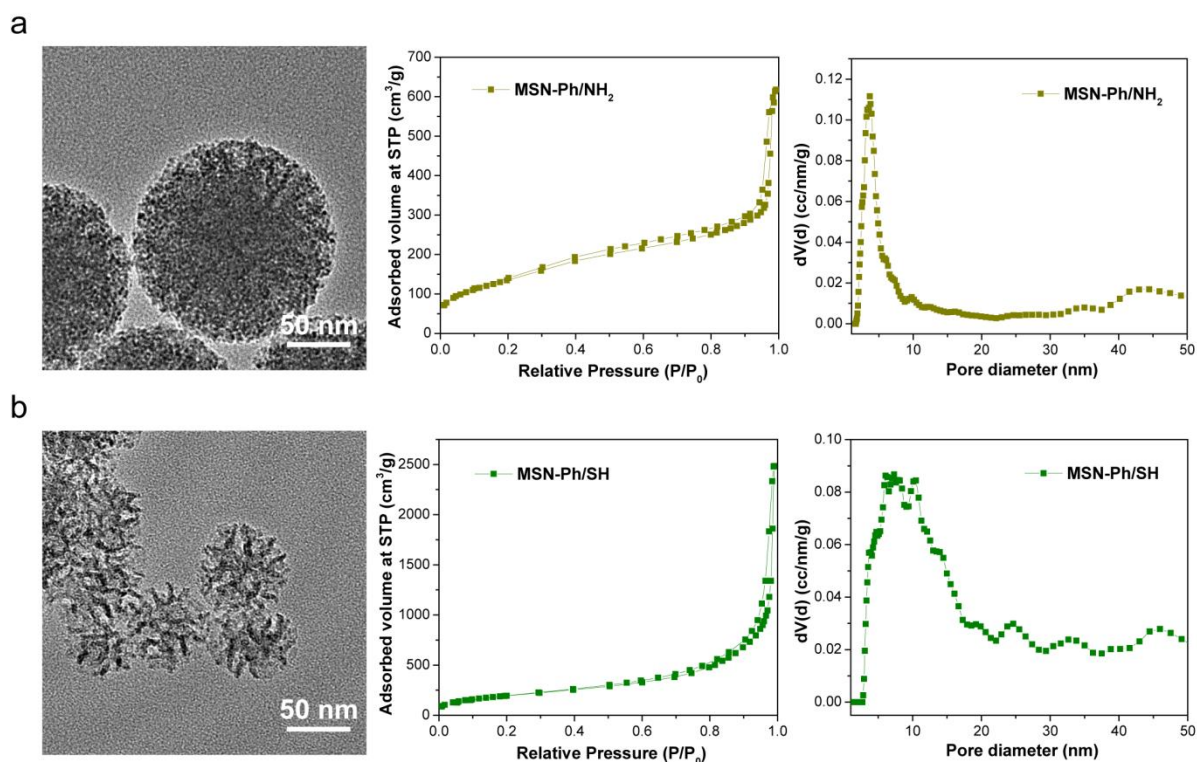
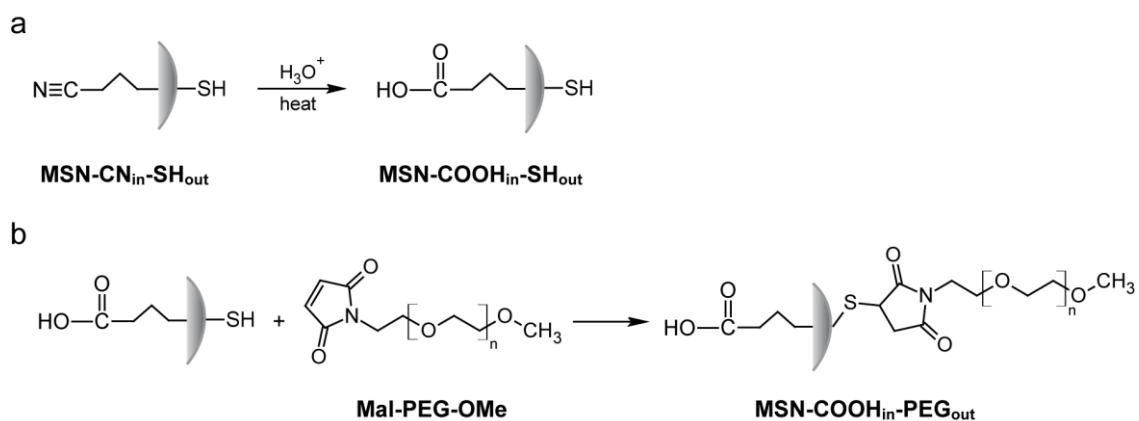


Figure 4-8 Characterization of (a) MSN-Ph/NH₂ and (b) MSN-Ph/SH. From left to right: TEM images, N₂ sorption isotherms and NLDFT pore size distributions obtained from adsorption branches.

Table 4-4 Synthesis and characterization information of MSN-Ph/NH₂ and MSN-Ph/Si.

Sample	Precursors	DFT Pore size distribution (nm)	Pore volume (cm ³ /g)	BET surface area (m ² /g)	Particle size (nm)	pH value after silane addition
MSN-Ph/NH₂	95 mol% TEOS					
	2.5 mol% PTES	2.5-5.0	0.9	496	190 ± 54	9.92
	2.5 mol% APTES					
MSN-Ph/Si	90 mol% TEOS					
	5 mol% PTES	3.5-22	2.6	712	73 ± 15	9.33
	5 mol% MPTES					

**Figure 4-9 Surface modification of core-shell MSNs.** (a) Hydrolysis of MSN-CN_{in}-SH_{out} particles in acidic condition at 90 °C. (b) PEGylation of MSN-COOH_{in}-SH_{out}.

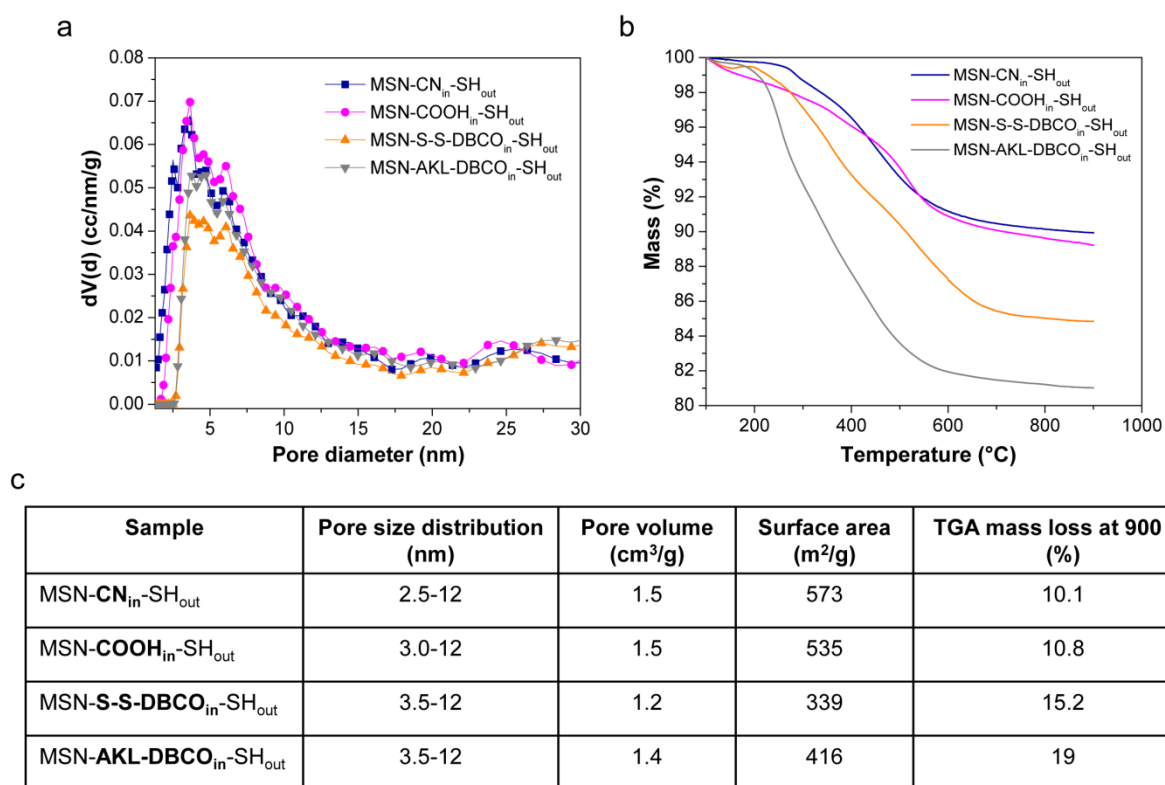


Figure 4-10 Characterization of core-shell MSNs. (a) NLDFT pore size distribution of core-shell MSNs calculated from adsorption branches of N₂ sorption isotherms. (b) Thermogravimetric analysis. (c) Summary of the core-shell MSN characterization. The TGA mass loss was calculated based on the mass differences between 100 °C and 900 °C.

4.6 References

- 1 Kresge, C. T., Leonowicz, M. E., Roth, W. J., Vartuli, J. C. & Beck, J. S. Ordered mesoporous molecular sieves synthesized by a liquid-crystal template mechanism. *Nature* **359**, 710-712, doi:10.1038/359710a0 (1992).
- 2 Beck, J. S. *et al.* A new family of mesoporous molecular sieves prepared with liquid crystal templates. *J. Am. Chem. Soc.* **114**, 10834-10843, doi:10.1021/ja00053a020 (1992).
- 3 Vallet-Regi, M., Rámila, A., del Real, R. P. & Pérez-Pariente, J. A New Property of MCM-41: Drug Delivery System. *Chem. Mater.* **13**, 308-311, doi:10.1021/cm0011559 (2001).
- 4 Lai, C. Y. *et al.* A mesoporous silica nanosphere-based carrier system with chemically removable CdS nanoparticle caps for stimuli-responsive controlled release of neurotransmitters and drug molecules. *J. Am. Chem. Soc.* **125**, 4451-4459, doi:10.1021/ja028650l (2003).
- 5 Díaz, J. F. & Balkus, K. J. Enzyme immobilization in MCM-41 molecular sieve. *J. Mol. Catal. B: Enzym.* **2**, 115-126, doi:10.1016/s1381-1177(96)00017-3 (1996).
- 6 Argyo, C., Weiss, V., Bräuchle, C. & Bein, T. Multifunctional Mesoporous Silica Nanoparticles as a Universal Platform for Drug Delivery. *Chem. Mater.* **26**, 435-451, doi:10.1021/cm402592t (2014).
- 7 Slowing, II, Vivero-Escoto, J. L., Wu, C. W. & Lin, V. S. Mesoporous silica nanoparticles as controlled release drug delivery and gene transfection carriers. *Adv. Drug Del. Rev.* **60**, 1278-1288, doi:10.1016/j.addr.2008.03.012 (2008).
- 8 Mamaeva, V., Sahlgren, C. & Linden, M. Mesoporous silica nanoparticles in medicine--recent advances. *Adv Drug Deliv Rev* **65**, 689-702, doi:10.1016/j.addr.2012.07.018 (2013).
- 9 Leader, B., Baca, Q. J. & Golan, D. E. Protein therapeutics: a summary and pharmacological classification. *Nat. Rev. Drug Discov.* **7**, 21-39, doi:10.1038/nrd2399 (2008).
- 10 Carter, P. J. Introduction to current and future protein therapeutics: a protein engineering perspective. *Exp. Cell Res.* **317**, 1261-1269, doi:10.1016/j.yexcr.2011.02.013 (2011).
- 11 Gavrillov, K. & Saltzman, W. M. Therapeutic siRNA: principles, challenges, and strategies. *Yale J Biol Med* **85**, 187-200 (2012).
- 12 Knezevic, N. Z. & Durand, J. O. Large pore mesoporous silica nanomaterials for application in delivery of biomolecules. *Nanoscale* **7**, 2199-2209, doi:10.1039/c4nr06114d (2015).

- 13 Zhang, K. *et al.* Facile large-scale synthesis of monodisperse mesoporous silica nanospheres with tunable pore structure. *J. Am. Chem. Soc.* **135**, 2427-2430, doi:10.1021/ja3116873 (2013).
- 14 Li, Y., Hei, M., Xu, Y., Qian, X. & Zhu, W. Ammonium salt modified mesoporous silica nanoparticles for dual intracellular-responsive gene delivery. *Int. J. Pharm.* **511**, 689-702, doi:10.1016/j.ijpharm.2016.07.029 (2016).
- 15 Xiong, L. *et al.* Tunable stellate mesoporous silica nanoparticles for intracellular drug delivery. *J. Mater. Chem. B* **3**, 1712-1721, doi:10.1039/c4tb01601g (2015).
- 16 Kecht, J., Schlossbauer, A. & Bein, T. Selective Functionalization of the Outer and Inner Surfaces in Mesoporous Silica Nanoparticles. *Chem. Mater.* **20**, 7207-7214, doi:10.1021/cm801484r (2008).
- 17 Möller, K. & Bein, T. Talented Mesoporous Silica Nanoparticles. *Chem. Mater.*, doi:10.1021/acs.chemmater.6b03629 (2016).
- 18 Huh, S., Wiench, J. W., Yoo, J.-C., Pruski, M. & Lin, V. S. Y. Organic Functionalization and Morphology Control of Mesoporous Silicas via a Co-Condensation Synthesis Method. *Chem. Mater.* **15**, 4247-4256, doi:10.1021/cm0210041 (2003).
- 19 Kobler, J., Möller, K. & Bein, T. Colloidal suspensions of functionalized mesoporous silica nanoparticles. *ACS Nano* **2**, 791-799, doi:10.1021/nn700008s (2008).
- 20 Cauda, V., Schlossbauer, A., Kecht, J., Zurner, A. & Bein, T. Multiple core-shell functionalized colloidal mesoporous silica nanoparticles. *J. Am. Chem. Soc.* **131**, 11361-11370, doi:10.1021/ja809346n (2009).
- 21 He, Q., Zhang, Z., Gao, F., Li, Y. & Shi, J. In vivo biodistribution and urinary excretion of mesoporous silica nanoparticles: effects of particle size and PEGylation. *Small* **7**, 271-280, doi:10.1002/smll.201001459 (2011).
- 22 Cauda, V., Argyo, C. & Bein, T. Impact of different PEGylation patterns on the long-term bio-stability of colloidal mesoporous silica nanoparticles. *J. Mater. Chem.* **20**, 8693, doi:10.1039/c0jm01390k (2010).
- 23 Chiu, H. Y. *et al.* Intracellular chromobody delivery by mesoporous silica nanoparticles for antigen targeting and visualization in real time. *Sci Rep* **6**, 25019, doi:10.1038/srep25019 (2016).
- 24 Debets, M. F. *et al.* Aza-dibenzocyclooctynes for fast and efficient enzyme PEGylation via copper-free (3+2) cycloaddition. *Chem Commun (Camb)* **46**, 97-99, doi:10.1039/b917797c (2010).
- 25 Kuzmin, A., Poloukhine, A., Wolfert, M. A. & Popik, V. V. Surface functionalization using catalyst-free azide-alkyne cycloaddition. *Bioconjug Chem* **21**, 2076-2085, doi:10.1021/bc100306u (2010).

- 26 Bouvet, V., Wuest, M. & Wuest, F. Copper-free click chemistry with the short-lived positron emitter fluorine-18. *Org Biomol Chem* **9**, 7393-7399, doi:10.1039/c1ob06034a (2011).
- 27 Koo, H. *et al.* Bioorthogonal copper-free click chemistry in vivo for tumor-targeted delivery of nanoparticles. *Angew. Chem. Int. Ed. Engl.* **51**, 11836-11840, doi:10.1002/anie.201206703 (2012).
- 28 Lee, S. B. *et al.* Mesoporous silica nanoparticle pretargeting for PET imaging based on a rapid bioorthogonal reaction in a living body. *Angew. Chem. Int. Ed. Engl.* **52**, 10549-10552, doi:10.1002/anie.201304026 (2013).
- 29 Jeon, J. *et al.* Efficient method for iodine radioisotope labeling of cyclooctyne-containing molecules using strain-promoted copper-free click reaction. *Bioorg. Med. Chem.* **23**, 3303-3308, doi:10.1016/j.bmc.2015.04.045 (2015).
- 30 Schlossbauer, A., Dohmen, C., Schaffert, D., Wagner, E. & Bein, T. pH-responsive release of acetal-linked melittin from SBA-15 mesoporous silica. *Angew. Chem. Int. Ed. Engl.* **50**, 6828-6830, doi:10.1002/anie.201005120 (2011).
- 31 Liu, R. *et al.* pH-responsive nanogated ensemble based on gold-capped mesoporous silica through an acid-labile acetal linker. *J. Am. Chem. Soc.* **132**, 1500-1501, doi:10.1021/ja907838s (2010).
- 32 Hermanson, G. T. *Bioconjugate Techniques*. 2nd edn, (Elsevier Science, 2008).

5 Intracellular Chromobody Delivery by Mesoporous Silica Nanoparticles for Antigen Targeting and Visualization in Real Time

This chapter is based on the following publication:

Hsin-Yi Chiu, Wen Deng, Hanna Engelke, Jonas Helma, Heinrich Leonhardt, and Thomas Bein, *Scientific Reports* 2016, 6, 25019

Abstract

Chromobodies have recently drawn great attention as bioimaging nanotools. They offer high antigen binding specificity and affinity comparable to conventional antibodies, but much smaller size and higher stability. Chromobodies can be used in live cell imaging for specific spatio-temporal visualization of cellular processes. To date, functional application of chromobodies requires lengthy genetic manipulation of the target cell. Here, we develop multifunctional large-pore mesoporous silica nanoparticles (MSNs) as nanocarriers to *directly* transport chromobodies into living cells for antigen-visualization in real time. The multifunctional large-pore MSNs feature high loading capacity for chromobodies, and are efficiently taken up by cells. By functionalizing the internal MSN surface with nitrilotriacetic acid-metal ion complexes, we can control the release of His₆-tagged chromobodies from MSNs in acidified endosomes and observe successful chromobody-antigen binding in the cytosol. Hence, by combining the two nanotools, chromobodies and MSNs, we establish a new powerful approach for chromobody applications in living cells.

5.1 Introduction

Today, antibodies are considered to be the most powerful tools for specific visualization of cellular compartments at the molecular level aimed at the study of cellular processes. They are indispensable for proteomic analyses, protein localization and detection of post-translational modifications. However, the application of full-length antibodies is restricted to fixed cells, meaning dead cells, since the massive sizes (~ 150 kD) and complex folding structures, including intermolecular disulphide bridges, limit their use in living cells *via* the transient expression approach or *via* direct delivery. As a result, the idea of engineering recombinant small antibodies for real time dynamic protein tracing in living cells has received much attention. A variety of recombinant small antibodies including immunoglobulin (Ig) derived Fab (~ 50 kD) and scFv (~ 25 kD), as well as non-Ig derived monobody (~ 10 kD) and affibody (~ 6.5 kD) protein scaffolds have been generated in the last decades for this purpose.¹ Nanobodies (~ 14 kD) are the single-domain antigen-binding fragments derived from camelid's single-chain IgG.² They have a binding affinity and specificity similar to conventional antibodies, but are much smaller in size and exhibit higher stability. When conjugated with fluorescent proteins or organic dyes, the fluorescent nanobodies, named chromobodies, become molecular probes that can trace the dynamics of endogenous cellular structures in living cells. Chromobodies have successfully shown their antigen detection efficacy on cytoskeleton, histone protein and DNA replication complexes, and have revealed the spatio-temporal protein changes during cell cycles.³ In our previous report,⁴ HIV-specific chromobodies have been generated and used for real time visualization of HIV assembly in living cells. These studies demonstrate that chromobodies are promising protein reporters for the study of cellular processes in living cells. However, to date the application of chromobodies for live cell imaging was limited due to the need to introduce them genetically, followed by subsequent cytosolic expression. To broaden the flexibility and use of chromobodies in biomedical applications (e.g., manipulation of cell function for disease treatment), direct intracellular delivery of the molecular probes would be highly desirable. However, intracellular protein delivery is challenging firstly because the large size of proteins leads to difficulties with passive diffusion through the cell membrane or with endocytosis. The following endosomal trapping of internalized proteins further limits the protein functions in cells. A few studies of non-carrier intracellular protein delivery aimed to enhance the cellular uptake efficiency in combination with endosomolytic agents and therefore to increase the protein delivery efficacy.^{5,6} For example, Erazo-Oliveras *et al.* co-

incubated dimerized cell-penetrating peptide TAT (dfTAT) with proteins (EGFP and Cre recombinase, etc.) in culture media, the results show that proteins were successfully crossing the cell membrane with the help of dfTAT and presenting their functions in cytosols⁵; D'Astolfo *et al.* used hyperosmolality NaCl buffer to induce the highly efficient micropinocytosis of proteins. In combination with a transduction compound (a propanebetaine), intracellular protein release was achieved.⁶ Alternatively, using carriers such as cationic polyplexes with high cellular uptake efficiency for proteins may improve the generally low efficiency of protein uptake. However, the complex structures and wide variety of surface charges of proteins make it difficult to design a general carrier for universal protein delivery.⁷ The second challenge of protein delivery is that proteins are susceptible to proteolytic cleavage. Proteins must maintain their tertiary structure to preserve their functionality during the delivery process.

To address these bottlenecks, we surmised that mesoporous silica nanoparticles (MSNs) could be promising candidates for serving as efficient and versatile protein delivery vehicles. For example, their surface can be modified with different functionalities and charges to accommodate different proteins; their pore sizes are tunable to fit different cargo sizes; their frameworks are stable and can effectively protect cargos from environmental degradation, and they can be efficiently taken up by cells. In the past years, the development of MSNs for biomedical applications has greatly increased. The achievements include delivery of chemotherapeutic agents for cancer therapy,⁸ intracellular protein delivery for manipulation of cell function,^{9,10} and oligonucleotide delivery for gene therapy.^{11,12} These studies demonstrate that MSNs can efficiently control the release of cargos in the target tissue/cells as well as effectively protect cargos from degradation. Importantly, MSNs were found to be biocompatible within certain concentration ranges.¹³

In this study, we synthesize multifunctional large-pore MSNs for intracellular chromobody delivery. Metal chelate complexes are covalently attached on the internal silica surface and used for pH-responsive coordination binding of His₆-tagged chromobodies. The binding affinity and pH-stimulated release of various metal ions (Fe²⁺, Co²⁺, Ni²⁺, Cu²⁺, Zn²⁺ and Ca²⁺) with His₆-tagged chromobodies are examined by colorimetric measurements *in vitro*. Mouse embryonic fibroblasts (MEFs) expressing EGFP fused to LMNA (an inner nuclear membrane protein) (MEF-G-LMNA) are generated for the detection of GFP-specific chromobody release and function in intracellular delivery experiments. The successful

chromobody delivery, release from the endosomes and binding to the target structures can be confirmed by the fluorescence co-localization signals of EGFP and chromobodies on the LMNA structure.

5.2 Results

Synthesis and characterization of large-pore MSNs

Mercapto-functionalized MSNs (MSN-SH) were synthesized using a sol-gel templating approach in a neutral pH reactive solution according to a modified protocol from the literature.¹⁴ During the synthesis process (Figure 5-1a) the structure directing agent cetyltrimethylammonium (CTA^+) formed micelles in the initial solution, silica precursors tetraethyl orthosilicate (TEOS) and (3-mercaptopropyl)triethoxysilane (MPTES) were then adsorbed and co-condensed around the micelles because of the electrostatic attraction between CTA^+ and negatively charged silica. In this neutral pH synthesis solution, the counter ions Tos^- compete with the silicate oligomers for association with the positively charged micelles, which results in sparse silica condensation and consequently the large stellate pore structure formation (Figure 5-1b).¹⁴ Mercapto-functional groups were introduced homogeneously into the silica framework *via* co-condensation for the purpose of further functionalization. According to the N_2 sorption analysis (Figure 5-1c), MSN-SH has a fairly wide pore size distribution from 10 nm to 20 nm, a BET surface area of $670 \text{ m}^2 \text{ g}^{-1}$ and a large pore volume of $3.06 \text{ cm}^3 \text{ g}^{-1}$. With these pore dimensions, chromobodies featuring a size of $2 \text{ nm} \times 4 \text{ nm}$ ¹⁵ are expected to be efficiently loaded into the mesopores. The hydrodynamic particle size (Figure 5-1d) measured by dynamic light scattering (DLS) was 100 – 200 nm. This particle size range is considered to be favorable for endocytosis.¹⁶

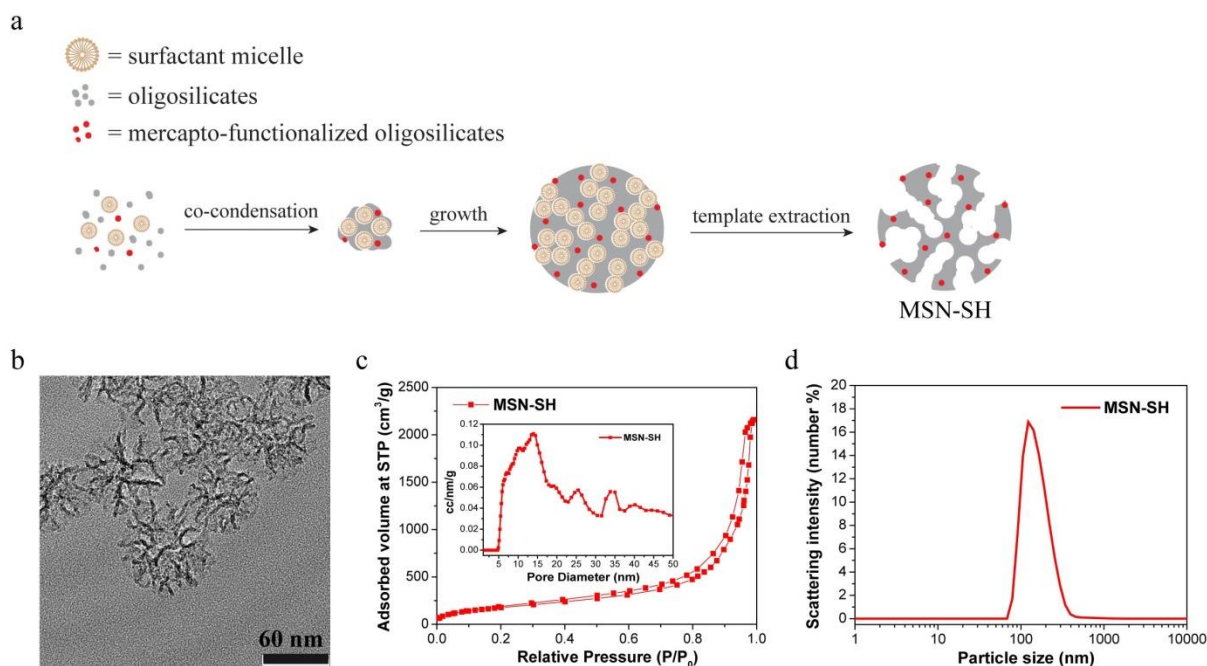


Figure 5-1 Synthesis and characterization of MSN-SH. (a) MSN-SH was synthesized through a modified protocol described earlier in the literature.¹⁴ MSN-SH was synthesized by co-condensation of oligosilicates (from TEOS) and mercapto-functionalized oligosilicates (from MPTES) in a neutral pH reaction mixture. (b) TEM image of MSN-SH. The high contrast areas indicate the dense silica backbones whereas the low contrast areas indicate the pore structure. The average particle size is about 100 nm according to the TEM image. *Scale bar: 60 nm.* (c) Nitrogen sorption isotherm (outer figure) of MSN-SH and its corresponding pore size distribution (inner figure) calculated by the NLDFT mode based on the adsorption branch of N₂ on silica. (d) Dynamic light scattering (DLS) of hydrodynamic particle size of MSN-SH in EtOH. The average hydrodynamic particle size is around 160 nm.

MSN-M²⁺ for controlled uptake and release of chromobodies

To control chromobody loading and release from the silica framework, nitrilotriacetic acid - metal ion complexes (NTA-M²⁺) were attached to the MSN surface as pH-responsive linkers. The recombinant GFP-specific chromobody possesses a built-in His₆-tag on its C-terminus for purification purposes. This His₆-tag can be used as a tether to conjugate chromobodies onto NTA-M²⁺ complexes because there are three potential coordination sites on the histidine molecule: the carboxyl group (pK_a = 1.9), the imidazole nitrogen (pK_a = 6.1) and the amino nitrogen (pK_a = 9.1). Among these coordination sites, the imidazole nitrogen is considered to

be the primary site for the conjugation with metal ions. The conjugation can be separated by high imidazole concentration buffer elution (free imidazole substitutes the coordination binding of histidine on the NTA-M²⁺ complexes). Alternatively, low pH buffer can also be used for elution since the imidazole nitrogen is protonated under acidic conditions (pH < 6) and therefore acidification results in the detachment of His₆-tagged chromobodies from NTA-M²⁺ complexes.

To carry out the MSN modification, MSN-SH was converted to carboxyl-functionalized MSN (MSN-COOH) by reacting MSN-SH with 6-maleimidohexanoic acid in ethanol. The MSN-COOH was then conjugated with N α ,N α -bis(carboxymethyl)-L-lysine hydrate (NTA-lysine) *via* an EDC-sulfo NHS coupling approach (Figure 5-2a). The 1700 cm⁻¹ peak attributed to a C=O vibration in the IR spectrum (Figure 5-2b, red line) indicated the successful coupling of 6-maleimidohexanoic acid with MSN-SH, while the conjugation of MSN-COOH and NTA-lysine was verified by the increased secondary amide bond signal at 1650 cm⁻¹ in the IR spectrum (Figure 5-2b, blue line). After this two-step modification, the final NTA-conjugated MSNs (MSN-NTA) still exhibit the desired large-pore structure as well as colloidal stability (appendix Figure 5-6). To compare the effect of different NTA-M²⁺ complexes for His₆-tagged chromobody conjugation, various metal ions: Fe²⁺, Co²⁺, Ni²⁺, Cu²⁺, Zn²⁺ and Ca²⁺ were immobilized onto MSN-NTA, yielding NTA-M²⁺-complex-modified MSNs (MSN-M²⁺) (Figure 5-2c). Chromobodies were then loaded on the MSN-M²⁺ carriers (MSN-Fe²⁺, MSN-Co²⁺, MSN-Ni²⁺, MSN-Cu²⁺, MSN-Zn²⁺ and MSN-Ca²⁺) as well as MSN-SH (as control group) in 0.05 M Tris-acetate buffer (pH 8). Subsequently, chromobody loading and release tests were performed *via* measurements of the fluorescence intensity (emission at 669 nm) of the loading/release supernatants. The fluorescent intensity of a dilution series of pure chromobodies was measured as standard curve for the following quantification. Based on the results shown in Figure 5-2d, all samples (MSN-Fe²⁺, MSN-Co²⁺, MSN-Ni²⁺, MSN-Cu²⁺, MSN-Zn²⁺, MSN-Ca²⁺ and MSN-SH; for the latter, see discussion below) exhibited a similarly high chromobody loading capacity of approximately 70 μ g per mg MSN. This loading capacity corresponds to about 600 chromobody molecules per MSN (for the detailed calculation, please see appendix 5-12). After incubation of the chromobody-loaded MSNs (MSN-M-Cb) in pH 7 buffer for 16 h, all the samples showed on average only 5 % release of the loaded chromobodies (Figure 5-2e). However, performing the chromobody release in pH 5 buffer, MSN-Ni²⁺, MSN-Cu²⁺, MSN-Zn²⁺ and MSN-Ca²⁺ exhibited significantly higher chromobody release efficiency than in pH 7 (Figure 5-2e).

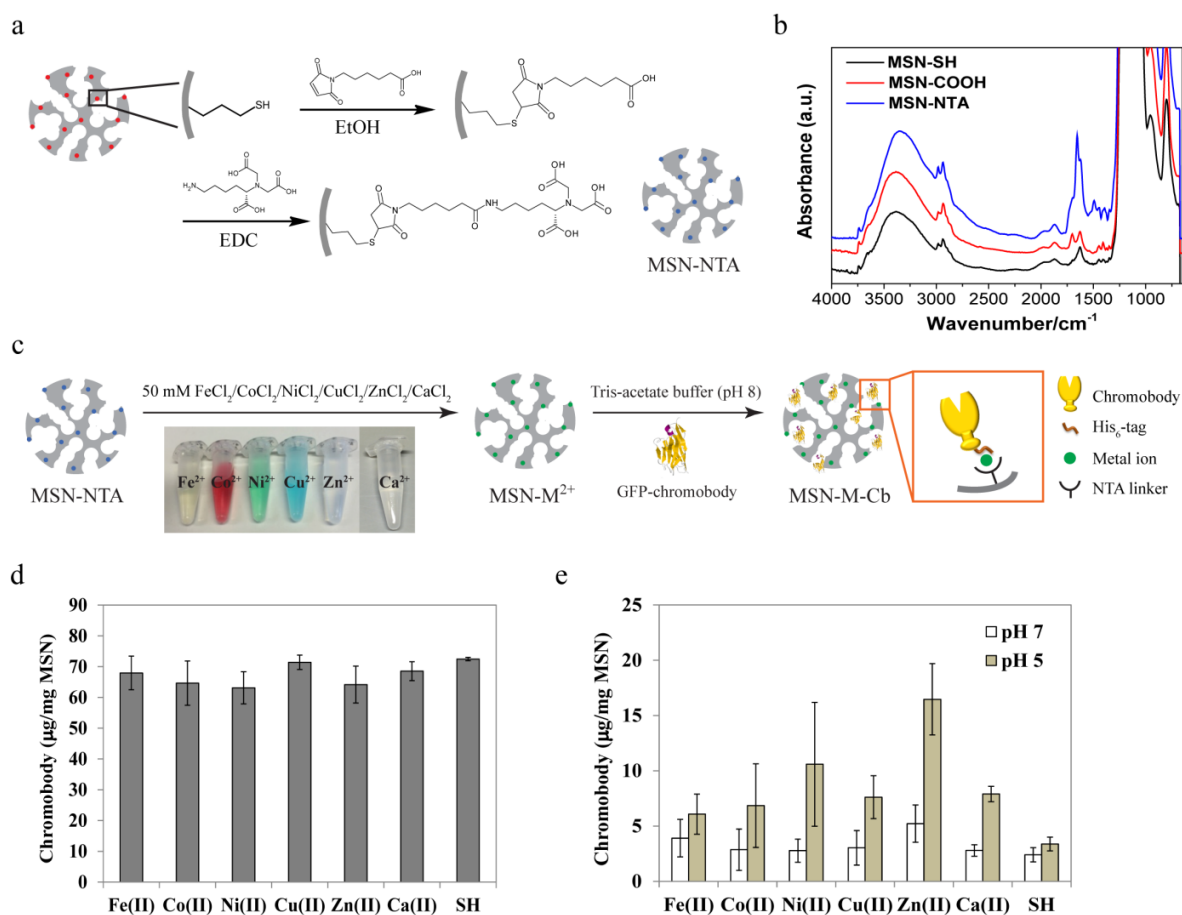


Figure 5-2 Surface modification of MSN and chromobody controlled release test *in vitro*.

(a) Modification process of MSN-SH to yield MSN-NTA. (b) IR spectra of the functionalized MSNs during each modification step. MSN-SH (black), MSN-COOH (red) and MSN-NTA (blue). (c) MSN-NTA particles were treated with different metal ion solutions (50 mM), respectively, at room temperature for 6 h. The free metal ions were then washed away with water, and the resulting metal-immobilized MSNs (MSN-M²⁺) were incubated with chromobody (ATTO 647N labelled) loading buffers (100 µg chromobody ml⁻¹ in Tris-acetate buffer, pH 8) at 4 °C for 2 h to bind the chromobodies to MSNs. (d) Chromobody loading capacity of different metal-immobilized MSNs. MSN-SH served as control group in the *in vitro* controlled release test. (e) Chromobody loaded MSN particles (MSN-M-Cb) were dispersed in PBS buffer (with pH 7 or pH 5) at 37 °C for 16 h. Afterwards, the supernatants were collected and the amounts of chromobody released were measured using colorimetric analysis. Pure chromobodies were diluted in PBS buffer at different concentrations for creating the standard curve. Experiments were triplicated. Error bars were calculated as s.e.m.

In general, the extent of release of His₆-tagged proteins from the NTA-M²⁺ moieties is determined by two factors: (i) the stability of the metal chelation by NTA, and (ii) the stability of the coordination between metal ions and histidine molecules. The general stability order of NTA-metal ion and histidine-metal ion complexes is: Cu²⁺ > Ni²⁺ > Zn²⁺ > Co²⁺ > Fe²⁺ > Ca²⁺.^{17,18} The results shown here indicate that Cu²⁺, Ni²⁺, Zn²⁺ and Ca²⁺ are able to allow for the chromobody release in an acidic environment at pH 5, while Cu²⁺, Ni²⁺ and Zn²⁺ show a rather high stability when incorporating to the MSN-NTA system. By contrast, Co²⁺ and Fe²⁺ showed no significant differences of chromobody controlled release in pH 7 and pH 5 buffers due to their weak complexing stability with either NTA or histidine. Interestingly, although the theoretical coordination stability of NTA-Ca²⁺ is low, His₆-tagged chromobodies still bind sufficiently to MSN-Ca²⁺ in pH 7 buffer. Practically, MSN-Ca²⁺ is favored for chromobody delivery because the decomposition of the NTA-Ca-chromobody complex starts already at pH 6 (data not shown), therefore more chromobodies can be released in the early endosome stage. Moreover, small amounts of Ca²⁺ are considered to be biocompatible and non-toxic.

The control group MSN-SH particles showed high chromobody loading capacity and low chromobody release in both pH 7 and pH 5 even without any capping system or chemical conjugation. This indicates that the negatively charged silica framework (zeta potential: -13.7 mV at pH 5, -30.8 mV at pH 7) exhibits non-specific binding to chromobodies. The MSN-M²⁺ carriers we developed here are not only useful for His₆-tagged chromobody controlled release, but also promising for universal His-tagged protein delivery to living cells. Several groups have previously shown the successful binding and release of His-tagged proteins on NTA-Ni²⁺-complex-modified silica substrates either for protein delivery or for biosensor detection.^{9,10,19} Similarly, these proteins could be attached to the large internal surface of our MSN-M²⁺ carrier system.

MSN-Ni²⁺, MSN-Zn²⁺ and MSN-Ca²⁺ (primary carrier) were used for the following intracellular chromobody delivery study in MEF-G-LMNA cells. To address possible concerns of cytotoxicity of the dissociated metal ions after uptake of the particles into the cells, we performed MTT assays after incubation of MSN-Ni²⁺, MSN-Zn²⁺ and MSN-Ca²⁺ particles with the MEF cells (wild type) for 24 h. The results (appendix Figure 5-7) indicate that these three metal-immobilized MSNs, as well as un-functionalized MSNs are non-toxic to MEF cells below a concentration of 100 µg ml⁻¹.

Cellular uptake of MSNs

After the study of chromobody loading and release from NTA-M²⁺-complex-modified MSNs, we further investigated the interactions between cells and MSNs. There are numerous studies about the cellular uptake of nanoparticles (e.g. liposomes, polyplexes and silica nanoparticles, etc.).^{16,20-28} These studies reveal that electrostatic surface charge of nanoparticles, functionalization, particle shape and particle size are key factors that can affect the endocytosis mechanisms. For example, positively charged nanoparticles are favored for cellular uptake because the negatively charged cell membrane tends to attract the positively charged particles on its surface; particle sizes below 200 nm are considered the most favorable size for cellular internalization. In addition, the endocytosis behavior for different nanoparticles is also dependent on cell-type.^{29,30} In this study, the MSN size used for intracellular chromobody delivery is about 100 – 200 nm. The endocytosis pathways are mostly clathrin-mediated or caveolin-mediated endocytosis.^{16,27} The confocal images in Figure 5-3a reveal the kinetics of cellular uptake of chromobody loaded-MSNs (MSN-Ca-Cbs) by MEF-G-LMNA cells. MSN-Ca-Cbs were added to the cells in serum free medium at a concentration of 5 $\mu\text{g ml}^{-1}$, and real-time live cell images at the indicated time points were acquired. As the incubation time increased, the number of MSN-Ca-Cbs co-localized with cells also increased. After 2 h of co-incubation with MSN-Ca-Cbs, almost all cells in the imaging frame co-localized with more than two MSN-Ca-Cb spots. High content statistics of cellular uptake of MSN-Ca-Cbs for different time points and concentrations were examined with a high throughput imaging system (Operetta[®], PerkinElmer). Different concentrations of MSN-Ca-Cb (5 $\mu\text{g ml}^{-1}$, 10 $\mu\text{g ml}^{-1}$ and 20 $\mu\text{g ml}^{-1}$) were added to each sample in a 24-well plate. At the indicated time points, cells were washed to remove free MSN-Ca-Cbs, and were then imaged by Operetta immediately. On average 600 cells were imaged and analyzed per sample. The evaluation sequence is shown in the supplementary information (appendix Figure 5-8). The results (Figure 5-3b and 5-3c) from the high content analysis illustrate that cellular uptake of MSN-Ca-Cbs is time and dose dependent. After 10 min of incubation, more than 30 % of the cells have taken up MSN-Ca-Cbs already (cells with more than two MSN-Ca-Cb spots within their cytosols and nuclear region are defined as MSN-uptake cells; each MSN-Ca-Cb spot might contain more than one MSN-Ca-Cb) both for low particle concentration (5 $\mu\text{g ml}^{-1}$) and for high particle concentration (20 $\mu\text{g ml}^{-1}$). After 2 h of incubation with MSN-Ca-Cbs, more than 90 % of the cells have taken up MSN-Ca-Cbs. This

result demonstrates the high cellular uptake efficiency of MSN-Ca-Cbs by MEF-G-LMNA cells.

To further visualize the MSN locations in the cytosol we used super-resolution microscopy (3D SIM). A stable MEF cell line (MEF-mEGFP) that expresses endogenous membrane co-localizing EGFP protein was developed to label the cell boundary. Cy3 labeled MSNs (MSN-Cy3s) at the concentration $10\ \mu\text{g ml}^{-1}$ were incubated with MEF-mEGFP cells on a glass coverslip in culture medium for 2 h. Afterwards, cells were washed to remove free MSNs and were fixed. DAPI counterstaining was performed after cell fixation. The super resolution microscope image (Figure 5-3d, XY view and XZ cross-section view) visually confirms that MSNs were internalized by MEF-mEGFP cells. The image clearly shows that the internalized MSN-Cy3s were equally distributed in the cytosol, and single particles can be seen in the magnified images.

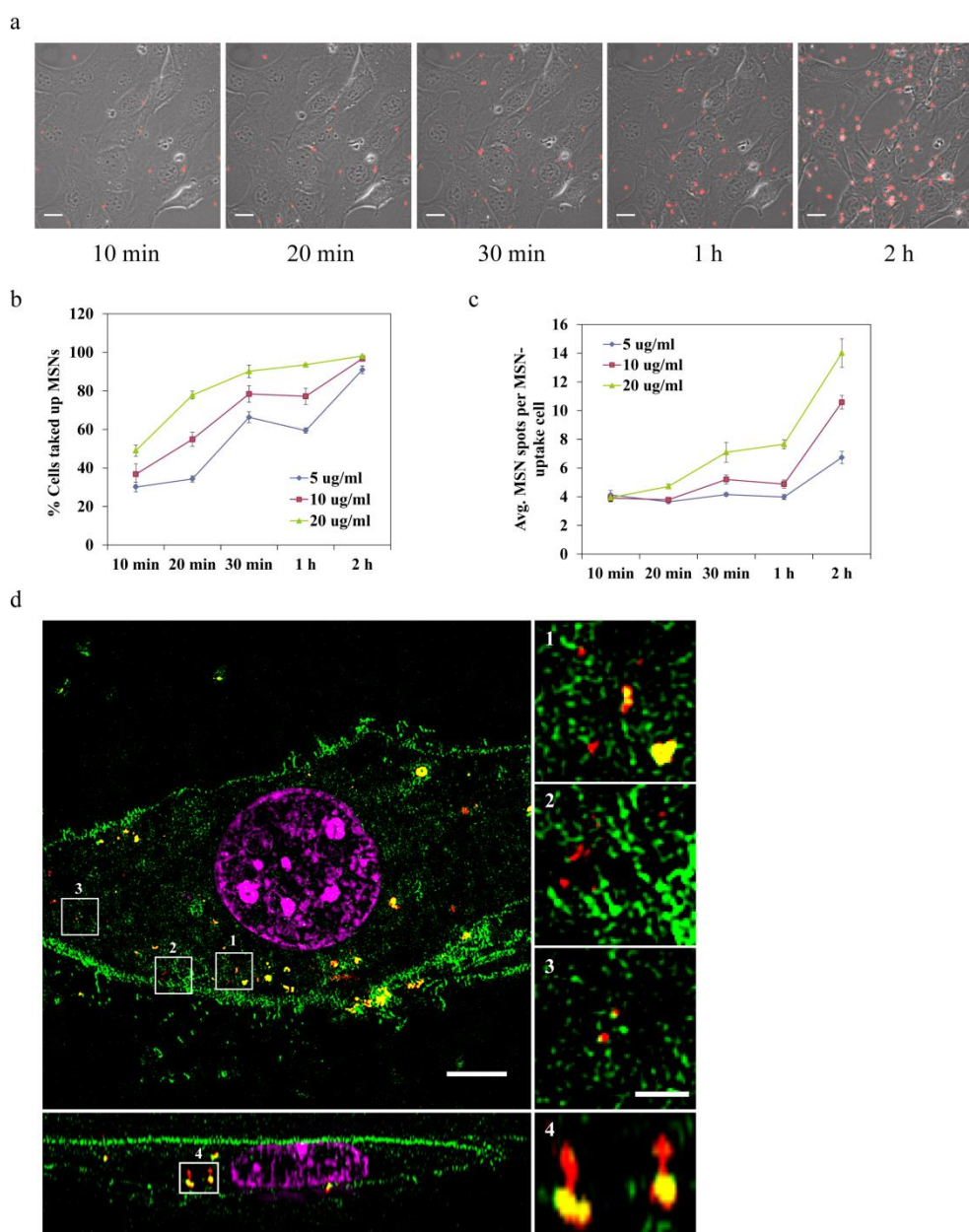


Figure 5-3 Cellular uptake of MSNs. (a) Real-time live cell imaging of the MSN-Ca-Cb uptake process by MEF-G-LMNA cells. Images were taken at the indicated time points after incubation with MSN-Ca-Cb ($5 \mu\text{g ml}^{-1}$) on MEF-G-LMNA cells in a 2-well ibidi cell culture slide. *Scar bar:* $20 \mu\text{m}$. (b), (c) Time-based analyses of cellular uptake of MSN-Ca-Cb using a high-throughput imaging system (Operetta[®], PerkinElmer). Cells were seeded on 24-well plates at the concentration of 3×10^4 cells per well and incubated at 37°C overnight. Cell culture medium was removed and different concentrations of MSN-Ca-Cb particles in serum free live cell imaging medium (LCIM) were then added to each well. After incubation of MSN-Ca-Cb particles with cells for the indicated time intervals, free particles were removed by washing with PBS, and high-throughput live cell imaging was performed. Experiments

were triplicated. An average of 600 cells were imaged in each experiment. Error bars were calculated as s.d. (d) Super-resolution microscopy (3D SIM) image of a cell after MSN internalization. Cy3-labeled MSNs ($10 \mu\text{g ml}^{-1}$) were incubated with MEF-mEGFP cells (3×10^5 cells per well) on a glass coverslip in a 6-well plate for 2 h. Afterwards, free MSNs were removed by washing with PBS. Cells were then fixed with 3.7 % formaldehyde and counterstained with DAPI ($1 \mu\text{g ml}^{-1}$ in PBS). Green: EGFP, red: Cy3 labeled MSNs, magenta: DAPI counterstaining. *Scale bars: 5 μm (main figure and XZ cross-section figure) and 1 μm (magnified figures).*

Intracellular chromobody delivery

In the intracellular chromobody delivery experiment we used MSN- Ca^{2+} as the main chromobody carrier. Above we have shown that the average chromobody loading capacity in MSN- M^{2+} is $70 \mu\text{g}$ per mg MSN (Figure 5-2c). Here we added the MSN-Ca-Cbs to the cell culture slide (μ -Slide 2-well, ibidi) at a concentration of $5 \mu\text{g ml}^{-1}$ (1 ml of culture medium per well), which yields a chromobody concentration for the intracellular delivery of approximately 25 nM. Importantly, compared to the recently published papers of direct protein delivery that use micromolar protein concentrations in each experiment, the amount of cargo we used in this work is 200 times less.^{5,6} MEF-G-LMNA cells were used to detect the release and function of GFP-specific chromobodies. When Atto 647N labeled GFP-specific chromobodies are delivered to and subsequently released from endosomes, they passively diffuse through the nuclear envelope and bind to GFP molecules on the LMNA structure. Therefore, a distinct microscopic co-localization signal from EGFP-LMNA and GFP-specific chromobodies can be observed. Figure 5-4 illustrates the successful delivery of GFP-specific chromobodies to MEF-G-LMNA cells. After 24 h of incubation with MSN-Ca-Cbs, several cells can be observed with chromobody release. In fact, chromobody release can already be seen after 4 h incubation of MSN-Ca-Cbs in some cells, and the chromobody staining remained on the EGFP-LMNA structure until 96 h after incubation (appendix Figure 5-9). We also examined two other carriers: MSN- Ni^{2+} and MSN- Zn^{2+} , and both of them allowed for intracellular chromobody delivery (appendix Figure 5-9). The application of MSNs for intracellular chromobody delivery allows for directly and efficiently transporting chromobodies into living cells. In comparison, incubation of free chromobodies with cells without carriers does not lead to any significant uptake (appendix Figure 5-10).

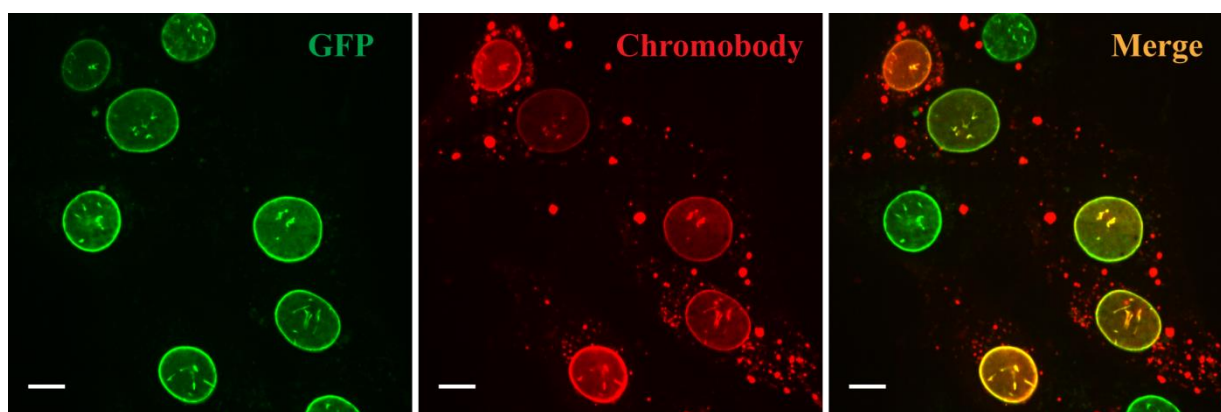


Figure 5-4 Live cell confocal imaging of intracellular chromobody delivery. 24 h post incubation of MSN-Ca-Cbs ($5 \mu\text{g ml}^{-1}$) with MEF-G-LMNA cells. *Scale bar: 10 μm .* Representative images are presented.

To systematically quantify the efficiency of chromobody delivery *via* MSNs, we then used a high-throughput imaging system to image a large quantity of cells and further calculate the chromobody release efficiency (chromobody release efficiency % = chromobody stained cells/GFP-LMNA-positive cells $\times 100$ %). The result (Figure 5-5a, the control group) showed only 1 – 2 % chromobody release efficiency after 24 h post MSN-Ca-Cbs incubation. We attribute the low release efficiency to endosomal trapping of most of the internalized particles, whereas the limited observed endosomal escape of chromobodies might result from the proton sponge effect generated by the His₆-tag on chromobodies.

To enhance endosomal release, we investigated 4 different endosomal escape triggers: fusogenic peptide INF7, acid shock, DMSO and chloroquine.

Fusogenic peptide INF7 is a peptide derivative from influenza virus hemagglutinin HA2 protein. Wagner *et al.* first reported in 1994 that the 23 N-terminal amino acid sequence of HA2 has liposome disruption ability and erythrocyte lysis activity.³¹ The derivative INF7 peptide exhibits more pH specificity with membrane disruption ability and erythrocyte lysis activity than HA2 due to its conformation change in acidic environment. Therefore, this pH-dependent conformation change and membrane-disruptive fusogenic peptide is promising for endosomal escape since the late endosomes feature an acidic environment at $\sim \text{pH } 5$. Here, we conjugated the INF7 peptide to MSNs using a pH-responsive acetal linker³² (appendix Figure 5-11), then co-incubated MSN-INF7s with MSN-Ca-Cbs to MEF-G-LMNA cells for 2 h. However, the result (Figure 5-5a) showed that INF7 has no enhancement for the

chromobody delivery efficiency. The second endosomal release trigger we used here is acid shock, that is, extracellular acidification of cells. The purpose of using acid shock is to generate external stress on cells and to investigate if the cellular stress response is to increase the endosomal leakage. However, the acid shock applied in this experiment had no effect on the chromobody delivery efficiency. Moreover, the acidic buffer incubation leads to 60% cell death (Figure 5-5b). The third endosomal release trigger DMSO has been reported to be capable of enhancing membrane permeability.³³⁻³⁶ A molecular dynamics simulation demonstrated that DMSO molecules can cause fluctuations on the two hydrophilic sides of the lipid bilayer followed by the formation of a water-permeable pore in the lipid bilayer.³⁵ Wang *et al.* used it to enhance the penetration efficiency of the cell-penetration peptide TAT fusion protein.³⁶ In our study a short incubation (5 – 10 min) with 7% DMSO indeed enhances the release of chromobodies from the endosomes. The chromobody release efficiency increased from 1% (control group) to 12% after this short incubation with DMSO (Figure 5-5a). Furthermore, the increased endosomal release of chromobodies can be detected right after the DMSO treatment (data not shown).

The most effective endosomal release trigger studied in this work is chloroquine. Chloroquine is a well-known lysosomotropic agent (and anti-malaria drug) that preferentially accumulates in lysosomes and destabilizes the lysosomal membrane. When chloroquine is used at low concentration, it increases the pH of the acidic endosomes.³⁷ When applied at high concentration ($> 100 \mu\text{M}$), chloroquine can generate a strong proton sponge effect and therefore destabilize the endosomal membrane.^{37,38} Our study shows that a short incubation of high concentration (500 μM) chloroquine facilitates endosomal release. In contrast to the DMSO treatment, the proton-sponge effect for increased endosomal release becomes obvious 24 h after the chloroquine treatment. To sum up the endosomal escape experiments, INF7 and acid shock showed no increase of chromobody release efficiency (same as the control group, 1 – 2%) while cells treated with DMSO or chloroquine showed 12 – 18 fold increase in efficiency. The corresponding live cell images of increased chromobody release efficiency after treatment with DMSO and chloroquine are shown in Figure 5-5d.

Since the introduction of endosomal triggers might induce cytotoxicity, we analyzed cell viability after each endosomal trigger treatment. The cultured cells were imaged before MSN-Ca-Cbs incubation, and the numbers of GFP-LMNA-positive cells were counted. After 2 h incubation of MSN-Ca-Cbs in serum-free medium and following the treatment with

endosomal release triggers, cells were imaged and counted again. The blank group refers to cells incubated in serum-free medium for 2 h without MSN-Ca-Cb treatment and no endosomal trigger treatment. Cell viability was calculated based on: GFP-LMNA-positive cells after drug treatment/GFP-LMNA-positive cells before MSN-Ca-Cb treatment x 100%. The cell viability analysis shown in Figure 5-5b indicates that, compared to the blank group and the control group, the short exposure to 7% DMSO or 500 μ M chloroquine has almost no effect on cell viability. The slight decrease in cell viability of the blank group, control group, DMSO-treated cells and chloroquine-treated cells might result from the serum free medium incubation. Cell proliferation was also studied after endosomal trigger treatment to ensure the drug treatment has no effect on cell proliferation. The result in figure 5-5c indicated that DMSO and chloroquine treated cells proliferate normally in the following days.

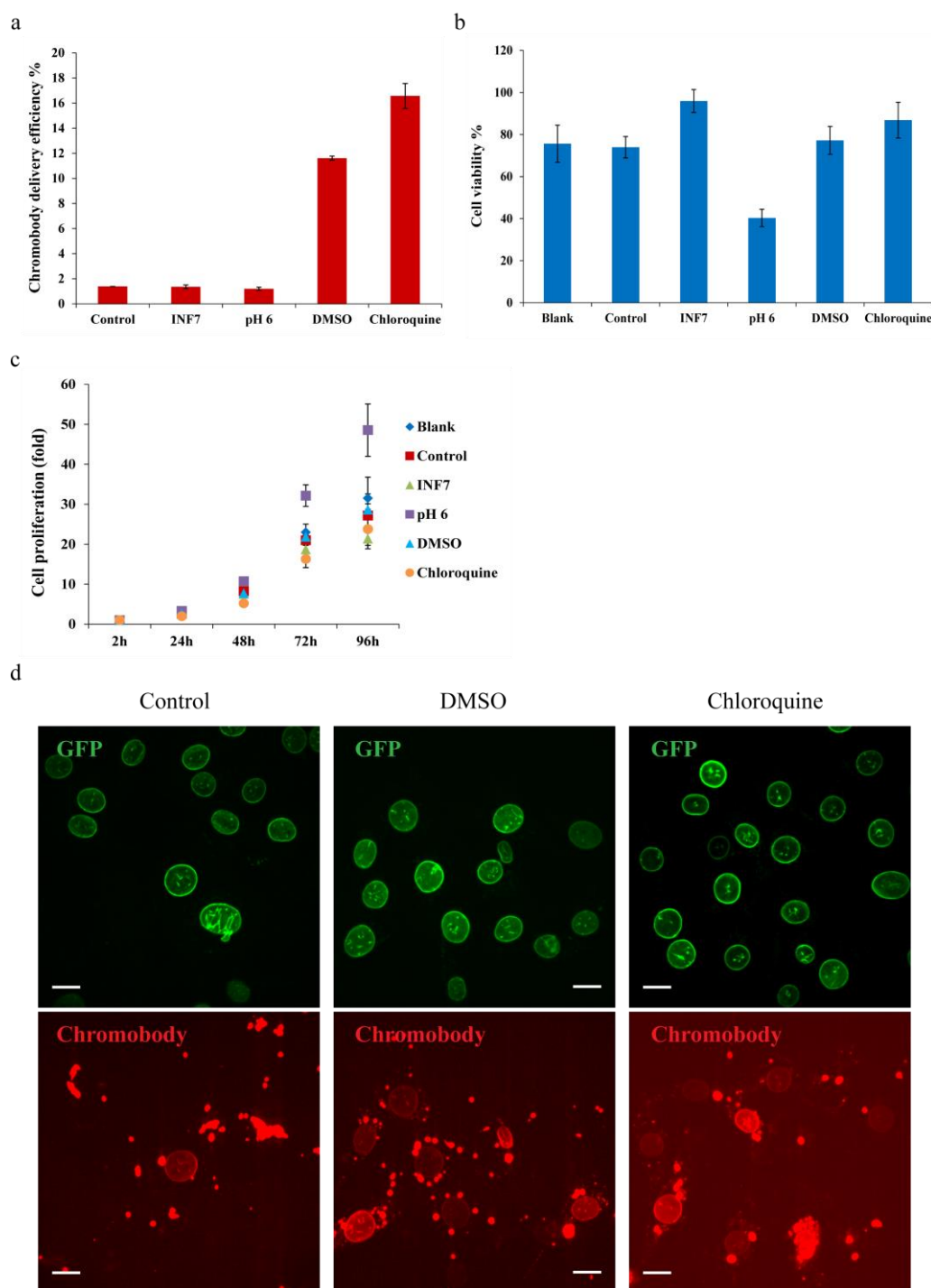


Figure 5-5 Comparison of different endosomal release triggers for chromobody delivery efficiency. High-throughput imaging system (Operetta[®], PerkinElmer) was used for chromobody delivery efficiency (a), cell viability (b) and cell proliferation (c) studies. (a) Chromobody delivery efficiency after treatment with different endosomal release triggers. 24 h after MSN-Ca-Cb incubation and endosomal release trigger treatment, cells were imaged by Operetta. GFP-positive cells were counted by Harmony software, and chromobody-stained cells were counted visually. Chromobody delivery efficiency % =

chromobody-stained cells/GFP-positive cells x 100 %. (b) Cell viabilities after treatment with different endosomal release triggers. Cells were imaged by Operetta before MSN-Ca-Cbs incubation. After 2 h incubation of MSN-Ca-Cbs and short treatment with different endosomal release triggers, cells in the same region of each plate were then imaged with Operetta again. Cell viability % = GFP-positive cells after drug treatment/ GFP-positive cells before drug treatment x 100 %. (c) Cell proliferations after treatment with different endosomal release triggers. The cell number immediately after drug treatment of each sample is defined as 1-fold. Cell numbers were then counted every 24 h by Operetta. (a), (b), (c) Experiments were triplicated. Error bars were calculated as s.d. (d) Live cell confocal images of intracellular chromobody delivery after non-treatment (control), DMSO-, and chloroquine-treated MEF-G-LMNA cells. *Scale bar: 20 μ m.*

5.3 Discussion

In this work, we successfully developed NTA-M²⁺-complex-modified MSNs as carriers for intracellular chromobody delivery. We systematically studied (1) the interactions between His₆-tagged chromobodies and NTA-M²⁺-complex-modified MSNs; (2) cellular uptake of MSNs, and (3) endosomal release triggers for the enhancement of chromobody release efficiency. MSN-Ca²⁺, MSN-Ni²⁺ and MSN-Zn²⁺ carriers all are applicable for successful intracellular chromobody delivery, while DMSO and chloroquine are effective triggers for drastically increased chromobody release efficiency. We could clearly demonstrate the functionality of the delivered chromobodies based on their specific binding to GFP-LMNA. Thus, the mesoporous MSN-M²⁺ carriers can now enable the direct delivery of chromobodies into cells to image and understand biological processes. Moreover, we envision that the novel delivery strategy based upon the MSN-M²⁺ carriers can be generalized toward the cellular delivery of other His-tagged proteins aimed at various biological applications.

5.4 Experimental

Materials

Tetraethyl orthosilicate (TEOS, Aldrich, $\geq 99\%$), (3-mercaptopropyl)triethoxysilane (MPTES, Aldrich, $\geq 80\%$), cetyltrimethylammonium p-toluenesulfonate (CTATos, Sigma), triethanolamine (TEA, Aldrich, 98%), bi-distilled water is obtained from a Millipore system (Milli-Q Academic A10). 6-Maleimidohexanoic acid (Aldrich), N(alpha),N(alpha)-bis(carboxymethyl)-L-lysine hydrate (NTA-lysine, Aldrich), N-(3-dimethylaminopropyl)-N-ethylcarbodiimide (EDC, Alfa-Aesar, 98%), N-hydroxysulfosuccinimide sodium salt (sulfo-NHS, Aldrich), iron (II) chloride tetrahydrate (Sigma Aldrich), cobalt (II) chloride hexahydrate (Aldrich), nickel chloride hexahydrate (Riedel-de Haen), copper chloride dihydrate (LMU, Germany), zinc chloride (Aldrich), calcium chloride dihydrate (LMU, Germany), magnesium chloride (Aldrich), tris(hydroxymethyl)-aminomethane (TRIS, $\geq 99\%$, ROTH), acetic acid (99% - 100%, ROTH), thiazolyl blue tetrazolium bromide (MTT, $\geq 97.5\%$, Sigma), dimethyl sulfoxide molecular biology grade (DMSO, Applichem), 3-Maleimidopropionic acid N-hydroxysuccinimide ester (99%, Sigma Aldrich), 3,9-Bis(3-aminopropyl)-2,4,8,10-tetraoxaspiro[5.5]undecane (AK linker, Tokyo Chemical Industry), formaldehyde solution (37 %, Applichem), SSC buffer 20x (Sigma), Dulbecco's Modified Eagle's Medium (DMEM, Sigma), Dulbecco's Phosphate Buffered Saline (PBS, Sigma), FBS Superior (Biochrom, S0615), Gentamycin solution (SERVA, 50 mg ml⁻¹), trypsin-EDTA solution (Sigma, T3924), Dulbecco's Modified Eagle's Medium – phenol red free (DMEM, Sigma), L-glutamine solution (200 mM, Sigma), HEPES solution (1 M, Sigma).

MSN synthesis and modification

The MSN-SH was synthesized following a modified recipe reported earlier.¹⁴ In brief, TEA (47 mg, 0.32 mmol), CTATos (0.263 g, 0.58 mmol) and H₂O (13.7 g, 0.77 mmol) were mixed in a 100 ml glass flask and vigorously stirred (1250 rpm) at 80 °C until the solution became homogeneous. A mixture of TEOS (1.8 g, 8.64 mmol) and MPTES (0.23 g, 0.96 mmol) was then added and the solution was continuously stirred (1250 rpm) at 80 °C for 2 h. Afterwards the reaction solution was cooled down to room temperature under ambient conditions, and the particles were collected by centrifugation (43146 x g, 20 min). The organic template extraction was carried out right after the particle collection. The particle pellet was re-suspended in an ethanolic solution (100 mL) containing 2 g of ammonium

nitrate, and the solution was heated to 90 °C under reflux for 1 h. The second template extraction step was subsequently performed by heating the particles under reflux at 90 °C in an ethanolic solution (100 mL) containing 10 mL of hydrochloric acid (37 %). The MSN-SH was collected by centrifugation (43146 x g, 20 min) and was washed with water and EtOH after each extraction step.

The template-extracted MSN-SH was then modified to yield NTA-functionalized MSN (MSN-NTA). 60 mg of MSN-SH and 30 mg (0.142 mmol) of 6-maleimidohexanoic acid were mixed in 12 ml of EtOH. The mixture was stirred at room temperature overnight. The resulting MSN-COOH particles were collected by centrifugation (43146 x g, 20 min), washed twice with EtOH and re-dispersed in 12 ml of EtOH. The amount of 40 mg of MSN-COOH in 8 ml of EtOH was then mixed with EDC (15 µl, 67.5 µmol) at room temperature for 10 min. Sulfo-NHS (14.6 mg, 67.5 µmol) and NTA-lysine (17.5 mg, 67.5 µmol) were mixed in 1 ml of H₂O and afterwards added to the MSN solution. The mixture was stirred at room temperature for 2 h, and the resulting MSN-NTA particles were washed twice with H₂O and EtOH to remove the residual chemicals. 20 mg each of MSN-SH, MSN-COOH and MSN-NTA were dried for further characterization.

Characterization of MSN

Transmission electron microscopy (TEM) was performed at 200 kV on a Jeol JEM-2010 instrument with a CCD detection system. A drop of diluted MSN suspension was dried on a carbon-coated copper grid at room temperature for several hours before TEM observation. Nitrogen sorption measurements were performed on a Quantachrome Instrument NOVA 4000e at 77 K. Samples (about 15 mg) were degassed at 120 °C under vacuum (10 mTorr) for 12 h before measurement. The pore volume and pore size distribution were calculated based on non-local NLDT procedures provided by Quantachrome, using the adsorption branch of N₂ on silica. The hydrodynamic sizes of MSNs were measured by dynamic light scattering (DLS) analysis using a Malvern Zetasizer-Nano instrument equipped with a 4 mW He-Ne laser (633 nm). Infrared spectra of different organic functional groups on MSNs were recorded on a Thermo Scientific Nicolet iN10 IR-microscope in reflection-absorption mode with a liquid-N₂ cooled MCT-A detector.

Generation of GFP-specific chromobody

GFP-specific nanobody³⁹ expression was performed in *E. coli* (JM109). Expression was induced with 0.5 mM of isopropyl beta-D-1-thiogalactopyranoside (IPTG, ROTH), and cells were incubated at 37 °C for 24 h. Cells were lysed in the presence of Lysozyme (100 µg ml⁻¹; Serva, Germany), DNase (25 µg ml⁻¹; Applichem, Germany) and phenylmethanesulfonyl fluoride (2 mM, PMSF, Sigma) followed by sonication (Branson® Sonifier; 16 x 8 sec, 20% Amplitude) and debris centrifugation at 20000 x g for 30 min. Protein purification was performed with an Äkta FPLC system (GE Healthcare, USA) using a 5 mL His-Trap column (GE Healthcare, USA); peak fractions were concentrated to 2 ml using Amicon filter columns (cut-off 10 kDa, Merck Millipore, Germany) followed by size exclusion chromatography using a Superdex 75 column (GE Healthcare, USA). Peak fractions were pooled and protein aliquots were shock-frozen and stored at -80 °C. 1 mg purified nanobody protein was then labeled with ATTO 647N (ATTO-TEC, Germany) with a theoretical DOL (degree of labeling) of 3, according to the manufacturers' instructions. Unbound dye was removed by gel filtration in PD10 columns (GE Healthcare, USA). The final ATTO 647N labelled GFP-specific chromobody was obtained and preserved in PBS in the concentration of 1 mg ml⁻¹.

Chromobody loading and release *in vitro* test

MSN-NTA (200 µg per vial, 6 vials) was treated with 50 mM solutions of different metal ions (0.5 mL each) (FeCl₂, CoCl₂, NiCl₂, CuCl₂, ZnCl₂ or CaCl₂) at room temperature for 6 h. After metal ion immobilization, the excess un-bound metal ions were washed out with 3 ml of H₂O. 200 µg of each NTA-M²⁺-complex-modified MSNs (MSN-M²⁺) was then suspended in 150 µl of chromobody loading buffer where the concentration of chromobody was 100 µg ml⁻¹ in 0.05 M Tris-acetate buffer (pH 8.0), and incubated at 4 °C for 2 h. The un-bound chromobodies were then removed by centrifugation (4218 x g, 3 min) and the chromobody-loaded MSNs (MSN-M-Cbs) were washed 3 times (1 ml per wash) with 0.05 M Tris-acetate buffer (pH 8.0). Centrifugation (4218 x g, 3 min) was applied in every wash step to separate the supernatant and particles. Before the buffer release experiments, each type of MSN-M-Cbs was separated into two vials holding equal amounts (100 µg MSN per vial). Subsequently, 150 µl of PBS having different pH values (pH 7 and pH 5) were added to suspend the MSN-M-Cbs (100 µg). The *in vitro* chromobody release experiments were performed at 37 °C for 16 h. The solutions with released chromobody were centrifuged

(4218 x g, 3 min) and then the supernatants were collected. The final chromobody release supernatants were quantified *via* their fluorescence intensity at 669 nm (excitation 644 nm) in a 96-well plate (Greiner Bio-One, Germany) by a microplate reader (Infinite® M1000 PRO, TECAN, Switzerland). The quantification was based on a calibration curve with a series of diluted pure chromobody solutions.

Cell culture and stable cell lines

MEF cells were cultured in DMEM medium supplemented with 10 % FBS and 50 µg ml⁻¹ gentamycin (cell culture medium) under 5 % CO₂ at 37 °C.

The plasmid construction for stable cell line generation was performed as follows. The plasmid pmEGFP-N1 was constructed by cloning of membrane EGFP⁴⁰ into pEGFP-N1 vector (Clontech) with AgeI and BsrGI endonucleases (Thermo Fisher Scientific) to substitute the EGFP with mEGFP. To prepare the pCAG-eG-LMNA-IB plasmid, the mouse Lmna/C gene was amplified with primers (forward primer: 5'-GGG CGA TCG CAT GGA GAC CCC GCT ACA and reverse primer: 5'-AGT CGC GGC CGC TTT ACA TGA TGC TGC) by PCR and cloned into plasmid under a CAG promoter with AsisI and NotI restriction sites.

To make the GFP-LMNA expression cell line, pCAG-eG-LMNA-IB was transfected into MEF cells with Lipofectamine 2000 reagent (Invitrogen), and positive cells (MEF-G-LMNA) were selected with 6 µg ml⁻¹ blasticidin (Sigma) for two weeks then sorted with a fluorescence-activated cell sorting (FACS) Aria II (Becton Dickinson) instrument. For the mEGFP expression cell line, pmEGFP-N1 was transfected into MEFs, and mEGFP stable expression cells (MEF-mEGFP) were purified by FACS two weeks after transfection.

Sample preparation for cellular uptake experiments of MSNs

Live cell imaging medium (LCIM) containing DMEM – phenol red free, FBS (10%), L-glutamine (200 µM), HEPES (20 mM) and gentamycin (50 µg ml⁻¹) was used for cell incubation in all live cell microscopy experiments.

For real-time tracing of cellular uptake of MSN-Ca-Cbs, MEF-G-LMNA cells were seeded on a 2-well µ-Slide (ibidi, Germany) in 50% confluence (the proportion of the culture slide surface which is covered by cells) for overnight incubation. In each culture well, 1 ml of

culture medium or LCIM was used for either cell culture or microscopy. $5\ \mu\text{g ml}^{-1}$ of MSN-Ca-Cb in serum-free LCIM was added to cells and images were acquired at 10 min, 20 min, 30 min, 1 h and 2 h after the addition of MSN-Ca-Cbs.

For the high content live cell imaging, MEF-G-LMNA cells were plated on 24-well plates (Corning, USA) in 70 % confluence. The working volume for all kinds of solution (cell culture medium, PBS, etc.) in the 24-well plate is 0.5 ml per well. MSN-Ca-Cb with different concentrations ($5\ \mu\text{g ml}^{-1}$, $10\ \mu\text{g ml}^{-1}$ and $20\ \mu\text{g ml}^{-1}$) in serum-free cell culture medium were added to cells. At indicated time points (10 min, 20 min, 30 min, 1 h and 2 h), cells were washed with PBS three times to remove residual MSN-Ca-Cbs in the medium. CellMaskTM orange (Thermo Fisher Scientific) ($5\ \text{mg ml}^{-1}$ in DMSO) was diluted 1000x in LCIM and incubated with cells at 37 °C for 10 min for plasma membrane staining. After the plasma membrane staining, the CellMask solution was removed. LCIM was then added to the sample and high content imaging was performed immediately.

For the super-resolution microscopy (3D SIM), MEF-mEGFP cells were cultured on an 18 x 18 mm coverslip in a 6-well plate (Corning, USA) (3×10^5 cells per well). $10\ \mu\text{g ml}^{-1}$ of Cy3 (Lumiprobe, Germany) -labelled MSNs (MSN-Cy3) in 2 ml of serum free cell culture medium were added to cells and incubated for 2 h. Cells were then washed with PBS three times to remove residual MSNs, followed by fixation using 3.7% of formaldehyde in PBS (10 min in room temperature). DAPI ($1\ \mu\text{g ml}^{-1}$ in PBS) counterstaining (10 min in room temperature) was performed after cell fixation. The sample was then mounted in Vectashield antifade mounting medium (Vector Laboratories, USA) to a glass slide.

Intracellular chromobody delivery - sample preparation

MEF-G-LMNA cells in cell culture medium were seeded on either a 2-well μ -Slide (1 ml per well) or a 24-well plate (0.5 ml per well) in 50% confluence one day before the intracellular chromobody delivery experiment. The applied culture medium or LCIM volume in each well (1 ml per well for 2-well μ -Slide; 0.5 ml per well for 24-well plate) is the same for all following intracellular delivery experiment. MSN-Ca-Cbs, MSN-Ni-Cbs and MSN-Zn-Cbs were prepared in serum-free cell culture media at a concentration of $5\ \mu\text{g ml}^{-1}$, respectively. The cell culture medium was removed from the pre-seeded cells followed by the addition of pre-mixed MSN-M-Cb containing medium. The MSN-M-Cbs were incubated with cells at

37 °C for 2 h. Afterwards, the residual particles in the medium were washed out by PBS, and the cells were incubated in LCIM for the following live cell imaging processes.

Experiments with samples treated with endosomal triggers were carried out according to two different approaches. MSN-Ca²⁺ was the main carrier used in the following experiments. For the INF7 treatment, INF7 peptide (Biosyntan GmbH) was conjugated on MSNs with pH-responsive acetal linkers as indicated in Figure S5. In brief, 10 mg (37 µmol) of 3-(Maleimido)propionic acid N-hydroxy succinimide (dissolved in 100 µl of DMSO) and 6 mg (22 µmol) of AK linker (dissolved in 1 ml of 1x SSC buffer, pH 7.4) were mixed at room temperature and stirred for 1 h. 5 mg of MSN-SH in stock solution (20 mg ml⁻¹ in EtOH) was collected by centrifugation (16837 x g, 5 min) and re-suspended in previous solution. The mixture was stirred at room temperature overnight. The resulting MSN-AK-linker particles were collected by centrifugation (16837 x g, 5 min) and washed by H₂O (10 ml per wash, 3 times wash). INF7 peptide consisting cysteine on its C-terminus was conjugated to 1 mg of MSN-AK-linker particle with a content of 10 INF7 molecules per MSN in 1 ml of DMSO. The mixture was stirred at room temperature for 1 h and the final MSN-INF7 particles were washed with 1 ml of DMSO two times. MSN-INF7s (1 µg ml⁻¹) and MSN-Ca-Cbs (5 µg ml⁻¹) were co-incubated with MEF-G-LMNA cells in serum-free cell culture medium for 2 h. The residual particles in the incubation medium were afterwards washed out by PBS (1 ml per well). The MSN-INF7 and MSN-Ca-Cb treated cells were then incubated in LCIM for live cell imaging. For the acid shock treatment, DMSO and chloroquine release trigger tests, PBS (pH 6), 7% DMSO in LCIM and 500 µM chloroquine in LCIM were introduced to MSN-Ca-Cb-treated cells and incubated at room temperature for 5 – 10 min. The release trigger solutions were then removed from the cells, and cells were then incubated in LCIM for live cell imaging.

Optical microscopy

Spinning Disc

MSN-M-Cb-treated cells plated on 2-well µ-Slide were selected and imaged in LCIM. 3D stacks were acquired with an UltraVIEW Vox spinning disc confocal system (PerkinElmer, UK) in a closed live cell microscopy chamber (ACU control, Olympus, Japan) heated to 37 °C, with 5% CO₂ and 60% humidified atmosphere, mounted on a Nikon Ti microscope (Nikon, Japan). Image acquisition was performed using either 63x/1.4 NA or 40x/1.3 NA

Plan-Apochromat oil immersion objective lenses. Images were obtained with a cooled 14-bit EMCCD camera (C9100-50, CamLink) with a frame size of 1024 x 1024 pixels. GFP and fluorophores were excited with 488 nm (10% power density), 561 nm (5% power density) or 647 nm (30% power density) solid-state diode laser lines.

High-throughput microscopy and analysis

High-throughput images of living cells on a 24-well plate (3×10^4 cells per well) were acquired automatically with an Operetta[®] High Content Imaging System (PerkinElmer, UK). Imaging was performed using a 40× air objective lens. GFP, CellMask and chromobody-ATTO 647N were excited and the emissions were recorded using standard filters. The exposure time was controlled at 200 – 400 ms to avoid pixel saturation, and 50 different fields were imaged in each well. In the cellular uptake experiment, on average 600 cells were imaged. The images were then analyzed by the Harmony[®] analysis software (PerkinElmer) with a sequence as described in Figure S3. In the endosomal release trigger, cell viability and cell proliferation analyses, MEF-G-LMNA cells before any treatment were first imaged and counted. After addition of MSNs and the following endosomal release triggers treatment, cells were imaged and counted again. The definition of cell viability % is: GFP-LMNA-positive cells after endosomal release trigger treatment/GFP-LMNA-positive cells before any treatment $\times 100\%$. The blank group refers to the cells incubated in serum-free DMEM culture medium for 2 h without MSN and endosomal release trigger treatment. Control group refers to the cells incubated with MSN-Ca-Cbs for 2 h, but no endosomal release trigger treatment afterwards. Chromobody release efficiency was recorded 24 h after MSN-Ca-Cbs introduction. Cells exhibiting a chromobody release signal were counted visually. The chromobody release efficiency is defined as: chromobody-LMNA-positive cells/GFP-LMNA-positive cells $\times 100\%$. Cells with different treatments were imaged and counted every 24 h for the cell proliferation calculation. 400 to 10000 cells were imaged in the endosomal release trigger, cell viability and cell proliferation tests depending on the recording time point.

Super-resolution microscopy (3D-SIM)

Super-resolution microscopy (3D-SIM) was performed with a Delta Vision OMX v3 (Applied Precision, GE Healthcare) instrument equipped with 405 nm, 488 nm and 593 nm laser diodes, a 100×/1.4 NA Plan-Apochromat oil immersion objective lens (Olympus) and Cascade II:512 EMCCD cameras (Photometrics). The image stacks were acquired with a z-

step of 125 nm and with 15 images per plane (five phases, three angles). The raw data were computationally reconstructed by using the SoftWorx 5.1.0 software.

MTT assay

MEF cells (wild type) were first seeded on 96-well microplates with the concentration of 5×10^3 cells per well in cell culture medium (100 μ l per well), and incubated at 37 °C for 16 h. MSNs (un-MSNs, MSN-Ni²⁺, MSN-Zn²⁺, MSN-Ca²⁺) (2 mg from stock solution) in EtOH were centrifuged down (16873 x g, 5 min), and re-suspended in cell culture medium at the concentration of 1 mg ml⁻¹. The MSN solutions were then series diluted to the desired particle concentrations. After removal of the culture medium, 100 μ l of MSN solution with different concentrations was added to each well. Also, 100 μ l of cell culture medium was added to cells to serve as control group. The wells with 100 μ l of cell culture medium but without cells were referred to as blank groups. MSN solutions and cells were then co-incubated at 37 °C overnight. Afterwards, the MSN-treated cells were washed with PBS buffer three times to remove the residual particles. MTT was diluted in cell culture medium at the concentration of 0.5 mg ml⁻¹ and then added to the cells (100 μ l per well). After incubating the MTT solution and cells for 4 h, purple crystals metabolized by healthy cells were observed. Subsequently, 100 μ l of pure DMSO was added to each well and the samples were incubated at 37 °C for 1 h until the purple crystals were dissolved. The absorbance at 570 nm and the reference absorbance at 655 nm were measured on each sample using a Microplate reader (Infinite® M1000 PRO, TECAN).

5.5 Appendix

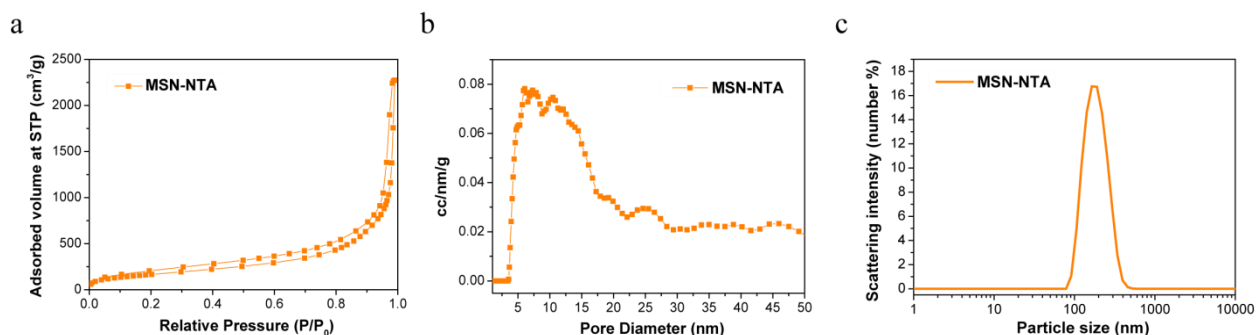


Figure 5-6 Characterization of NTA-conjugated MSNs (MSN-NTA). (a) Nitrogen sorption isotherm, (b) pore size distribution and (c) DLS analysis (particles suspended in EtOH) indicated that MSN-NTA preserved the large-pore mesoporosity and colloidal stability after surface modification.

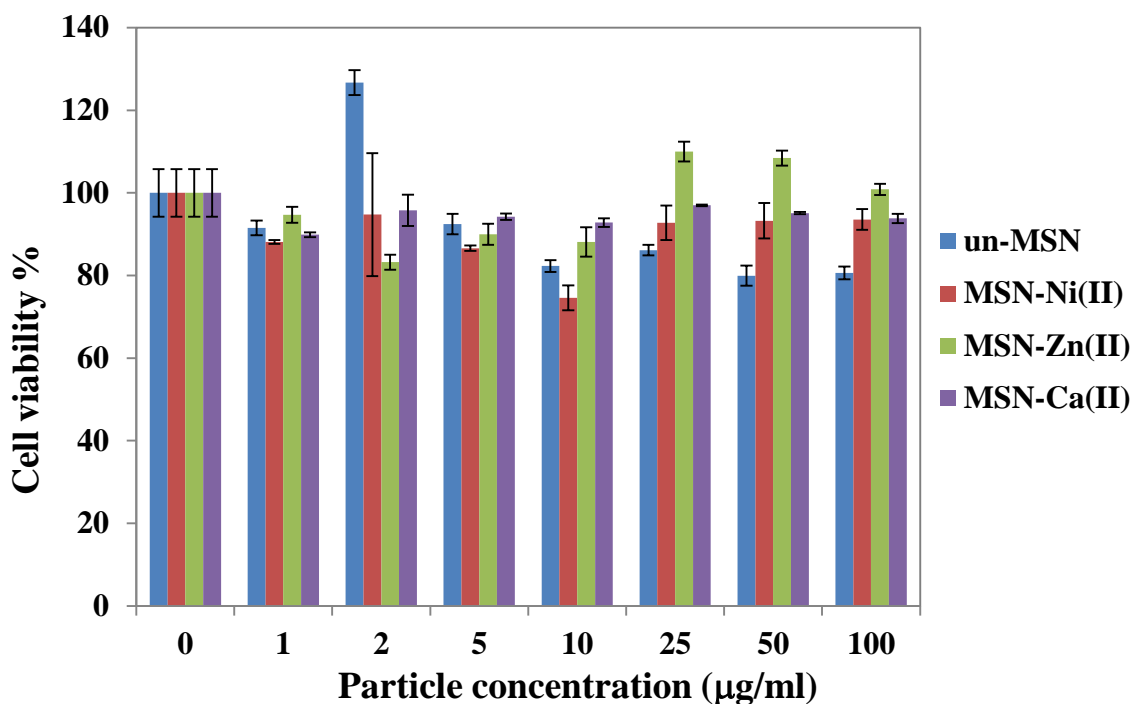


Figure 5-7 Cytotoxicity tests (MTT assay) of different metal-treated MSN-NTA samples (MSN-Ni²⁺, MSN-Zn²⁺ and MSN-Ca²⁺) and un-functionalized MSN (un-MSN) on MEF cells (wild type). All the particle types show no significant cytotoxicity below the particle concentration of 100 µg ml⁻¹.

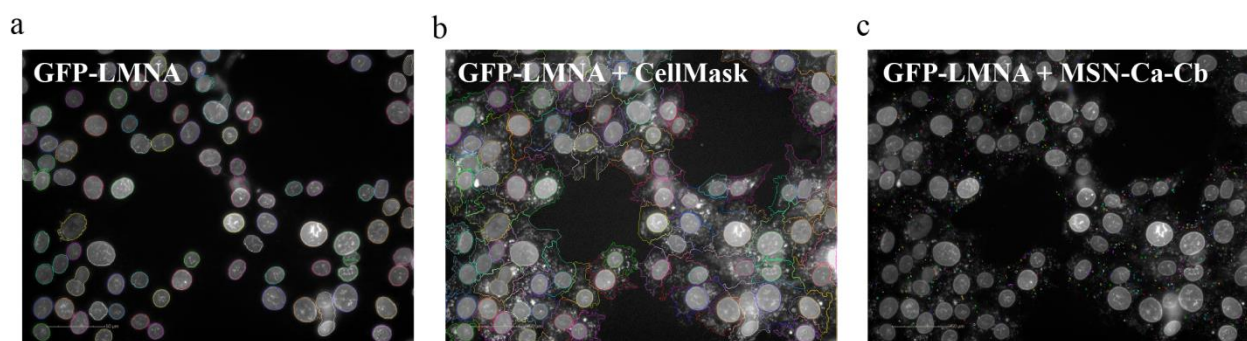


Figure 5-8 High-throughput imaging evaluation of cellular uptake of MSN-Ca-Cbs.

MEF-G-LMNA living cells were stained with CellMask orange and imaged at indicated time points after the addition of MSN-Ca-Cbs. Fluorescence from GFP, CellMask orange, and ATTO 647N (labeled on chromobodies) were recorded separately with Operetta high content image analysis system using standard filter for 488 nm, 546 nm and 647 nm emission. Images were analyzed with Harmony[®] analysis software as the following sequence. (a) The nuclear region is segmented from the background according to GFP-LMNA signal where the GFP-LMNA signal is shown in grey and the circular color lines stand for the segmentation results. Most of the recognized nuclear region fit the GFP-LMNA signal, which indicates a correct segmentation. (b) The cytoplasm region was recognized *via* CellMask signal segmentation. The cytoplasm region is obtained by subtraction of nuclear region obtained from step (a). The border of the segmented cell region was shown as closed color lines around the nuclear region. (c) Recognition of MSN-Ca-Cbs taken up by the cells. Internalized MSN-Ca-Cbs were visualized as spots within the cytoplasm region, and the spots recognition was presented as color dots in the image. The segmented results (nuclei, cytoplasm and MSN-Ca-Cb spots) were used to define populations. Population 1: Cell = GFP-LMNA nucleus plus its surrounding cytoplasm region. Population 2: MSN-uptake cell = cell with more than two MSN-Ca-Cb spots in its cytoplasm and nucleus region. The evaluation results were based on the calculation: (i) % cell take up MSN-Ca-Cbs = MSN-uptake cells/total cells; (ii) average MSN-Ca-Cb spots per MSN-uptake cell = total spots number in all MSN-uptake cells/MSN-uptake cells.

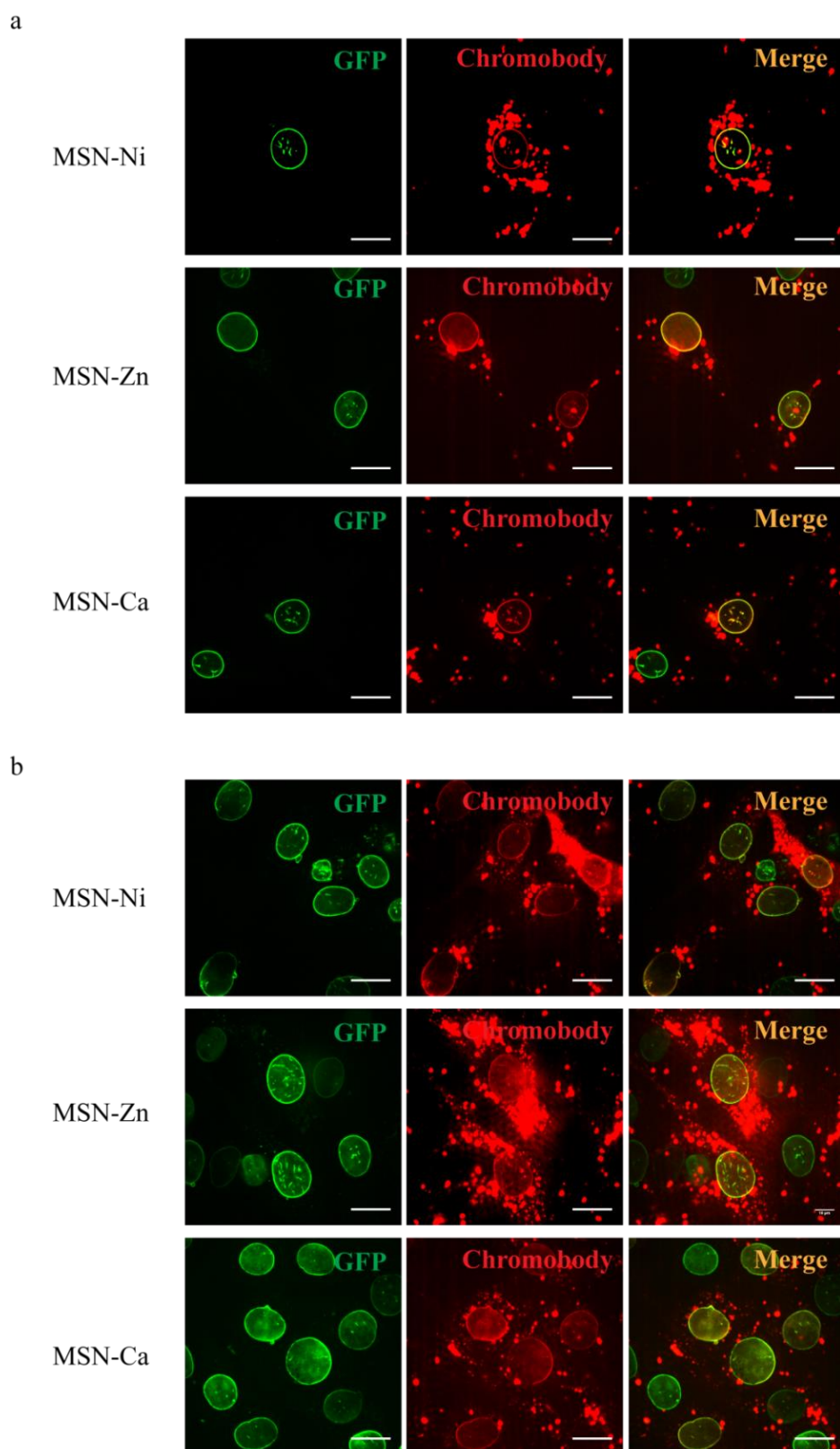


Figure 5-9 Intracellular delivery of chromobodies via different metal-treated MSNs. (a) 4 h after MSN-Ni-Cb/MSN-Zn-Cb/MSN-Ca-Cb incubation. (b) 96 h after MSN-Ni-Cb/MSN-Zn-Cb/MSN-Ca-Cb incubation.

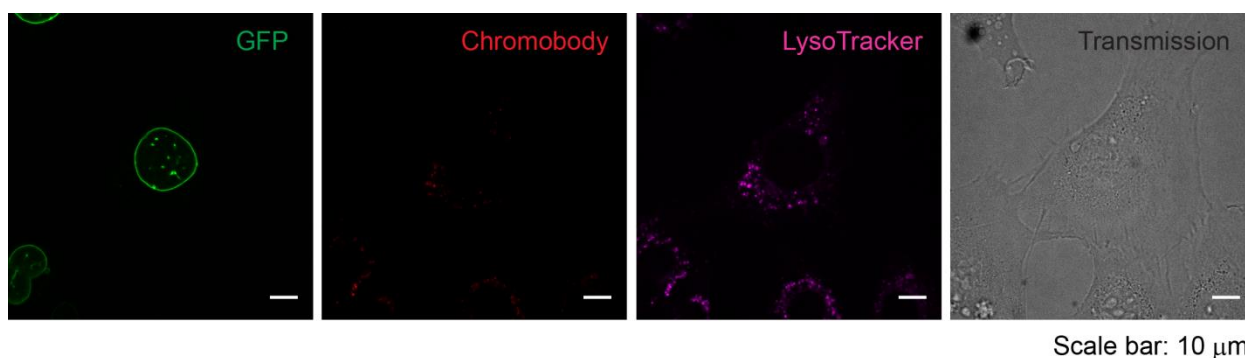


Figure 5-10 Delivery of free chromobodies into MEF-G-LMNA cell. 25 nM free chromobodies was incubated with MEF-G-LMNA. 2 h after incubation, the residual free chromobodies in the medium were washed out by PBS, and the cells were incubated in Live Cell Imaging Medium for the following live cell imaging process. LysoTracker was used for lysosomes tracking during the imaging process.

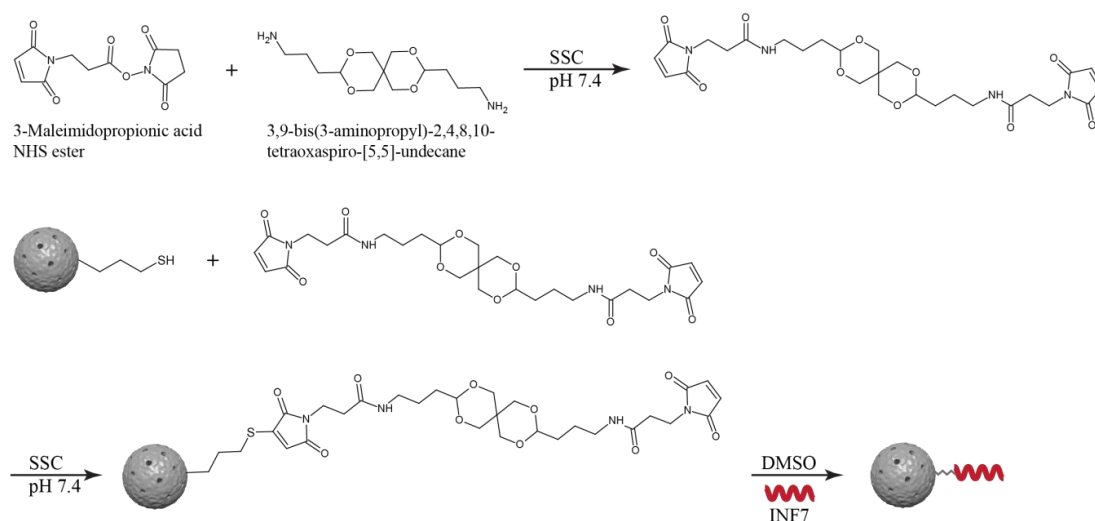


Figure 5-11 Conjugation of INF7 peptide to MSNs via pH-responsive acetal linker. MSN-SH was conjugated with pH-responsive acetal linker (3,9-bis(3-aminopropyl)-2,4,8,10-tetraoxaspiro-[5,5]-undecane) (AK linker) via the maleimide-NHS heterobifunctional crosslinker (3-Maleimidopropionic acid NHS ester) yielding MSN-AK-linker. INF7 peptide consisting of cysteine on its C-terminus was covalently attached to MSN-AK-linker through the maleimide-thiol reaction.

Appendix 5-12

The calculation of chromobody loading capacity in MSNs

- The radius of a MSN= 50 *nm*
- Particle volume (sphere) = $\frac{4}{3}\pi r^3 = 5.236 \times 10^5 \text{ nm}^3 = 5.236 \times 10^{-16} \text{ cm}^3$
- Pore volume of MSNs (measured by N₂ sorption): 2.3 *cm*³/*g*
- Pure silica density: 2.648 *g/cm*³
- 1 g silica has: $\frac{1\text{g}}{2.648\frac{\text{g}}{\text{cm}^3}} = 0.38 \text{ cm}^3$
- 1 g MSN has: $0.38 \text{ cm}^3 + 2.3 \text{ cm}^3 = 2.68 \text{ cm}^3$
- MSN density assumption: $\frac{1\text{g}}{2.68 \text{ cm}^3} = 0.37 \text{ g/cm}^3$
- Single particle weight = $5.236 \times 10^{-16} \text{ cm}^3 \times 0.37 \text{ g/cm}^3 = 1.94 \times 10^{-16} \text{ g}$
- **1 mg MSN has** $\frac{10^{-3}\text{g}}{1.94 \times 10^{-16} \text{ g}} = 5 \times 10^{12}$ **particles**
- Molecular weight of chromobody: 14000 *g/mol*
- **Chromobody loading capacity: 70 μg chromobody/mg MSN**
- **70 μg chromobody** = $\frac{70 \times 10^{-6} \text{ g}}{14000\frac{\text{g}}{\text{mol}}} = 5 \times 10^{-9} \text{ mol}$
 $= 5 \times 10^{-9} \text{ mol} \times 6.02 \times 10^{23} \frac{\text{molecules}}{\text{mol}} = 3 \times 10^{15}$ **chromobody molecules**
- **Chromobody loading capacity**
 $= \frac{3 \times 10^{15} \text{ chromobody molecules}}{5 \times 10^{12} \text{ nanoparticles}} = \frac{600 \text{ chromobody molecules}}{\text{MSN}}$

Table 5-1

Sample	Element	mg ^[1]	mmol ^[1]	Molar ratio
MSN-Ca ²⁺	Si	563.3 ± 91.3	20.1	1
	S	10.07 ± 0.34	0.31	0.016
	Ca	0.29 ± 0.09	0.007	0.0004
MSN-Ca-Cb	Si	476.8 ± 9.97	17.0	1
	S	9.11 ± 1.15	0.28	0.017
	Ca	0.17 ± 0.03	0.004	0.0003
MSN-Ni ²⁺	Si	532.0 ± 47.73	19.0	1
	S	9.8 ± 0.32	0.31	0.016
	Ni	0.44 ± 0.01	0.007	0.0004
MSN-Zn ²⁺	Si	507.8 ± 4.45	18.1	1
	S	10.12 ± 0.55	0.32	0.017
	Zn	1.49 ± 0.03	0.023	0.0013

Notes: [1] The element amount is relative to 1 g of the measured sample.

[2] Triplicate experiments were performed in each sample.

Table 5-1. Elemental analysis of MSN-M²⁺ and MSN-M-Cb samples *via* ICP-OES approach.

5.6 References

- 1 Helma, J., Cardoso, M. C., Muyldermans, S. & Leonhardt, H. Nanobodies and recombinant binders in cell biology. *J. Cell Biol.* **209**, 633-644 (2015).
- 2 Hamers-Casterman, C. *et al.* Naturally occurring antibodies devoid of light chains. *Nature* **363**, 446-448 (1993).
- 3 Rothbauer, U. *et al.* Targeting and tracing antigens in live cells with fluorescent nanobodies. *Nat. Methods* **3**, 887-889 (2006).
- 4 Helma, J. *et al.* Direct and dynamic detection of HIV-1 in living cells. *PLoS One* **7**, e50026 (2012).
- 5 Erazo-Oliveras, A. *et al.* Protein delivery into live cells by incubation with an endosomolytic agent. *Nat. Methods* **11**, 861-867 (2014).
- 6 D'Astolfo, D. S. *et al.* Efficient intracellular delivery of native proteins. *Cell* **161**, 674-690 (2015).
- 7 Marschall, A. L. J., Frenzel, A., Schirrmann, T., Schüngel, M. & Dubel, S. Targeting antibodies to the cytoplasm. *mAbs* **3**, 3-16 (2014).
- 8 van Rijt, S. H. *et al.* Protease-mediated release of chemotherapeutics from mesoporous silica nanoparticles to ex vivo human and mouse lung tumors. *ACS Nano* **9**, 2377-2389 (2015).
- 9 Chen, Y. P. *et al.* A new strategy for intracellular delivery of enzyme using mesoporous silica nanoparticles: superoxide dismutase. *J. Am. Chem. Soc.* **135**, 1516-1523 (2013).
- 10 Han, D. H. *et al.* Direct cellular delivery of human proteasomes to delay tau aggregation. *Nat. Commun.* **5**, 5633 (2014).
- 11 Meng, H. *et al.* Codelivery of an optimal drug/siRNA combination using mesoporous silica nanoparticles to overcome drug resistance in breast cancer in vitro and in vivo. *ACS Nano* **7**, 994-1005 (2013).
- 12 Xia, T. *et al.* Polyethyleneimine coating enhances the cellular uptake of mesoporous silica nanoparticles and allows safe delivery of siRNA and DNA constructs. *ACS Nano* **3**, 3273-3286 (2009).
- 13 Slowing, II, Vivero-Escoto, J. L., Wu, C. W. & Lin, V. S. Mesoporous silica nanoparticles as controlled release drug delivery and gene transfection carriers. *Adv. Drug Del. Rev.* **60**, 1278-1288 (2008).
- 14 Zhang, K. *et al.* Facile large-scale synthesis of monodisperse mesoporous silica nanospheres with tunable pore structure. *J. Am. Chem. Soc.* **135**, 2427-2430 (2013).

- 15 Schmidthals, K., Helma, J., Zolghadr, K., Rothbauer, U. & Leonhardt, H. Novel antibody derivatives for proteome and high-content analysis. *Anal. Bioanal. Chem.* **397**, 3203-3208 (2010).
- 16 Oh, N. & Park, J. H. Endocytosis and exocytosis of nanoparticles in mammalian cells. *Int J Nanomedicine* **9 Suppl 1**, 51-63 (2014).
- 17 Sundberg, R. J. & Martin, R. B. Interactions of histidine and other imidazole derivatives with transition metal ions in chemical and biological systems. *Chem. Rev.* **74**, 471-517 (1974).
- 18 Anderegg, G. Critical survey of stability constants of NTA complexes. *Pure Appl. Chem.* **54** (1982).
- 19 Liu, Y. C. *et al.* Specific and reversible immobilization of histidine-tagged proteins on functionalized silicon nanowires. *Nanotechnology* **21**, 245105 (2010).
- 20 Düzgüneş, N. & Nir, S. Mechanisms and kinetics of liposome–cell interactions. *Adv. Drug Del. Rev.* **40**, 3-18 (1999).
- 21 van der Aa, M. A. *et al.* Cellular uptake of cationic polymer-DNA complexes via caveolae plays a pivotal role in gene transfection in COS-7 cells. *Pharm. Res.* **24**, 1590-1598 (2007).
- 22 Rejman, J., Oberle, V., Zuhorn, I. S. & Hoekstra, D. Size-dependent internalization of particles via the pathways of clathrin- and caveolae-mediated endocytosis. *Biochem. J.* **377**, 159-169 (2004).
- 23 Chithrani, B. D. & Chan, W. C. Elucidating the mechanism of cellular uptake and removal of protein-coated gold nanoparticles of different sizes and shapes. *Nano Lett.* **7**, 1542-1550 (2007).
- 24 Gan, Q. *et al.* Effect of size on the cellular endocytosis and controlled release of mesoporous silica nanoparticles for intracellular delivery. *Biomed. Microdevices* **14**, 259-270 (2012).
- 25 Slowing, I., Trewyn, B. G. & Lin, V. S. Effect of surface functionalization of MCM-41-type mesoporous silica nanoparticles on the endocytosis by human cancer cells. *J. Am. Chem. Soc.* **128**, 14792-14793 (2006).
- 26 Chung, T. H. *et al.* The effect of surface charge on the uptake and biological function of mesoporous silica nanoparticles in 3T3-L1 cells and human mesenchymal stem cells. *Biomaterials* **28**, 2959-2966 (2007).
- 27 Albanese, A., Tang, P. S. & Chan, W. C. The effect of nanoparticle size, shape, and surface chemistry on biological systems. *Annu. Rev. Biomed. Eng.* **14**, 1-16 (2012).
- 28 Walker, W. A., Tarannum, M. & Vivero-Escoto, J. L. Cellular endocytosis and trafficking of cholera toxin B-modified mesoporous silica nanoparticles. *J. Mater. Chem. B* (2016).

- 29 Blechinger, J. *et al.* Uptake kinetics and nanotoxicity of silica nanoparticles are cell type dependent. *Small* **9**, 3970-3980, 3906 (2013).
- 30 Dobay, M. P., Schmidt, A., Mendoza, E., Bein, T. & Radler, J. O. Cell type determines the light-induced endosomal escape kinetics of multifunctional mesoporous silica nanoparticles. *Nano Lett.* **13**, 1047-1052 (2013).
- 31 Plank, C., Oberhauser, B., Mechtler, K., Koch, C. & Wagner, E. The influence of endosome-disruptive peptides on gene transfer using synthetic virus-like gene transfer systems. *J. Biol. Chem.* **269**, 12918-12924 (1994).
- 32 Schlossbauer, A., Dohmen, C., Schaffert, D., Wagner, E. & Bein, T. pH-responsive release of acetal-linked melittin from SBA-15 mesoporous silica. *Angew. Chem. Int. Ed. Engl.* **50**, 6828-6830 (2011).
- 33 Anchordoguy, T. J., Carpenter, J. F., Crowe, J. H. & Crowe, L. M. Temperature-dependent perturbation of phospholipid bilayers by dimethylsulfoxide. *Biochim. Biophys. Acta* **1104**, 117-122 (1992).
- 34 Smondyrev, A. M. & Berkowitz, M. L. Molecular Dynamics Simulation of DPPC Bilayer in DMSO. *Biophys. J.* **76**, 2472-2478 (1999).
- 35 Notman, R., Noro, M., O'Malley, B. & Anwar, J. Molecular basis for dimethylsulfoxide (DMSO) action on lipid membranes. *J. Am. Chem. Soc.* **128**, 13982-13983 (2006).
- 36 Wang, H., Zhong, C. Y., Wu, J. F., Huang, Y. B. & Liu, C. B. Enhancement of TAT cell membrane penetration efficiency by dimethyl sulphoxide. *J Control Release* **143**, 64-70 (2010).
- 37 Mellman, I., Fuchs, R. & Helenius, A. Acidification of the endocytic and exocytic pathways. *Annu. Rev. Biochem* **55**, 663-700 (1986).
- 38 Wadia, J. S., Stan, R. V. & Dowdy, S. F. Transducible TAT-HA fusogenic peptide enhances escape of TAT-fusion proteins after lipid raft macropinocytosis. *Nat. Med.* **10**, 310-315 (2004).
- 39 Kirchhofer, A. *et al.* Modulation of protein properties in living cells using nanobodies. *Nat. Struct. Mol. Biol.* **17**, 133-138 (2010).
- 40 Kennedy, M. J. *et al.* Rapid blue-light-mediated induction of protein interactions in living cells. *Nat. Methods* **7**, 973-975 (2010).

6 Optimisation and Live Cell Tracking of Nanoparticle Mediated Protein Delivery Through an Inducible Split Venus Based System

This chapter is based on the following manuscript:

Hsin-Yi Chiu, Jack Bates, Jonas Helma, Hanna Engelke, Hartmann Harz, Thomas Bein and Heinrich Leonhardt, *to be submitted*.

Abstract

Mesoporous silica nanoparticles (MSNs) are promising nanocarriers for intracellular protein delivery with potential applications in disease treatment as well as cell research. To optimize and investigate their use we have developed a convenient, background free, live-cell Venus complementation based molecular sensor that exclusively detects delivered protein that is both functionally viable and bioavailable. We have applied this sensor in parallel with the MTT assay to maximize the protein delivery and biocompatibility of our large-pore multifunctional MSNs and have shown highly efficient protein transfection rates of about 80%. Furthermore, we have demonstrated tracking of live cell protein delivery with good temporal resolution and disentangled the timing of protein uptake from that of sensor dynamics through the use of built-in chemically inducible components. We believe that the sensor will be suitable for application with a wide range of protein nanocarriers enabling simple multi-parameter optimization as well as comparison between nanocarriers.

6.1 Introduction

Despite the increasing promise of protein therapeutics,^{1,2} their cellular delivery remains a major barrier to successful *in vivo* and medical implementation. Any technology addressing this challenge must tackle complications including short protein serum half-life, cellular uptake and endosomal entrapment. Mesoporous silica nanoparticles (MSNs) feature properties that make it possible to overcome these challenges. Specifically, a stable framework to shelter cargo from proteases and the immune machinery in addition to high cellular uptake efficiency and flexible surface functionalization for controlled drug release³⁻⁶ make them particularly promising candidates. This versatility of MSNs has been utilized for the delivery of chemotherapeutic agents,^{7,8} proteins,⁹⁻¹¹ oligonucleotides,^{12,13} and chromobodies.¹⁴ Having previously delivered bioactive proteins using MSNs,^{10,11,14} researchers have also sought to maximize the protein delivery efficiency whilst retaining good biocompatibility. For the determination of the delivery efficiency it is important to take into account that successfully delivered proteins must have both undergone endosomal escape and retained their function.¹⁵

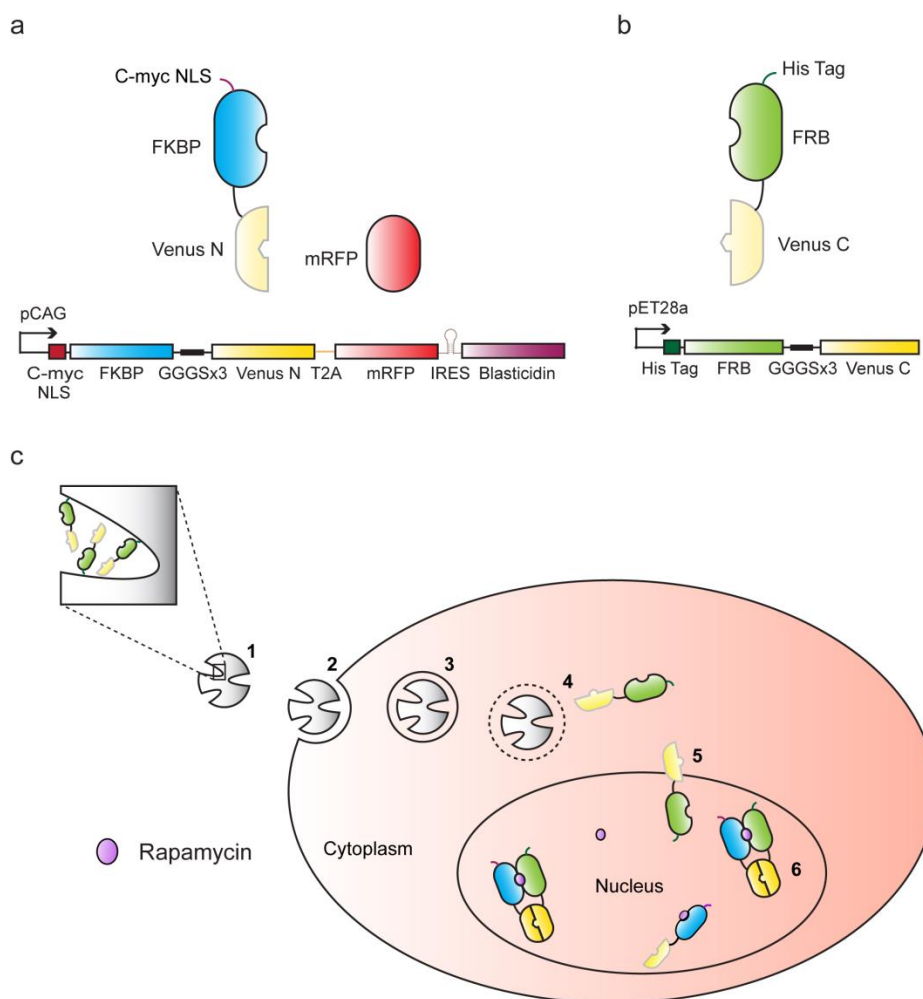
An array of techniques has been developed to quantify efficiencies of cellular protein delivery. The methods often exploit pre-existing cytoplasm/endosome differences such as pH,¹⁶ enzyme content,¹⁷ access to DNA,¹⁸ redox status,^{19,20} or localization,²¹ others still have utilized the physical separation of the compartments to create exploitable distinctions between the two environments.^{22,23} However, despite the advantages of each of these methods, many of these techniques do not provide a real-time readout, give a non-linear output due to amplification, transcription or recombination, give no indication of post-endosome protein functionality, or require more complex image analysis. Quantifying delivery efficiencies of functional proteins in real-time still remains challenging.

Recently GFP-based bimolecular fluorescence complementation (BiFC) assays have been developed, consisting of two proteins derived from genetic splitting of a fluorescent protein that fluoresce after dimerisation only. With one protein already present in the cell and the other being delivered, they produce direct fluorescent readouts for endosomal escape whilst retaining a functional element demonstrative of at least partial protein integrity.²⁴⁻²⁶ These assays have been successfully employed for the comparison of cell penetrating peptide (CPP) function as well as assessment of antibody internalization. Unfortunately, fluorescent tracking of protein uptake using these systems is complicated by the absence of a mechanism to

distinguish the timing of protein release from that of system complementation. It is therefore not possible to determine if, for example, a gradual increase in fluorescence is indicative of slow protein release or simply of a delay due to fluorescent protein formation and fluorophore maturation timing.

When designing a method to quantify the efficiency of our protein delivery system, we reasoned that an understanding of system dynamics and efficacy could be attained with a BiFC sensor if it could be inducibly controlled. To this end, here the chemically induced dimerisation (CID) components FKBP/FRB²⁷ are utilized and serve to strongly heterodimerise the complex exclusively in the presence of rapamycin²⁸. The two CID units are genetically fused to BiFC protein halves. The split Venus fluorescent protein (split 154/155) was selected for its high fluorescence signal, rapid maturation at 37 °C and low auto-complementation.^{29,30}

In our study, the complete BiFC/CID system is divided onto two constructs. A mammalian expression cassette is used for stable cell line production (Scheme 6-1a) and features the N-terminal portion of Venus (VN) fused C-terminally to FKBP *via* a flexible linker (GGGSx3). The protein expressed also contains an N-terminal c-myc nuclear localization signal (NLS)³¹ which serves to concentrate fluorescence in the nucleus of the cell enabling nuclear/cytoplasm fluorescence comparison and easy visual cell segregation. Furthermore, an mRFP follows VN which detaches *via* a T2A peptide³² and acts as an expression reporter used during stable cell line production. Moreover, it serves as calibration marker of the sensor intensity. Using HeLa Kyoto cells³³ we produced a monoclonal stable cell line (HeLa-FKBP-VN) that expresses the cassette at a high level using the CAG promoter.^{34,35} The complementary half of the BiFC/CID complex (Scheme 6-1b) consisting of His-tagged FRB domain fused N-terminally to the C-terminal half of Venus (VC) is expressed and purified using *E. coli* and affinity chromatography. The protein can thereafter be loaded into the MSNs for cellular delivery (Scheme 6-1c).



Scheme 6-1 Two-component cytosolic protein delivery detection system. (a) Layout of the mammalian expression cassette used to generate the HeLa-FKBP-VN stable cell line. (b) Layout of the bacterial expression cassette. (c) MSN-mediated application of the cytosolic protein delivery detection system. **1** Purified His-tagged FRB-VC proteins are loaded into MSNs *via* interaction with Ni-NTA groups on the surface of the MSN pore system. **2** Charged MSN-FRB-VC complexes bind to the cell surface and are **3** endocytosed into the cell. Lower pH in the endosomal system causes accelerated FRB-VC dissociation from the MSN. **4** Chloroquine shock (0.5 mM in the medium, RT, 5 min) triggers endosomal protein release followed by **5** free protein diffusion in the cytoplasm and further into the nucleus. **6** Addition of rapamycin leads to the formation of FRB/rapamycin/FKBP ternary complexes subsequently driving Venus complementation and fluorophore maturation.

Following cellular internalization of FRB-VC loaded MSNs (MSN-FRB-VC) *via* endocytosis,³⁶ the MSN carrier with cargo proceeds through the endosomal system where a decrease in pH causes dissociation of His-tagged FRB-VC from the MSN. An endosomal release trigger (chloroquine shock) is then applied to prompt endosomal rupture and cytosolic release of FRB-VC. FRB-VC can then diffuse to the nucleus and interact with FKBP-VN which is primed with rapamycin at saturation levels. FKBP-rapamycin-FRB forms a ternary complex which approximates the Venus halves thus facilitating complementation and chromophore maturation. Successful protein delivery can then be observed in a rapid and non-amplifying manner through visualization and measurement of Venus fluorescence in the nucleus. The fluorescent protein requires reconstitution prior to chromophore formation and thus only protein that has either evaded or escaped the endosome system and remains functional is able to produce signal in the nucleus.

6.2 Results and Discussion

Large-pore MSNs were surface-functionalized with NTA-Ni complexes (MSN-Ni) through a series of post-modifications (Figure 6-1a) to accommodate pH dependent binding and release of the His-tagged FRB-VC.^{11,14,37} STEM and SEM images (Figure 6-1b) indicated that the resulting nitrilotriacetic acid-modified MSNs (MSN-NTAs) exhibit uniform particle size, coral surface morphology consisting of irregular pore shape (pore size ranging from 10 – 40 nm) consistent with the structure of the un-functionalized form (appendix Figure 6-6). DLS measurements (Figure 6-1c) and N₂ sorption analyses (Figure 6-1d-e) further confirmed these findings. Appendix Table 1 summarizes the characterization results of MSNs before and after NTA modification.

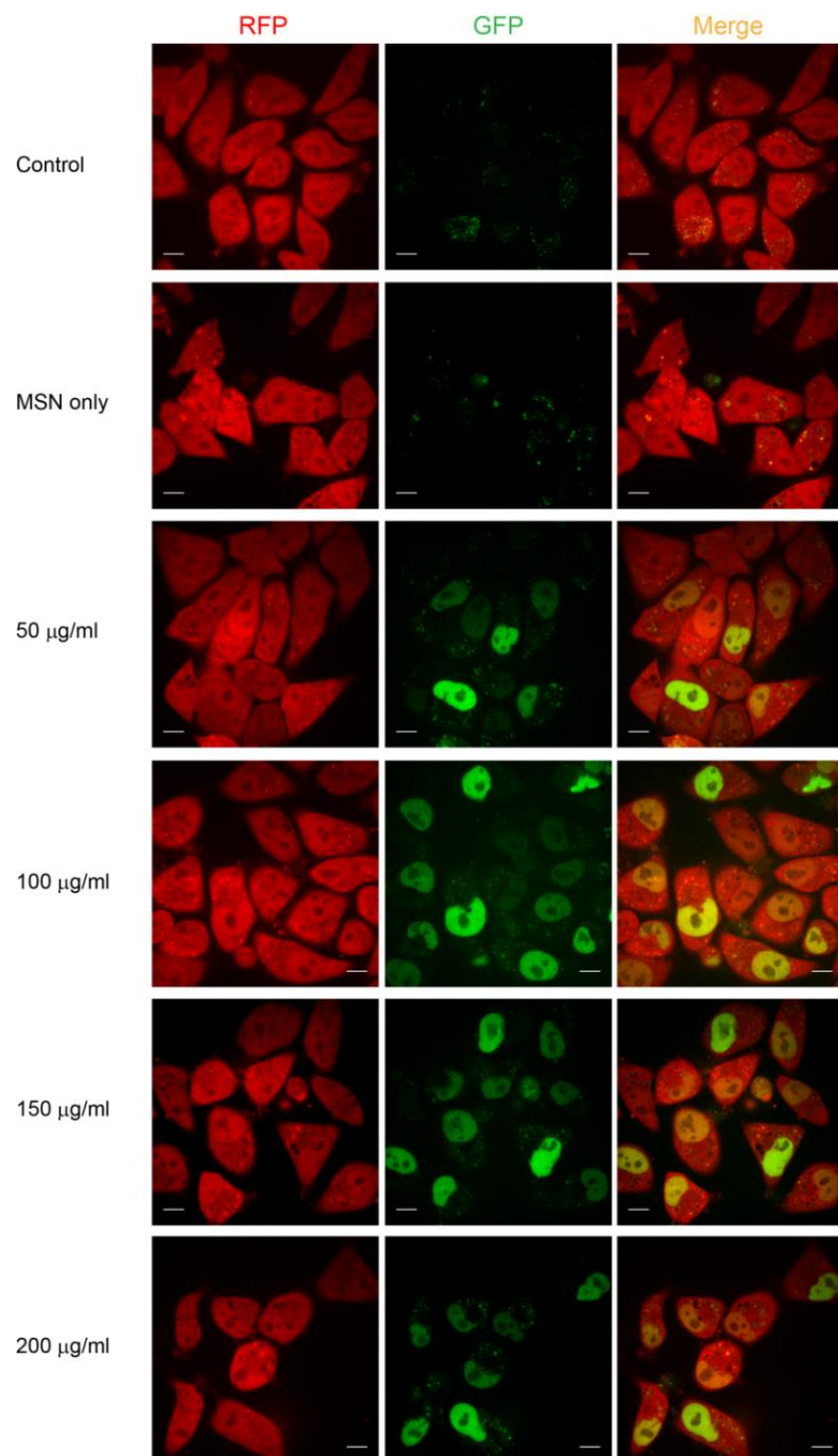


Figure 6-2 Live cell confocal imaging of MSN-mediated intracellular protein delivery in the cytosolic protein delivery detection system. Different MSN-FRB-VC concentrations were incubated with HeLa-FKBP-VN cells. Images were taken 20 h post endosomal release trigger (chloroquine shock). *Scale bar: 10 µm.*

Introduction of unloaded MSNs to the cells also did not increase Venus fluorescence (Figure 6-2, 6-3a, 6-3b). In contrast, application of MSN-FRB-VC complexes at all examined concentrations generated nuclear Venus signal in the cells (Figure 6-2). To quantify the gross Venus signal present in the cell populations we used microplate fluorometry. Whilst a significant increase in protein delivery is seen between the 50 $\mu\text{g/ml}$ and 100 $\mu\text{g/ml}$ concentrations, the fluorescent signal saturated thereafter (Figure 6-3a). When we quantified the percentage of Venus positive cells *via* flow cytometry we saw a similar pattern (Figure 6-3b). A significant increase in protein transfection percentage was seen between the 50 $\mu\text{g/ml}$ and 100 $\mu\text{g/ml}$ concentrations indicating some dose dependency, with higher concentrations having no further positive effect on uptake efficiency.

In parallel with protein delivery experiments, MTT assays were performed to evaluate cytotoxicity at different MSN concentrations. No significant difference in cell viability was seen at concentrations of 50 $\mu\text{g/ml}$ and 100 $\mu\text{g/ml}$ when compared to the no-MSN control population. However, concentrations of 150 $\mu\text{g/ml}$ and 200 $\mu\text{g/ml}$ were shown to be significantly more cytotoxic than the control. The cytotoxicity displayed at higher levels of MSN concentration may explain the plateau in the Venus signal we see in the protein delivery experiments, as damage to the cells may impair protein uptake. Further, it might explain the slight decrease in delivery efficiency measured with microplate fluorometry above 100 $\mu\text{g/ml}$. Through combination of the three data sets (Figure 6-3a-c) 100 $\mu\text{g/ml}$ was determined to be an optimal MSN concentration due to its high protein transfection efficiency and low cytotoxicity.

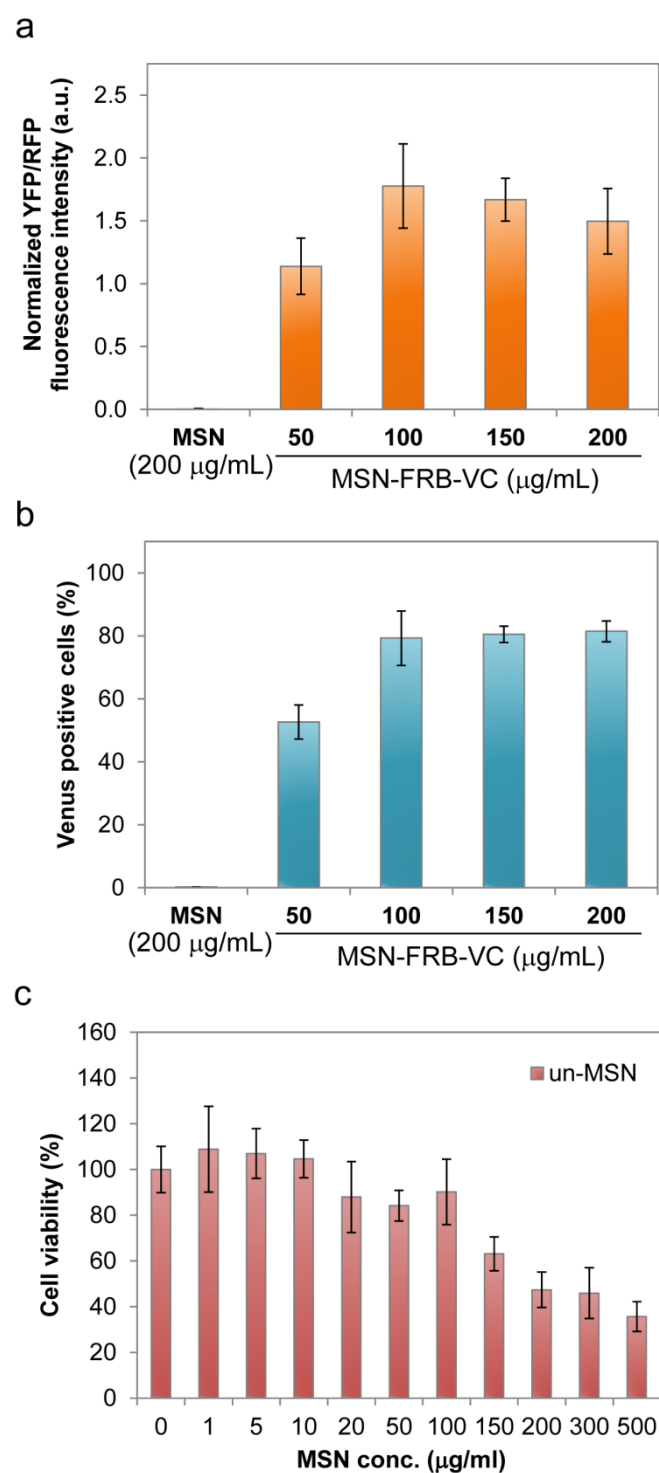


Figure 6-3 Protein delivery efficiency analyses and cytotoxicity assay. (a) Fluorescence readout from microplate reader. (b) FACS analysis. (c) MTT assay. The results shown in (a) were calculated based on six biological repeats, (b) and (c) were triplicated. Error bars represent SDs.

Next we sought to observe protein delivery in a cell population over time. Using spinning disc microscopy, HeLa-FKBP-VN cells incubated with MSN-FRB-VC complexes (100 µg/ml) and rapamycin were imaged at time points prior to and following chloroquine shock (2 h after MSN-FRB-VCs incubation). Before the chloroquine shock, no released FRB-VC protein was detected (Figure 6-4a). However, following destabilization of the endosomes with the chloroquine shock, Venus fluorescence was visible within the nuclei of some cells (1%) within just 30 minutes. At a time point of 5.5 h after chloroquine shock, over 50% of the cells can be seen to have functional proteins released to the nuclei. At 9 h protein release had reached a plateau where approximately 85% of the cells exhibit fluorescent nuclei. A live cell image of protein release saturation (10 h post chloroquine shock) is shown in Figure 6-4c. A timelapse video further demonstrates sensor detection of intracellular protein release (Appendix Figure 6-7). An alteration of the above experiment was performed where rapamycin addition (250 nM) was delayed until 24 h after MSN-FRB-VC incubation (Figure 6-4b). We reasoned that at this point the protein was likely already released into 80% of the cells and therefore the timing of Venus fluorescence should represent sensor complex formation and maturation rather than protein release. When comparing the onset of nuclear fluorescence within cells of a population between the rapamycin primed and rapamycin delayed experiments (Figure 6-4a-b) a far greater spread (50% timings of the two experiments) can be seen in the rapamycin primed experiment indicating a staggered release timing in the population.

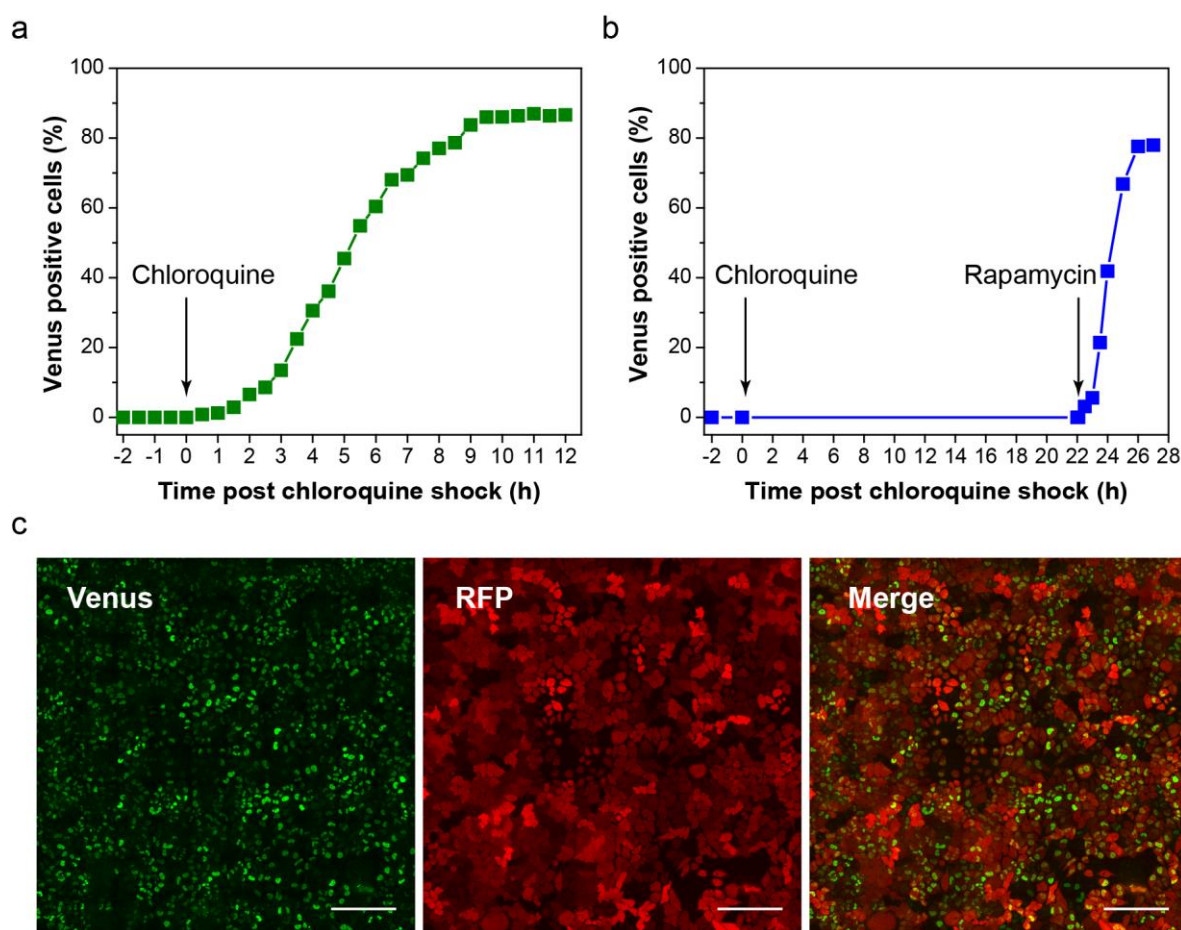


Figure 6-4 Live cell tracking of protein release. (a) HeLa-FKBP-VN cells were primed with rapamycin before imaging. MSN-FRB-VC was added to the cells and the first image was recorded (time point -2 h). After 2 h, particles were washed away using PBS and followed by a chloroquine shock (0.5 mM in the medium, RT, 5 min) (time point: 0 h). Cells were tracked using confocal microscopy (spinning disc) for 22 h. (b) MSN-FRB-VC were incubated with HeLa FKBP-VN cells for 2 h, and subsequently the endosomal protein release was triggered by chloroquine shock. 22 h after endosomal protein release trigger, rapamycin was added to the medium, and cells were tracked using confocal microscopy (spinning disc) for another 5 h. (c) Live cell confocal imaging of rapamycin-primed sample 10 h after chloroquine shock. *Scale bar: 200 μm .*

However, when we compared the timing of fluorescence increase after onset within individual cells between the two conditions, we observed similar durations (Figure 6-5a-b). We interpret these results to be consistent with the aforementioned model for MSN uptake and his-tag mediated protein release (Figure 6-1c). The delay in fluorescence onset within cells in the rapamycin primed experiment can be attributed to the time taken for the

relevant endosomal rupture event to occur. (Further evidence that the delay may be due to endosomal rupture timing is the prolonged presence of enlarged endosomes after chloroquine shock (appendix Figure 6-8).

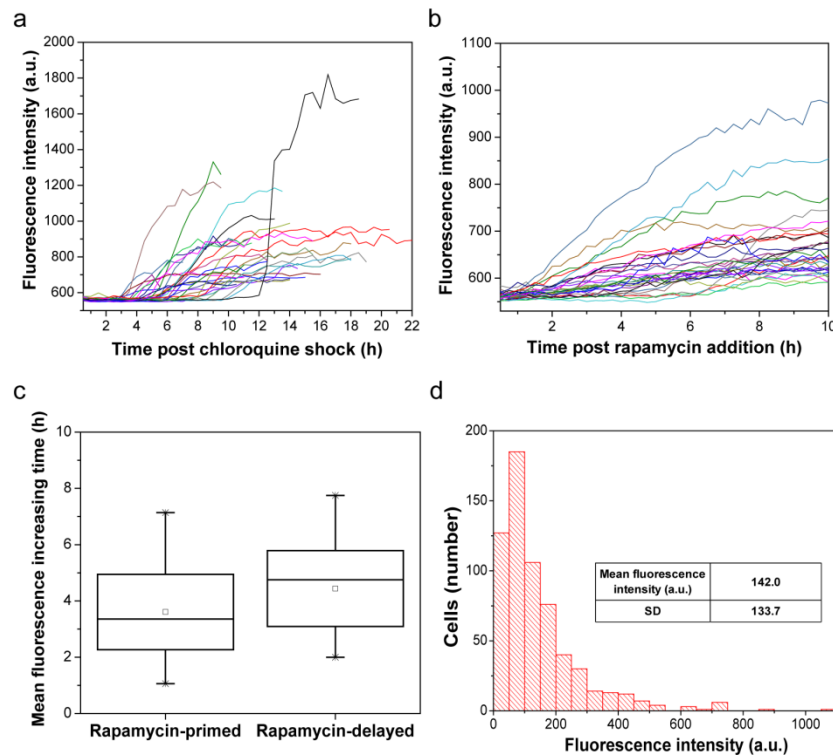


Figure 6-5 Live cell tracking of protein release in individual cells within a population.

Fluorescence intensity tracking from 30 cells in (a) rapamycin-primed sample and (b) rapamycin-delayed sample. (c) Mean fluorescence increasing time evaluated from (a) and (b). The central 70% of the release curves from both (a) and (b) were evaluated. Mean values are indicated within the box. Box range represents standard deviation and the whisker range displays the minimum and maximum values in the population. (d) Fluorescence intensity distribution among 625 cells in the rapamycin-primed sample recorded at 15 h post chloroquine shock.

The similarity between the experiments in single cell fluorescence increase once initiated suggests that we are, in all likelihood, observing roughly analogous processes (Figure 6-5c). Therefore, it seems probable that the once protein release begins it proceeds in a rapid fashion and that in both experimental variations we are simply observing sensor complementation and maturation timing. This logically aligns with the proposed mechanism of delivery, as bulk release of already MSN-detached protein should occur

when the endosomal barrier is breached, thus permitting prompt protein complementation between the corresponding halves.

Unlike sensors that rely upon transcription or amplification mechanisms, the ratio-metric nature of our sensor enables us to measure variations not only between but also within populations. For example, through image analysis of cell nuclei we can assess parameters such as the range of protein released within a population as well as means and standard deviations of protein released (Figure 6-5c). In consideration of the significance of cellular protein stoichiometry, this should be a useful tool for understanding and adapting nanocarriers for various tasks.

6.3 Conclusion

In conclusion, we have developed an inducible two-component fluorescent live cell protein delivery sensor that facilitates simple relative quantification of bioavailable protein levels and cell protein transfection efficiency. We have demonstrated that it can be used in parallel with the MTT assay to optimize protein loaded MSN dosage for delivery efficiency and biocompatibility. Moreover, we have demonstrated that it can be effectively used to track protein uptake in a live cell population with temporal resolution far superior to transcription-dependent systems. Furthermore, our data demonstrate that when optimal concentrations are used, MSNs can achieve formidable protein delivery efficiency with a mean delivery in about 80% of cells. We propose that the system demonstrated would be suitable for multi-parameter optimization, comparison, and investigation of many of the expanding repertoire of protein nanocarriers.

6.4 Experimental

Materials

Tetraethyl orthosilicate (TEOS, Aldrich, $\geq 99\%$), (3-glycidyloxypropyl)trimethoxysilane (GPTMS, Fluka, $\geq 97\%$), cetyltrimethylammonium p-toluenesulfonate (CTATos, Sigma), triethanolamine (TEA, Aldrich, 98%), magnesium sulfate anhydrous (99.9%, Sigma), toluene anhydrous (Sigma), bi-distilled water obtained from a Millipore system (Milli-Q Academic A10). N(alpha),N(alpha)-bis(carboxymethyl)-L-lysine hydrate (NTA-lysine, Aldrich), sodium carbonate (Sigma), sodium bicarbonate (Sigma), nickel chloride hexahydrate (Riedel-de Haen), tris(hydroxymethyl)-aminomethane (TRIS, $\geq 99\%$, ROTH), acetic acid (99% - 100%, ROTH), thiazolyl blue tetrazolium bromide (MTT, $\geq 97.5\%$, Sigma), dimethyl sulfoxide molecular (DMSO, Applichem, biology grade), Dulbecco's Modified Eagle's Medium (DMEM, Sigma), Dulbecco's Phosphate Buffered Saline (PBS, Sigma), FBS Superior (Biochrom, S0615), Gentamycin solution (SERVA, 50 mg ml⁻¹), trypsin-EDTA solution (Sigma, T3924), Dulbecco's Modified Eagle's Medium – phenol red free (DMEM, Gibco), ethanol (EtOH, Aldrich, absolute).

Synthesis and functionalization of mesoporous silica nanoparticles (MSNs)

Un-functionalized MSNs were synthesized using a modification of a previously reported procedure³⁸. In brief, a mixture of TEA (0.49 g, 3.3 mmol), CTATos (2.73 g, 6 mmol) and H₂O (144 g, 8 mol) was vigorously stirred (1250 rpm) at 80°C in a 250 ml glass flask until the solution became homogeneous. TEOS (20.83 g, 0.1 mol) was then added and the solution was continuously stirred (1250 rpm) at 80°C for another 2 h, afterwards the synthesized particles can be observed as whitening of the solution. The as-synthesized particles were collected by centrifugation (7000 x g, 15 min) and subsequently subjected to organic template extraction. The organic template extraction was carried out by heating particles in an ethanolic solution (150 mL) containing 3 g of ammonium nitrate at 90 °C under reflux for 1 h followed by a second reflux at 90 °C in a 2 M HCl/ethanolic solution (150 mL) for 1 h. The un-functionalized mesoporous silica nanoparticles (un-MSNs) were collected by centrifugation (7000 x g, 20 min) and were washed with water and EtOH after each extraction step.

To attach epoxy groups to the surface of the MSNs, a post-synthetic grafting procedure was performed. 500 mg of un-MSNs were de-hydrated under reflux (130 °C) in 150 mL of toluene in the presence of MgSO_4 for 4 h. GPTMS (190 mg, 0.83 mmol, 10 mol% of total silica) was subsequently added to the toluene solution, and the solution was stirred (500 rpm) at 130 °C for 2 h. After the solution had cooled to room temperature, the toluene was removed by rotary evaporator (77 mbar, 45 °C, 250 rpm). The resulting epoxy group-modified MSNs (MSN-Epoxy) were washed three times with 150 mL of EtOH and preserved in 50 mL of absolute EtOH. Centrifugation (7000 x g, 20 min) was used to collect particles after each washing step.

MSN-Epoxy particles were then modified to yield NTA-functionalized MSNs (MSN-NTA). 360 mg of MSN-Epoxy and 200 mg (0.6 mmol) of NTA-lysine were mixed in 10 ml of carbonate-bicarbonate buffer (100 mM, pH 9) and the mixture was stirred at RT overnight. The functionalized MSN-NTA particles were washed three times with 100 mL of tris-acetate (TA) buffer (pH 8) at RT and re-suspended in 36 mL of EtOH. Centrifugation (7000 x g, 20 min) was used to collect particles after each washing step. To immobilize Ni^{2+} on the surface of MSN-NTAs, 5 mg of MSN-NTA was dispersed in 5 ml of NiCl_2 (50 mM in H_2O) and stirred at RT for 4 h. The un-bound Ni^{2+} was washed out with H_2O (three times with 5 ml) and the particles were collected following centrifugation (17000 x g, 5 min). The final NTA-Ni complex modified MSNs (MSN-Ni) were stored in 5 mL of EtOH (MSN concentration: 1 mg/mL) for further use.

Characterization of MSNs

Scanning electron microscopy (SEM) and scanning-transmission electron microscopy (STEM) were performed at 30 kV on a Helios NanoLab G3 UC instrument (FEI, USA) with a detection system containing a TLD detector and a STEM ADF detector. A drop of EtOH diluted MSN suspension was dried on a carbon-coated copper grid at room temperature for several hours before SEM/STEM observation. Dynamic light scattering (DLS) measurements were performed on a Malvern Zetasizer-Nano instrument equipped with a 4 mW He-Ne laser (633 nm). Nitrogen sorption analysis was performed on a Quantachrome Instrument NOVA 4000e at 77 K. Samples (15 – 20 mg) were degassed at 120 °C under vacuum (10 mTorr) one day before measurement. Pore size distribution curves were obtained based on non-local

density functional theory (NLDFT) procedures provided by Quantachrome, using the adsorption branch of N₂ on silica.

Plasmid Construction

A previously described pCAG mammalian expression vector containing an IRES-Blasticidin selection gene following the ORF was used for creation of the pCAG-FKBP-VN-T2A-mRFP cassette³⁹ (Scheme 1a). The protein expression vector pET28a was used for FRB-VC-Histag expression (Scheme 1b). The Gibson assembly method was applied for all cloning⁴⁰.

FRB-VC protein expression and purification

FRB-VC protein was expressed in *E. coli* (BL21 strain) and was further purified in a His-trap column. Expression was induced through addition of 0.5 mM of isopropyl beta-D-1-thiogalactopyranoside (IPTG, ROTH) and cells were further cultured at 18 °C overnight. Cells were harvested and lysed in PBS buffer containing 100 µg/ml of lysozyme (Serva, Germany), 2 mM of phenylmethanesulfonyl fluoride (PMSF, sigma) and 25 µg/ml of DNase (Applichem, Germany) followed by sonication (Branson® Sonifier; 16 x 8 sec, 20% amplitude). Cell debris was collected by centrifugation at 20000 x g for 30 min. Protein purification was performed using an 8 M Urea purification protocol⁴¹ including renaturation of the protein *via* FPLC (Äkta Purifier Amersham Biosciences, GE Healthcare, USA) on a 1 ml His-trap column (GE Healthcare, USA). Elution was performed using an increasing imidazole gradient rather than the step-wise imidazole increase outlined in the protocol. Eluted protein was desalted using the PD-10 (GE Healthcare, USA) column and concentrated by an Amicon filter column (cut-off 10 kDa, Merck Millipore, Germany). Purified protein in PBS was aliquoted followed by shock-freezing and storing at -80 °C.

FRB-VC protein loading to MSN-Ni

1 mg of MSN-Ni was mixed with 500 µg of FRB-VC protein in 500 µl of PBS at 4 °C with shaking (400 rpm) for 1.5 h. The resulting MSN-FRB-VC complexes were collected by centrifugation (3000 x g, 3 min), washed with PBS (1 mL per wash) twice, and re-suspended in 100 µl of PBS.

Cell culture and stable cell line

HeLa Kyoto cells⁴¹ (HeLa k, a modified HeLa cell line characterized by little cell motility and thus suitable for live cell time-lapse imaging) were cultured in DMEM medium supplemented with 10% FBS and gentamycin (50 µg/ml in cell culture medium) under 5% CO₂ at 37°C. To generate a cell line stably expressing the pCAG-FKBP-VN-T2A-mRFP construct, pCAG-FKBP-VN-T2A-mRFP was transfected into HeLa k cells using Lipofectamine 3000 reagent (Invitrogen). Blasticidin (10 µg/ml in cell culture medium) was used to select cells between 48 h after transfection and 3 weeks. Highly mRFP fluorescent cells were then isolated *via* flow cytometry (FACS Aria II, BD Biosciences) to produce a monoclonal cell line (HeLa-FKBP-VN).

Intracellular protein delivery for MSN concentration optimisation

HeLa-FKBP-VN cells in DMEM culture medium were seeded on either a 2-well ibiTreat slide (ibidi, Germany) or a 6-well plate (Corning, USA) at 50% confluency 12 h before the intracellular protein delivery experiment. MSNs loaded with FRB-VC proteins (MSN-FRB-VCs) in PBS were added to cell culture in a serum free DMEM and incubated with cells at 37 °C for 2 h. Afterwards, the residual particles in the medium were washed out using PBS (1.5 mL per well) followed by a short chloroquine shock (0.5 mM in cell culture medium, 1.5 mL per well in cell culture medium, RT, 5 min) to trigger endosomal protein release. Cells were then incubated in fresh cell culture medium (phenol red free). All the assays (live cell imaging, FACS analysis and fluorescence readout) were performed at 24 h post MSN-FRB-VCs addition.

Live cell imaging was performed using an UltraVIEW Vox spinning disc confocal system (PerkinElmer, UK) in a closed live cell microscopy chamber (ACU control, Olympus, Japan) mounted on a Nikon Ti microscope (Nikon, Japan). The microscopy chamber was held at 37 °C, 5% CO₂ and 60% humidity. Venus and RFP were excited with 488 nm (30% output power) and 561 nm (30% output power) solid-state diode laser lines, respectively. Image acquisition was carried out through a 63x/1.4 NA plan-apochromat oil immersion objective lens. Images were obtained by a cooled 14-bit EMCCD camera (C9100-50, CamLink) with a frame size of 1024 x 1024 pixels and a pixel size of 110 nm.

Flow Cytometry

Cells were washed with PBS, detached from a 6-well plate using 0.25% Trypsin-EDTA and finally re-suspended in PBS (3 mL per well) prior to flow cytometry (FACS Aria II, BD Biosciences). Data were analyzed using FlowJo (8.1) software. Non-MSN treated HeLa-FKBP-VN-RFP cells were used to gate out dead cells and aggregates and to calibrate appropriate Venus (using FITC settings) and mRFP gating. Venus +ve and -ve cells were analysed from the RFP +ve group. 10,000 cells were measured per sample. Experiments were triplicated. Error bars represent standard deviations.

Microplate reader for cell fluorescence readout

Cells were detached from a 6-well plate using 0.25% Trypsin-EDTA, harvested and washed with PBS. After centrifugation (150 g, 5 min), cells were re-suspended in 100 µl of PBS and pipetted into a 96-well microplate (Greiner Bio-One, Germany). Fluorescence was measured using a microplate reader (Infinite® M1000 PRO, TECAN) with 515 nm excitation and 528 nm emission for Venus measurements and 556 nm excitation and 586 nm emission for RFP measurements. Four readings were taken per well. Background fluorescence in the Venus channel was measured using the stable cell line without addition of the complementing protein and subtracted from other readings. Measurements were normalized against the RFP channel to account for variations in cell number. Experiments were performed in six biological repeats. Error bars represent standard deviations.

MTT assay

One day prior to MTT assay HeLa Kyoto cells were plated on a 96-well microplate (5×10^3 cells per well) in DMEM and incubated at 37 °C. After removal of culture medium, cells were exposed to 100 µl of MSN-DMEM solution per well (serum free) with various MSN concentrations, while the control group was incubated with 100 µl of serum-free DMEM. Following 2 h incubation, the cells were washed with PBS three times to remove the residual particles. Freshly prepared MTT solution (0.5 mg/ml in DMEM) was added to the cells (100 µl/well) and the cells were incubated at 37 °C for another 4 h. The purple crystals metabolized from healthy cells were then dissolved in 100 µl of DMSO and the absorbance was measured at 570 nm, while the reference absorbance was measured at 655 nm using a

Microplate reader (Infinite® M1000 PRO, TECAN). Experiments were triplicated. Error bars represent standard deviations.

Live cell tracking of protein release

Rapamycin-primed sample

HeLa-FKBP-VN-RFP cells were seeded onto a 2-well ibi-Treat slide 12 h before the experiment. For the rapamycin-primed protein release tracking experiment, 1 µl of rapamycin (from 250 µM stock solution), 100 mg of MSN-FRB-VC and 0.5 µl of SiR-DNA (a nuclear-staining dye, Spirochrome, Germany) were mixed in 1 mL of serum-free DMEM, and the mixture was added to the cells before the first image was acquired. After 2 h, particles were washed away using PBS and followed by a chloroquine shock (0.5 mM of chloroquine in standard DMEM, 1.5 mL/well) at RT for 5 min triggering endosomal protein release. Cells were tracked at indicated time points for 24 h. Microscopic images were acquired with a Nikon TiE microscope equipped with perfect focus, Yokogawa CSU-W1 spinning disk unit (50 µm pinhole size), Andor ALC600 laser-beamcombiner: 405nm/488nm/561nm/640nm, Yokogawa CSU-W1 dichroic mirror 405/488/561/640 LD Quad, Andor Borealis illumination unit and Andor IXON 888 Ultra EMCCD camera using a Nikon CFI P-Apo 100x Lambda oil immersion objective NA 1.45. The setup was equipped with an environmental chamber (Okolab BIO 1, Bold Line CO₂ and temperature module, gas chamber and humidifying module) and controlled by software from Nikon (NIS elements, version 4.51.01). The environmental conditions during the experiment were set to 37 °C, 5 % CO₂ and humidified atmosphere. Focus drifts during the long-term experiments were compensated by the Nikon perfect focus system. Tiled images (10x10 image fields, 15 % overlap, stitched by NIS elements) were acquired throughout this study to investigate many cells per experiment. 4 colour tiles (488 nm, 561 nm, 640 nm and differential interference contrast) were acquired with a frequency of 3 images per hour. On chip binning (2x2) was used throughout to reduce the data amount and to improve the signal to noise ratio. Fluorescence images were acquired with an exposure time of 1 s and an EM gain setting of 160. For the population protein delivery tracking analysis, a single large field area with 200 -300 cells were assessed at each interval.

Rapamycin-delayed sample

For the Venus reconstitution kinetics tracking (rapamycin-delayed sample), 100 mg of MSN-FRB-VC and 0.5 μ l of SiR-DNA were mixed in 1 mL of serum-free DMEM, and the mixture was added to the cells before the first image was acquired. After 2 h, particles were washed away using PBS and followed by a chloroquine shock. Cells were tracked at indicated time points using confocal microscopy (an UltraVIEW Vox spinning disc confocal system, PerkinElmer, UK). Rapamycin (1 μ l, final conc. 250 nM in standard DMEM) was added to the sample 22 h after chloroquine shock. Live cell images were acquired at randomly chosen areas to prevent Venus fluorescence bleaching. 200 – 300 cells were imaged and counted at each time point. Venus positive cells were counted visually. Venus positive cells in % correspond to the number of nuclei with Venus fluorescence divided by the number of cells with RFP fluorescence * 100.

Measuring Nuclear Fluorescence Intensity

Nuclear Venus signal was tracked in individual cells post imaging using Image J software. All readings were obtained using a circular ROI of consistent size measuring a region of cell nuclei at each time point. The ROIs excluded nucleoli to obtain more homogenous signal. The mean fluorescence of each ROI was used for data points. To reduce ambiguity regarding start and stop points of fluorescent increase in cells we started timing increase at the first timepoint that was consistently 15% above the minimum fluorescent value measured in that cell. We timed until the first timepoint above 15% below the maximum value seen, therefore timing the central 70% of fluorescent increase in each cell.

Acknowledgements

Financial support from the Deutsche Forschungsgemeinschaft (SFB 1032 and SPP1623/LE721/13-1), the Center for Nano Science (CeNS) and the Excellence Cluster Nanosystems Initiative Munich (NIM) are gratefully acknowledged. Moreover, we thank Dr. Steffen Schmidt for technical assistance with the STEM/SEM microscopy.

6.5 Appendix

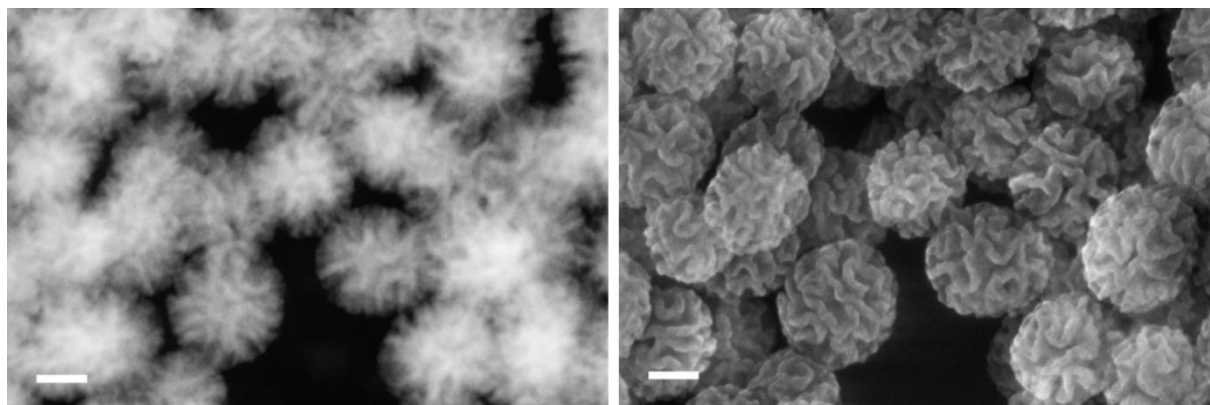


Figure 6-6 STEM (left) and SEM (right) images of un-functionalized MSNs. *Scale bar: 50 nm.*

Table 6-1 Summary of characterization data of un-MSN and MSN-NTA.

Sample	Particle size (nm)	Pore size distribution (nm)	Pore volume (cm ³ /g)	Surface area (m ² /g)
Un-MSN	133 ± 50	4 - 45	1.4	390
MSN-NTA	152 ± 54	4 - 40	1.1	275

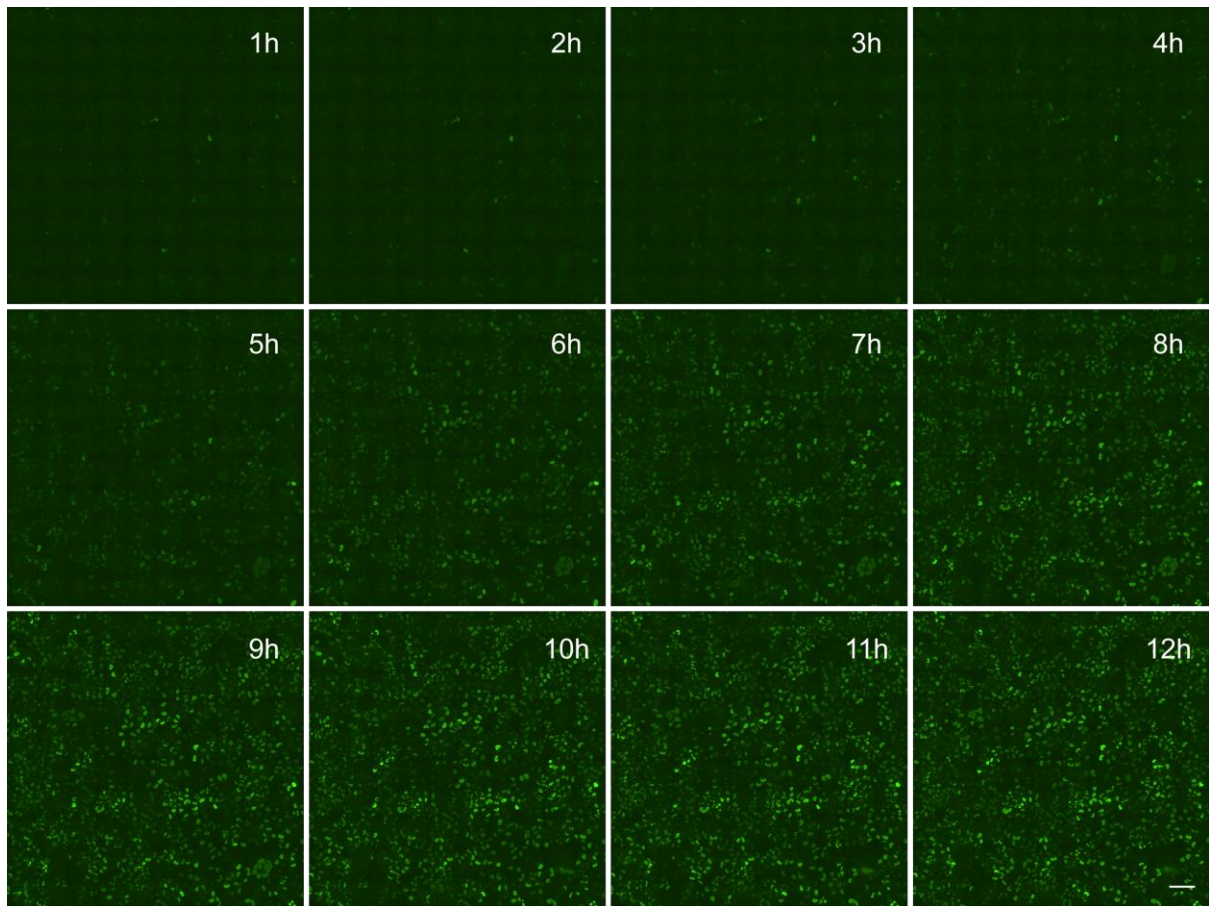


Figure 6-7 Time course live cell imaging (cropped from a time-lapse video) of Venus fluorescent nuclei from rapamycin-primed sample. *Scale bar: 100 μ m.*

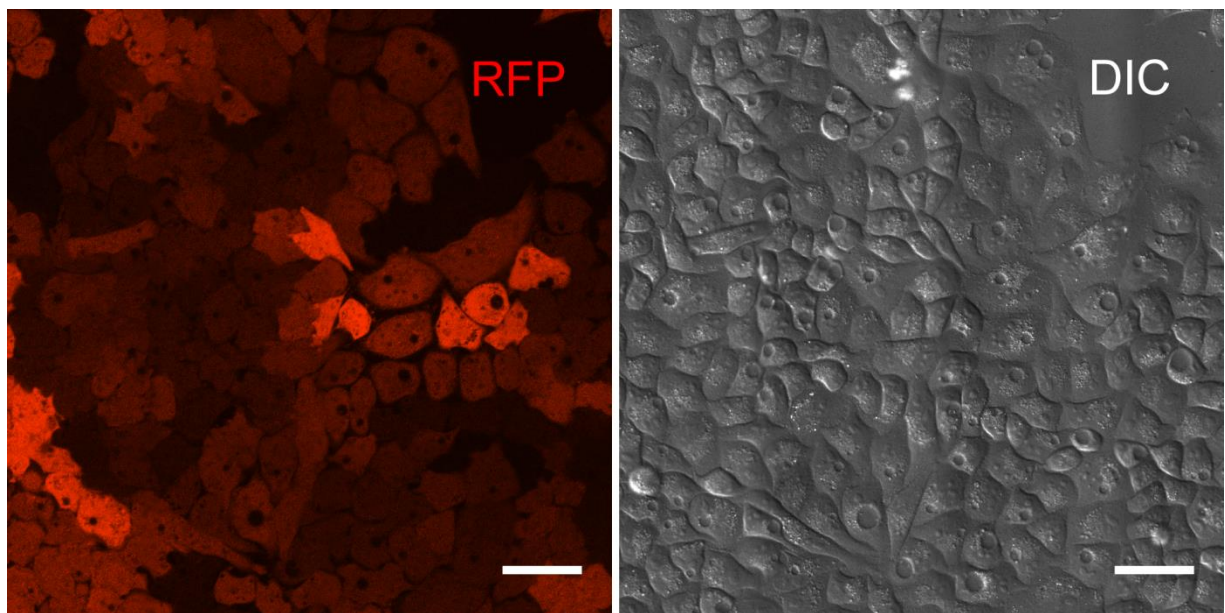


Figure 6-8 Live cell images at 15 h post chloroquine shock. Swollen vesicles can be observed in cells after 15 h of chloroquine shock. *Scale bar: 50 μ m.*

6.6 References

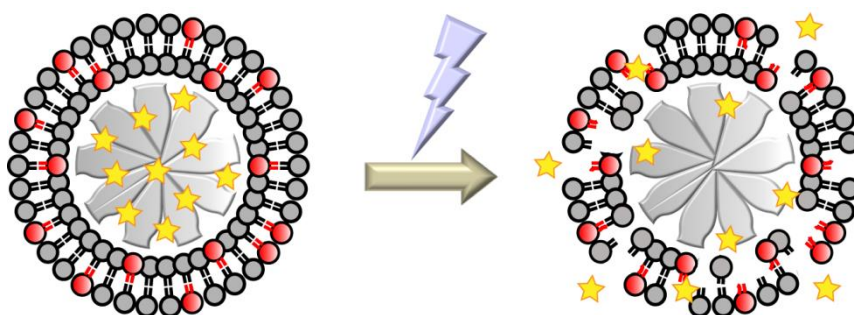
- 1 Mitragotri, S., Burke, P. A. & Langer, R. Overcoming the challenges in administering biopharmaceuticals: formulation and delivery strategies. *Nat. Rev. Drug Discov.* **13**, 655-672, doi:10.1038/nrd4363 (2014).
- 2 Leader, B., Baca, Q. J. & Golan, D. E. Protein therapeutics: a summary and pharmacological classification. *Nat. Rev. Drug Discov.* **7**, 21-39, doi:10.1038/nrd2399 (2008).
- 3 Slowing, II, Vivero-Escoto, J. L., Wu, C. W. & Lin, V. S. Mesoporous silica nanoparticles as controlled release drug delivery and gene transfection carriers. *Adv Drug Deliv Rev* **60**, 1278-1288, doi:10.1016/j.addr.2008.03.012 (2008).
- 4 Lu, J., Liong, M., Li, Z., Zink, J. I. & Tamanoi, F. Biocompatibility, biodistribution, and drug-delivery efficiency of mesoporous silica nanoparticles for cancer therapy in animals. *Small* **6**, 1794-1805, doi:10.1002/sml.201000538 (2010).
- 5 Vivero-Escoto, J. L., Slowing, II, Trewyn, B. G. & Lin, V. S. Mesoporous silica nanoparticles for intracellular controlled drug delivery. *Small* **6**, 1952-1967, doi:10.1002/sml.200901789 (2010).
- 6 Heidegger, S. *et al.* Immune response to functionalized mesoporous silica nanoparticles for targeted drug delivery. *Nanoscale* **8**, 938-948, doi:10.1039/c5nr06122a (2016).
- 7 Xu, R. *et al.* An injectable nanoparticle generator enhances delivery of cancer therapeutics. *Nat Biotechnol* **34**, 414-418, doi:10.1038/nbt.3506 (2016).
- 8 van Rijt, S. H. *et al.* Protease-mediated release of chemotherapeutics from mesoporous silica nanoparticles to ex vivo human and mouse lung tumors. *ACS Nano* **9**, 2377-2389, doi:10.1021/nn5070343 (2015).
- 9 Kilpelainen, M. *et al.* In vivo delivery of a peptide, ghrelin antagonist, with mesoporous silicon microparticles. *J Control Release* **137**, 166-170, doi:10.1016/j.jconrel.2009.03.017 (2009).
- 10 Han, D. H. *et al.* Direct cellular delivery of human proteasomes to delay tau aggregation. *Nat Commun* **5**, 5633, doi:10.1038/ncomms6633 (2014).
- 11 Chen, Y. P. *et al.* A new strategy for intracellular delivery of enzyme using mesoporous silica nanoparticles: superoxide dismutase. *J. Am. Chem. Soc.* **135**, 1516-1523, doi:10.1021/ja3105208 (2013).
- 12 Moller, K. *et al.* Highly efficient siRNA delivery from core-shell mesoporous silica nanoparticles with multifunctional polymer caps. *Nanoscale* **8**, 4007-4019, doi:10.1039/c5nr06246b (2016).
- 13 Dengler, E. C. *et al.* Mesoporous silica-supported lipid bilayers (protocells) for DNA cargo delivery to the spinal cord. *J Control Release* **168**, 209-224, doi:10.1016/j.jconrel.2013.03.009 (2013).

- 14 Chiu, H. Y. *et al.* Intracellular chromobody delivery by mesoporous silica nanoparticles for antigen targeting and visualization in real time. *Sci Rep* **6**, 25019, doi:10.1038/srep25019 (2016).
- 15 Varkouhi, A. K., Scholte, M., Storm, G. & Haisma, H. J. Endosomal escape pathways for delivery of biologicals. *J Control Release* **151**, 220-228, doi:10.1016/j.jconrel.2010.11.004 (2011).
- 16 Qian, Z. *et al.* Discovery and Mechanism of Highly Efficient Cyclic Cell-Penetrating Peptides. *Biochemistry* **55**, 2601-2612, doi:10.1021/acs.biochem.6b00226 (2016).
- 17 Loison, F. *et al.* A ubiquitin-based assay for the cytosolic uptake of protein transduction domains. *Mol. Ther.* **11**, 205-214, doi:10.1016/j.ymthe.2004.10.010 (2005).
- 18 D'Astolfo, D. S. *et al.* Efficient intracellular delivery of native proteins. *Cell* **161**, 674-690, doi:10.1016/j.cell.2015.03.028 (2015).
- 19 Cheung, J. C., Kim Chiaw, P., Deber, C. M. & Bear, C. E. A novel method for monitoring the cytosolic delivery of peptide cargo. *J Control Release* **137**, 2-7, doi:10.1016/j.jconrel.2009.02.022 (2009).
- 20 Eiriksdottir, E., Mager, I., Lehto, T., El Andaloussi, S. & Langel, U. Cellular internalization kinetics of (luciferin-)cell-penetrating peptide conjugates. *Bioconjug Chem* **21**, 1662-1672, doi:10.1021/bc100174y (2010).
- 21 Holub, J. M., Larochelle, J. R., Appelbaum, J. S. & Schepartz, A. Improved assays for determining the cytosolic access of peptides, proteins, and their mimetics. *Biochemistry* **52**, 9036-9046, doi:10.1021/bi401069g (2013).
- 22 Verdurmen, W. P., Luginbuhl, M., Honegger, A. & Pluckthun, A. Efficient cell-specific uptake of binding proteins into the cytoplasm through engineered modular transport systems. *J Control Release* **200**, 13-22, doi:10.1016/j.jconrel.2014.12.019 (2015).
- 23 Chao, T. Y. & Raines, R. T. Fluorogenic label to quantify the cytosolic delivery of macromolecules. *Mol Biosyst* **9**, 339-342, doi:10.1039/c3mb25552b (2013).
- 24 Milech, N. *et al.* GFP-complementation assay to detect functional CPP and protein delivery into living cells. *Sci Rep* **5**, 18329, doi:10.1038/srep18329 (2015).
- 25 Kim, J. S. *et al.* Quantitative assessment of cellular uptake and cytosolic access of antibody in living cells by an enhanced split GFP complementation assay. *Biochem. Biophys. Res. Commun.* **467**, 771-777, doi:10.1016/j.bbrc.2015.10.066 (2015).
- 26 Schmidt, S. *et al.* Detecting Cytosolic Peptide Delivery with the GFP Complementation Assay in the Low Micromolar Range. *Angew. Chem. Int. Ed. Engl.* **54**, 15105-15108, doi:10.1002/anie.201505913 (2015).
- 27 Choi, J., Chen, J., Schreiber, S. L. & Clardy, J. Structure of the FKBP12-rapamycin complex interacting with the binding domain of human FRAP. *Science* **273**, 239-242 (1996).

- 28 Banaszynski, L. A., Liu, C. W. & Wandless, T. J. Characterization of the FKBP.rapamycin.FRB ternary complex. *J. Am. Chem. Soc.* **127**, 4715-4721, doi:10.1021/ja043277y (2005).
- 29 Nagai, T. *et al.* A variant of yellow fluorescent protein with fast and efficient maturation for cell-biological applications. *Nat. Biotechnol.* **20**, 87-90, doi:10.1038/nbt0102-87 (2002).
- 30 Shyu, Y. J., Liu, H., Deng, X. & Hu, C. D. Identification of new fluorescent protein fragments for bimolecular fluorescence complementation analysis under physiological conditions. *Biotechniques* **40**, 61-66 (2006).
- 31 Dang, C. V. & Lee, W. M. Identification of the human c-myc protein nuclear translocation signal. *Mol Cell Biol* **8**, 4048-4054 (1988).
- 32 Donnelly, M. L. *et al.* The 'cleavage' activities of foot-and-mouth disease virus 2A site-directed mutants and naturally occurring '2A-like' sequences. *J Gen Virol* **82**, 1027-1041 (2001).
- 33 Landry, J. J. *et al.* The genomic and transcriptomic landscape of a HeLa cell line. *G3 (Bethesda)* **3**, 1213-1224, doi:10.1534/g3.113.005777 (2013).
- 34 Qin, J. Y. *et al.* Systematic comparison of constitutive promoters and the doxycycline-inducible promoter. *PLoS One* **5**, e10611, doi:10.1371/journal.pone.0010611 (2010).
- 35 Niwa, H., Yamamura, K. & Miyazaki, J. Efficient selection for high-expression transfectants with a novel eukaryotic vector. *Gene* **108**, 193-199 (1991).
- 36 Oh, N. & Park, J. H. Endocytosis and exocytosis of nanoparticles in mammalian cells. *Int J Nanomedicine* **9 Suppl 1**, 51-63, doi:10.2147/IJN.S26592 (2014).
- 37 Han, D. H. *et al.* Direct cellular delivery of human proteasomes to delay tau aggregation. *Nat. Commun.* **5**, 5633, doi:10.1038/ncomms6633 (2014).
- 38 Zhang, K. *et al.* Facile large-scale synthesis of monodisperse mesoporous silica nanospheres with tunable pore structure. *J. Am. Chem. Soc.* **135**, 2427-2430, doi:10.1021/ja3116873 (2013).
- 39 Chen, T., Ueda, Y., Dodge, J. E., Wang, Z. & Li, E. Establishment and Maintenance of Genomic Methylation Patterns in Mouse Embryonic Stem Cells by Dnmt3a and Dnmt3b. *Mol. Cell. Biol.* **23**, 5594-5605, doi:10.1128/mcb.23.16.5594-5605.2003 (2003).
- 40 Gibson, D. G. *et al.* Enzymatic assembly of DNA molecules up to several hundred kilobases. *Nat. Methods* **6**, 343-345, doi:10.1038/nmeth.1318 (2009).
- 41 Hancock, K. *et al.* A Recombinant Protein from *Schistosoma mansoni* Useful for the Detection of *S. mansoni* and *Schistosoma haematobium* Antibodies. *The Journal of Parasitology* **83**, 612, doi:10.2307/3284233 (1997).

7 Photoswitchable Supported Lipid Bilayers on Large-Pore Mesoporous Silica Nanoparticles For Controlled Release Applications

This chapter is based on a collaborative project with Manuel Gebauer, Hanna Engelke, James Frank and Dirk Trauner.



7.1 Introduction

Stimuli-responsive nanocarriers have attracted increasing attention for nanomedicine applications based on their ability to control the pharmacokinetics and biodistribution of their payload. The utilization of nanocarriers for drug delivery promises to offer advantages because nanocarriers can offer high loading capacity per particle, protect cargos from premature degradation, enhance the circulation half-life in the body, reduce the immunogenicity and toxicity of drugs, and potentially target specific cells or tissues for drug release.¹⁻⁶ Incorporating stimuli-responsive assemblies on nanocarriers can further allow for drug release in spatio-, temporal-, and dosage-controlled manners. Several types of nanocarriers have been developed to serve these purposes. Among these, liposomes represent one of the well-developed and promising family of nanocarriers for delivery of various therapeutics either *in vitro* or *in vivo*.⁷⁻⁹ Liposomes can feature high drug loading capacity (depending on the drug), good biocompatibility, low immunogenicity, flexible formulation, and facile scalable synthesis, which render them attractive carriers for nanomedicine applications.⁸⁻¹⁰ However, their rather unstable fluidic nature can also cause challenges including cargo leakage and uncontrollable payload release profiles (often burst release).

These issues can still be problematic for liposomal nanocarriers in terms of storage and long-term drug release (especially *in vivo*).⁸⁻¹⁰

Mesoporous silica nanoparticles (MSNs), consisting of inorganic frameworks and capable of stably accommodating diverse cargo molecules in their pore system, can offer properties that complement the features of liposomes. MSNs also feature several advantageous properties such as high surface area and large pore volume for high level cargo loading, tunable pore size and particle morphology for accommodating a variety of guest molecules, and flexible surface functionalization for various applications.¹¹ Notably, it is possible to combine the solid MSNs and fluidic liposomes, that is, coating a liposome on the surface of an MSN to form a supported lipid bilayer (SLB) for the construction of a new type of nanocomposite. The SLB-coated MSNs (SLB@MSNs) synergistically combine the strengths of liposomes and MSNs such that they are able to stably encapsulate the cargo without premature leakage, while retaining the high biocompatibility and low toxicity/immunogenicity properties of the liposomes.^{6,12}

In our previous studies we created SLB@MSN nanocomposites where the SLB was comprised of 1,2-dioleoyl-sn-glycero-3-phosphocholine (DOPC) and 1,2-dioleoyl-3-trimethylammonium-propane (DOTAP), showing high encapsulation efficiency for anti-cancer drugs, peptides, nanobodies and dye molecules.¹³⁻¹⁵ When exploiting photosensitizers as endosomal escape agents in the SLB@MSN nanocomposites, the loaded cargos can be released to the cytosol upon light-induced SLB/endosomal membrane rupture.^{14,15} In addition to the non-stimuli responsive DOPC/DOTAP lipid composite, pH-responsive^{16,17} (containing 1,2-dioleoyl-sn-glycero-3-phosphoethanolamine, DOPE) and pH/thermo dual responsive lipid composites¹⁸ (containing DOPE, 1,2-dipalmitoyl-sn-glycero-3-phosphocholine (DPPC) and copolymer poly(N-isopropylacrylamide-methacrylic acid-octadecyl acrylate)) have been used for creating SLBs around MSNs, respectively. Apart from the pH- and thermo-responsive SLBs, photoswitchable SLBs for controlled payload release would also be of great interest, as the photonic trigger is non-invasive and offers the possibility of remote spatiotemporal control for release of cargo.

Several photosensitive lipids have been synthesized and used to create photoswitchable liposomes for drug delivery purposes.^{19,20} These photoswitchable liposomes can be destabilized upon illumination at a certain wavelength, which subsequently induces isomerization,²¹ polymerization²² or cleavage²³ of the photosensitive moieties in the lipid

phase, leading to the destabilization of liposomal structure. Azobenzene is the most frequently used integral group in the photoisomerizable lipids. Upon irradiation with ultraviolet light (UV, 320 – 380 nm), azobenzene undergoes conformational change from an extended *trans* form to a twisted *cis* form. Moreover, this process is reversible such that the twisted *cis* configuration can be relaxed back to the *trans* configuration by illumination with blue light (400 – 450 nm) or heat.²⁴ In collaboration with Prof. Trauner's group, we constructed a photoswitchable SLB (opto-SLB) on MSNs based on this type of photoisomerizable phospholipid, named AzoPC. This AzoPC contains an azobenzene in one of the aliphatic tails of a phospholipid (Figure 7-1a), where the conformation of the azobenzene-containing tail can be switched forth and back to the *trans* and *cis* states *via* UV or blue light. We expected that the AzoPC-SLBs will be capable of sealing MSNs and preventing cargo leakage when the AzoPC is in *trans* configuration. Upon UV illumination, the AzoPC should isomerize to *cis* configuration, creating space or causing defects in the SLB structure, thereby allowing the cargo to diffuse out of the MSN pore system (Figure 7-1b). To test this concept, membrane-impermeable calcein was used as a model cargo for an *in vitro* encapsulation and release experiment of the photoswitchable SLB@MSNs. Additionally, the commercially available photopolymerizable lipid 1,2-bis(10,12-tricosadiynoyl)-sn-glycero-3-phosphocholine (DC_{8,9}PC) was employed with DOPC and DOTAP to create a second type of photoswitchable SLB on MSNs (Figure 7-1a). The photopolymerization of DC_{8,9}PC upon UV (254 nm) illumination is expected to create defects in the SLB structure (Figure 7-1c), followed by the destabilization of the SLB. *In vitro* calcein encapsulation and release experiments were also performed with these DC_{8,9}PC-SLB@MSNs. Strikingly, both the photoswitchable lipids proved to be able to impart light-induced dye release abilities as SLBs on the MSN cores, with a photo-induced dye release efficiency similar to that of reference surfactant (Triton X-100)-triggered dye release.

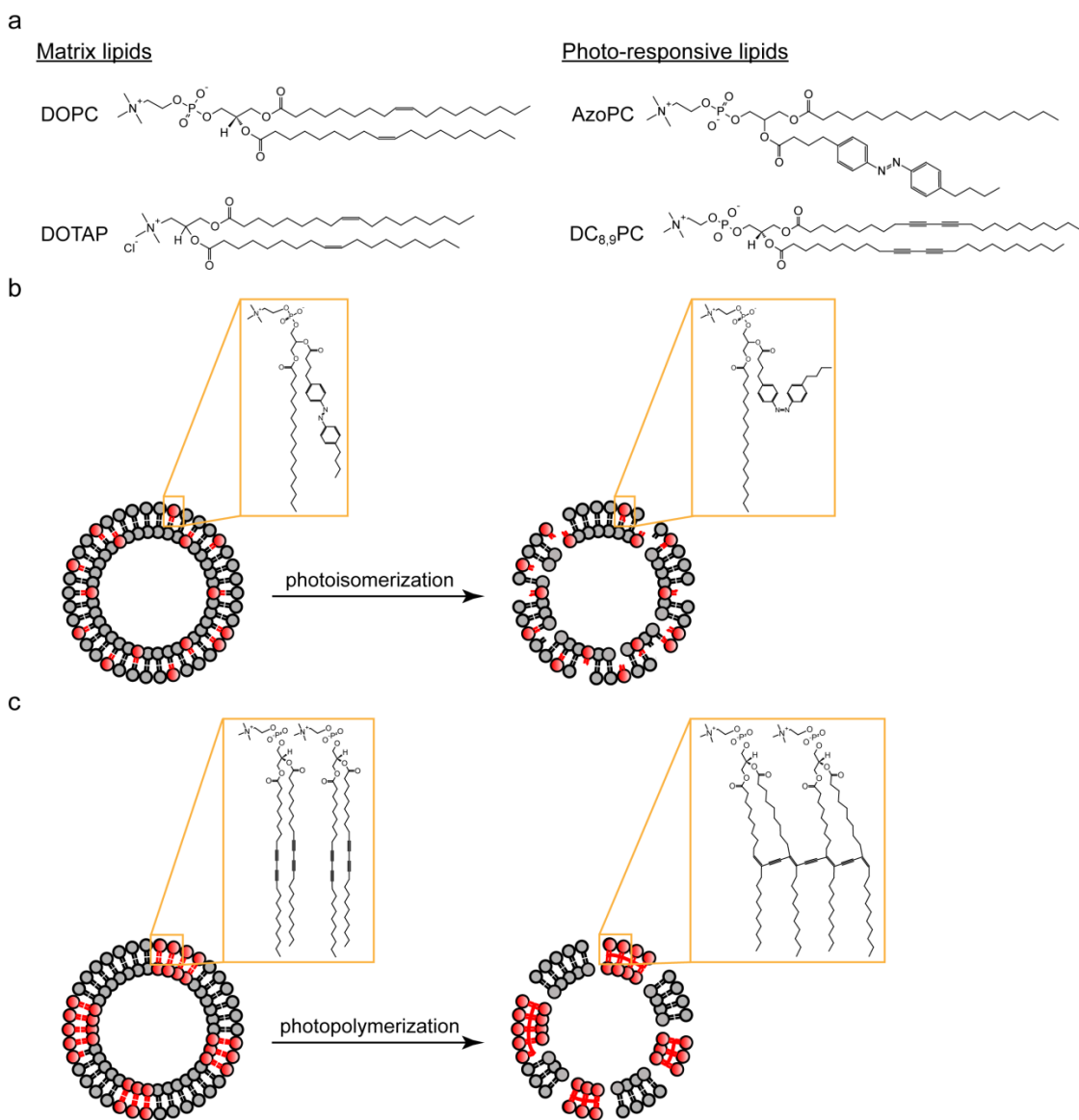


Figure 7-1 Lipid compositions for creating supported photosensitive lipid bilayers (SLBs) on MSNs and the photo activities of the photosensitive lipids in SLBs upon UV illumination. (a) Lipid compositions. (b) AzoPC undergoes photoisomerization when irradiated at wavelengths between 320 – 380 nm, generating space and defects in the SLB structure. (c) The diacetylene tails on DC_{8,9}PC are polymerized upon UV (254 nm) illumination, resulting in destabilization of the SLB.

7.2 Results and Discussion

To test the photoswitching abilities of the lipids, we first formed liposomes and characterized their photoswitching properties. Liposomes with different lipid compositions are listed in Table 1. In the present work, we employed DOPC and DOTAP as matrix lipids (Figure 7-1a) as they showed good MSN sealing abilities in our previous studies.¹³⁻¹⁵ Liposomes prepared with 70 wt% DOPC and 30 wt% DOTAP (matrix-liposome) served as the non-photoactive control group. AzoPC-liposomes were prepared by substitution of the DOPC content in the matrix liposomes with AzoPC, resulting in 70 wt% AzoPC and 30 wt% DOTAP in the composition. DC_{8,9}PC-liposomes were prepared by incorporating 20 wt% DC_{8,9}PC into the matrix liposomes, yielding 20 wt% DC_{8,9}PC, 56 wt% DOPC and 24 wt% DOTAP in the composition (Table 1). All the liposomes were prepared in 0.5X PBS (commercial PBS diluted with bidistilled water in the 1:1 v/v ratio) followed by extrusion through a 100 nm-pore membrane.

Table 1 Composition of liposomes

Liposomes	Lipid composition
Matrix-liposome	70 wt% DOPC + 30 wt% DOTAP
AzoPC-liposome	70 wt% AzoPC + 30 wt% DOTAP
DC _{8,9} PC-liposome	20 wt% DC _{8,9} PC + 56 wt% DOPC + 24 wt% DOTAP

Note: All the liposomes were prepared in 0.5X PBS buffer

Hydrodynamic sizes and zeta potentials of liposomes

According to the dynamic light scattering (DLS) analysis, the three as-prepared liposomes exhibit similar size around 70 – 80 nm in 0.5X PBS buffer (Figure 7-2a). This result indicates that the extrusion method has a dominant impact on the size distribution of these liposomes, independent of the lipid compositions. However, the hydrodynamic sizes of the liposomes are solvent-dependent; they are around 20 nm larger in water than in 0.5X PBS buffer (appendix Figure 7-7). The zeta potential of these liposomes in their storage buffer (0.5X PBS, pH 7.4) showed that although these liposomes were all made with a combination of zwitterionic phosphatidylcholines (PC) and positively charged lipid (DOTAP), matrix-liposomes and

DC_{8,9}PC-liposomes are positively charged while AzoPC-liposomes are negatively charged (Figure 7-2b). Makino *et al.* reported that the head-group region (from the choline group to the phosphatidyl group) of a neutral phospholipid varies its orientation in a liposome (i.e., with the phosphatidyl groups or choline groups facing the outer surface of liposomes) depending on the ionic strength and the temperature of the buffers.²⁵ They measured the zeta potentials of dimyristoylphosphatidylcholine (DMPC)-liposomes, dipalmitoylphosphatidylcholine (DPPC)-liposomes and distearoylphosphatidylcholine (DSPC)-liposomes, respectively in buffers containing different ionic strength at constant temperature as well as in buffers with constant ionic strength at different temperatures. They proposed that in low ionic strength buffer, the phosphatidyl groups orient towards the outside of the head region (appendix Figure 7-8), resulting in a negative surface charge. When increasing the ionic strength at constant temperature, the choline groups approach the outer region of the bilayer surface, leading to a more positive surface charge. In the present work, the three prepared types of liposomes all consist of more than one type of lipids, and the interactions between the lipids in the liposomes could also influence the orientation of the phosphocholine heads. Therefore, the variation of the zeta potential within these three types of liposomes is possibly attributed to the distinct orientation of their phosphocholine heads affected by the interactions of the mixed lipids.

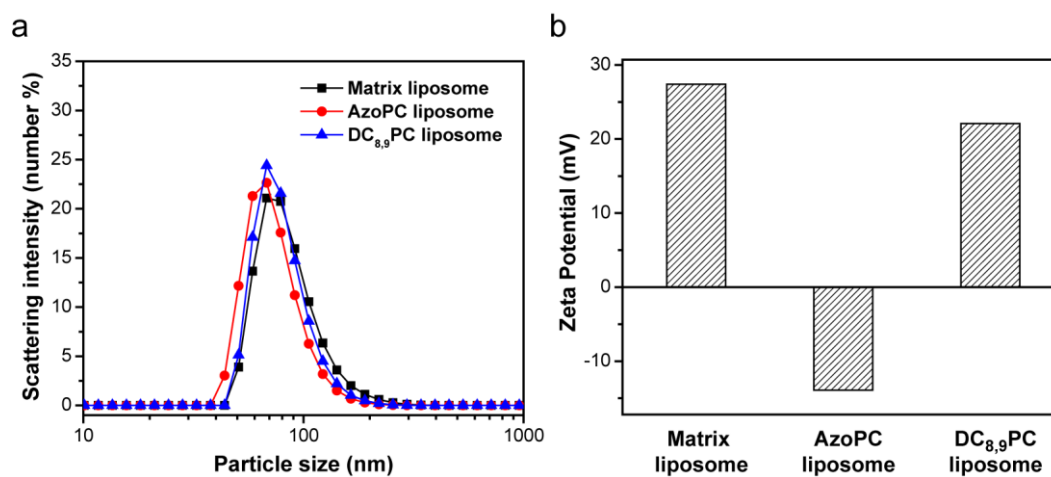


Figure 7-2 Hydrodynamic sizes and zeta potentials of liposomes in 0.5X PBS (pH 7.4). (a) Hydrodynamic sizes of liposomes measured by dynamic light scattering (DLS). (b) Zeta potentials of liposomes at pH 7.4. Matrix-liposome: 70 wt% DOPC + 30 wt% DOTAP; AzoPC-liposome: 70 wt% AzoPC + 30 wt% DOTAP; DC_{8,9}PC-liposome: 20 wt% DC_{8,9}PC + 56 wt% DOPC + 24 wt% DOTAP.

Photoswitching behavior of AzoPC-liposomes in 0.5X PBS buffer

The azobenzene group in the AzoPC can be switched from the thermally stable *trans* configuration to the *cis* configuration by UV irradiation (320 – 380 nm). This isomerization is reversible under blue light (400 – 450 nm) or heat (Figure 7-3a). Ultraviolet-visible (UV-Vis) spectroscopy was applied to identify the *trans* and *cis* isomers of the azobenzene. At room temperature in the dark, the AzoPCs in liposomes exist predominantly in their thermally stable extended *trans* form,²⁴ as illustrated in the UV-Vis absorption spectrum where the corresponding $\pi \rightarrow \pi^*$ transition (300 nm – 350 nm) is observed (Figure 7-3b, black line). Upon UV (365 nm) irradiation for 5 min, the azobenzene moieties in the liposomes isomerize to the *cis* form (Figure 7-3b, red line), causing the emergence of an $n \rightarrow \pi^*$ transition (400 – 480 nm) in the spectrum while the $\pi \rightarrow \pi^*$ absorption band shifts towards shorter wavelength and decreases in intensity.²⁴ We examined the feasibility to switch the AzoPC-liposomes back to their *trans* configuration using blue light (455 nm). As shown in Figure 7-3b (blue line, overlap with black line), the azobenzene moieties in the liposomes was successfully converted back to the *trans* configuration after illuminating with $\lambda = 455$ nm for 5 min. To investigate their continuous conformation switching ability, the AzoPC-liposomes were then illuminated with $\lambda = 365$ nm followed by $\lambda = 455$ nm for 5 min, respectively, and measured their UV-Vis spectra after each illumination. The results (Figure 7-3b, pink line and green line) indicated that the conformation of azobenzene moieties is able to be switched back and forth, meaning the possibilities of switching “open” and “close” of the AzoPC-liposomes.

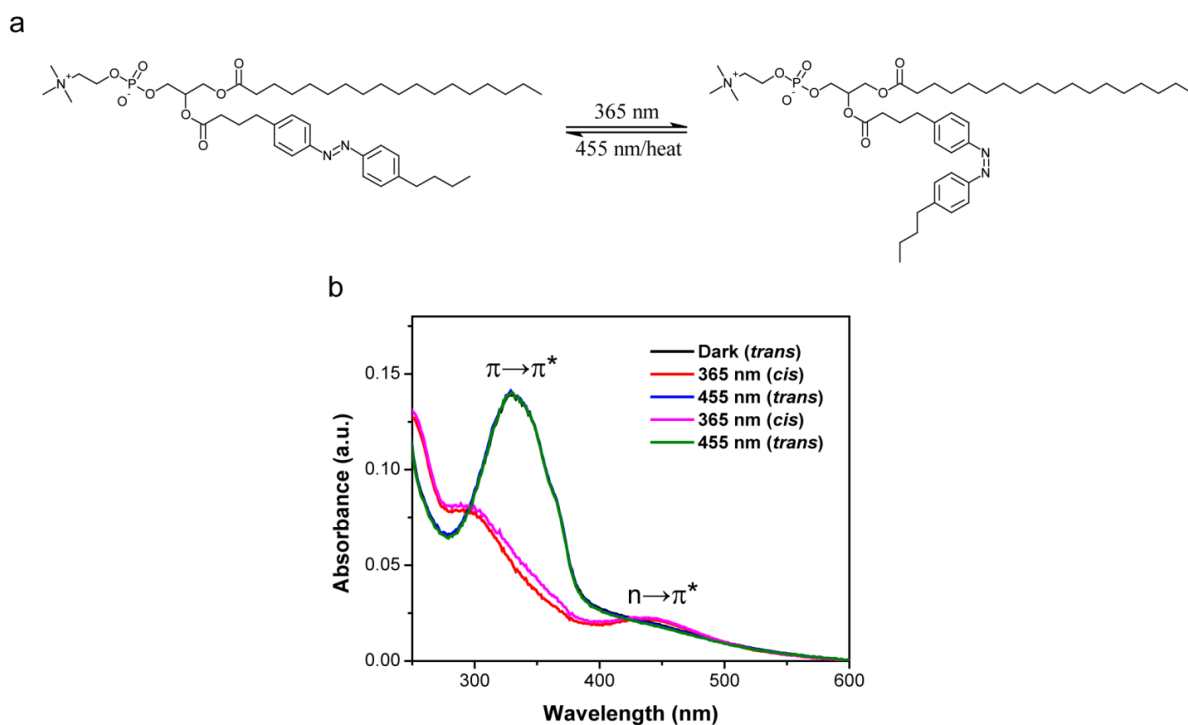


Figure 7-3 Photoswitching behavior of AzoPCs in liposomes. (a) Conformational change of AzoPC under light/heat induction. (b) UV-Vis spectra of AzoPC-liposomes (70 wt% AzoPC + 30 wt% DOTAP) in 0.5X PBS. Black line: liposomes preserved in dark. Red line: AzoPC-liposomes were illuminated with $\lambda = 365$ nm for 5 min. Blue line and green line: AzoPC-liposomes in *cis* configuration (the sample shown with red line) were irradiated with $\lambda = 455$ nm for 5 min. Pink line: AzoPC-liposomes in *trans* configuration (the sample shown with blue line) were irradiated with $\lambda = 365$ nm for 5 min. Green line: AzoPC-liposomes in *cis* configuration (the sample shown with pink line) were irradiated with $\lambda = 455$ nm for 5 min.

Photoswitchable supported lipid bilayers on mesoporous silica nanoparticles (opto-SLB@MSNs)

Next, we synthesized large-pore stellate MSNs with particle sizes of about 100 nm and a pore size distribution ranging from about 8 - 40 nm as the “hard cores” for creating opto-SLBs (Figure 7-4). *In vitro* fluorescent dye release experiments were performed to confirm the efficacy of opto-SLB@MSNs for controlled release applications.

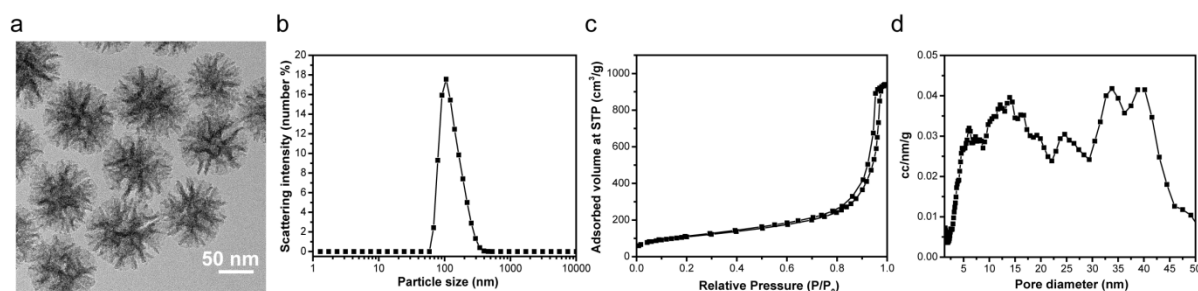


Figure 7-4 Large-pore stellate MSNs. (a) TEM micrograph. (b) DLS analysis of particle size distribution in ethanol. (c) N₂ sorption isotherm and (d) NLDFT pore size distribution.

Before dye loading, MSNs collected from the stock solution (in ethanol) were washed with PBS once to balance their surface charge. Membrane impermeable calcein was used as model cargo for release experiments and was loaded into MSNs *via* a simple MSN-calcein solution (1 mM in H₂O, pH 7.4) co-incubation method. Liposomes were then added to the MSN-calcein solutions for the fusion to create a supported lipid bilayer on the MSNs (Figure 7-5a). The opto-SLB@MSN samples were washed with 0.5X PBS to remove the free dyes followed by dispersing in 0.5X PBS for *in vitro* dye release experiments at 22 °C. As indicated in Figure 7-5, a negligible amount of calcein was released from the samples control-SLB@MSNs (Figure 7-5a) and AzoPC-SLB@MSNs (Figure 7-5b) while we found a small, but slightly enhanced leakage from the sample DC_{8,9}PC-SLB@MSNs (Figure 7-5c) in the first 2 h. After UV illumination (365 nm for control-SLB@MSNs and AzoPC-SLB@MSNs, 254 nm for DC_{8,9}PC-SLB@MSNs), the control-SLB still tightly capped the MSNs as there was no photo-responsive lipid in the SLB. On the other hand, both the photoswitchable AzoPC-SLBs and DC_{8,9}PC-SLBs were strongly destabilized followed by a significant release of calcein from the MSN pore system. In order to clarify whether the calcein release rate from the AzoPC-SLB@MSNs and DC_{8,9}PC-SLB@MSNs was already at maximum, we added Triton X-100 surfactant to the samples for complete SLB destabilization. As shown in Figure 7-6, calcein now started to diffuse out from the control-SLB@MSNs (destabilized by Triton) whereas the AzoPC-SLB@MSNs and DC_{8,9}PC-SLB@MSNs exhibited similar calcein release profiles as the photo-induced calcein release. This confirms that the photo-induced SLB destabilization for both photoswitchable opto-SLB systems occurred with the same high efficiency as the SLB destabilization achieved with Triton surfactant.

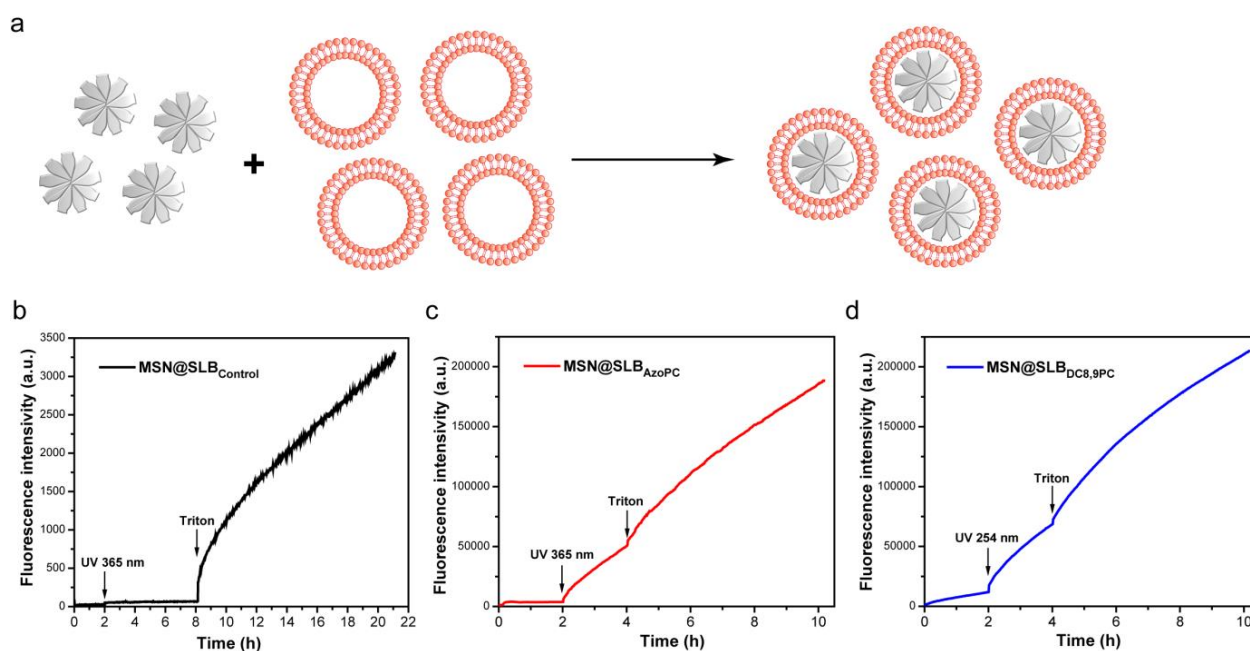


Figure 7-5 *In vitro* dye release experiments from SLB@MSN samples in 0.5X PBS at 22 °C. (a) SLB@MSNs were created by fusion of liposomes to MSNs. Calcein release from (b) control-SLB@MSNs, (c) AzoPC-SLB@MSNs and (d) DC_{8,9}PC-SLB@MSNs. Control-SLB: 70 wt% DOPC + 30 wt% DOTAP; AzoPC-SLB: 70 wt% AzoPC + 30 wt% DOTAP; DC_{8,9}PC-SLB: 20 wt% DC_{8,9}PC + 56 wt% DOPC + 24 wt% DOTAP. To trigger the light-induced dye release, control-SLB@MSNs and AzoPC-SLB@MSNs were illuminated with LED 365 nm (Thorlabs) in a constant current (500 mA) mode with a path length of 1 cm for 5 min. The DC_{8,9}PC-SLB@MSNs were illuminated with a UV lamp at a wavelength of 254 nm with a path length of 1 cm for 5 min. Triton (5 μ L, 20 wt% in H₂O) was then added to the sample to trigger a complete SLB destabilization.

To explore the potential of these novel opto-SLB@MSNs as nanocarriers for nanomedicine, we further performed the *in vitro* dye release experiments at 37 °C. As illustrated in Figure 7-6, the AzoPC-SLB capped MSNs now exhibit slight calcein leakage in the first 2 h. Upon photo-switching, a strong increase of the release rate of calcein from the AzoPC-SLB@MSNs was observed. Moreover, addition of Triton for complete SLB destabilization did not change the calcein release profile. Hence, we conclude that the AzoPC-SLB is photoswitchable and that the photo-induced dye release rate is as high as the Triton-induced dye release rate (at complete SLB destabilization) not only at 22 °C but also at body temperature (37 °C).

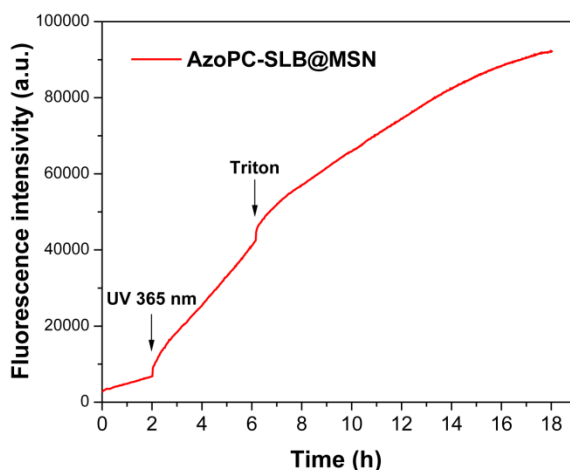


Figure 7-6 *In vitro* dye (calcein) release experiment from AzoPC-SLB@MSNs in 0.5X PBS at 37 °C. AzoPC-SLB@MSNs were illuminated with LED 365 nm (Thorlabs) in a constant current (500 mA) mode with a path length of 1 cm for 5 min. Triton (5 μ l, 20 wt% in H₂O) was then added to the sample to trigger a complete SLB destabilization.

7.3 Conclusions and Outlook

In summary, we have successfully created two types of photoswitchable supported lipid bilayers, AzoPC-SLB and DC_{8,9}PC-SLB, on large-pore MSNs for controlled release applications. The incorporated photosensitive lipids, AzoPC and DC_{8,9}PC, exhibit distinct photochemical responses and are sensitive to different wavelengths of light. AzoPC undergoes photoisomerization in liposomes when irradiated at $\lambda = 365$ nm, followed by generating space or defects in the supported lipid bilayers for payload release. DC_{8,9}PC lipids are photopolymerized when illuminated at $\lambda = 254$ nm, leading to SLB destabilization and offering a means to release cargo from MSNs. In the *in vitro* dye release experiments, both AzoPC-SLB@MSNs and DC_{8,9}PC-SLB@MSNs showed calcein encapsulation as well as efficient light-induced release in 0.5X PBS buffer at 22 °C. AzoPC-SLB@MSNs further demonstrated their photoswitchable ability for controlled cargo release at 37 °C. In the future, both types of opto-SLB@MSN nanocomposites will be attractive candidates for research with 3D cell cultures embedded in hydrogels to release chemo-attractants or other drugs under spatio-temporal control.

7.4 Experimental

Materials

1,2-Dioleoyl-sn-glycero-3-phosphocholine (DOPC, Avanti Polar Lipids), 1,2-dioleoyl-3-trimethylammonium-propane (DOTAP, Avanti Polar Lipids), AzoPC (azobenzene-containing lipid)²⁶ was synthesized in Prof. Dirk Trauner's group (LMU). 1,2-Bis(10,12-tricosadiynoyl)-sn-glycero-3-phosphocholine (DC_{8,9}PC, Avanti Polar Lipids), calcein (Aldrich), phosphate buffered saline (PBS, Sigma), Triton X-100 (Aldrich), tetraethyl orthosilicate (TEOS, Aldrich, $\geq 99\%$), cetyltrimethylammonium p-toluenesulfonate (CTATos, Sigma), triethanolamine (TEA, Aldrich, 98%), ethanol (EtOH, Aldrich, absolute), hydrochloric acid (HCl, Aldrich, 37%). Bidistilled water is obtained from a Millipore system (Milli-Q Academic A10). 0.5X PBS was prepared by mixing PBS buffer and bidistilled water in a 1:1 v/v ratio.

Preparation of liposomes

Lipids were dissolved in chloroform at the concentration of 10 mg/mL as lipid stock solutions and were stored at -20 °C for further liposome preparation. Lipids from stock solutions were mixed in the required mass ratio (see Table 1) in an Eppendorf tube, which contained 2.5 mg lipids in total. The lipid mixture was dried in a round-bottom flask to form lipid thin films using a rotary evaporator (15 min, 40 °C water bath, 100 mbar, 200 rpm). The dried lipid thin films were re-suspended in 1 mL of 0.5X PBS buffer, and the lipid suspension was further rotated (250 rpm) at RT for 1 h. The lipid suspension then stayed static for 2 h at RT for aging, and was stored at 4 °C overnight. To reduce and homogenize the size of the liposomes, the lipid suspension was extruded by a mini-extruder (Avanti Polar Lipids) with a 100 nm-pore membrane for 11 extrusion cycles. The final liposome solution (2.5 mg/mL) was stored at 4 °C in the dark till further use. Light was avoided in all procedures for the preparation of photosensitive liposomes.

Characterization of liposomes

Dynamic light scattering (DLS) and zeta potential measurements were performed on a Malvern Zetasizer-Nano instrument equipped with a 4 mW He-Ne laser (633 nm) and an avalanche photodiode. DLS measurements were directly recorded in diluted suspensions of liposomes at a concentration of 50 µg/ml in 0.5X PBS buffer. For zeta potential measurements, liposomes were measured in 0.5X PBS (pH 7.4) with the concentration of

25 µg/mL. UV-Vis spectroscopy was performed on a Perkin Elmer Lambda 1050 UV/Vis/NIR spectrophotometer equipped with a deuterium arc lamp (UV), a tungsten filament (visible) and an InGaAs integrating sphere detector. AzoPC-liposomes were diluted to the concentration of 50 µg/ml in 0.5X PBS buffer in a quartz cuvette for the measurement. The initial spectrum (dark adapted state) was first recorded. The sample was illuminated with $\lambda = 365$ nm (power density: 255 mW/cm²) for 10 min (*cis*-adapted state), then the second spectrum was subsequently recorded. The third spectrum was recorded after irradiation with $\lambda = 455$ nm (power density: 226 mW/cm²) for 10 min on the *cis*-adapted state sample. The illumination was conducted using mounted LEDs (Thorlabs, USA) having wavelengths of 365 nm and 455 nm, respectively, at constant current (500 mA) mode and an illumination path length of 1 cm for 10 min at room temperature.

MSN synthesis and characterization

Large-pore stellate MSNs were synthesized based on an adapted recipe reported in the literature.²⁷ Briefly, TEA (0.047 g, 0.32 mmol), CTATos (0.263 g, 0.58 mmol) and H₂O (13.7 g, 0.77 mmol) were mixed in a 100 mL round bottom flask and stirred vigorously (1250 rpm) at 80 °C until the surfactants were totally dissolved. TEOS (2.013 g, 9.6 mmol) was added to the surfactant solution drop-wise, and the mixture was continuously stirred at 80 °C for 2 h. The molar ratio of the above mixture was TEOS : CTATos : TEA : H₂O = 1 : 0.06 : 0.033 : 80. The as-synthesized particles were cooled down to RT and were collected by centrifugation (7197 g, 20 min). To remove the organic surfactant from MSNs, the as-synthesized particles were heated in an ethanolic solution (150 mL) containing 3 g of ammonium nitrate at 90 °C under reflux for 1 h. The solution was then cooled and the particles were collected by centrifugation (7197 g, 20 min). A second extraction step was subsequently performed in a 2 M HCl/ethanolic solution (150 mL) under reflux at 90 °C for 1 h. Afterwards, samples were washed in the sequence of EtOH, H₂O, EtOH and were finally kept in EtOH. Particles were collected by centrifugation (7197 g, 20 min) after each washing step.

MSN Characterization

For transmission electron microscopy (TEM), samples were prepared by drying a diluted MSN suspension (in ethanol) on a carbon-coated copper grid at room temperature for several hours before measurement. The measurement was performed on a FEI Titan 80-300 kV

microscope operating at 300 kV . Nitrogen sorption analyses were performed on a Quantachrome Instrument NOVA 4000e at 77 K. Sample outgassing was performed at 120 °C under vacuum (10 mTorr) 16 h before measurement. Pore size distribution curves were calculated with non-local density functional theory (NLDFT) procedures provided by Quantachrome based on the adsorption branch of N₂ on silica. Dynamic light scattering (DLS) was performed on a Malvern Zetasizer-Nano instrument equipped with a 4 mW He-Ne laser (633 nm) and an avalanche photodiode. DLS measurements were directly recorded in diluted suspensions of the particles at a concentration of 1 mg/ml in ethanol.

Fusion of liposomes with MSNs

The amount of 2 mg of MSNs from stock solution (in ethanol) was collected by centrifugation (14000 rpm, 5 min) and washed with PBS buffer once before loading with calcein. The MSNs were dispersed in 400 µL of calcein solution (1 mM in H₂O, pH 7) and incubated under shaking at RT for 1 h in the dark. 100 µL of the MSN-calcein solution (containing 0.5 mg of MSNs) was mixed with 100 µL of liposome solution (containing 250 µg of liposomes), and the mixture was incubated at RT under shaking for 1 h in the dark for the liposome-MSN fusion. The resulting opto-SLB@MSNs were subsequently washed with 0.5X PBS three times. In each washing step, centrifugation (8000 rpm, 4 min, 15 °C) was applied to remove the residual dyes and liposomes. The final opto-SLB@MSN sample was re-suspended in 200 µL of 0.5X PBS buffer for the following release experiment.

Release experiments

SLB@MSNs in 200 µl of 0.5X PBS were transferred to a custom-made Teflon cap fitting on a fluorescence cuvette. The cap was sealed with a dialysis membrane (ROTH Visking type 8/32, MWCO 14,000 g/mol) and placed on top of a fluorescence cuvette filled with 3 mL 0.5X PBS. Time-based fluorescence release experiments were performed at 22 °C or 37 °C on a PTI spectrofluorometer equipped with a xenon short arc lamp (UXL-75XE USHIO) and a photomultiplier detection system (model 810/814). The excitation wavelength was set to $\lambda = 495$ nm and the emission fluorescence intensity was recorded at $\lambda = 520$ nm. All slits were adjusted to 2.0 mm. To trigger the light-induced dye release, control-SLB@MSNs and AzoPC-SLB@MSNs were illuminated with LED 365 nm (Thorlabs) in a constant current (500 mA, power density: 255 mW/cm²) mode with a path length of 1 cm for 5 min. The DC_{8,9}PC-SLB@MSNs were illuminated with a UV lamp at a wavelength of 254 nm with a

path length of 1 cm (power density: 0.7 mW/cm^2) for 20 min. Afterwards, all samples were sealed with the dialysis membranes and the release setups were reassembled. The fluorescence cuvettes were re-filled with fresh 0.5X PBS before reassembly. Fluorescence spectra ($\lambda_{\text{ex}} = 495 \text{ nm}$, $\lambda_{\text{em}} = 520 \text{ nm}$) were recorded continuously for 2 to 4 h. To destabilize the SLBs completely, 5 μl of Triton X-100 (20 w/v% in H_2O) was added to each sample, respectively. Fluorescence spectra ($\lambda_{\text{ex}} = 495 \text{ nm}$, $\lambda_{\text{em}} = 520 \text{ nm}$) were recorded continuously overnight.

7.5 Appendix

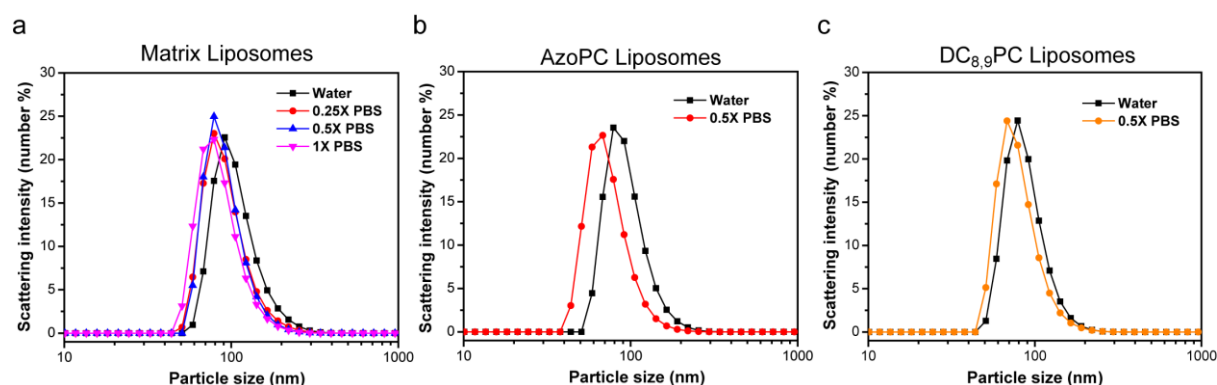


Figure 7-7 Hydrodynamic sizes of liposomes in different buffers. (a) Matrix-liposomes (70 wt% DOPC + 30 wt% DOTAP). (b) AzoPC-liposomes (70 wt% AzoPC + 30 wt% DOTAP). (c) DC_{8,9}PC-liposomes (20 wt% DC_{8,9}PC + 56 wt% DOPC + 24 wt% DOTAP).

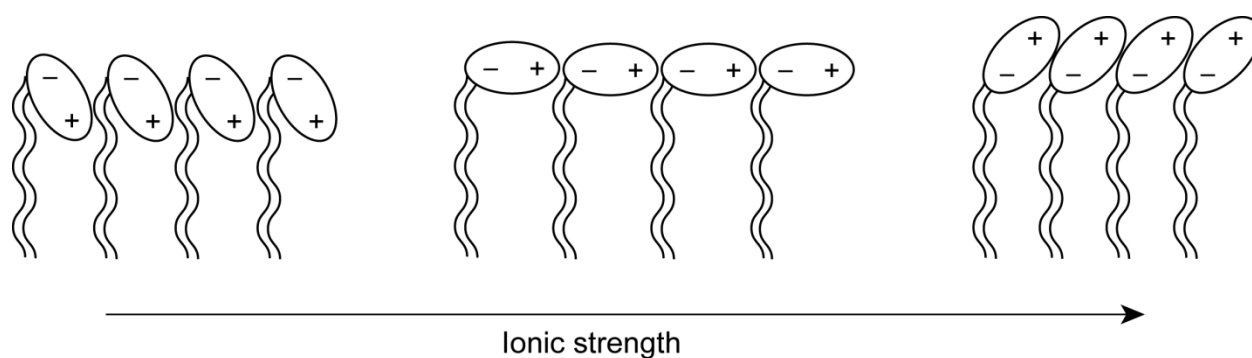


Figure 7-8 Schematic illustration of the orientation of the head groups in phospholipids. This figure is adapted from Makino *et al.*²⁵

7.6 References

- 1 Torchilin, V. P. Multifunctional, stimuli-sensitive nanoparticulate systems for drug delivery. *Nat. Rev. Drug Discov.* **13**, 813-827 (2014).
- 2 Mura, S., Nicolas, J. & Couvreur, P. Stimuli-responsive nanocarriers for drug delivery. *Nat Mater* **12**, 991-1003 (2013).
- 3 Lu, Y., Sun, W. & Gu, Z. Stimuli-responsive nanomaterials for therapeutic protein delivery. *J Control Release* **194**, 1-19 (2014).
- 4 Stewart, M. P. *et al.* In vitro and ex vivo strategies for intracellular delivery. *Nature* **538**, 183-192 (2016).
- 5 Blanco, E., Shen, H. & Ferrari, M. Principles of nanoparticle design for overcoming biological barriers to drug delivery. *Nat. Biotechnol.* **33**, 941-951 (2015).
- 6 Butler, K. S. *et al.* Protocells: Modular Mesoporous Silica Nanoparticle-Supported Lipid Bilayers for Drug Delivery. *Small* (2016).
- 7 Torchilin, V. P. Multifunctional nanocarriers. *Adv Drug Deliv Rev* **58**, 1532-1555 (2006).
- 8 Allen, T. M. & Cullis, P. R. Liposomal drug delivery systems: from concept to clinical applications. *Adv Drug Deliv Rev* **65**, 36-48 (2013).
- 9 Laouini, A. *et al.* Preparation, Characterization and Applications of Liposomes: State of the Art. *Journal of Colloid Science and Biotechnology* **1**, 147-168 (2012).
- 10 Mashaghi, S., Jadidi, T., Koenderink, G. & Mashaghi, A. Lipid nanotechnology. *Int J Mol Sci* **14**, 4242-4282 (2013).
- 11 Argyo, C., Weiss, V., Bräuchle, C. & Bein, T. Multifunctional Mesoporous Silica Nanoparticles as a Universal Platform for Drug Delivery. *Chem. Mater.* **26**, 435-451 (2014).
- 12 Tarn, D. *et al.* Mesoporous silica nanoparticle nanocarriers: biofunctionality and biocompatibility. *Acc. Chem. Res.* **46**, 792-801 (2013).
- 13 Cauda, V. *et al.* Colchicine-loaded lipid bilayer-coated 50 nm mesoporous nanoparticles efficiently induce microtubule depolymerization upon cell uptake. *Nano Lett.* **10**, 2484-2492 (2010).
- 14 Schlossbauer, A. *et al.* Cascaded photoinduced drug delivery to cells from multifunctional core-shell mesoporous silica. *Adv Healthc Mater* **1**, 316-320 (2012).
- 15 Mackowiak, S. A. *et al.* Targeted drug delivery in cancer cells with red-light photoactivated mesoporous silica nanoparticles. *Nano Lett.* **13**, 2576-2583 (2013).
- 16 Ashley, C. E. *et al.* The targeted delivery of multicomponent cargos to cancer cells by nanoporous particle-supported lipid bilayers. *Nat Mater* **10**, 389-397 (2011).

- 17 Wang, D. *et al.* The eradication of breast cancer cells and stem cells by 8-hydroxyquinoline-loaded hyaluronan modified mesoporous silica nanoparticle-supported lipid bilayers containing docetaxel. *Biomaterials* **34**, 7662-7673 (2013).
- 18 Wu, X. *et al.* pH and thermo dual-stimuli-responsive drug carrier based on mesoporous silica nanoparticles encapsulated in a copolymer-lipid bilayer. *ACS applied materials & interfaces* **5**, 10895-10903 (2013).
- 19 Leung, S. J. & Romanowski, M. Light-activated content release from liposomes. *Theranostics* **2**, 1020-1036 (2012).
- 20 Puri, A. Phototriggerable liposomes: current research and future perspectives. *Pharmaceutics* **6**, 1-25 (2013).
- 21 Bisby, R. H., Mead, C. & Morgan, C. G. Wavelength-programmed solute release from photosensitive liposomes. *Biochem. Biophys. Res. Commun.* **276**, 169-173 (2000).
- 22 Yavlovich, A., Singh, A., Blumenthal, R. & Puri, A. A novel class of photo-triggerable liposomes containing DPPC:DC(8,9)PC as vehicles for delivery of doxorubicin to cells. *Biochim. Biophys. Acta* **1808**, 117-126 (2011).
- 23 Anderson, V. C. & Thompson, D. H. Triggered release of hydrophilic agents from plasmalogen liposomes using visible light or acid. *Biochim. Biophys. Acta* **1109**, 33-42 (1992).
- 24 Merino, E. & Ribagorda, M. Control over molecular motion using the cis-trans photoisomerization of the azo group. *Beilstein J Org Chem* **8**, 1071-1090 (2012).
- 25 Makino, K. *et al.* Temperature- and ionic strength-induced conformational changes in the lipid head group region of liposomes as suggested by zeta potential data. *Biophys. Chem.* **41**, 175-183 (1991).
- 26 Pernpeintner, C. *et al.* Light-Controlled Membrane Mechanics and Shape Transitions of Photoswitchable Lipid Vesicles. *Langmuir* (2017).
- 27 Zhang, K. *et al.* Facile large-scale synthesis of monodisperse mesoporous silica nanospheres with tunable pore structure. *J. Am. Chem. Soc.* **135**, 2427-2430 (2013).

8 Conclusions and Outlook

In the present work, we have established diverse multifunctional large-pore mesoporous silica nanoparticles (MSNs) for macromolecule immobilization and transportation, especially for intracellular protein delivery. We demonstrated the approaches regarding tailoring the particle sizes, pore structures and surface chemistry of these newly developed large-pore MSNs to fit the purposes of different applications.

In the first project (chapter 3), we adopted a dual-surfactant synthesis strategy containing fluorocarbon surfactant FC-4 and triblock-copolymer P123 for the synthesis of nanosized SBA-15 particles. The SBA-15-like MSNs feature well-ordered 2D hexagonal mesostructure with pore size of 7 nm. After size separation by filtration, we obtained particles with a size of 100–200 nm. A delayed co-condensation method was further applied to the synthesis approach, yielding spatially defined, core-shell bifunctional SBA-15 MSNs. Cellular studies with the SBA-15 MSNs illustrated that these particles can be efficiently taken up by HeLa cells and are non-cytotoxic up to a concentration of 200 $\mu\text{g/ml}$, promising prospects for using these particles for cellular delivery applications. However, the as-synthesized materials often contain bulk precipitates as well as particles with irregular morphology. A further investigation regarding optimization of the synthesis parameters, for example the molar composition of the reaction solution, the stirring rate during the reaction and reaction time, etc., to gain more homogeneous particle morphology and narrow particle size distribution would be highly desirable.

In the project described in chapter 4, we synthesized and tailored the surface properties of ultra-large-pore stellate MSNs. The impact of different organosilanes on the formation of mesostructure and particle morphology was studied. A core-shell bifunctional MSN structure was also created using a sequential co-condensation method to spatially confine one functional group in the interior core while the second functional group resides on the external surface. With this core-shell structure, we demonstrated the feasibility of both external and internal MSN surface modification. DBCO derivatives were covalently attached on the interior surface of the MSNs, allowing for a facile cargo conjugation *via* copper-free click chemistry. In combination with redox-sensitive disulfide bridged or pH-sensitive acetal linkers in our multifunctional MSN system, we were able to control the cargo release in specific buffer conditions. An outlook for this work will focus on exploiting the copper-free

click chemistry for bioorthogonal conjugation of biomolecules and applying the system for cellular delivery as well as for different controlled release applications.

In the work described in chapter 5, we designed a nitrilotriacetic acid-metal ion-complexed moiety on the surface of MSNs for pH-responsive coordination binding and release of His-tagged chromobodies (fluorescent nanobodies). Chromobodies offer high antigen binding specificity and affinity comparable to conventional antibodies and can be used in live cell imaging for specific spatio-temporal visualization of cellular processes. The results demonstrated that MSN-Ca²⁺, MSN-Ni²⁺ and MSN-Zn²⁺ carriers all exhibit high chromobody loading capacities (about 70 µg/mg MSNs) and are applicable for successful intracellular chromobody delivery. Various endosomal destabilization strategies were investigated in this study where DMSO and chloroquine performed as the most effective triggers for cytosolic release. By combining chromobodies and MSNs, we aimed to establish a powerful and generalized platform that provides an easy transportation route for all types of chromobodies into living cells for quick antigen targeting and visualization.

In chapter 6, we developed a chemically inducible two-component fluorescent live cell sensor for the investigation of MSN-mediated protein delivery efficiency. This live cell sensor features background-free and molecular ratio-metric fluorescence properties that facilitate direct relative quantification of bioavailable protein levels and cell protein transfection efficiency. MSN-NTA-Ni was used as a vector here for protein transfection. In parallel with an MTT assay, we maximized the protein delivery efficiency up to about 80%. We further demonstrated a real-time protein delivery process with good temporal resolution to study the protein release kinetics and the system fluorescence complementation rate. Unlike sensors that rely upon transcription or amplification mechanisms, the ratio-metric nature of our sensor enables us to measure protein delivery variations not only between but also within cell populations. With this system, we envision a protein delivery efficiency measurement that can be extended to precisely calculate delivered molecular numbers within individual cells.

Apart from the direct conjugation of cargos *via* chemical bonding, we also created supported lipid bilayers on MSNs for guest molecule encapsulation. In chapter 7, we developed two types of photoswitchable supported lipid bilayers (opto-SLBs), AzoPC-SLB and DC_{8,9}PC-SLB, on MSNs and demonstrated their photo-induced cargo release abilities. The azobenzene groups in AzoPC-SLB undergo photoisomerization upon irradiation at $\lambda = 350$ nm that

generates space between the SLB structure for payload release. The diacetylene acyl chains in DC_{8,9}PC-SLB are photopolymerized when illuminated at $\lambda = 254$ nm, causing defects in the SLB structure thus enabling cargo release. As an outlook, we can envision embedding the opto-SLB capped MSNs in hydrogels for use in 3D cell culture research.

In summary, we have developed a general and highly tunable platform based on large-pore MSNs for large biomolecule delivery. The versatile surface modifications with release-on-demand properties established here allow for a broad spectrum of applications involving spatiotemporal control of drug or protein release. These properties make them powerful nanoagents in theranostic applications as well as cell biology research. While the high efficacy of MSNs in protein delivery has been demonstrated *in vitro*, it would be highly desirable to extend these strategies to future *in vivo* studies.

9 Curriculum Vitae

Personal Information

Name:	Chiu, Hsin-Yi
Date of Birth:	14. Jan. 1985
Place of Birth:	Taoyuan, Taiwan
Nationality:	Taiwan
Address:	Ruffiniallee 18h, 82152 Planegg, Germany

Education

2011/10 - 2017/08	PhD in Chemistry Ludwig-Maximilians Universität München, Munich, Germany Supervisors: Prof. Dr. Thomas Bein and Prof. Dr. Heinrich Leonhardt <u>PhD thesis:</u> Synthesis and functionalization of multifunctional large-pore mesoporous silica nanoparticles for intracellular protein delivery
2007/09 - 2009/07	Mater of Science in Materials Science and Engineering National Tsing-Hua University, Hsinchu, Taiwan. <u>Master thesis:</u> ZnO nanostructures: synthesis, characterization and applications Supervisor: Prof. Ta-Jen Yen
2003/09 - 2007/06	Bachelor of Science in Chemical Engineering National Tsing-Hua University, Hsinchu, Taiwan. <u>Bachelor thesis:</u> Ex vivo enhancement in re-differentiation of passaged chondrocytes by baculovirus-mediated growth factors Supervisor: Prof. Yu-Chen Hu

Professional Experience

2009/08 - 2011/08

Research Assistant in Chemical Engineering

National Tsing-Hua University, Hsinchu, Taiwan.

Project: Development of enterovirus 71 virus-like particle vaccine

Supervisor: Prof. Yu-Chen Hu

Publications

1. **Chiu, H.-Y.**, Bates, J., Helma, J., Engelke, H., Bein, T., Leonhardt, H.. Optimisation and live cell tracking of nanoparticle mediated protein delivery through an inducible split venus based system, *to be submitted*.
2. **Chiu, H.-Y.**, Bein, T.. Clickable Multifunctional Large-Pore Mesoporous Silica Nanoparticles as Nanocarriers, *to be submitted*.
3. **Chiu, H.-Y.**, Bein, T.. Synthesis and functionalization of ordered large-pore mesoporous silica nanoparticles for biomedical applications. 2017. *Chem. Ing. Tech.* 89, 876-886. (Dedication contribution for the 65th birthday of Professor Wihelm Schwieger)
4. **Chiu, H.-Y.**, Deng, W., Engelke, H., Helma, J., Leonhardt, H., Bein, T.. 2016. Intracellular chromobody delivery by mesoporous silica nanoparticles for antigen targeting and visualization in real time. *Scientific Reports*. 6, 25019.
5. Nowald, C., Penk, A., **Chiu, H.-Y.**, Bein, T., Huster, D., Lieleg, O.. A selective mucin/methylcellulose hybrid gels with tailored mechanical properties. 2016. *Macromolecular Bioscience*. 16, 567-579.
6. Lin, S.-Y., Chung, Y.-C., **Chiu, H.-Y.**, Chi, W.-K., Chiang, B.-L., Hu, Y.-C.. 2014. Evaluation of the stability of enterovirus 71 virus-like particle. *J. Biosci. Bioeng.* 117, 366-371
7. Lu, C.-H., Lin, K.-J., **Chiu, H.-Y.**, Chen, C.-Y., Yen, T.-C., Hwang, S.-M., Chang, Y.-H., Hu, Y.-C.. 2012. Improved chondrogenesis and engineered cartilage formation from TGF- β 3-expressing adipose-derived stem cells cultured in the rotating-shaft bioreactor.

8. Chung, C.-Y., Chen, C.-Y., Lin, S.-Y., Chung, Y.-C., **Chiu, H.-Y.**, Chi, W.-K., Lin, Y.-L., Chiang, B.-L., Chen, W.-J., Hu, Y.-C.. 2010. Enterovirus 71 virus-like particle vaccine: Improved production conditions for enhanced yield. *Vaccines*. 28, 6951-6857.
9. Lin, C.-Y., Lu, C.-H., Luo, W.-Y., Chang, Y.-H., Sung, L.-Y., **Chiu, H.-Y.**, Hu, Y.-C.. 2010. Baculovirus as a gene delivery vector for cartilage and bone tissue engineering. *Curr. Gene Ther.* 10, 242-254.
10. Sung, L.-Y., **Chiu, H.-Y.**, Chen, H.-C., Chen, Y.-L., Chuang, C.-K., Hu, Y.-C.. 2009. Baculovirus-mediated growth factors expression in de-differentiated chondrocytes accelerates re-differentiation: Effects of combinational transduction. *Tissue Eng. Part A.* 15, 1353-1362.
11. Sung, L.-Y., Lo, W.-H., **Chiu, H.-Y.**, Chen, H.-C., Chuang, C.-K., Lee, H.-P., Hu, Y.-C.. 2007. Modulation of chondrocyte phenotype via baculovirus-mediated growth factor expression. *Biomaterials*. 28, 3437-3447.